Filter Theory Inspired Antenna Decoupling Technologies

By

Jianfeng Qian

Submitted for the Degree of

Doctor of Philosophy

in

Electronic Engineering

From the

University of Kent

Feb 2024

Declaration

This thesis is dedicated to

My parents

My Wife

And

My Daughter

Abstract

In modern communication systems, the growing challenge of reconciling diminishing spatial resources with increasing wireless performance demands has become increasingly pronounced. The issue of mutual coupling between antennas has garnered widespread attention to accommodate more antennas with reduced spatial resources. Extensive research has been conducted by researchers to address these problems. Different from conventional antenna decoupling techniques, this dissertation presents an innovative investigation of antenna coupling issues from the perspective of filter theory.

This thesis first introduces the background, motivation, and contributions of this work. Then, the general mutual coupling problems and corresponding decoupling techniques are reviewed. To address these problems, multiple novel techniques are presented in this thesis. A hybrid feeding network is presented for achieving two isolated filtering antennas. Cascaded resonator decoupling networks are investigated to provide two isolated antenna channels. Co-synthesis method and steps are provided. Then, a novel concept of designing two slot antennas as a bandstop filter, to achieve self-decoupled antenna ports, is presented. Two low-cost decoupling techniques are presented to decouple two closely placed patch antennas. The first technique is inspired by the electric and magnetic coupling theory in filter design whereas the other technique is inspired by the coupled transmission line theory in filter design.

All contributions have been experimentally validated. These exciting results robustly affirm the practical utility of filter theory in the context of antenna decoupling design, offering valuable insights and directions for antenna design in practice.

Terms and Abbreviations

ACLR	Adjacent Channel Leakage Ratio
ADS	Advanced Design System
ANT	Antenna
AP	Access Point
BAW	Bulk Acoustic Wave
BPF	Bandpass Filter
BS	Base Station
BSF	Bandstop Filter
BW	Bandwidth
CT	Cascaded Trisection
CTL	Coupled Transmission Line
DN	Decoupling Network
E	Electric
ECC	Envelope Correlation Coefficient
EM	Electromagnetic
EMCC	Electric and Magnetic Coupling Cancellation
FA	Filtering Antenna
FBW	Fractional Bandwidth
FDD	Frequency Division Duplex
FPD	Filtering Power Divider
FR	Frequency Ratio
GHz	Gigahertz
GNSS	Global Navigation Satellite System
GPS	Global Position System
H	Magnetic
HFSS	High Frequency Structure Simulator
IAD	Isolation After Decoupling
IBFD	In-Band Full Duplex
IBMC	In-Band Mutual Coupling
IoT	Internet of Things
LTCC	Low-Temperature-Co-fired-Ceramic
LTE	Long Term Evolution
LU	Length Unbalance
MHz	Megahertz
MIMO	Multi-Input-Multi-Output
MSHM	Microstrip-Slotline Hybrid Mode
NoP	Number of Ports
NR	New Radio
N.G.	Not Given
N.A.	Not Available
OBD	Out-of-Band Decoupling

OBMC	Out-of-Band Mutual Coupling
PCB	Printed Circuit Board
PD	Power Dividing
PIFA	Planar Inverted-F Antenna
Q	Quality factor
RF	Radio Frequency
RL	Return Loss
RoR	Roll-off-Ratio
RSHM	Resonator-Slotline Hybrid Mode
RX	Receive
SNR	Signal-to-Noise Ratio
SAW	Surface-Acoustic Wave
SIW	Substrate-Integrated Waveguide
TDD	Time-Division Duplex
TL	Transmission Lines
TX	Transmit
TZ	Transmission Zero
UD	User Device
V2X	Vehicle-to-Everything
w.	with
wo.	without

Acknowledgments

First of all, I want to thank Professor Steven Gao for providing me with a very interesting research topic for my thesis and for his kind supervision, his support, and his encouragement.

I would like to thank my supervisor Dr. Benito Sanz-Izquierdo for his valuable support after Professor Steven Gao's leave. Meeting him every week really inspired me significantly.

I would like to thank my industrial supervisors Dr. Hanyang Wang, Dr. Hai Zhou, and Dr. Huiliang Xu, for sharing their extensive industrial experience in antenna design and academic work. Especially, I want to thank Dr. Wang for giving me tremendous freedom in my research and for his support. Everything I learned from Dr. Wang will always be my lifetime treasure.

I am also grateful to Mr. Antonio Mendoza for his technical support on antenna measurements. The radiation performance of all the antennas in this thesis was measured by Mr. Mendoza using the anechoic chamber at the University of Kent. All the antenna prototypes were fabricated by Guangdong HuiXinPu Circuit Co. Ltd (HXP Circuit) and I extend my thanks to HXP Circuit for their excellent fabrication services. Special thanks also go to my other brilliant colleagues and very nice friends.

Finally, I would like to express my deepest gratitude to my parents for their unconditional support and love. I would also like to give my utmost gratitude to my wife Nana Ma. Thanks for her support over the years.

Publications

Journal papers:

[1] **Jianfeng Qian** *et al*., “Mutual coupling suppression between two closely placed patch antennas using higher order modes,” *IEEE Transactions on Antennas and Propagation*, pp. 1-1, 2023.

[2] **Jianfeng Qian** *et al*., “A filtering antenna using transversal coupling topology,” *IEEE Antennas and Wireless Propagation Letters*, vol. 21, no. 12, pp. 2342-2346, 2022.

[3] **Jianfeng Qian** *et al*., “A common-resonator filtering hybrid with a wide stopband and compact size*,” IEEE Transactions on Circuits and Systems II: Express Briefs*, vol. 70, no. 9, pp. 3358-3362, 2023.

[4] **Jianfeng Qian**, B. Sanz Izquierdo, S. Gao, H. Wang, H. Zhou and H. Xu, "A Cascaded Resonator Decoupling Network for Two Filtering Antennas," *IEEE Antennas and Wireless Propagation Letters*, doi: 10.1109/LAWP.2023.3313049.

[5] **Jianfeng Qian**, S. Gao, B. S. Izquierdo, H. Wang, H. Zhou and H. Xu, "Compact Dual-Polarized/Duplex Filtering Antenna with High Isolation," *IEEE Open Journal of Antennas and Propagation*, vol. 4, pp. 677-685, 2023.

[6] **Jianfeng Qian,** B. S. Izquierdo, S. Gao, H. Wang, H. Zhou and H. Xu, "A Novel Low-Cost H-Plane Decoupling Technique for Two Closely Placed Patch Antennas Using Electric and Magnetic Coupling Cancellation," *IEEE Transactions on Antennas and Propagation*, vol. 72, no. 5, pp. 3864-3873, May 2024.

[7] **Jianfeng Qian,** B. S. Izquierdo, S. Gao, H. Wang, H. Zhou and H. Xu, "Quadruplex Slot Antenna for Dual-Standard Operation with Small Frequency Ratio," *IEEE Transactions on Antennas and Propagation*, vol. 72, no. 3, pp. 2909-2914, March 2024.

Conferences

[1] **Jianfeng Qian**, S. Gao, H. Wang and H. Zhou, "A Novel Filtering Antenna with Transversal Coupling Topology," 2022 International Workshop on Antenna Technology (iWAT), Dublin, Ireland, 2022, pp. 21-24.

[2] **Jianfeng Qian**, B. S. Izquierdo, S. Gao and H. Wang, "A Cascaded Resonator Decoupling Network for Two Filtering Antennas with Adjacent Operating Bands," *2024 18th European Conference on Antennas and Propagation (EuCAP)*, Glasgow, United Kingdom, 2024, pp. 1-4.

[3] **Jianfeng Qian**, B. S. Izquierdo, S. Gao and H. Wang, "On the Synthesis of Filtering Antennas (Invited)," *2023 IEEE 11th Asia-Pacific Conference on Antennas and Propagation (APCAP)*, Guangzhou, China, 2023, pp. 1-2

Patent

Jianfeng Qian, Steven Gao, Hanyang Wang, Hai Zhou, Huiliang Xu (2023), 'Antenna structure and electronic devices', International PCT/Publication NO. WO/2023/125207.

Table of Contents

List of Figures

List of Tables

Chapter 1
Introduction

1.1 Motivation

Wireless technologies have evolved very rapidly over the last few decades. From 2G to 5G, the throughput of civil wireless communication devices has multiplied several times. More spectrums have been released for civil use in the last several decades. A brief spectrum map for modern 4G and 5G networks is provided in Fig. 1.1. Excluding the mmWave bands, the sub-6 GHz frequency range is already highly congested. Although different regions and countries have different standards according to their wireless policies, to embrace the global market, terminal devices need to cover all the potential spectrum to ensure they can work well no matter where the customers are [1].

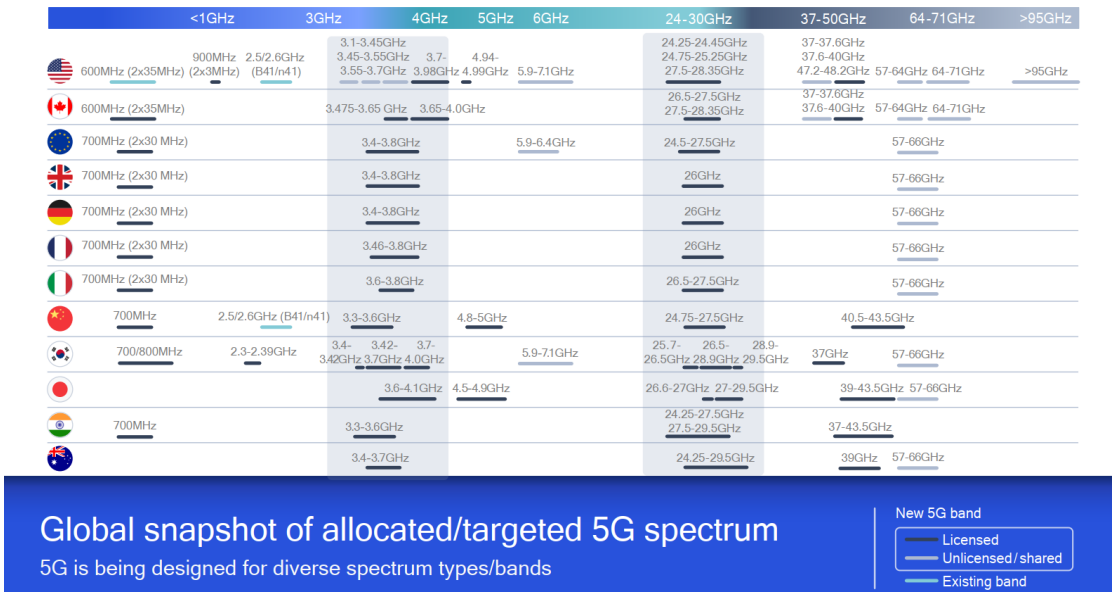

Fig. 1.1. Part of the spectrum for 5G communication [2].

To satisfy consumers' demand for small form factors and high performance while maintaining price competitiveness, manufacturers are continually striving to reduce the

size of their wireless devices. In this circumstance, to put more antennas with wide and multi-frequency band requirements into one single housing, the space for each antenna needs to be carefully considered [3]. However, when antennas are placed at a small distance, the mutual coupling between these antennas will increase. When the mutual coupling is high, the transmitted signal from one antenna may be received by another antenna. Especially, when this transmitted signal is amplified for a higher power, the resulting interference may potentially damage the receiver of another channel [4]. The mutual coupling also makes the active impedance of each antenna element in a phased array change substantially with the scan angle, which consequently limits the beam scanning angle of the system [5]. Under the natural constraint on antenna sizes regarding their operating frequencies, the mutual coupling problem is unlikely to be fully addressed by making them physically far away. Under this circumstance, the mutual coupling problem between antennas has drawn much attention among researchers and engineers these years.

Filters, especially bandpass filters, are usually connected to antennas to suppress interference. Over the past few decades, filter theory has evolved into a comprehensive and independent subject [6]. While the use of filters is often closely associated with antennas, few have considered applying certain circuit theories of filters to antenna design, especially in the scope of antenna decoupling. Many antenna decoupling techniques can be found in the literature. Most of them are developed from the antennas' field perspective. Some decoupling techniques based on circuitry theory suffer from complicated schemes or low performance.

Filter theory is the art concerning multi-port networks. Translated to antennas, multi-antenna systems can also be regarded as lossy multi-port networks. Consequently, there may exist significant correlations between the two. Inspired by this, in this research, the filter theory will be used to guide the multi-port antenna design with higher isolation.

1.2 Objective of the Project and Main Contributions

The objective of this work is to investigate novel decoupling techniques for antennas. This work focuses on extending some filter concepts to create new multi-port antenna module designs, including filtering antennas, multiplex antennas, and antenna decoupling networks. This job represents a preliminary attempt to apply filter theory to antenna design, particularly in the area of decoupling design. Starting with some classical theory in filter design, this work will apply these concepts to achieve several high-performance multi-antenna systems. This work intends to provide a new direction for multi-antenna system design.

The main contributions of this work can be concluded as follows.

1) A novel filtering feeding network addressing the mutual coupling problem between two identical and adjacent channels.
    - A stub-loaded dual-mode resonator is used as the shared resonator.
    - The even and odd modes of the stub-loaded resonator are deliberately designed to serve two different channels.
    - Isolation is then achieved by properly exciting both modes.
2) Decoupling techniques for filtering antennas.
    - A filtering decoupling network is constructed according to the filtering function of the target filtering antennas. This network can be used to decoupler two antennas with the same/different operating bands.
    - A step-by-step realization process for such a network is provided.
    - By connecting this network to the coupled filtering antennas, the mutual coupling can be dramatically reduced without affecting the original filtering function of these antennas.
3) A new concept for the realization of multi-port antenna for terminal applications.
    - A hybrid mode concept is proposed.
    - Two microstrip slot antennas are co-designed to form a radiative bandstop filtering structure.

- The energy, which is expected to be reflected back to the antenna port in this bandstop filtering structure, is radiated. As a result, low reflections are achieved at both antennas' ports.

4) Self-decoupled patch antennas using electric and magnetic coupling cancellation.

- Electric and magnetic couplings between two patch antennas are studied.
- Mutual coupling is significantly reduced by adjusting the weight of electric and magnetic coupling between two patch antennas.
- This simple yet effective technique is experimentally verified with both two-element and four-element MIMO arrays.

5) Self-decoupled patch antennas using higher-order modes.

- Inspired by coupled transmission line theory in filter designs, a new dual-antenna MIMO is realized.
- Two patch antennas are operating over their higher-order modes.
- The coupled sections introduce a transmission zero near the operating band and improve the isolation between the antenna ports.

1.3 Outlines of the Thesis

In this thesis, the contents are organized as follows.

In Chapter 1, the motivation and objective of this research are introduced. The technical contributions of this work are summarized.

Chapter 2 first discusses the general mutual coupling problems in modern communication systems. Regarding their frequency bands of operation, the mutual coupling problems are categorized into two parts: in-band mutual coupling and out-of-band mutual coupling. Then the decoupling techniques addressing both kinds of mutual coupling problems are introduced. Filtering antenna techniques for out-of-band decoupling are also investigated.

Chapter 3 presents two decoupling techniques for two filtering antennas operating over the same and adjacent bands. These techniques are developed based on the classical filter theory. They are all co-synthesized according to the target filtering

antennas. Using these techniques, two filtering antennas can be dramatically decoupled with good filtering performance maintained.

Chapter 4 presents a novel concept for the realization of a multi-port antenna. By designing two slot antennas as a bandstop filter, two antenna ports are well decoupled by the bandstop response. Then, the in-band reflection at two antenna ports is absorbed by the radiation process, achieving low in-band reflection coefficients. This concept provides a new direction for the design of multiplex antenna with shared radiators.

Chapter 5 presents two techniques for decoupling patch antennas. The electric and magnetic coupling theory and coupled transmission line theory in filter designs are investigated and extended to guide the designs. Both techniques feature low cost, simple design processes, and compact structures.

A conclusion is made in chapter 6. Possible directions for future works are also provided.

References

[1] Z. Zhang, *Antenna design for mobile devices*, Hoboken, NJ: Wiley, 2011.

[2] Online available: Https://www.Qualcomm.Com/content/dam/qcomm-martech/dm-assets/_documents/messaging _ presentation _-_4g_5g_spectrums_-_december_2020.Pdf.

[3] H. Wang, "Overview of future antenna design for mobile terminals," *Engineering,* vol. 11, pp. 12-14, 2022.

[4] K. E. Kolodziej, B. T. Perry, and J. S. Herd, "In-band full-duplex technology: Techniques and systems survey," *IEEE Transactions on Microwave Theory and Techniques,* vol. 67, no. 7, pp. 3025-3041, 2019.

[5] R.-L. Xia *et al.*, "Wide-angle scanning phased array using an efficient decoupling network," *IEEE Transactions on Antennas and Propagation,* vol. 63, no. 11, pp. 5161-5165, 2015.

[6] J. S. Hong, and M. J. Lancaster, *Microstrip filters for rf/microwave applications*, New York, NY, USA: Wiley, 2001.

Chapter 2
Overview of Mutual Coupling Problems and Decoupling Techniques

In this chapter, a detailed discussion of the mutual coupling problems and corresponding decoupling techniques are introduced. Regarding the frequency bands of the antennas involved, the mutual coupling problems are divided into two categories: in-band mutual coupling (IBMC) and out-of-band mutual coupling (OBMC). IBMC represents the scenario where two antennas are operating over the same frequency bands whereas the OBMC corresponds to the case when two antennas have different operating frequencies. Decoupling philosophies for both scenarios are also different, which are also reviewed in this chapter. In addition, the filtering antenna technique is introduced at the end of this chapter. The out-of-band decoupling ability of a filtering antenna is also investigated. The results demonstrate the limitation of filtering antennas for addressing the close-band OBMC problems.

2.1 A Brief Review of the Mutual Coupling Problem

2.1.1 Increasing Crowded Spectrum VS. Smaller Form Factor

Fig. 2.1 provides a brief overview of the typical standards covered in a user device (UD) such as laptop, tablet, smartphone, and car. Take a car as an example, antennas enabling a car's access to 4G and 5G networks are necessary. In-car WiFi is also always provided for high-end cars. In addition, accommodating GNSS (Global Navigation Satellite System) such as GPS (Global Position System) is obviously essential. Bluetooth antenna enables the remote control of cars such as remote door control. Future V2X communication antennas (5855-5925 MHz) may be added to cars for IoT applications. In some cases, some of these antennas may need to be integrated into one housing, such as a shark fin, for a small form factor. As a result, there will be serious mutual coupling problems among them, especially for the antennas operating over overlapping frequency ranges and adjacent bands as indicated in Fig. 2.1.

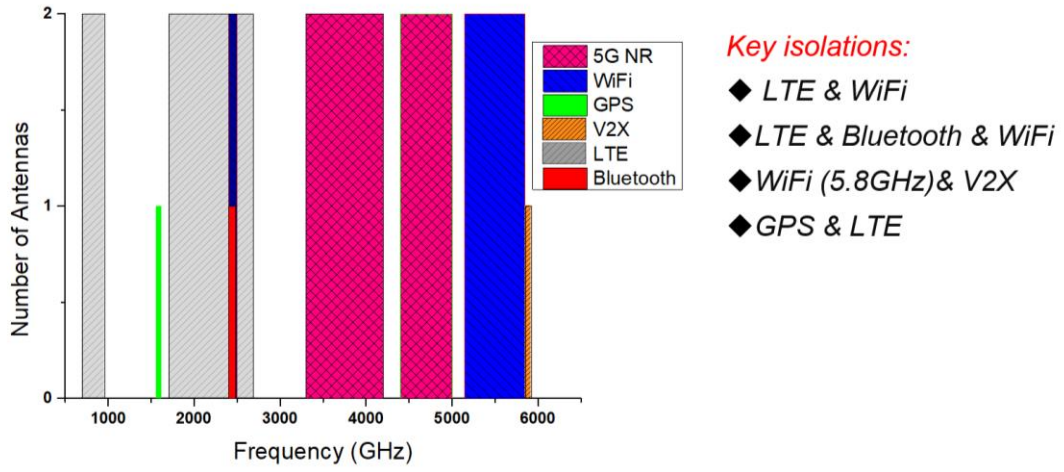

Fig. 2.1. Typical standards covered in modern UDs.

Fig. 2.2 shows a common scenario where a UD is communicating with a base station (BS). These devices are always equipped with wireless modules for WiFi and cellular network communications. Here let us concentrate on the 5-GHz WiFi band (5.15–5.8 GHz) and 5G NR bands (3.3–5 GHz). Suppose both wireless modules are with 2×2 MIMO architectures.

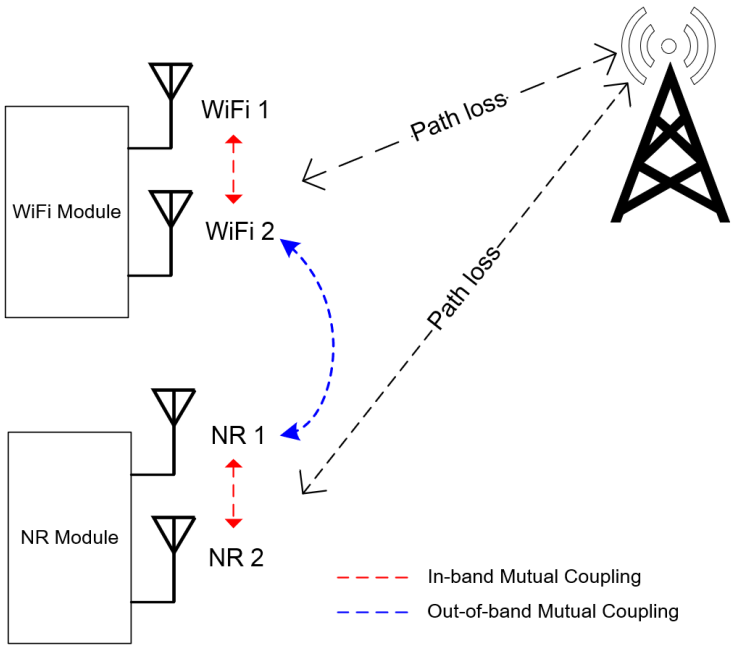

Fig. 2.2. Illustration of the interference scenario in a modern communication system.

The mutual coupling problems in modern communication systems can be roughly divided into two categories: in-band mutual coupling and out-of-band mutual coupling. In-band mutual coupling happens between two antennas serving a common standard (WiFi 1 and WiFi 2), while out-of-band mutual coupling represents the interference between two different wireless networks (WiFi and NR). To address these two mutual coupling problems, the decoupling problems can also be divided into corresponding two parts: in-band decoupling and out-of-band decoupling.

2.1.2 In-Band Decoupling (IBD)

In-band decoupling (IBD) represents the cases where the antenna elements are operating over an overlapping frequency band. Sometimes, they may have identical physical structures, which is very common in most academic studies.

2.1.2.1 MIMO Technology

There are two typical scenarios for this case. The first case happens in MIMO applications, where more than one antenna is used to transmit and receive signals in the same frequency bands [1, 2]. The MIMO technology is believed to be one of the most

important technologies for modern communication systems. When the bandwidth of the standard is limited, MIMO architecture can enlarge the system throughput by increasing the number of antennas in the system.

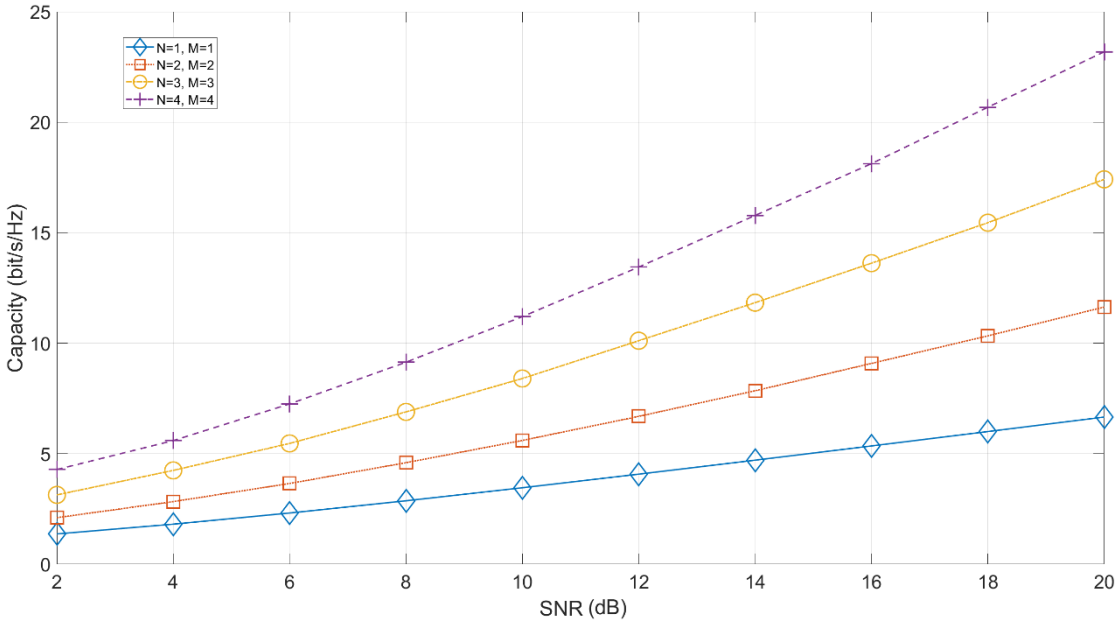

Fig. 2.3. Channel capacity of a MIMO system with different numbers of transmit and receiver antennas.

For a multi-antenna system, suppose there are M receiving antennas and N transmitting antennas. The channel capacity of this MIMO can be calculated as [3]

$$\mathrm{C} = \log_2 \det\left(\mathbf{I} + \frac{SNR}{N}\mathbf{H}\mathbf{H}^H\right) \text{ bit/s/Hz} \tag{1.1}$$

Here $\boldsymbol{I}$ is the identity matrix of size $M \times N$, SNR is the signal-to-noise ratio, $\boldsymbol{H}$ is the channel matrix of size $M \times N$. The capacity of an ideal MIMO system over a Rayleigh fading channel with different numbers of transmit and receive antennas is plotted in Fig. 2.3. When the SNR is adequately high, the capacity of the system can be increased linearly by increasing the number of antennas at the transmitting and receiving ends.

However, when the antennas are mutually coupled, and channels are correlated, the channel matrix can be expressed as

$$\mathbf{H} = \mathrm{R}_r^{1/2} \cdot H_w \cdot R_t^{1/2} \tag{1.2}$$

Where $\boldsymbol{H}_w$ is the ideal channel matrix and $\boldsymbol{R}_r$, and $\boldsymbol{R}_t$ are the correlation matrix. When the independence between channels is low, the channel capacity will be much poorer than the ideal results.

2.1.2.2 In-band Duplex

A modern communication system mainly utilizes two technologies to achieve isolated transmitting and receiving channels: frequency division duplex (FDD) and time division duplex (TDD). FDD technology separates the uplink and downlink of a system into two parts and allocates them at different frequency bands, with a specific guard band in between. Then with the aid of a filter/duplexer/multiplexer, the system can transmit and receive simultaneously, over different frequency bands. A duplexer/multiplexer is a multi-port device that can separate one signal into multiple isolated signals at different frequency bands. To ensure adequate isolation, a guard band is always needed between the uplink and downlink bands. TDD isolates the transmitting and receiving channels by making them operate over different time slots. Transmit and receive functions of the system occur in the same frequency band but at different times. To prevent uplink and downlink transmissions from clashing, a guard period is required. These half-duplex techniques transmit and receive signals either at different times or over different frequency bands, which consequently will decrease the system capacity, increase the cost, and lower the spectrum efficiency.

By allowing the transmitter and receiver to operate over the same frequency bands simultaneously, the in-band full duplex (IBFD) provides the potential to double the system capacity and spectral efficiency [4, 5]. However, IBFD suffers from a critical problem: self-interference. To prevent the receiver from receiving the signal from its own transmitter, the isolation between the transmitting antenna and the receiving antenna must be adequately high.

Consider the communication scenario between a BS and a UD as illustrated in Fig. 2.4. Suppose the transmit power of the BS is 24 dBm while that of the UD is 21 dBm, which are very typical values for modern devices. With a common path loss of

110 dB, the signal received by the BS which is transmitted by the UD is 21 – 110 = -89 dBm. If the BS is operating with IBFD mode with a transmitter-receiver isolation of 20 dB, the received power by the BS's receiver from its own transmitter will be 24 – 20 = 4 dBm, which is much higher than the signal from the UD as indicated in Fig. 2.4. In this circumstance, the BS can no longer recognize the signal from the UDs when it is also transmitting.

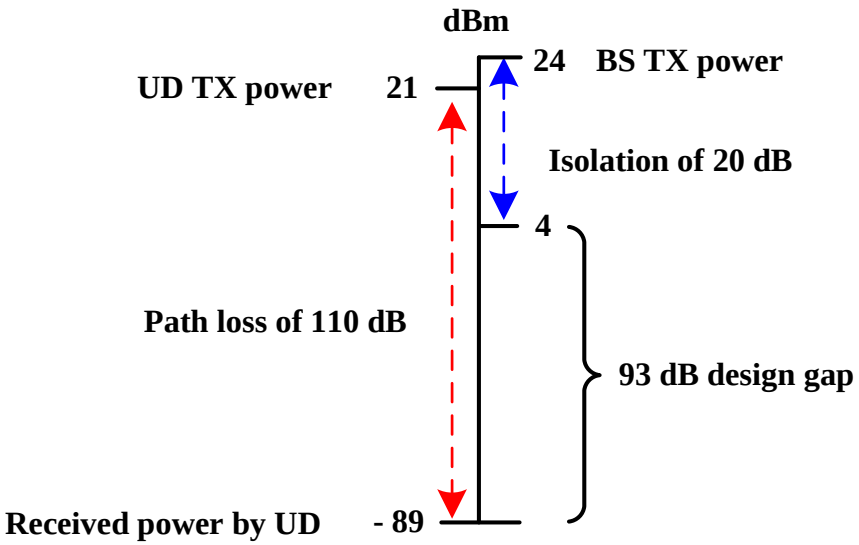

Fig. 2.4. An illustrative example of signal and self-interference levels.

To overcome this design gap, different techniques based on different domains are proposed by researchers, such as analogue domain techniques [6, 7] and digital domain techniques [8]. From an antenna design point of view, a very useful solution for decreasing the self-interference of an IBFD system is increasing the isolation between the antennas of the transmitter and receiver channels.

2.1.3 Out-of-Band Decoupling (OBD)

Another decoupling scenario happens between two antennas operating over different frequency bands. This is a very common problem in modern communication systems due to the limited space for allocating different radio systems in the same UD. The out-of-band mutual coupling is more likely to happen between two RF channels when their operating frequency bands are close while their antenna separation is not

sufficiently large. One direct way to resolve this problem is by using filters to suppress the out-of-band spurious emissions [9-12]. Generally, to suppress the signal at a spurious band, transmission zeros (TZs) are needed. However, when the TZ of a filter is very close to the passband, the insertion loss of the filter will be very high. Up to now, no filter technology can provide a perfect isolation at a closely arranged frequency channel, without increasing the insertion loss at its own band.

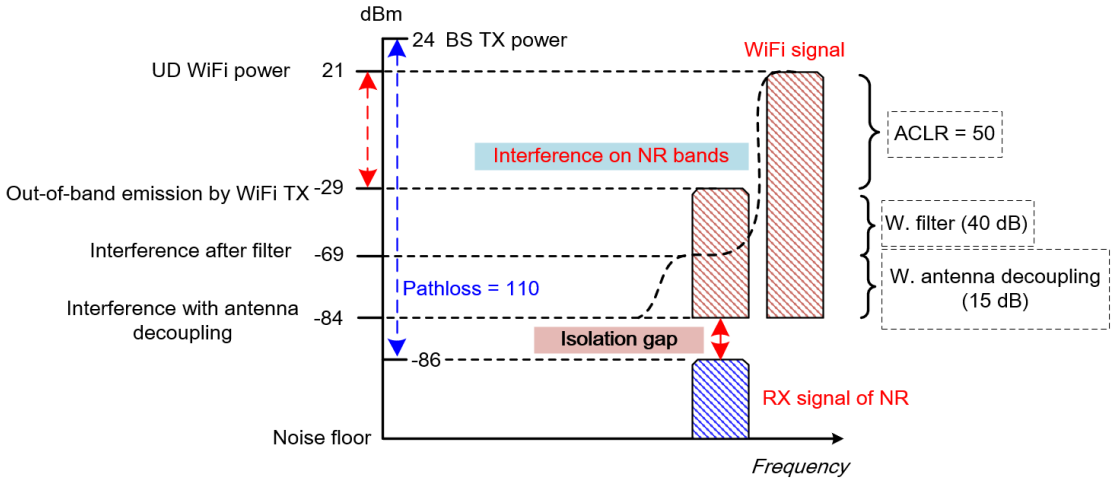

Fig. 2.5. Illustration of interference from WiFi transmitter to NR receiver.

The interference between the WiFi channel and 5G NR bands will be a good example to help understand this issue, as shown in Fig. 2.5. Within the same UD, the 5-GHz WiFi band (5.15–5.8 GHz) and 5G NR bands (3.3–5 GHz) are within a very close frequency range. Assuming the UD is receiving NR signals from the BS with BS's TX power of 24 dBm. With a path loss of 110 dB, the power received by the NR receiver is -86 dB. In this situation, supposing that the UD is transmitting WiFi signals to the tower with a TX power of 21 dBm and its interference to the NR bands is 50 dB lower than this value. Here the ratio between the WiFi's interference on the NR bands to its own TX power is called Adjacent Channel Leakage Ratio (ACLR), for which 50 dB is a common value [13]. If the filter rejection level at the NR bands is 40 dB, the interference will reduce to – 69 (21 dB – 50 dB – 40 dB) dBm after the filtering. Taking a common spatial isolation of 15 dB between antennas into consideration, the final

interference level will be -84 dBm, which is still 2 dB higher than the original NR signal as shown in Fig. 2.5. In this situation, the spurious emission will cause strong interference and additional isolation method is needed.

2.2 Literature Review

Significant effort has been made by researchers and engineers to reduce the mutual coupling between antennas. As mentioned in section 2.1, the mutual coupling problems between two antennas can be categorized into two parts: IBD and OBD.

2.2.1 In-Band Decoupling Techniques

The decoupling between two antennas owning an overlapping frequency band has been studied for many years. From the academic scope, these studies always involve two or more identical antennas as the target elements.

2.2.1.1 Decoupling with Spatial and Polarization Diversity

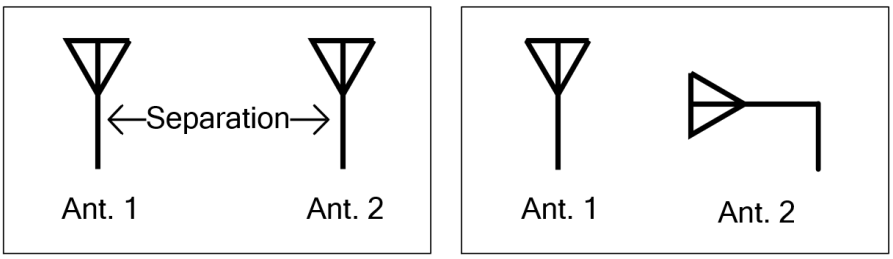

(a) (b)

Fig. 2.6. (a) Spatial and (b) Polarization diversity decoupling methods.

To address the mutual coupling problem between two identical antennas, the most direct method is increasing the antenna spacing. Generally, the isolation between two identical antennas will be improved when the distance between them is increased. This phenomenon is always true for most balanced antennas such as half-wavelength patch antennas [14, 15], half-wavelength dipoles [16, 17], and short-end slot antennas [18]. However, for some quarter-wavelength antenna structures such as PIFAs and open-end slot antennas, the isolation is not always in direct proportion to the antenna spacing [19-

21]. This phenomenon is very common for antennas in handheld devices. Because of their unbalanced feeding scheme, these antennas also use their ground planes as radiators, to obtain wider bandwidth and efficiency. The strong current on the ground plane should always be considered when a decoupling process is carried out for these antennas [22].

Another effective way to reduce the mutual coupling between two antennas is by making them operate over different polarizations as illustrated in Fig. 2.6(b). Such an arrangement can provide inherent isolation since waves with different polarizations cannot couple to one another. This concept has been widely verified in the literature [23-25].

2.2.1.2 Decoupling Networks

An early work on this topic can be found in the literature which was published in 1976 [26], as shown in Fig. 2.7(a). This work introduced the possibility of using a transmission line structure connecting the feedlines of antennas to reduce the mutual coupling. It was found that the individual antenna's impedance behaviour and mutual impedance between the antennas are critical for the decoupling process. Thus, antennas are arranged with some specific spacing to ensure that the antennas' self-impedances are real and the mutual impedances are reactive.

Instead of connecting the network at the feedlines of the antennas, Aliou Diallo *et al*. found that the mutual coupling between two PIFAs can be effectively reduced by connecting their radiators with a narrow metallic strip [19]. This technique is later known as a neutralization line and found intensive applications in industrial products. In 2008, a more general decoupling network concept was developed in [27]. In this work, the idea is to introduce an additional path between the input ports of two antennas. The mutual admittance between antennas was changed to zero by adding transmission lines at the antennas' feedlines. Then a lossless network with the pure imaginary mutual admittance is connected between the two antennas at the point where the mutual admittance between antennas is also purely imaginary. The properly designed network

can then cancel the mutual coupling between two antennas. A similar concept is then applied to the tri-antenna module in [28]. This idea is also applicable to coupled resonator networks [29, 30].

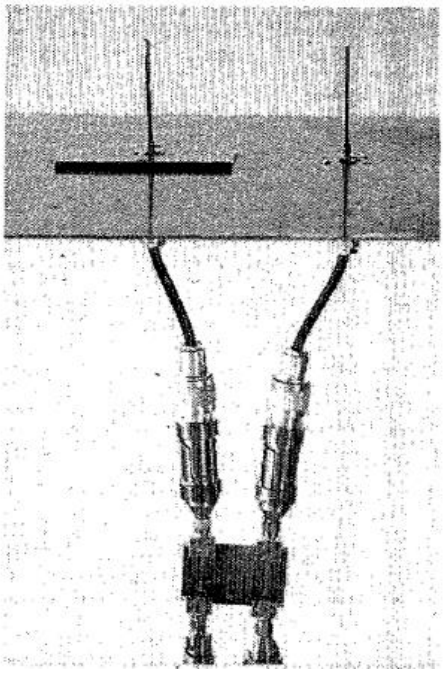

(a)

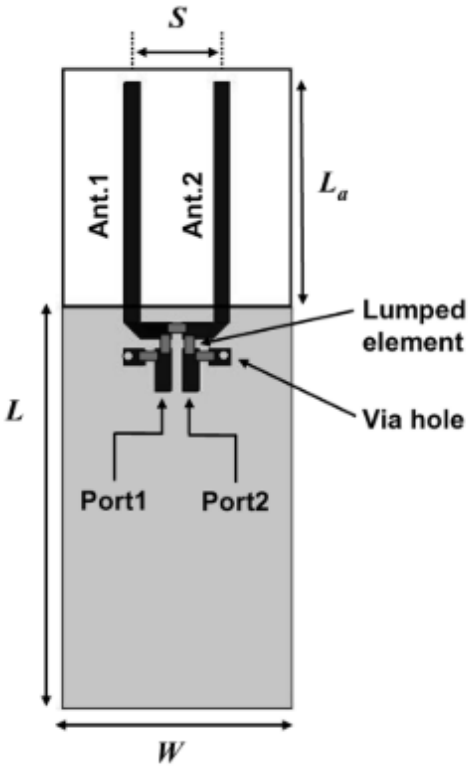

(b)

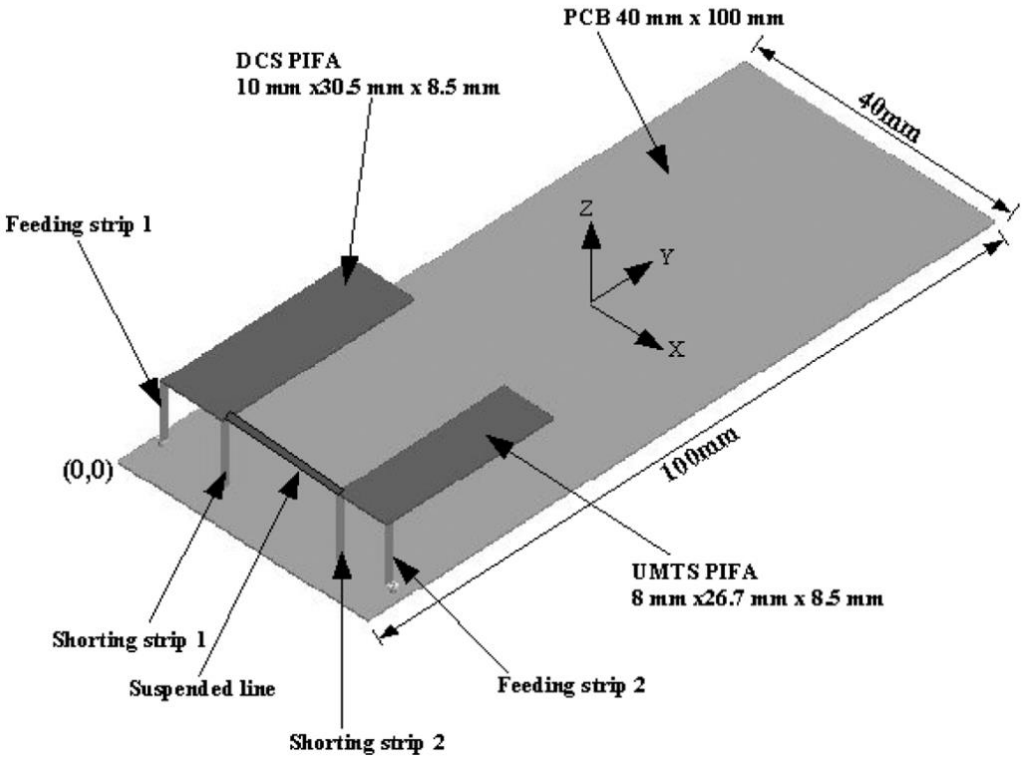

(c)

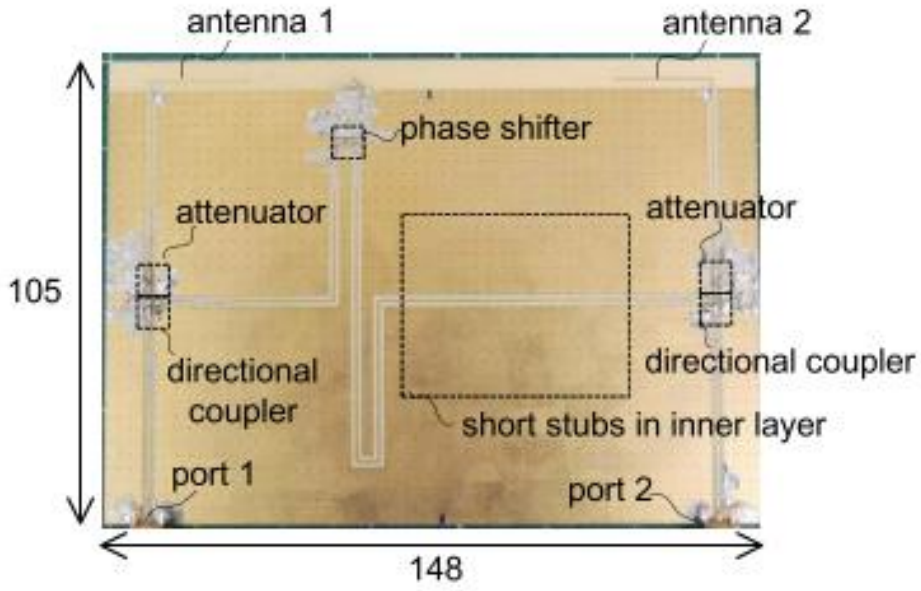

(d)

Fig. 2.7. (a) Decoupling structure in [26], (b) Decoupled monopoles in [27], (c) Neutralization line structure in [19], (d) Decoupling technique based on S-parameter [31].

In [31], another decoupling network concept developed from the S-parameter aspect is presented. The transmission characteristic of the decoupling path, which is achieved using lumped elements and transmission lines, should be designed with equal magnitude, but 180° phase difference to the original antenna mutual coupling. Then the energy from the two paths will cancel out at the frequency of interest. Unfortunately, the control of the phase and magnitude behaviours of the decoupling network is very complicated as shown in Fig. 2.7(d). To ensure the phase and magnitude error is as small as possible, additional elements such as phase shifter, attenuator, and directional couplers are needed in this work. These limitations make it unsuitable for space-limited applications. Besides, this method also suffers from efficiency reduction because the decoupling network is not lossless [32].

2.2.1.3 Metallic Surfaces

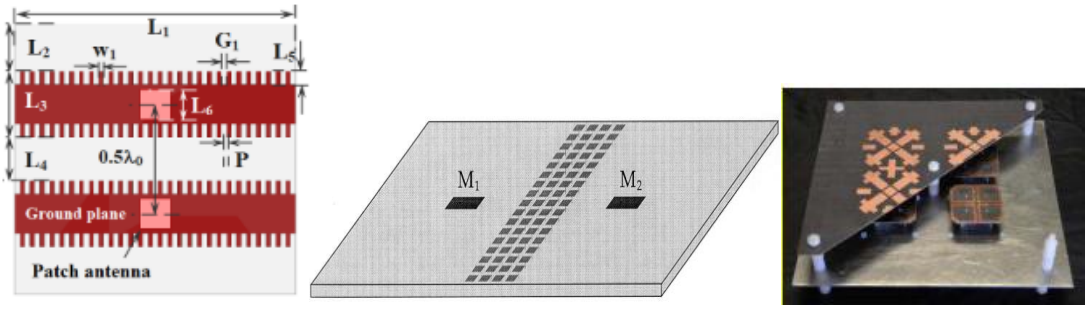

(a) (b) (c)

Fig. 2.8. Decoupling surfaces with different patterns. (a) Modified ground [36], (b) Co-planar patch array [39], (c) Stacked surface [38].

Metallic decoupling surfaces can also serve for the decoupling between patch antennas, which is widely used for BSs. Metallic surface arrays with various patterns are widely used to suppress the surface waves between two antennas [33-36]. By adding one additional layer of the metal surface array above the patch antennas, a large-scale antenna array can be decoupled with minor distortion on the original antenna characteristics regarding impedance and radiation performance [37, 38]. These printed metallic surfaces are designed with different patterns [36, 39-41] as shown in Fig. 2.8. From these examples it can be observed that these metallic surfaces will always occupy

additional space in the system. Thus, this method is more suitable for applications where system size is not a higher priority.

2.2.2 Out-of-band Decoupling Techniques

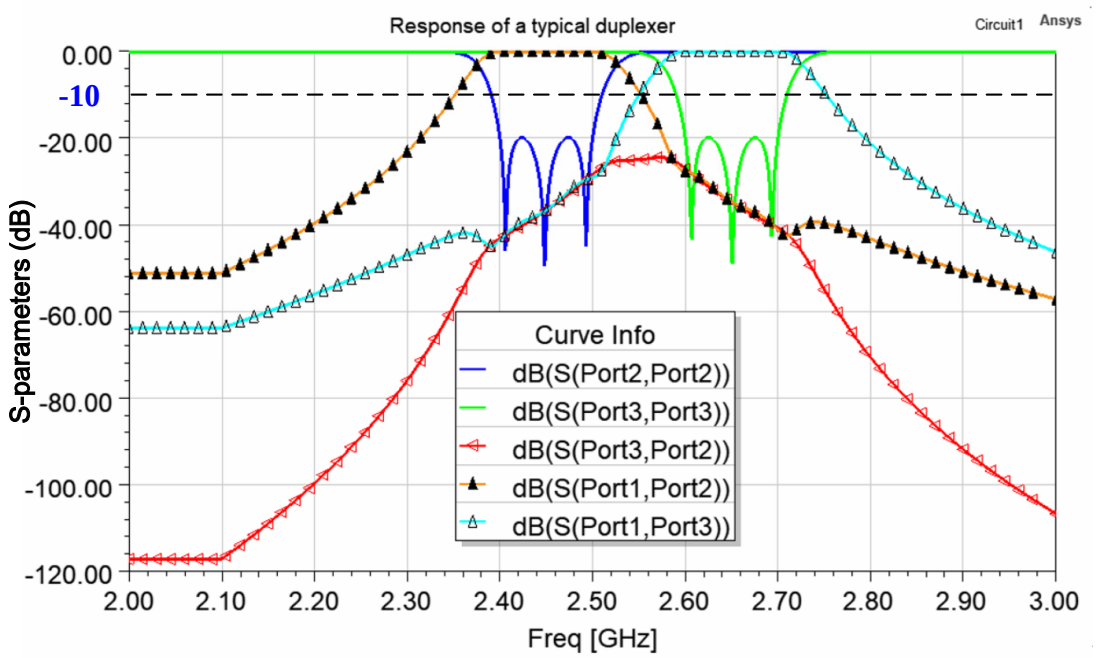

Fig. 2.9. The simulated typical response of a duplexer.

The decoupling between two different bands (OBD) is quite different from the IBD. Because in this case where two antennas are operating over different bands, the decoupling process happens in two frequency ranges. As mentioned in section 2.1, one of the most common methods to address the out-of-band mutual coupling problem is using filters. A filter is a device that allows the signal in a specific frequency range to pass while suppressing the signal in other frequency bands. Filter theory has been developed for many years [42]. Filters, especially bandpass filters, with different filtering functions can be synthesized with different technologies such as waveguides [43, 44], microstrip lines [45-47], low-temperature-co-fired-ceramic (LTCC) [48], and hybrid structures [49, 50]. Combining multiple filtering channels into one single device can form a multiplexer. A multiplexer can split one signal into more than one isolated RF path with different frequency bands [51-54]. A typical response for a duplexer is

plotted in Fig. 2.9. In this duplexer, the isolation between port 2 and port 3 decides the mutual coupling level between these two channels when it is connected to antenna ports.

However, most of the multiplexer/duplexer designs are too bulky for commercial applications because the resonators involved are commonly in proportion to the wavelengths at their operating frequencies. Fortunately, RF acoustic technique enabled surface-acoustic wave (SAW) and bulk acoustic wave (BAW) filters allows us to minimize the low frequency (lower than 6 GHz) filters within a small volume of only several millimetres [9, 11, 12, 55, 56], commonly with a surface area of smaller than 5 mm×5 mm for commercially available products [57].

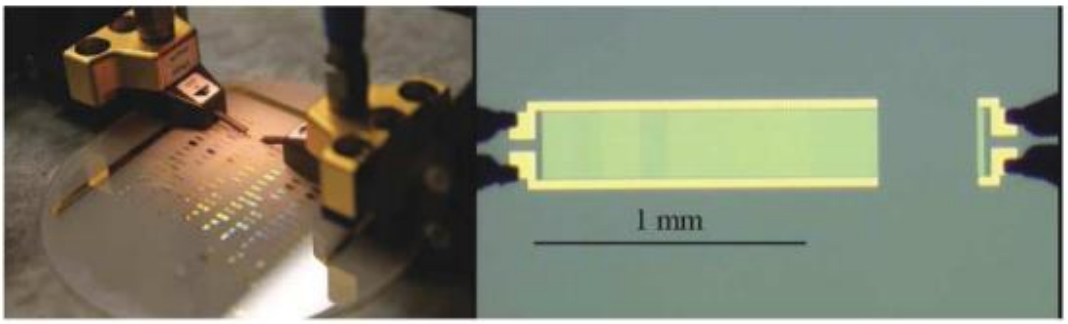

Fig. 2.10. (left) SAW filter measurement and (right) microscope view of the filter [55].

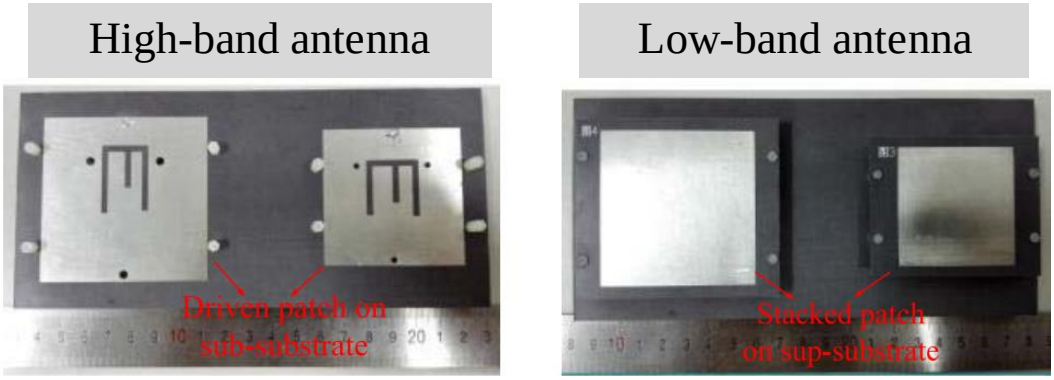

Fig. 2.11. Filtering antennas for adjacent band decoupling [58].

Despite the filter solutions, from the antenna aspect, some decoupling techniques can also be found in the literature. In [58], filtering antenna architectures are for the first time used to achieve isolation between two closely placed base station antennas,

as shown in Fig. 2.11. Two bandstop filter structures are integrated into the feedlines of patch antennas to suppress the out-of-band mutual coupling in [59], as illustrated in Fig. 2.12. Band-notch structures are utilized in [60] for the same purpose. Coupled resonator decoupling networks are constructed in [61] to suppress the adjacent frequency mutual coupling.

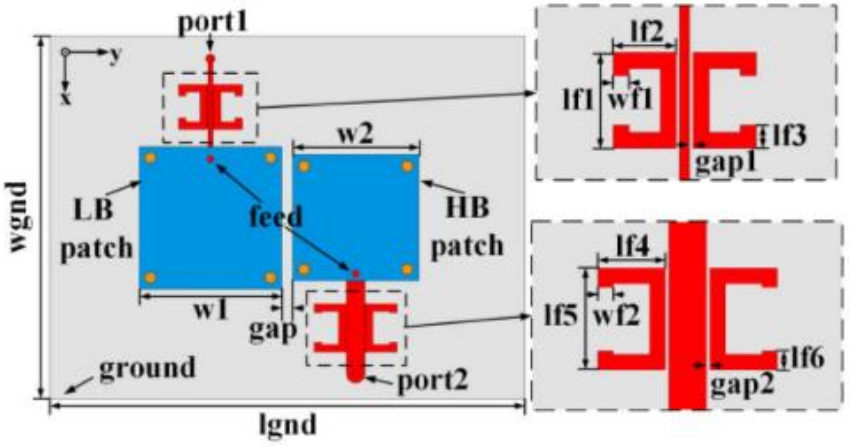

Fig. 2.12. Integrate Bandstop filter into the feedline of antennas [59].

For out-of-band decoupling, the difficulty increases dramatically when the frequency ratio between channels gets smaller. When the frequency ratio between two antennas is very small, the decoupling through filters will be very challenging unless we sacrifice the antennas' performance. As a result, out-of-band decoupling techniques for small frequency-ratio scenarios are highly demanded.

2.2.3 Multiplex Antennas

Another solution to address the mutual coupling problem between antenna is a multiplex antenna. Instead of decoupling the pre-designed antennas after the antenna arrangements are fixed, the multiplex antenna concept aims at designing multiple antennas in one common module. These antennas are usually designed with shared and/or embedded radiators.

A self-diplex dual-circular-polarized antenna is presented in [63]. The antenna is composed of a ring patch and a circular patch inside it. The isolation between two

antenna ports is highly related to the polarization purity as pointed out in this work. A similar structure is used in [64] to achieve a triplex antenna, in which two orthogonal patch modes and one monopole mode are excited simultaneously. Because all these modes have different polarizations, these antenna ports are decoupled with isolation higher than 20 dB. In [62], a four-port antenna module for access point (AP) is presented, as shown in Fig. 2.13. Four antennas are co-designed with a shared radiator. Isolation between antenna ports is achieved by a gap-feeding scheme and the metallic posts between them. Other in-band multiplex antennas can also be found in the literature [62, 65-72].

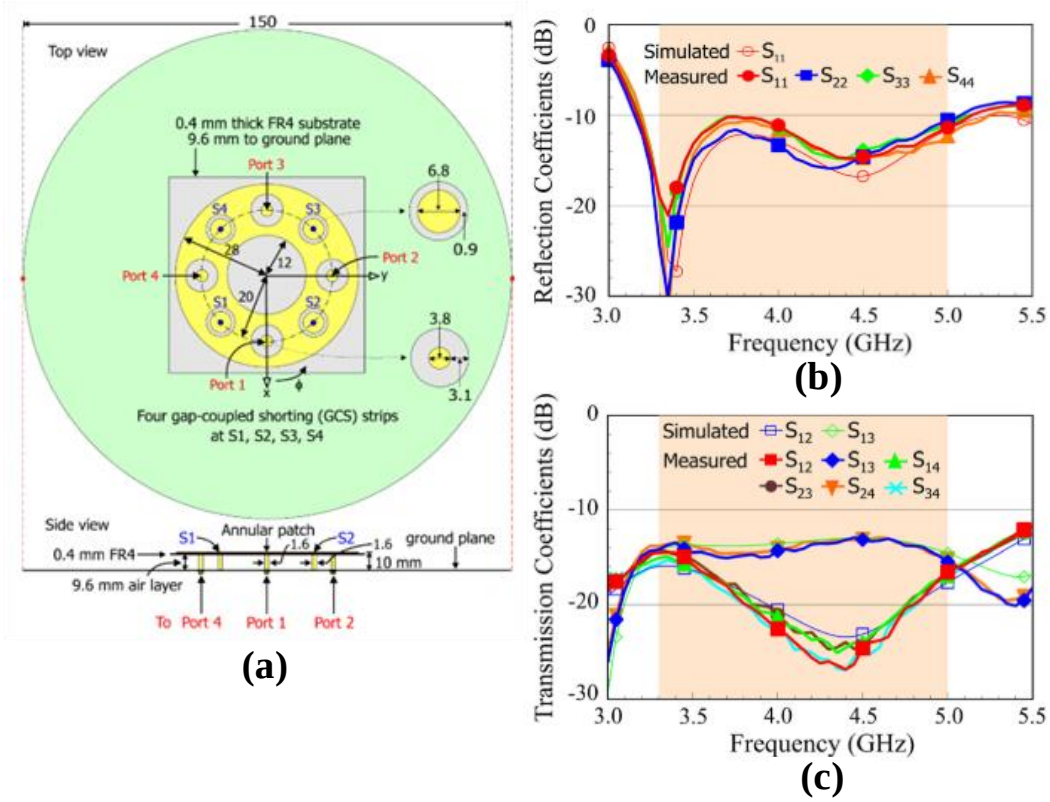

Fig. 2.13. In-band quadruplex antenna in [62]. (a) Structure. (b) Reflection coefficients. (c) Isolations.

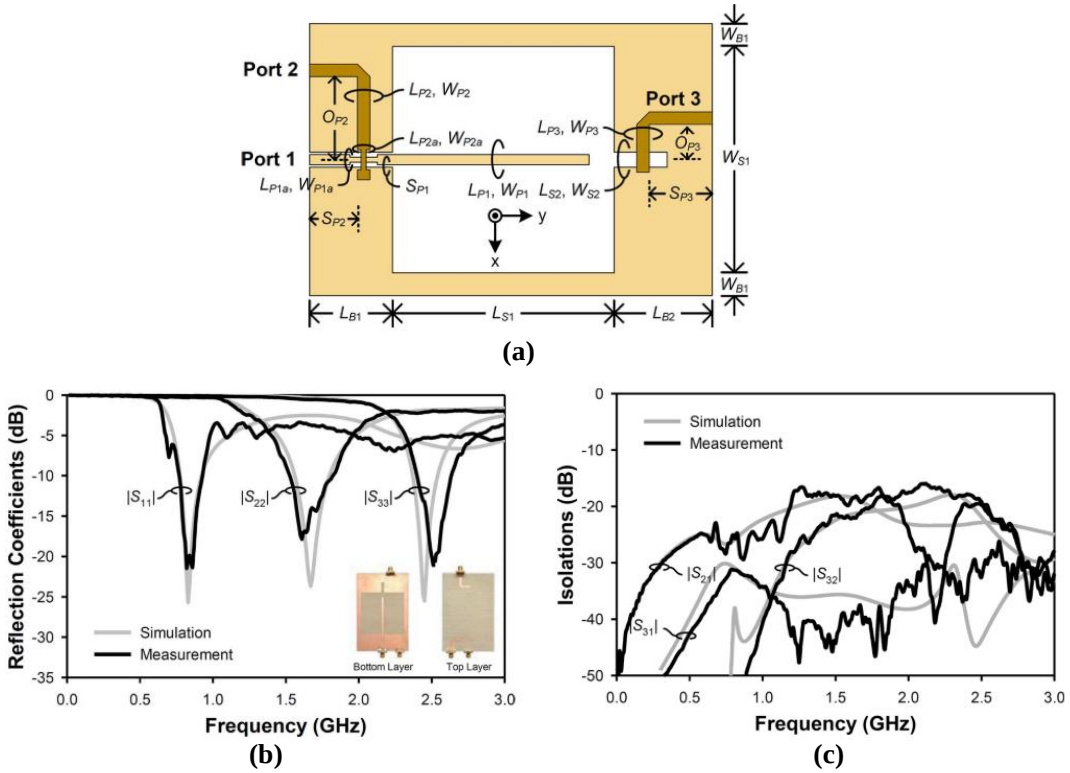

Fig. 2.14. Out-of-band triplex slot antenna in [73]. (a) Structure. (b) Reflection coefficients. (c) Isolations.

Multiplex antennas with different operating bands are much less studied [73-77]. A triplex slot antenna is reported in [73] as shown in Fig. 2.14. In this work, three antennas operating over different frequency bands are co-designed sharing one common slot radiator. The isolation between these ports is higher than 22 dB according to the results presented. A SIW-based quadruplex antenna is presented in [74]. Four isolation antennas are achieved sharing one cavity radiator. However, the bandwidths are quite narrow, and the size of the cavity is slightly large.

Generally, most of the multiplex antennas are for in-band scenarios while studies on out-of-band multiplex antenna is relatively less. In addition, most of the presented works suffer from narrow bandwidths or large antenna sizes. More work is still needed to address the multiplex antenna problem with wider bandwidth, smaller form factor, high isolation, and ease of fabrication.

2.3 Filtering Antenna: The Past and the Status Quo

As one of the most important components in modern RF systems, the bandpass filter (BPF) plays a key role in interference suppression as mentioned in section 2.2. Especially for the OBD, the performance of the BPF determines the final isolation between two channels in a major way. However, this architecture nowadays seems not good enough for our daily increasing demands. Simply cascading a BPF into a system will inevitably introduce additional insertion loss to the system, not to mention the extra cost. Nevertheless, without filtering functionality, the interference between two RF channels may result in some deadly errors. Against this background, the concept of filtering antenna has stepped into the spotlight, which provides us with another option, to some extent, better than the conventional filter-plus-antenna solution.

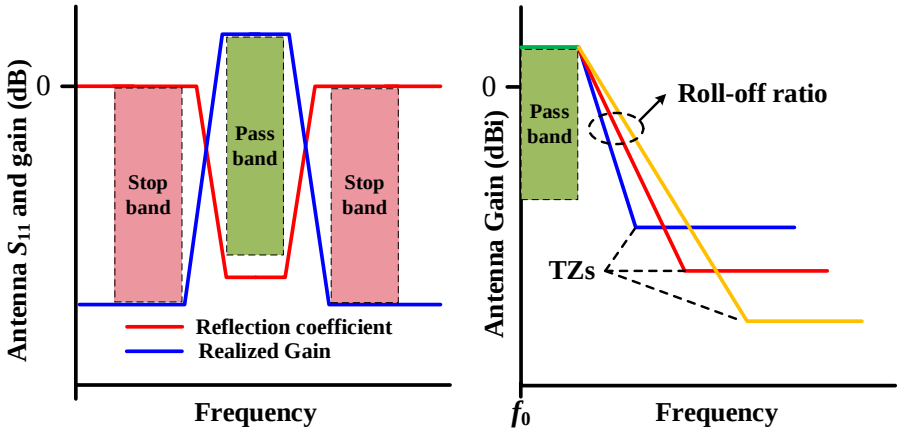

Fig. 2.15. (a) Required response of a filtering antenna. (b) Filter function with different suppression levels.

Any antenna, which can transmit and receive signals in some specific frequency ranges while showing high attenuation in the other frequency bands, can be called a filtering antenna, as illustrated in Fig. 2.15(a). Generally, the filtering antenna is a component that combines the functions of the filter and antenna into one module [78, 79]. It means that only the signal needed can be radiated and received while the out-of-

band signal will be suppressed. Such a design has some very attractive advantages such as low loss, compact size, and cost-efficiency.

The current concept of filter antenna can be traced to the wideband matching network design of antennas. Some fundamental works on this topic can be found in the early literature [80, 81]. In [80] Fano studied the impedance matching of arbitrary impedance. Then the impedance matching concept is applied for bandwidth enhancement of microstrip antennas [82, 83]. In the very beginning, researchers concentrated more on the bandwidth of the antenna, because the interference between antennas was not a serious problem at that time. Most terminal devices have adequate space for the implementation of a limited number of antennas, which is much less than the antennas included in current devices. Nevertheless, some of these works such as wideband matched antenna [82, 83], stacked patch [84, 85], and coupled multi-patch structure [86], can already be regarded as filtering antennas according to the current definition. In 1998, Person *et al*. proposed the concept of the filtering antenna for the first time [87]. A general synthesis method for an antenna/filter was presented. From then on, different filtering antenna concepts and structures have been presented [88-90]. Now, the filtering antenna technology has become one of the most popular topics in the antenna community. One can find many different filtering antenna designs in the literature by searching keywords such as ‘filtering antenna’, ‘filter/antenna’, and ‘filtenna’.

Generally, the mainstream for the realization of the filtering antenna can be roughly divided into two different categories. The first one is the classical synthesis method which allows the designer to develop a filtering function based on the well-developed filter theory. The second method is by introducing multiple out-of-band TZs on the gain response of a wideband antenna to improve the selectivity. The locations of these TZs have a strong effect on the out-of-band suppression level. Commonly, the closer the TZ is to the edges of the operating band, the lower the suppression level, as illustrated in Fig. 2.15(b). The second method is more direct and sometimes simpler compared with the cascaded resonator structure. However, most of these designs are

very specific. For example, cutting slots and shorting posts are widely used in filtering patch antenna designs to introduce gain zeros [58, 91-93]. These technologies may not work for other antenna structures.

Compared to this method, the synthesis method provides a more universal realization procedure for a filtering antenna. This concept is not limited to one specific antenna type but can be applied to various antenna structures, such as patch antennas [94, 95], waveguide antennas [96-98], SIW antennas [99-105], and slot antennas [88, 106-108]. The global synthesized filtering antennas can provide a high roll-off ratio in the skirts of the gain response depending on the order and topology of the filtering function. For an higher selectivity, multiple attenuation poles can be synthesized in the gain response, referring to the methods used for introducing TZs in BPFs [43, 45, 109, 110].

However, there will always be a cascaded network in the front of the antenna when such an architecture is used, making the overall size somewhat bulky. Even though, this global synthesis method is still very useful for its flexible design procedure, high selectivity, and ease of filtering specifications control. More importantly, it provides a more general theory for the design of filtering antennas, which is very useful for filtering antennas with more complex functionality, such as filtering antenna arrays [95, 97, 98, 111], multiplexing filtering antennas [112-114], dual-polarized filtennas [25, 115], and circularly polarized filtennas [116-118].

Although the theory of BPF has been well-developed for many years and some ideas in filter designs can be directly borrowed for filtering antenna designs, there is still a lack of a systematic synthesis guideline for such a cascaded resonator filtering antenna. Because it requires the designer to have the knowledge background of both antenna and filter. This part will provide a detailed description of filtering antenna synthesis and a comprehensive design guideline for readers who want to engage in this research field. Important design formulas and techniques are included.

2.3.1 From Filter to Filtering Antenna

The most widely used design method for filtering antenna is cascading resonators and a resonating antenna according to the synthesis theory of BPF. In these designs, the antenna works not only as the radiator but also as the last stage of the corresponding bandpass filter. To get a better understanding of the transformation from a BPF to a filtering antenna, an equivalent circuit of a filtering antenna and corresponding BPF are presented in Fig. 2.16. Fig. 2.16(a) shows an N_{th} order BPF, in which coupling between resonators is represented by J inverters between them.

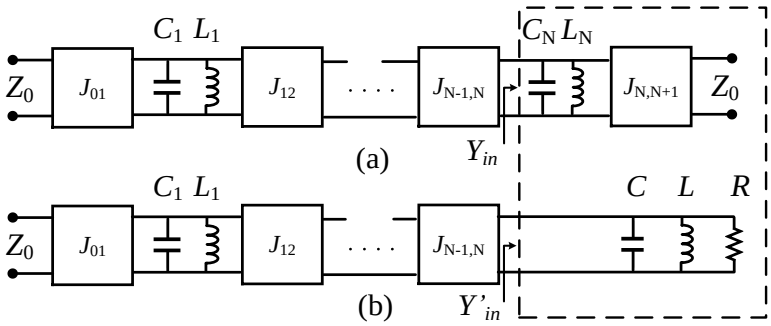

Fig. 2.16. Equivalent circuits of BPF and filtering antenna. (a) BPF. (b) Filtering antenna.

In this equivalent model, the output of the BPF is a lossless LC resonator loaded with a resistance Z_0 transformed through an inverter $J_{N,N+1}$. Based on these circuit models, if we assign the left port as the input and replace the last order resonator and right port with a lossy resonator, then a filtering antenna can be obtained as shown in Fig. 2.16(b). This lossy resonator denotes the radiator, in which the resistor represents the total loss for the antenna resonator.

For a resonating antenna that can be modelled as a lossy resonator as shown in Fig. 2.16(b), we have

$$\frac{1}{Q_u} = \frac{1}{Q_r} + \frac{1}{Q_d} + \frac{1}{Q_c} \tag{2.3}$$

Where Q_u is the unloaded quality factor and Q_r, Q_d, *and* Q_c represent quality factors associated with radiation loss, dielectric loss, and conductor loss, respectively. If we

want to achieve the same reflection coefficients at the left port for both circuits, the following relationship should be satisfied at the operating frequency (f_0)

$$Y_{in} = Y_{in}^{'} \tag{2.4}$$

This can be achieved by making the resonant frequency of these two circuits (dash line enclosed) the same and the external quality factor of the BPF (Q_e) equal to the unloaded quality factor of the *RLC* circuit (Q_u) which represents the antenna.

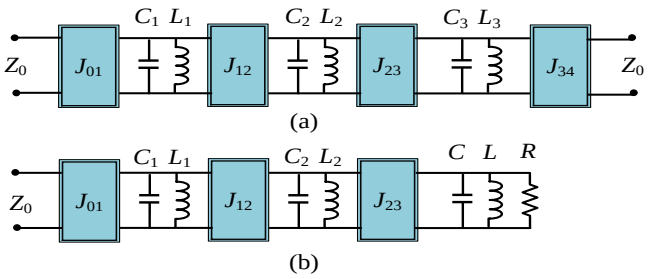

Fig. 2.17. Lumped circuit for (a) 3rd-order bandpass filter. (b) 3rd-order filtering antenna.

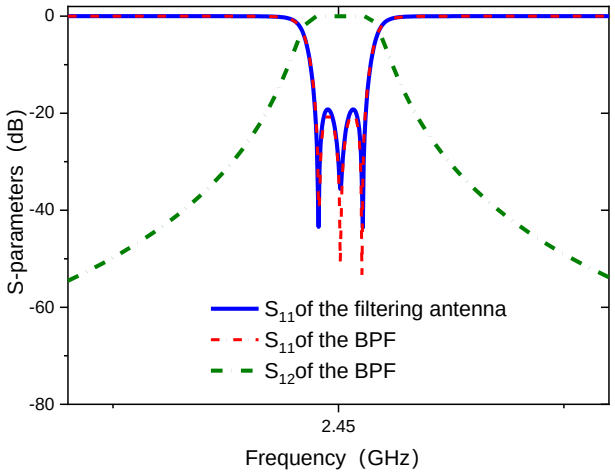

Fig. 2.18. Simulated response of the lumped circuits BPF and filtering antenna.

For verification, two lumped-circuit examples are simulated as shown in Fig. 2.17(a) shows a lumped BPF with a third-order Chebyshev response. The specifications of this BPF are given as follows:

Passband	2.447 GHz -2.453 GHz (*FBW*=0.22%)
Ripple level	0.4321 (S_{11}=-20dB)
Port impedance	50 Ω

The design values needed can be calculated using the following formulas

$$M_{12} = M_{23} = \frac{FBW}{\sqrt{g_1 g_2}} \qquad Q_e = \frac{g_0 g_1}{FBW} = 378 \tag{2.5}$$

where g_i is the value of the low-pass filter prototype element which can be found in a filter design handbook for some typical prototypes [50], and FBW represents the required fractional bandwidth. For convenience, we make both resonators have the same inductor and capacitor values. Then the R in Fig. 2.17(b) can be decided according to the definition of Q_u, that is

$$Q_u = \omega_0 RC \tag{2.6}$$

Here ω_0 is the resonant frequency of the resonator. Since the C is already known and Q_u is equal to Q_e, then the R can be deduced to be 383 Ω. Both circuits are simulated, and their responses are plotted in Fig. 2.18. It should be noted because the filtering antenna in the circuit is a one-port network only the reflection coefficient is plotted here. As can be observed both circuits have the same S_{11}. As indicated in some open literature [94-98], we can believe the gain response of the filtering antenna will obtain the same trend as S_{21} of the corresponding filter, as long as they have the same reflection coefficient.

2.3.2 Design Process for Filtering Antennas

Fig. 2.19(a) shows the universal circuit model of an N_{th} order filtering antenna. Some of the most significant parameters for the synthesis are highlighted in the model with the corresponding circuit model parameters. $M_{i,j}$ is the coupling coefficient between the ith and jth resonators. $M_{N,R}$ represents the coupling coefficient between the Nth resonator and radiator. With given specifications, these parameters can be determined as follows if classical low-pass prototypes are used

$$M_{i,j} = \frac{FBW}{\sqrt{g_i g_j}} \tag{2.7}$$

$$M_{N,R} = \frac{FBW}{\sqrt{g_N g_{N+1}}} \tag{2.8}$$

Following the design flow presented in Fig. 2.19(b), these classical prototypes can provide some general filter responses with different in-band reflection coefficients. However, sometimes these simple functions may not provide adequate selectivity for

the target applications. Filtering functions described by the coupling matrix can provide a more complex filter function for higher filter performance. The concept of coupling matrix was first presented in [119] and then extended to the N+2 general coupling matrix by R. J. Cameron [110, 120].

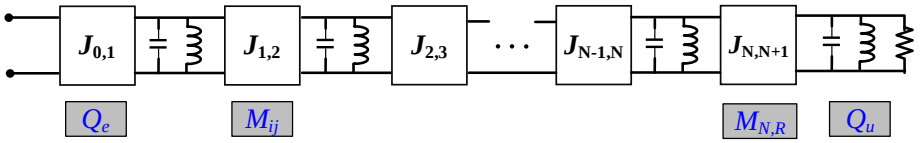

(a)

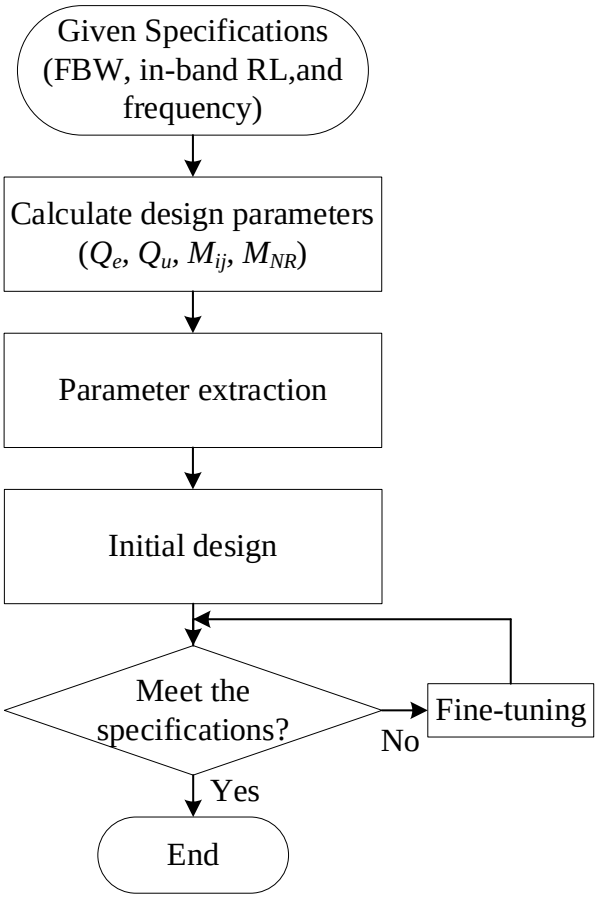

(b)

Fig. 2.19. (a) Key steps in the filtering antenna synthesis procedure. (b) Flowchart of filtering antenna design.

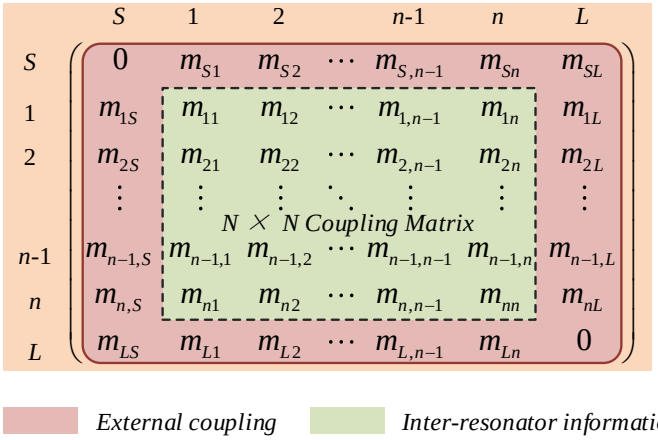

Fig. 2.20. A *N*+2 general coupling matrix.

A coupling matrix describes the relationship between every two elements in a filter circuit. Fig. 2.20 shows an example of an *N*+2 general coupling matrix. In this matrix, the port information is included and is represented by 'Source' (*S*) and 'Load' (*L*). The numbers from 1 to *n* denote each resonator, respectively. The green area gives the information of the coupling coefficients between every two resonators while the outer red area shows the coupling between resonators and external ports. A nonzero value of $m_{i,j}/m_{S,j}/m_{L,j}$ means the corresponding resonator/source/load is coupled to the *j*-th resonator. Because a BPF is always a reciprocal two-port network, the coupling matrix is symmetric, that is $m_{ij}=m_{ji}$, for $i,j=1, 2, \ldots$ n.

The relationship between the coupling matrix and *S* parameters is given as follows,

$$S_{21} = 2\frac{1}{\sqrt{q_{e1} \cdot q_{en}}}[A]_{n1}^{-1} \tag{2.9}$$

$$S_{11} = \pm(1 - \frac{2}{q_{e1}}[A]_{11}^{-1}) \tag{2.10}$$

with

$$[A] = [q] + p[U] - j[m] \tag{2.11}$$

where $[U]$ is the $n \times n$ unit or identity matrix, $[q]$ is an $n \times n$ matrix with all entries zero, except for $q_{11} = 1/q_{e1}$ and $q_{nn} = 1/q_{en}$, and $[m]$ is the general matrix, which is an $n \times n$ reciprocal matrix (that is, $m_{ij} = m_{ji}$).

The key design values in Fig. 2.19(a) can be calculated from the coupling matrix using the following formulas

$$f_i = f_0 \cdot \left(\sqrt{1+\left(m_{i,i} \cdot \frac{FBW}{2} \right)^2} - m_{i,i} \cdot \frac{FBW}{2} \right) \tag{2.12}$$

$$M_{i,j} = m_{i,j} \cdot FBW \tag{2.13}$$

$$Q_e = Q_u = \frac{1}{m_{1s}^2 \bullet FBW} \tag{2.14}$$

These important parameters for filtering antenna synthesis are concluded in Table 2-1.

Table 2-1. Key parameters for filtering antenna design.

Parameters	Description
Q_e	Input port external quality factor
M_{ij}	Coupling coefficients between non-radiative resonators
$M_{N,R}$	Coupling coefficients between non-radiative resonator and radiator
Q_u	The unloaded quality factor of the radiator

2.3.3 Filtering Antenna Performance Evaluation

As a filtering device, the performance of a filtering antenna is decided by several aspects. Fig. 2.21 shows an illustrative response for a filtering antenna. The frequency response of the filtering antenna near the passband is simplified. First, the bandwidth (f_1 - f_2) of the antenna is important. As the filtering network in front of the original antenna is a wide-band impedance-matching network, the final impedance bandwidth of a filtering antenna usually is much wider than the original antenna. The extended bandwidth enables the antenna to provide higher throughput.

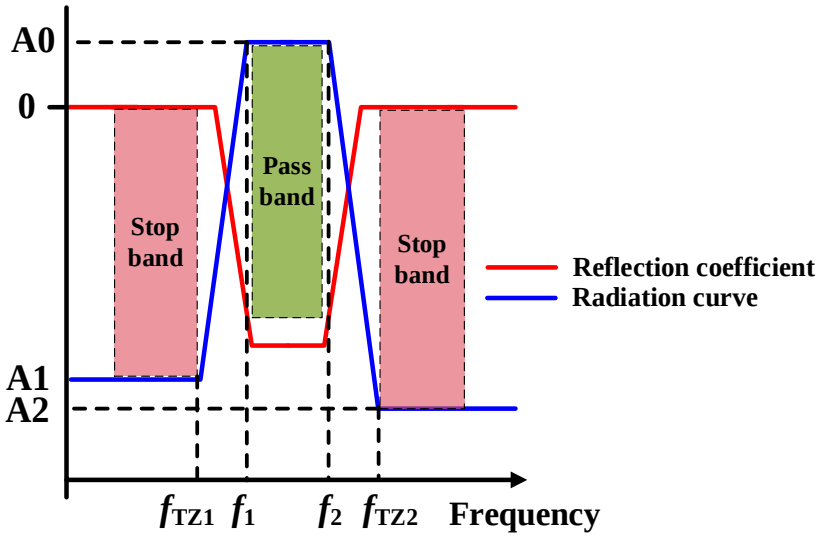

Fig. 2.21. Filtering antenna performance evaluation conceptual framework.

Second, the selectivity of the filter function is one of the most critical features of a filtering antenna. The selectivity of a filtering antenna is mainly decided by two factors: the location of TZs and suppression levels of TZs. These effects of two factors can be expressed by calculating the roll-off-ratio (RoR) of the radiation curve. Take the response in Fig. 2.21 as an example, the RoR can be calculated as

$$\begin{aligned} RoR_{\,low-band} &= \frac{A_0 - A_1}{f_1 - f_{TZ1}} \\ RoR_{\,high-band} &= \frac{A_0 - A_2}{f_{TZ2} - f_2} \end{aligned} \tag{2.15}$$

From Fig. 2.21 and (2.15) one can notice that the selectivity (RoR) is determined by the slope of the radiation curve. Generally, the closer the TZ is to the passband, the lower their suppression levels, and the higher the RoR. However, it should be noted that RoR is not always the higher the better. There is always a compromise between the RoR, suppression level, and loss. As we have mentioned before, the close-to-passband TZs will deteriorate the in-band filtering performance regarding the bandwidth and insertion loss. Other specifications such as total efficiency, realized gain, and overall size are also very important for the evaluation of the performance of a filtering antenna (FA).

2.3.3.1 An Example of OBD Scenario

Fig. 2.22 shows a filtering antenna fed by a multi-mode resonator. This structure can provide multiple TZs along each side of the operating band. When two of such filtering antennas are placed close to each other (d = 20 mm), the isolation between them is plotted in Fig. 2.23. When no filtering function is integrated, the mutual coupling between two classic patch antennas will reach -19 dB as shown in Fig. 2.23.In the first case (case 1), the guard band between two filtering antennas is about 100 MHz. As can be observed, the higher-band TZs of FA1 help reduce the mutual coupling at the FA2's operating bands when they are placed closely, while the lower-band TZ of FA2 improves the isolation at the frequency of the FA1's operating band. With this architecture, the isolation between two antenna is higher than 35 dB over the whole band of interest. The isolation level even reaches 50 dB at the operating band of the second antenna.

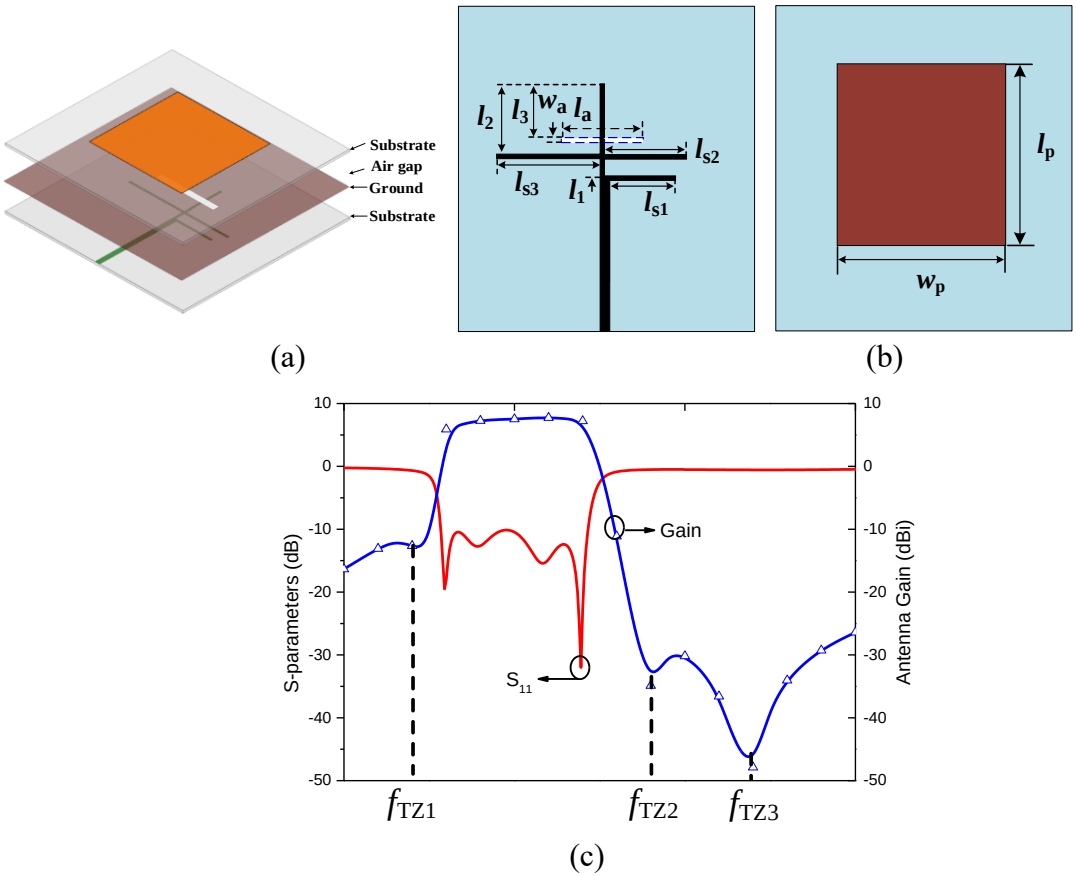

Fig. 2.22. An example filtering antenna. (a) 3D view of the antenna structure. (b) The geometry of the antenna. (c) Antenna responses.

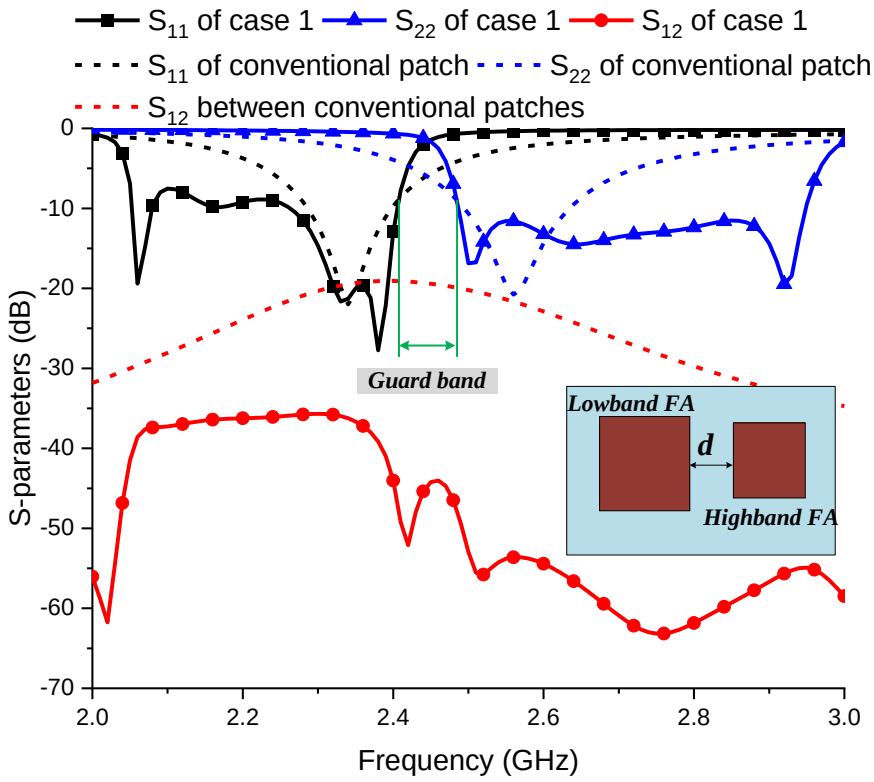

(a)

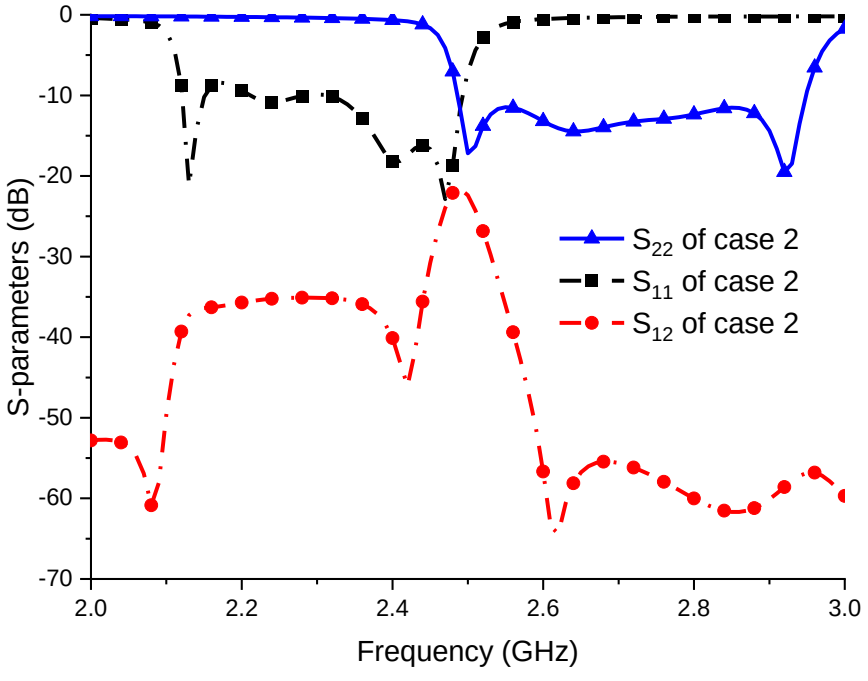

(b)

Fig. 2.23. Responses for two coupled antennas. (a) Coupled conventional patch antennas and filtering antennas with the same guard band. (b) Two coupled filtering antennas with a smaller guard band.

In the second case, the guard band between two filtering antennas is almost zero. In this extreme scenario, the filtering function does not provide too much improvement on the overall isolation between two operating bands. The filtering response of each filtering antenna cannot cover the entire frequency band, especially for the frequency range between two bands.

In summary, the filtering antenna structure is very useful in out-of-band decoupling scenarios. However, due to the limitation on the nearest achievable transmission zero of a filtering function, its ability to suppress the mutual coupling at the frequency range, which is extremely close to their own operating bands, will be very limited.

2.4 Summary

General mutual coupling concepts and decoupling techniques have been reviewed in this chapter. Depending on the operating bands of the antennas involved, different decoupling techniques should be used. The filtering antenna technique is also introduced and evaluated regarding its mutual coupling suppression ability. From these literature reviews, some key challenges for antenna decoupling techniques can be concluded as follows:

- Decoupling techniques without occupying too large a space.
- Simple and low-cost in-band/out-of-band decoupling solutions.
- Wideband in-band decoupling.
- Out-of-band decoupling when the frequency ratio between the two antennas involved is small.

References

[1] E. G. Larsson, O. Edfors, F. Tufvesson, and T. L. Marzetta, “Massive MIMO for next generation wireless systems,” *IEEE Communications Magazine,* vol. 52, no. 2, pp. 186-195, February 2014.

[2] Y.-H. N. *et al.*, “Full-dimension MIMO (FD-MIMO) for next-generation cellular technology,” *IEEE Communications Magazine,* vol. 51, no. 6, pp. 172-179.

[3] M. Chiani, M. Z. Win, and A. Zanella, “On the capacity of spatially correlated MIMO rayleigh-fading channels,” *IEEE Transactions on Information Theory,* vol. 49, no. 10, pp. 2363-2371, 2003.

[4] F. Capozzi *et al.*, “Downlink packet scheduling in lte cellular networks: Key design issues and a survey,” *IEEE Communications Surveys & Tutorials,* vol. 15, no. 2, pp. 678-700, 2013.

[5] K. E. Kolodziej, B. T. Perry, and J. S. Herd, “In-band full-duplex technology: Techniques and systems survey,” *IEEE Transactions on Microwave Theory and Techniques,* vol. 67, no. 7, pp. 3025-3041, 2019.

[6] M. Duarte, C. Dick, and A. Sabharwal, “Experiment-driven characterization of full-duplex wireless systems,” *IEEE Transactions on Wireless Communications,* vol. 11, no. 12, pp. 4296-4307, 2012.

[7] M. Jain *et al.*, “Practical, real-time, full duplex wireless,” *Proceedings of the ACM Mobicom*, Sep. 2011.

[8] S. H. *et al.*, “Applications of self-interference cancellation in 5G and beyond,” *IEEE Communications Magazine,* vol. 52, no. 2, pp. 114-121, Feb 2014.

[9] D. Neculoiu, A.-C. Bunea, A. M. Dinescu, and L. A. Farhat, “Band pass filters based on Gan/Si lumped-element SAW resonators operating at frequencies above 5 GHz,” *IEEE Access,* vol. 6, pp. 47587-47599, 2018.

[10] A. Muller *et al.*, “SAW devices manufactured on Gan/Si for frequencies beyond 5 GHz,” *IEEE Electron Device Letters,* vol. 31, no. 12, pp. 1398-1400, 2010.

[11] V. Chauhan *et al.*, “Enhancing RF bulk acoustic wave devices: Multiphysical modeling and performance,” *IEEE Microwave Magazine,* vol. 20, no. 10, pp. 56-70, 2019.

[12] P. Warder, and A. Link, “Golden age for filter design: Innovative and proven approaches for acoustic filter, duplexer, and multiplexer design,” *IEEE Microwave Magazine,* vol. 16, no. 7, pp. 60-72, 2015.

[13] 3gpp tr 36.816 v11.2.0, online available: Https://portal.3gpp.Org/desktopmodules/specifications/specificationdetails.Aspx?Specificationid=2495.

[14] D. Pozar, “Input impedance and mutual coupling of rectangular microstrip antennas,” *IEEE Transactions on Antennas and Propagation,* vol. 30, no. 6, pp. 1191-1196, Nov. 1982.

[15] A. Derneryd, “A theoretical investigation of the rectangular microstrip antenna element,” *IEEE Transactions on Antennas and Propagation,* vol. 26, no. 4, pp. 532-535, Jul. 1978.

[16] N. Alexopoulos, and I. Rana, “Mutual impedance computation between printed dipoles,” *IEEE Transactions on Antennas and Propagation,* vol. 29, no. 1, pp. 106-111, Jan. 1981.

[17] H. King, “Mutual impedance of unequal length antennas in echelon,” *IRE Transactions on Antennas and Propagation,* vol. 5, no. 3, pp. 306-313, July 1957.

[18] H. G. Booker, "Slot aerials and their relation to complementary wire aerials (Babinet’s principle)", *J. Inst. Elect. Eng. IIIA Radiolocation*, vol. 93, no. 4, pp. 620-626, 1946.

[19] A. Diallo *et al.*, “Study and reduction of the mutual coupling between two mobile phone PIFAs operating in the DCS1800 and UMTS bands,” *IEEE Transactions on Antennas and Propagation,* vol. 54, no. 11, pp. 3063-3074, 2006.

[20] C. B. Dietrich, K. Dietze, J. R. Nealy and W. L. Stutzman, "Spatial, polarization, and pattern diversity for wireless handheld terminals," in IEEE Transactions on Antennas and Propagation, vol. 49, no. 9, pp. 1271-1281, Sept. 2001.

[21] M. Pelosi, M. B. Knudsen, and G. F. Pedersen, “Multiple antenna systems with inherently decoupled radiators,” *IEEE Transactions on Antennas and Propagation,* vol. 60, no. 2, pp. 503-515, 2012.

[22] X. Zhao, S. P. Yeo, and L. C. Ong, “Decoupling of inverted-F antennas with high-order modes of ground plane for 5G mobile MIMO platform,” *IEEE Transactions on Antennas and Propagation,* vol. 66, no. 9, pp. 4485-4495, 2018.

[23] J.-F. Qian *et al.*, “A wide stopband filtering patch antenna and its application in MIMO system,” *IEEE Transactions on Antennas and Propagation,* vol. 67, no. 1, pp. 654-658, 2019.

[24] J.-F. Qian *et al.*, “A novel electric and magnetic gap-coupled broadband patch antenna with improved selectivity and its application in MIMO system,” *IEEE Transactions on Antennas and Propagation,* vol. 66, no. 10, pp. 5625-5629, 2018.

[25] C.-X. Mao *et al.*, “A shared-aperture dual-band dual-polarized filtering-antenna-array with improved frequency response,” *IEEE Transactions on Antennas and Propagation,* vol. 65, no. 4, pp. 1836-1844, April 2017.

[26] J. Andersen, and H. Rasmussen, “Decoupling and descattering networks for antennas,” *IEEE Transactions on Antennas and Propagation,* vol. 24, no. 6, pp. 841-846, November 1976.

[27] S.-C. Chen, Y.-S. Wang, and S.-J. Chung, “A decoupling technique for increasing the port isolation between two strongly coupled antennas,” *IEEE Transactions on Antennas and Propagation,* vol. 56, no. 12, pp. 3650-3658, 2008.

[28] Y.-F. Cheng, and K.-K. M. Cheng, “A novel and simple decoupling method for a three-element antenna array,” *IEEE Antennas and Wireless Propagation Letters,* vol. 16, pp. 1072-1075, 2017.

[29] L. Zhao, L. K. Yeung, and K.-L. Wu, “A coupled resonator decoupling network for two-element compact antenna arrays in mobile terminals,” *IEEE Transactions on Antennas and Propagation,* vol. 62, no. 5, pp. 2767-2776, 2014.

[30] L. Zhao, and K.-L. Wu, “A dual-band coupled resonator decoupling network for two coupled antennas,” *IEEE Transactions on Antennas and Propagation,* vol. 63, no. 7, pp. 2843-2850, 2015.

[31] H. Makimura *et al.*, “Novel decoupling concept for strongly coupled frequency-dependent antenna arrays,” *IEEE Transactions on Antennas and Propagation,* vol. 65, no. 10, pp. 5147-5154, 2017.

[32] S. N. Venkatasubramanian *et al.*, “Impact of using resistive elements for wideband isolation improvement,” *IEEE Transactions on Antennas and Propagation,* vol. 65, no. 1, pp. 52-62, 2017.

[33] M. M. Nikolic, A. R. Djordjevic, and A. Nehorai, “Microstrip antennas with suppressed radiation in horizontal directions and reduced coupling,” *IEEE Transactions on Antennas and Propagation,* vol. 53, no. 11, pp. 3469-3476, 2005.

[34] H. Oraizi, and B. Rezaei, “Improvement of antenna radiation efficiency by the suppression of surface waves,” *Journal of Electromagnetic Analysis and Applications,* vol. 03, no. 03, pp. 79-83, 2011.

[35] R. Bancroft, “Microstrip antenna efficiency and surface wave loss,” *IEEE Transactions on Antennas and Propagation,* vol. 69, no. 8, pp. 5032-5035, 2021.

[36] A. Askarian, J. Yao, Z. Lu, and K. Wu, “Surface-wave control technique for mutual coupling mitigation in array antenna,” *IEEE Microwave and Wireless Components Letters,* vol. 32, no. 6, pp. 623-626, 2022.

[37] Y.-F. Cheng *et al.*, “Analysis and design of wide-scan phased array using polarization-conversion isolators,” *IEEE Antennas and Wireless Propagation Letters,* vol. 18, no. 3, pp. 512-516, 2019.

[38] K.-L. Wu, C. Wei, X. Mei, and Z.-Y. Zhang, “Array-antenna decoupling surface,” *IEEE Transactions on Antennas and Propagation,* vol. 65, no. 12, pp. 6728-6738, 2017.

[39] Y. Fan, and Y. Rahmat-Samii, “Microstrip antennas integrated with electromagnetic band-gap (ebg) structures: A low mutual coupling design for array applications,” *IEEE Transactions on Antennas and Propagation,* vol. 51, no. 10, pp. 2936-2946, 2003.

[40] S. Ghosal, A. De, R. M. Shubair, and A. Chakrabarty, “Analysis and reduction of mutual coupling in a microstrip array with a magneto-electric structure,” *IEEE Transactions on Electromagnetic Compatibility,* vol. 63, no. 5, pp. 1376-1383, 2021.

[41] F. Liu *et al.*, “Ceramic superstrate-based decoupling method for two closely packed antennas with cross-polarization suppression,” *IEEE Transactions on Antennas and Propagation,* vol. 69, no. 3, pp. 1751-1756, 2021.

[42] J. S. Hong, and M. J. Lancaster, *Microstrip filters for RF/microwave applications*, New York, NY, USA: Wiley, 2001.

[43] D. Schmitt, F. J. Goertz, Z. Thiel, and U. Rosenberg, “New type of mixed modes dielectric cavity filter for multiplexers,” *17th AIAA International Communications Satellite Systems Conference and Exhibit*, 1998.

[44] X. Shang, Y. Wang, G. L. Nicholson, and M. J. Lancaster, “Design of multiple-passband filters using coupling matrix optimisation,” *IET Microwaves, Antennas & Propagation,* vol. 6, no. 1, 2012.

[45] H. Heng-Tung, Z. Zhenyu, K. A. Zaki, and A. E. Ati, “Parameter extraction for symmetric coupled-resonator filters,” *IEEE Transactions on Microwave Theory and Techniques,* vol. 50, no. 12, pp. 2971-2978, 2002.

[46] D. R. Jacjowski, “Passive enhancement of resonator q in microwave notch filters,” *IEEE MIT-S Int. Microw. Symp. Dig.*, pp. 13 15-13 18, 2004.

[47] Q.-X. Chu, and H. Wang, “A compact open-loop filter with mixed electric and magnetic coupling,” *IEEE Transactions on Microwave Theory and Techniques,* vol. 56, no. 2, pp. 431-439, 2008.

[48] T. Ching-Wen, L. Yin-Ching, and C. Chi-Yang, “Realization of transmission zeros in combline filters using an auxiliary inductively coupled ground plane,” *IEEE Transactions on Microwave Theory and Techniques,* vol. 51, no. 10, pp. 2112-2118, 2003.

[49] M. Martinez-Mendoza *et al.*, “Design of bandpass transversal filters employing a novel hybrid structure,” *IEEE Transactions on Microwave Theory and Techniques,* vol. 55, no. 12, pp. 2670-2678, 2007.

[50] M. Bekheit, S. Amari, and W. Menzel, “Modeling and optimization of compact microwave bandpass filters,” *IEEE Transactions on Microwave Theory and Techniques,* vol. 56, no. 2, pp. 420-430, 2008.

[51] C.-F. Chen, T.-M. Shen, T.-Y. Huang, and R.-B. Wu, “Design of compact quadruplexer based on the tri-mode net-type resonators,” *IEEE Microwave and Wireless Components Letters,* vol. 21, no. 10, pp. 534-536, 2011.

[52] S. C. Weng, K. W. Hsu, and W. H. Tu, “Microstrip bandpass single-pole quadruple-throw switch and independently switchable quadruplexer,” *IET Microwaves, Antennas & Propagation,* vol. 8, no. 4, pp. 244-254, 2014.

[53] M.-L. Chuang, and M.-T. Wu, "Microstrip multiplexer and switchable diplexer with joint T-shaped resonators," *IEEE Microwave and Wireless Components Letters,* vol. 24, no. 5, pp. 309-311, 2014.

[54] S. Taravati, and M. Khalaj-Amirhosseini, "Design method for matching circuits of general multiplexers," *IET Microwaves, Antennas & Propagation,* vol. 7, no. 4, pp. 237-244, 2013.

[55] T. Fromenteze *et al.*, "Passive beamforming using surface acoustic wave filters," *IEEE Antennas and Wireless Propagation Letters,* vol. 14, pp. 76-79, 2015.

[56] C. C. W. Ruppel, "Acoustic wave filter technology-A review," *IEEE Trans Ultrason Ferroelectr Freq Control,* vol. 64, no. 9, pp. 1390-1400, Sep, 2017.

[57] Online datasheets available at: Https://abracon.Com/parametric/sawfilters?Orderby=frequency _center:True.

[58] Y. Zhang, X. Y. Zhang, L.-H. Ye, and Y.-M. Pan, "Dual-band base station array using filtering antenna elements for mutual coupling suppression," *IEEE Transactions on Antennas and Propagation,* vol. 64, no. 8, pp. 3423-3430, 2016.

[59] J. Guo *et al.*, "Isolation improvement of two tightly coupled antennas operating in adjacent frequency bands using filtering structures," *IEEE Open Journal of Antennas and Propagation,* vol. 1, pp. 207-214, 2020.

[60] M. Li *et al.*, "A miniaturized dual-band base station array antenna using band notch dipole antenna elements and amc reflectors," *IEEE Transactions on Antennas and Propagation,* vol. 66, no. 6, pp. 3189-3194, 2018.

[61] K.-W. Qian, "A compact ltcc decoupling-network based on coupled-resonator for antenna interference suppression of adjacent frequency bands," *IEEE Access,* vol. 7, pp. 25485-25492, 2019.

[62] K.-L. Wong, J.-Z. Chen, and W.-Y. Li, "Four-port wideband annular-ring patch antenna generating four decoupled waves for 5G multi-input–multi-output access points," *IEEE Transactions on Antennas and Propagation,* vol. 69, no. 5, pp. 2946-2951, 2021.

[63] M. Nakano *et al.*, "Feed circuits of double-layered self-diplexing antenna for mobile satellite communications," *IEEE Transactions on Antennas and Propagation,* vol. 40, no. 10, pp. 1269-1271, Oct. 1992.

[64] X. Gao *et al.*, "Low-profile planar tripolarization antenna for wlan communications," *IEEE Antennas and Wireless Propagation Letters,* vol. 9, pp. 83-86, 2010.

[65] K. Saurav, N. K. Mallat, and Y. M. M. Antar, "A three-port polarization and pattern diversity ring antenna," *IEEE Antennas and Wireless Propagation Letters,* vol. 17, no. 7, pp. 1324-1328, 2018.

[66] A. H. Abdelrahman, and D. S. Filipovic, "Antenna system for full-duplex operation of handheld radios," *IEEE Transactions on Antennas and Propagation,* vol. 67, no. 1, pp. 522-530, 2019.

[67] L. Liu *et al.*, "Slit-slot line and its application to low cross-polarization slot antenna and mutual-coupling suppressed tripolarized MIMO antenna," *IEEE Transactions on Antennas and Propagation,* vol. 67, no. 1, pp. 4-15, 2019.

[68] K. Zhang, Z. H. Jiang, W. Hong, and D. H. Werner, "A low-profile and wideband triple-mode antenna for wireless body area network concurrent on-/off-body communications," *IEEE Transactions on Antennas and Propagation,* vol. 68, no. 3, pp. 1982-1994, 2020.

[69] Y. He, and Y. Li, "Compact co-linearly polarized microstrip antenna with fence-strip resonator loading for in-band full-duplex systems," *IEEE Transactions on Antennas and Propagation,* vol. 69, no. 11, pp. 7125-7133, 2021.

[70] D. Inserra, and G. Wen, “Dual orthogonal port stacked patch antenna with vertical pins for simultaneous transmit and receive application,” *IEEE Transactions on Antennas and Propagation,* vol. 69, no. 12, pp. 8908-8913, 2021.

[71] B. Yang *et al.*, “Tri-port antenna with shared radiator and self-decoupling characteristic for 5G smartphone application,” *IEEE Transactions on Antennas and Propagation,* vol. 70, no. 6, pp. 4836-4841, 2022.

[72] A. Zhang, K. Wei, Y. Hu, and Q. Guan, “High-isolated coupling-grounded patch antenna pair with shared radiator for the application of 5G mobile terminals,” *IEEE Transactions on Antennas and Propagation,* vol. 70, no. 9, pp. 7896-7904, 2022.

[73] P. Cheong, K.-F. Chang, W.-W. Choi, and K.-W. Tam, “A highly integrated antenna-triplexer with simultaneous three-port isolations based on multi-mode excitation,” *IEEE Transactions on Antennas and Propagation,* vol. 63, no. 1, pp. 363-368, 2015.

[74] K. Kumar, S. Priya, S. Dwari, and M. K. Mandal, “Self-quadruplexing circularly polarized siw cavity-backed slot antennas,” *IEEE Transactions on Antennas and Propagation,* vol. 68, no. 8, pp. 6419-6423, 2020.

[75] P. Pourmohammadi *et al.*, “Substrate integrated waveguide-based full-duplex antenna with improved out-of-band suppression,” *IEEE Transactions on Circuits and Systems II: Express Briefs,* vol. 70, no. 4, pp. 1430-1434, 2023.

[76] W. Chujo, M. Fujise, H. Arai, and N. Goto, "A two-layer self-diplexing antenna using a circularly polarized ring patch antenna," p.^pp. 338-341 vol.1.

[77] A. Boukarkar, X. Q. Lin, Y. Jiang, and Y. Q. Yu, “A tunable dual-fed self-diplexing patch antenna,” *IEEE Transactions on Antennas and Propagation,* vol. 65, no. 6, pp. 2874-2879, 2017.

[78] C. X. Mao *et al.*, “Filtering antennas: Design methods and recent developments,” *IEEE Microwave Magazine,* vol. 22, no. 11, pp. 52-63, 2021.

[79] Y.-f. Cao, Y. Zhang, and X.-y. Zhang, “Filtering antennas: From innovative concepts to industrial applications,” *Frontiers of Information Technology & Electronic Engineering,* vol. 21, no. 1, pp. 116-127, 2020.

[80] R. M. Fano, “Theoretical limitations on the broadband matching of arbitrary impedances,” *J. Franklin Inst.,* vol. 249, pp. 57-154, Jan. Fab. 1950.

[81] G. Matthaei, “Synthesis of tchebycheff impedance-matching networks, filters, and interstages,” *IRE Transactions on Circuit Theory,* vol. 3, no. 3, pp. 163-172, 1956.

[82] H. F. Pues and A. R. Van de Capelle, “An impedance-matching technique for increasing the bandwidth of microstrip antennas,” *IEEE Transactions on Antennas and Propagation,* vol. 37, no. 11, pp. 1345-1354, Nov. 1989.

[83] H. An, B. Nauwelaers and A. Van de Capelle, “A new approach of broadband microstrip antenna design,” *IEEE Antennas and Propagation Society International Symposium 1992 Digest*, June 1992, pp. 475-478.

[84] A. Sabban, “A new broadband stacked two-layer microstrip antenna,” *1983 Antennas and Propagation Society International Symposium*, 1983, pp. 63-66.

[85] C. Chen, A. Tulintseff, and R. Sorbello, “Broadband two-layer microstrip antenna,” *1984 Antennas and Propagation Society International Symposium*, 1984, pp. 251-254.

[86] G. Kumar, and K. Gupta, “Directly coupled multiple resonator wide-band microstrip antennas,” *IEEE Transactions on Antennas and Propagation,* vol. 33, no. 6, pp. 588-593, 1985.

[87] T. L. Nadan, J. P. Coupez, S. Toutain, and C. Person, "Integration of an antenna/filter device, using a multi-layer, multi-technology process," *1998 28th European Microwave Conference*, 1998, pp. 672-677.

[88] K. Yoshida *et al.*, "Superconducting slot antenna with broadband impedance matching circuit," *IEEE Transactions on Applied Superconductivity,* vol. 11, no. 1, pp. 103-106, Mar. 2001.

[89] T. L. Nadan, J. P. Coupez, and C. Person, "Optimization and miniaturization of a filter/antenna multi-function module using a composite ceramic-foam substrate," *1999 IEEE MTT-S International Microwave Symposium Digest*, Anaheim, CA, USA, Jun. 1999, pp. 13-19.

[90] H. M. Hizan, I. C. Hunter, and A. I. Abunjaileh, "Integrated dual-band radiating bandpass filter using dual-mode circular cavities," *IEEE Microwave and Wireless Components Letters,* vol. 21, no. 5, pp. 246-248, 2011.

[91] X. Y. Zhang, W. Duan, and Y.-M. Pan, "High-gain filtering patch antenna without extra circuit," *IEEE Transactions on Antennas and Propagation,* vol. 63, no. 12, pp. 5883-5888, 2015.

[92] W. Duan *et al.*, "Dual-polarized filtering antenna with high selectivity and low cross polarization," *IEEE Transactions on Antennas and Propagation,* vol. 64, no. 10, pp. 4188-4196, 2016.

[93] Y. Zhang, X. Y. Zhang, and Y.-M. Pan, "Compact single- and dual-band filtering patch antenna arrays using novel feeding scheme," *IEEE Transactions on Antennas and Propagation,* vol. 65, no. 8, pp. 4057-4066, 2017.

[94] M. Ohira, and Z. Ma, "An efficient design method of microstrip filtering antenna suitable for circuit synthesis theory of microwave bandpass filters," *2015 International Symposium on Antennas and Propagation (ISAP)*, Hobart, TAS, Australia, 2015, pp. 1-4.

[95] C.-K. Lin, and S.-J. Chung, "A filtering microstrip antenna array," *IEEE Transactions on Microwave Theory and Techniques,* vol. 59, no. 11, pp. 2856-2863, 2011.

[96] M. Troubat *et al.*, "Mutual synthesis of combined microwave circuits applied to the design of a filter-antenna subsystem," *IEEE Transactions on Microwave Theory and Techniques,* vol. 55, no. 6, pp. 1182-1189, 2007.

[97] F.-C. Chen, J.-F. Chen, Q.-X. Chu, and M. J. Lancaster, "X-band waveguide filtering antenna array with nonuniform feed structure," *IEEE Transactions on Microwave Theory and Techniques,* vol. 65, no. 12, pp. 4843-4850, 2017.

[98] R. H. Mahmud, and M. J. Lancaster, "High-gain and wide-bandwidth filtering planar antenna array-based solely on resonators," *IEEE Transactions on Antennas and Propagation,* vol. 65, no. 5, pp. 2367-2375, 2017.

[99] Y. Yusuf, C. Haitao, and G. Xun, "A seamless integration of 3-D vertical filters with highly efficient slot antennas," *IEEE Transactions on Antennas and Propagation,* vol. 59, no. 11, pp. 4016-4022, 2011.

[100] Y. Yusuf, and X. Gong, "Compact low-loss integration of high-*Q* 3-D filters with highly efficient antennas," *IEEE Transactions on Microwave Theory and Techniques,* vol. 59, no. 4, pp. 857-865, 2011.

[101] H. Chu, C. Jin, J.-X. Chen, and Y.-X. Guo, "A 3-D millimeter-wave filtering antenna with high selectivity and low cross-polarization," *IEEE Transactions on Antennas and Propagation,* vol. 63, no. 5, pp. 2375-2380, 2015.

[102] P. K. Li *et al.*, "Codesigned high-efficiency single-layered substrate integrated waveguide filtering antenna with a controllable radiation null," *IEEE Antennas and Wireless Propagation Letters,* vol. 17, no. 2, pp. 295-298, 2018.

[103] T. Li, and X. Gong, "Vertical integration of high-*Q* filter with circularly polarized patch antenna with enhanced impedance-axial ratio bandwidth," *IEEE Transactions on Microwave Theory and Techniques,* vol. 66, no. 6, pp. 3119-3128, 2018.

[104] R. Lovato, and X. Gong, "A third-order siw-integrated filter/antenna using two resonant cavities," *IEEE Antennas and Wireless Propagation Letters,* vol. 17, no. 3, pp. 505-508, 2018.

[105] K.-Z. Hu *et al.*, "Design of compact, single-layered substrate integrated waveguide filtenna with parasitic patch," *IEEE Transactions on Antennas and Propagation,* vol. 68, no. 2, pp. 1134-1139, 2020.

[106] K. Yoshida, T. Takahashi, and H. Kanaya, "Superconducting slot antenna with broadband impedance matching circuit," *IEEE Transactions on Applied Superconductivity,* vol. 11, no. 1, pp. 103-106, May 2001.

[107] Y. Tsutsumi, H. Kanaya, and K. Yoshida, "Design and performance of an electrically small slot loop antenna with a miniaturized superconducting matching circuit," *IEEE Transactions on Appiled Superconductivity,* vol. 15, no. 2, pp. 1020-1023, 2005.

[108] H.-W. Deng *et al.*, "Closely spaced broadband MIMO differential filtering slotline antenna with cm suppression," *IEEE Antennas and Wireless Propagation Letters,* vol. 17, no. 12, pp. 2498-2502, 2018.

[109] S. Amari, and M. Bekheit, "Physical interpretation and implications of similarity transformations in coupled resonator filter design," *IEEE Transactions on Microwave Theory and Techniques,* vol. 55, no. 6, pp. 1139-1153, 2007.

[110] R. Cameron, "Advanced filter synthesis," *IEEE Microwave Magazine,* vol. 12, no. 6, pp. 42-61, 2011.

[111] C.-X. Mao *et al.*, "An integrated filtering antenna array with high selectivity and harmonics suppression," *IEEE Transactions on Microwave Theory and Techniques,* vol. 64, no. 6, pp. 1798-1805, 2016.

[112] C.-X. Mao *et al.*, "Compact highly integrated planar duplex antenna for wireless communications," *IEEE Transactions on Microwave Theory and Techniques,* vol. 64, no. 7, pp. 2006-2013, 2016.

[113] X.-J. Lin, Z.-M. Xie, P.-S. Zhang, and Y. Zhang, "A broadband filtering duplex patch antenna with high isolation," *IEEE Antennas and Wireless Propagation Letters,* vol. 16, pp. 1937-1940, 2017.

[114] K.-Z. Hu *et al.*, "Compact, vertically integrated duplex filtenna with common feeding and radiating siw cavities," *IEEE Transactions on Antennas and Propagation,* vol. 69, no. 1, pp. 502-507, 2021.

[115] J.-F. Li *et al.*, "Compact dual-polarized antenna for dual-band full-duplex base station applications," *IEEE Access,* vol. 7, pp. 72761-72769, 2019.

[116] Z. H. Jiang, and D. H. Werner, "A compact, wideband circularly polarized co-designed filtering antenna and its application for wearable devices with low SAR," *IEEE Transactions on Antennas and Propagation,* vol. 63, no. 9, pp. 3808-3818, 2015.

[117] Y. Lu *et al.*, "Circularly polarised integrated filtering antenna with polarisation reconfigurability," *IET Microwaves, Antennas & Propagation,* vol. 11, no. 15, pp. 2247-2252, 2017.

[118] J.-F. Li *et al.*, "A left/right-handed dual circularly-polarized antenna with duplexing and filtering performance," *IEEE Access,* vol. 7, pp. 35431-35437, 2019.

[119] A. E. Atia, and A. E. Williams, "Narrow-bandpass waveguide filters," *IEEE Transactions on Microwave Theory and Techniques,* vol. 20, no. 4, pp. 258-265, Apr. 1972.

[120] R. J. Cameron, "Advanced coupling matrix synthesis techniques for microwave filters," IEEE Transactions on Microwave Theory and Techniques, vol. 51, no. 1, pp. 1-10, 2003.

Chapter 3
Decoupled Filtering Antennas

As the suppression level of a filtering network is mainly decided by the order of the circuit, the decoupling between two antennas with extremely small frequency ratios is very challenging for filters. To reduce the mutual coupling from the adjacent frequency bands, new techniques are needed. In addition, in-band decoupling between two identical filtering antennas is also very important when MIMO architecture is involved. However, most of the decoupling techniques in the literature affect the original impedance characteristics of the antennas, which are not desirable for filtering antennas.

In this chapter, two novel methods for decoupling between filtering antennas are presented. The first technique investigates a decoupling network concept for the mutual coupling reduction between two filtering antennas. This coupled-resonator decoupling network (DN) can be co-designed with the coupled filtering antennas with little effect on the original filtering responses. By connecting this network in parallel to the coupled antennas, the mutual coupling between the two filtering antennas can be dramatically suppressed, regardless of whether they operate over the same or adjacent frequency bands.

The second technique achieves two isolated filtering antennas using a novel filtering feeding network. The feeding network consists of an all-resonator structure, which shares a common dual-mode resonator. This structure facilitates the isolation of two well-isolated channels through the exploitation of the even and odd modes of the dual-mode resonator. By applying balanced excitation to the odd mode and unbalanced excitation to the even mode, the two modes can be separated, creating a hybrid-like feeding structure. With this feeding scheme, two isolated filtering antennas are co-designed with a shared radiator.

In this chapter, all the prototypes were fabricated by HXP Circuits and assembled by the author. The S-parameters were measured by the author in the Antenna Lab at the University of Kent. The radiation performance of all the prototypes was measured using the anechoic chamber at the University of Kent, with the assistance of Technician Mr. Antonio Mendoza.

3.1 Decoupling Network for In-Band and Out-of-Band Decoupling

3.1.1 Conceptual Framework

The main idea of this work is to find a neutralization network of the coupled filtering antennas. The DN is expected to be a filtering circuit such that the magnitude of the transmission coefficient for both paths can be the same in the band of interest. To build such a DN, the impedance behaviour of the coupled filtering antennas should be studied first.

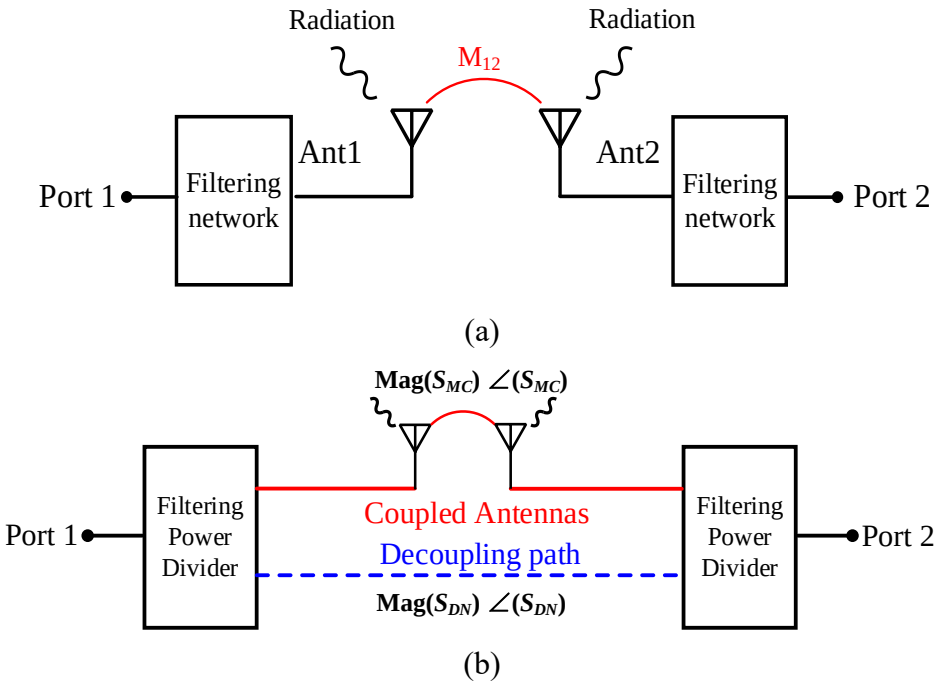

Fig. 3.1. Conceptual framework of (a) coupled filtering antennas and (b) decoupled filtering antennas.

Fig. 3.1(a) shows the conceptual frameworks for the coupled antennas. Suppose a signal is injected into the Antenna1 (ANT1). Part of the energy will radiate into the free space. The remaining energy is then coupled to the second antenna, assuming that the energy wasted in the material is negligible. The challenge lies in the fact that radiation and mutual coupling are almost indistinguishable from each other on a physical level. Consequently, in this work, a power-dividing network for decoupling needs is

constructed before the radiators to assign the power for the decoupling path and radiating path. Fig. 3.1(b) shows the framework of the proposed decoupling idea, where S_{MC} and S_{DC} represent the S-parameters related to mutual coupling and decoupling path, respectively. As can be seen, a decoupling path is introduced parallel to the coupling path between the antennas. This path can be achieved by cascading two more 2-way power dividers in front of each filtering antenna to split the input signal into two different parts. Then to make sure the transmission from port1 to port 2 is perfectly suppressed, the following conditions need to be met, at least in the band of interest:

1. *The transmission coefficients for both paths should have the same amplitude, that is Mag (S_{MC})=Mag (S_{DC}).*

2. *The phase slopes of the transmission coefficients should be the same for both paths, that is*

$$\tau\left(S_{MC}(\omega)\right) = -\frac{\partial \angle S_{MC}(\omega)}{\partial \omega} = \tau\left(S_{DC}(\omega)\right) = -\frac{\partial \angle S_{DC}(\omega)}{\partial \omega} \tag{3.1}$$

for $2\pi \cdot f_1 < \omega < 2\pi \cdot f_2$, where f_1 and f_2 are the lower and upper boundaries of the band of interest, respectively.

3. *The phase difference between the transmission coefficients for both paths needs to be 180°, that is $\angle(S_{MC}) = \angle(S_{DC}) + 180°$.*

To ensure that all these constraints are met over a wide frequency range, a novel coupled resonator decoupling network will be introduced in the subsequent section.

3.1.2 Circuit Models and Analysis

The frequency responses of a 2nd-order Chebyshev BPF with a ripple level of 0.1 dB are plotted in Fig. 3.2. As can be observed, the phase response of a 2nd order BPF keeps being a constant value at its centre frequency under different bandwidths. Besides, the phase slope increases with increased bandwidth. It can be concluded that the phase response of a bandpass filter network is determined by its bandwidth and the lowpass prototype used.

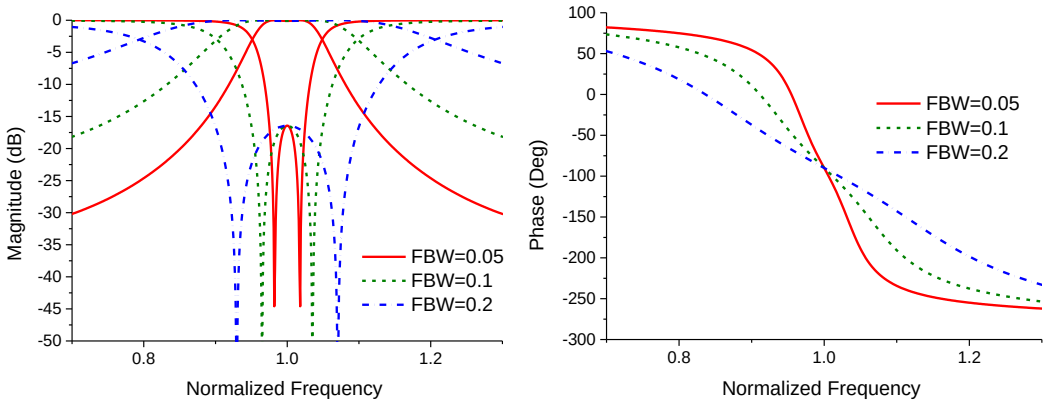

(a) (b)

Fig. 3.2. (a) magnitude and (b) phase responses of 2nd-order Chebyshev BPF network as a function of normalized frequency under different FBWs (Ripple level = 0.1 dB).

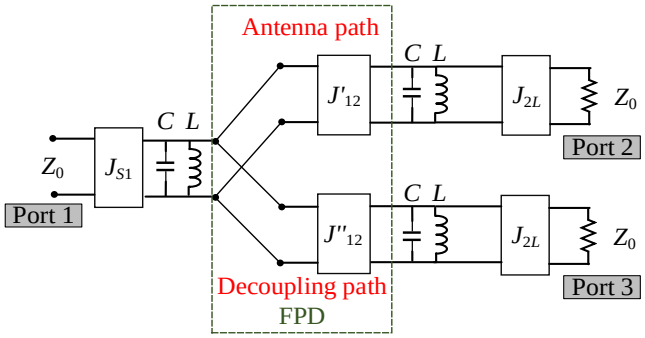

Fig. 3.3. Circuit model for filtering antenna with a decoupling path.

Based on the analysis above, Fig. 3.3 depicts the circuit model of a filtering antenna that incorporates an additional decoupling path. It is a filtering power divider (FPD). The power dividing happens just before the antenna element. This FPD is built according to the cascaded filtering circuit theory which has been stated in detail in [1, 2].

As the antenna is a single-port device, we only need to concentrate on its reflection coefficient. For the circuit shown in Fig. 3.3, S_{11} will remain unchanged after adding an additional decoupling path, provided the following condition is met

$$J'^2_{12} + J''^2_{12} = J^2_{12} \tag{3.2}$$

where J_{12} denotes the original coupling strength between the last stage resonator and patch. The ratio of J'^2_{12} to J''^2_{12} ($k = J'^2_{12}/ J''^2_{12}$) decides the power division ratio of the FPD. For this filtering power dividing circuit, if port 1 is matched and supposing the

circuit is lossless, then the transmission coefficients for both output channels are related to each other according to the energy conservation as follows

$$|S_{12}|^2 = \frac{k^2}{1+k^2}(1-|S_{11}|^2) \tag{3.3}$$

$$|S_{13}|^2 = \frac{1}{1+k^2}(1-|S_{11}|^2) \tag{3.4}$$

These relationships indicate that the difference between the transmission coefficients for both paths just reflects that they are multiplied by a different constant. As k is a real constant, then we can see that the power dividing ratio does not influence the phase responses of the transmission coefficients for the two paths. According to the results in Fig. 3.2(b), the phase slope for both paths can be forced to be the same as long as they are synthesized with the same bandwidths and lowpass prototype. For demonstration, a lumped circuit model is built in the Advanced Design System (ADS). Simulated responses with different power dividing ratios are plotted in Fig. 3.4 together with element values. Three cases are studied here which are corresponding to S_{31} = -10 dB (case 1), -15 dB (case 2), and -20 dB (case 3), respectively. For all the cases, they share the same filter prototype, which is given as follows:

In-band return loss: -15 dB.

Centre frequency: 2.45 GHz.

Fractional bandwidth: 3.26%.

During the tuning, the reflection coefficient at the driven port (port 1) is forced to be the same. For conciseness, only the S_{11} and S_{21} for the first case are provided. All the cases share the same lowpass prototype. The only difference between them is that they are designed with different power-dividing ratios. The phase responses for both S_{31} and S_{21} are always the same for all the cases as can be observed. Only one curve can be observed in Fig. 3.4 as they overlap with each other. These results agree well with the previous analyses. This characteristic is one of the most important premises for this work. It allows us to control the amplitude and phase of the transmission coefficient of the decoupling path independently, such that satisfaction of condition 1 and condition 3 is possible.

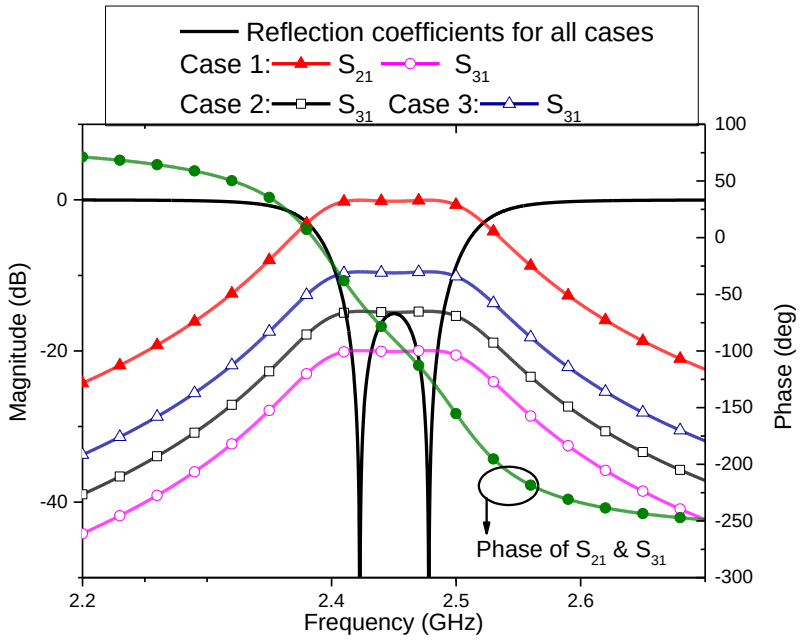

Fig. 3.4. Frequency responses of the equivalent circuit model with different power dividing ratios. $Z_0 = 50\ \Omega$, $J_{2L} = J_{s1} = 26.10$ mS, $C = 64.17$ pF, $L = 65.75$ pH; Case 1: $J'_{12} = 38.40$ mS, $J''_{12} = 13.61$ mS. Case 2: $J'_{12} = 40.02$ mS, $J''_{12} = 7.44$ mS. Case 3: $J'_{12} = 40.52$ mS, $J''_{12} = 4.12$ mS.

According to the schematic given in Fig. 3.3, the power injected into the driven port can be divided into two parts. One path will transmit the energy to the antenna for radiation. The other path serves for the decoupling. The power dividing (PD) ratio of this two-way unequal power divider can be decided according to the mutual coupling amplitude to be suppressed.

Let us consider the three conditions mentioned above again. The first condition can be met by the properly designed PD network (ratio of J'_{12} and J''_{12}). For the other two conditions, two basic premises for filtering circuits should be mentioned here.

The first one is that for a filtering circuit, the phase slope of its transmission coefficient is decided by its bandwidth and in-band ripple level used. As a result, to meet the second condition, the coupling path and decoupling path must share the same bandwidth and in-band ripple level [3]. The other premise is that the phase response for the S_{21} of a filtering circuit will not be affected by its amplitude. In this work, the unequal power dividing means that the original transmission coefficients multiply different constants for both paths and will not change the phase response as long as the reflection

coefficient of the driven port (input port of the antenna) remains unchanged as shown in Fig. 3.4. These two premises allow the possibility of controlling the amplitude and phase responses of the decoupling path separately.

3.1.3 Physical Realization

In this section, the detailed design procedure for the proposed DN is explained. The DN will be designed step-by-step, based on the aforementioned analysis.

3.1.3.1 Step 1: Power Dividing Network

Fig. 3.5 shows the structure of the filtering antenna for demonstration in this chapter. For the sake of generality and simplicity, a classical design of a 2nd-order resonator-fed aperture coupled filtering antenna is used as the test antenna. It consists of two substrates with a 2 mm air gap between them. The common ground plane is located on the upper surface of the bottom substrate. The feeding structures on the lower surface of the bottom substrate are then aperture coupled to the patch which is on the upper surface of the top substrate. The whole structure is composed of a half-wavelength resonator, a patch antenna and a feedline which is gap-coupled to the first resonator. The substrates used in this study are all Rogers 4003, having a dielectric constant of 3.55 and a thickness of 0.813mm. The simulations are all carried out in the High Frequency Structure Simulator (HFSS). The response of this second-order filtering antenna is given in Fig. 3.6. As can be seen, this antenna shows 2nd order filtering performance. The specifications for this filtering antenna are given as follows: fractional bandwidth (FBW) = 6.1%, centre frequency = 2.45 GHz, ripple level = 0.3 dB. The design procedure of such a filtering antenna is out of the scope of this chapter and it can be found in many works in the literature [4, 5], so it is not given here for brevity.

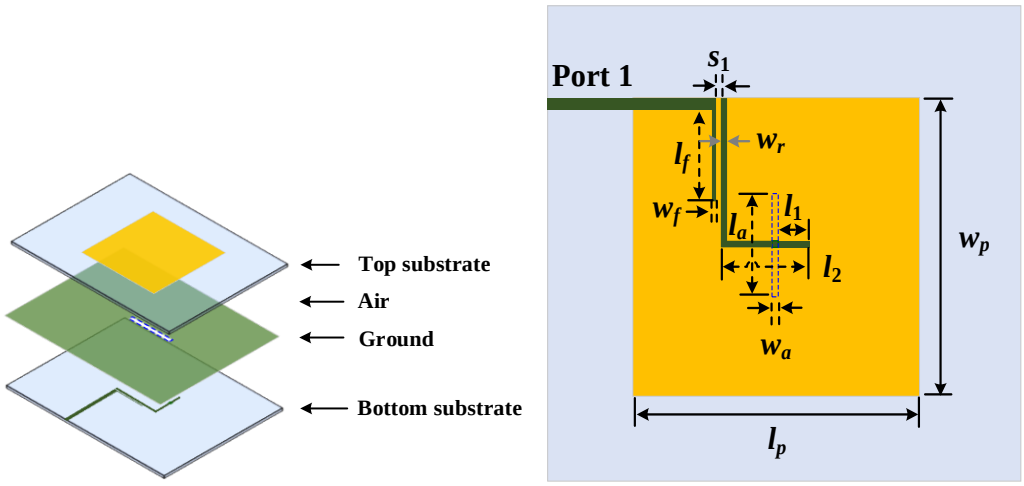

(a) (b)

Fig. 3.5. Configurations of the filtering antenna. (a) Exploded view. (b) Top view. Dimensions in mm: l_1 = 5.04, l_2 = 12.75, l_a = 16.9, w_a = 1, l_f = 13.98, w_f = 0.4, S_1 = 0.35, l_p = 45.67, w_p = 45.5, w_r = 0.5.

Fig. 3.6 also provides the S-parameters when two identical filtering antennas are placed close to each other. The distance between the two patches is randomly set as 16.2 mm, which is about 0.13 λ_0, where λ_0 is the free-space wavelength. The mutual coupling is about -16 dB in the operating band. One may also notice that the S_{11} for both antennas are almost unchanged as the mutual coupling between the two antennas is not very strong. It can be observed that the shape of the curve representing the mutual coupling (S_{21}) between these two antennas is very similar to the transmission coefficient of a lossy BPF [6-8]. Besides, the phase slope of the S_{21} is very stable in the frequency band of interest. Through the previous study, such a phase behaviour can be achieved with two coupled second-order filtering networks. This can be understood by the fact that the signal goes through four resonators when it is transferred from one port to the other. Considering the coupled antennas given in Fig. 3.6, we can find that the coupling between two antennas is about -16 dB. According to *Condition* 1, the insertion loss for the decoupling path should also be -16 dB. As a result, the insertion loss for the decoupling path should be -8 dB. However, this value should be increased slightly to compensate for the loss introduced by the coupling structure and transmission lines. Thus, in this design, an initial value for the insertion loss of 6.5 dB is chosen.

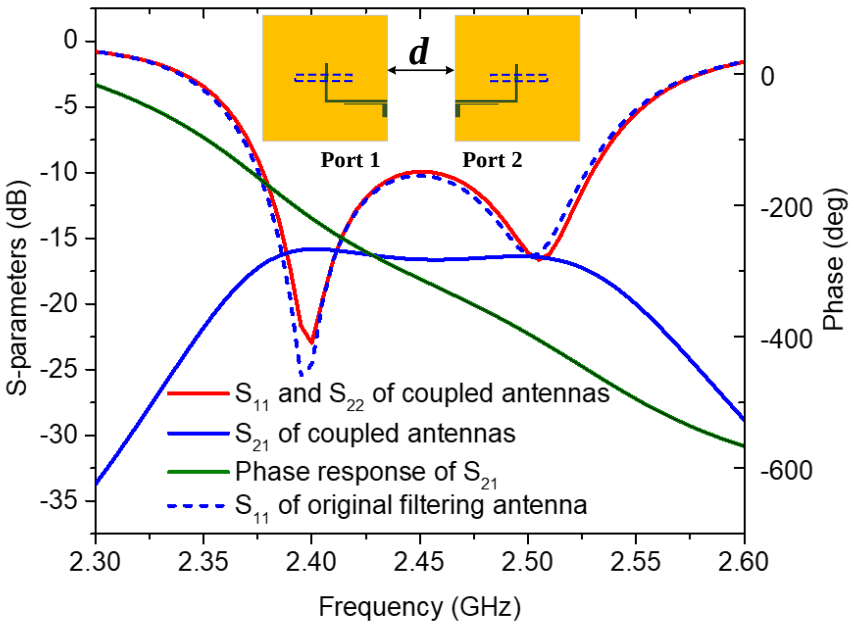

Fig. 3.6. Frequency responses for the filtering antenna under test and coupled antennas.

Fig. 3.7(a) shows the structure for electromagnetic (EM) simulations. As can be observed, another resonator is coupled to the first-stage resonator, dividing the energy into two parts. The J'_{12} and J''_{12} are controlled by the location and size of the aperture (l_1, w_a, l_a) and gap size (l_3, S_3), respectively. This structure can be easily built based on the structure in Fig. 3.5. For instance, one can add another resonator to the first-stage resonator in Fig. 3.5. Then the coupling between the first-stage resonator and patch should be decreased to maintain the impedance matching of the driven port. Fig. 3.7(b) shows the frequency responses for the structure. This PD network shows almost the same S_{11} as the original filtering antenna. Besides, the insertion loss for the path from the driven port (port 1) to the decoupling port (port 2) is about 6.5 dB. It should be noted here all the ports are designed with 50 Ω impedance matching in this structure. Then, the first step is done.

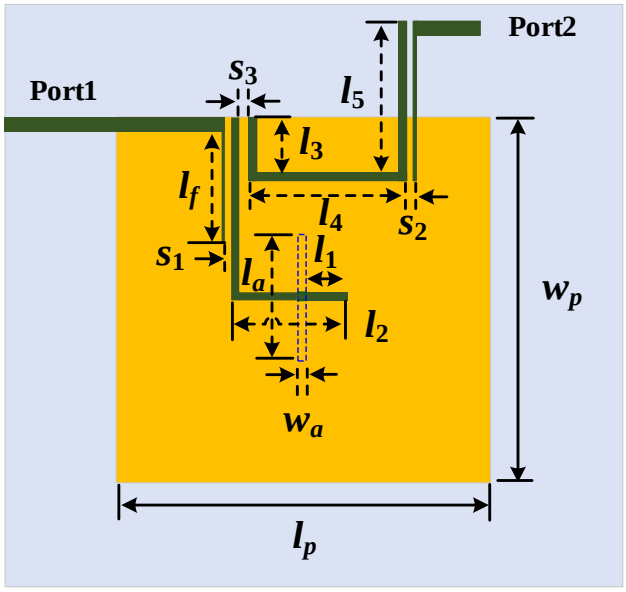

(a)

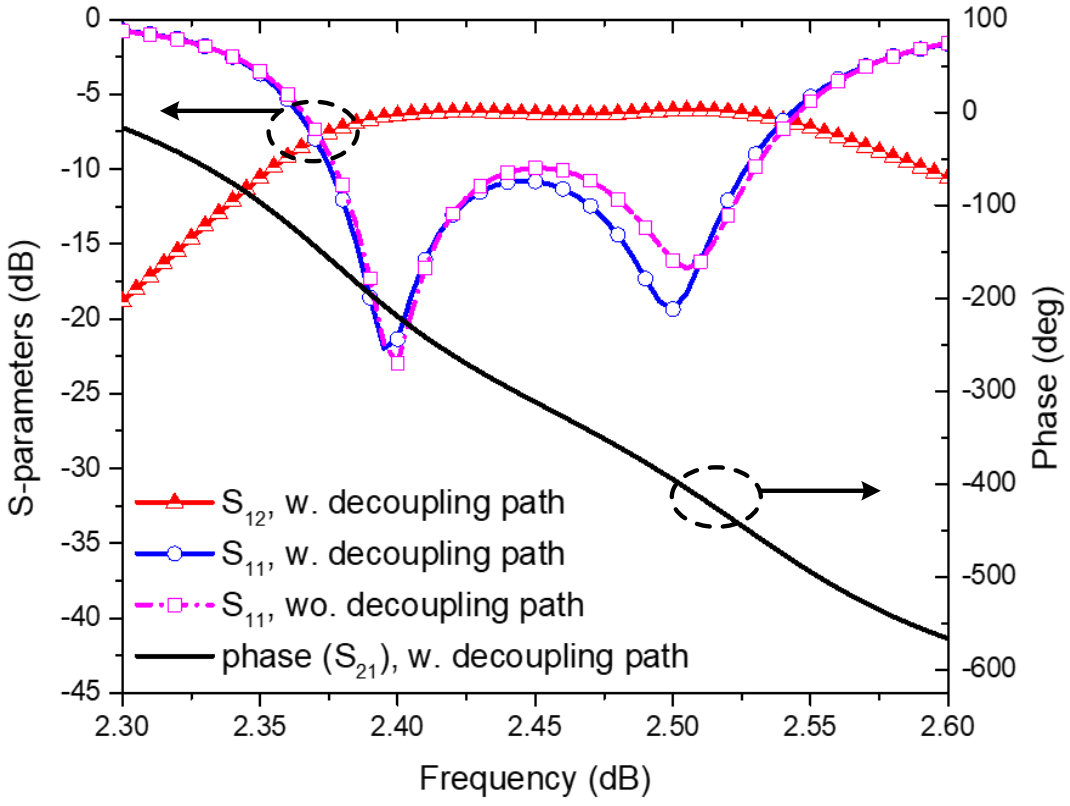

(b)

Fig. 3.7. (a) EM structure of the proposed filtering antenna with PD. Dimensions in mm: l_1 = 4.14, l_2 = 14.25, l_3 = 9.4, l_4 = 11.26, l_5 = 14.25, l_a = 17.09, w_a = 1, l_f = 13.98, w_f = 0.4, S_1 = 0.35, S_2 = 0.35, S_3 = 0.54, l_p = 45.62, w_p = 45.5. (b) S-parameters of the filtering antennas with/without decoupling path.

3.1.3.2 Step 2: Construction of the Decoupling Path

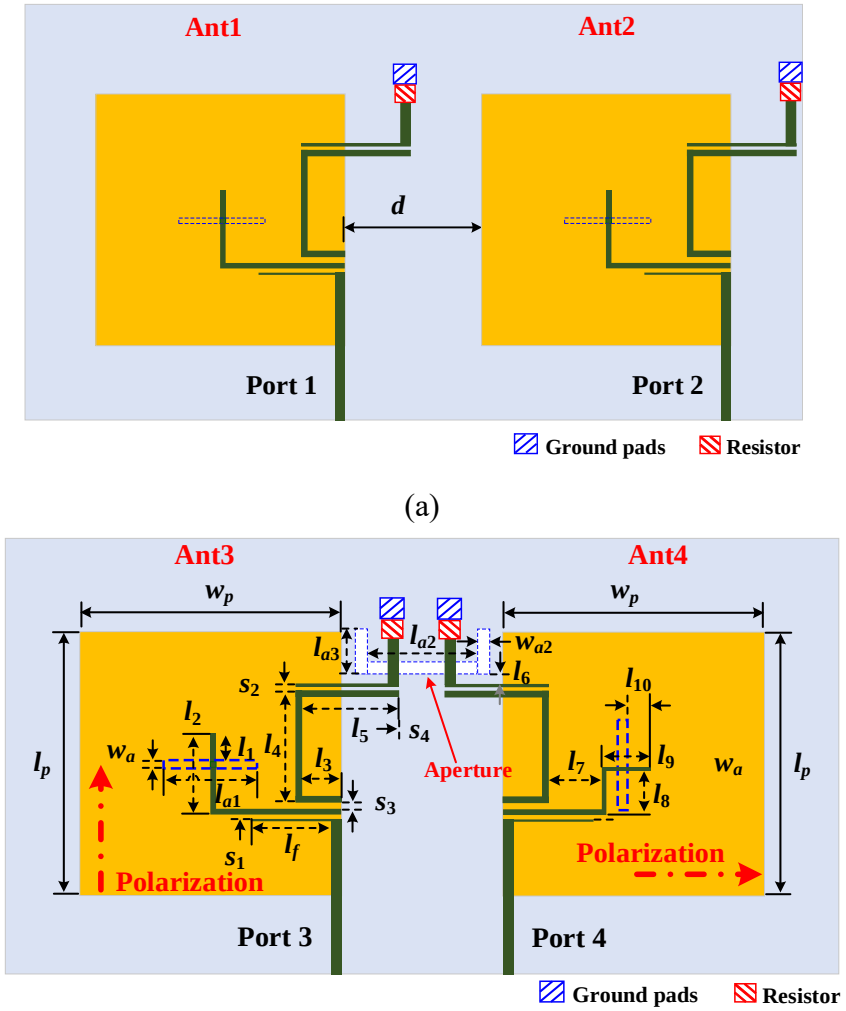

Fig. 3.8. Test structures used to find the decoupling path. (a) Coupled antennas without DN. (b) Weakly-coupled antennas with DN.

In this step, we need to connect two identical PD networks obtained in *step* 1 to imitate the behaviour of the coupled dual-antenna structure shown in Fig. 3.6. To study the decoupling path solely, the mutual coupling effect should be eliminated first in this step. This can be realized by making the polarizations of two antennas orthogonal to each other, such that only the coupling related to the DN can be observed.

Fig. 3.8(a) shows the structure of two coupled filtering antennas for reference. The edge-to-edge distance (d) between two antennas is set as 16.2 mm. Both filtering

antennas are directly copied from Fig. 3.7. The only difference is that the port related to the decoupling path is terminated with a 50 Ω resistor. With this structure, the coupling strength between two identical filtering antennas under investigation can be found, which is reflected by the transmission coefficient between port 1 and port 2 in Fig. 3.8(a).

With results obtained from Fig. 3.8(a) ready, then the dimensions of the DN can be decided through a curve-fitting procedure. The test structure for the establishment of DN is shown in Fig. 3.8(b). The physical dimensions in mm are: $l_1 = 4.14$, $l_2 = 14.25$, $l_3 = 9.4$, $l_4 = 11.26$, $l_5 = 14.25$, $l_6 = 2.35$, $l_7 = 11.39$, $l_8 = 6.35$, $l_9 = 7.55$, $l_{a1} = 16.9$, $l_{a2} = 11.8$, $l_{a3} = 4$, $w_a = 1$, $l_f = 13.98$, $w_a = 1$, $w_{a2} = 0.8$, $l_f = 13.98$, $w_f = 0.4$, $S_1 = 0.35$, $S_2 = 0.35$, $S_3 = 0.54$, $S_4 = 0.72$, $l_p = 45.62$, $w_p = 45.5$. In this structure, two filtering antennas are designed with the same filter function but with orthogonal polarizations. By this method, the coupling strength dominated by the DN can be studied solely. The connection between two sub-DN is realized by an aperture on the ground. To avoid the aperture coupling to the patch radiator, the aperture is folded into a U shape. With this coupling structure, the energy from port 1 can be transmitted to port 2 without destroying the filter function of the decoupling path. Besides, as can be observed the transmission path for decoupling is composed of 4 resonators, which is precisely the same as the antennas' mutual coupling counterparts. By this method, the slopes of the phase response for both mutual coupling path and decoupling paths can be the same as long as they share the same filter function.

For the structure in Fig. 3.8, the dimensions of the U-shaped aperture dominate the transmission of the decoupling path. Besides, the loading effect introduced by the U-shaped aperture will result in a slight shift in the resonance frequencies of the resonators in the decoupling path. After some fine-tuning in the simulator, the magnitude of the transmission coefficient between port 3 and port 4 in Fig. 3.8(b) can be made to fit the one between port 1 and port 2 in Fig. 3.8(a) as indicated in Fig. 3.9(a).

In Fig. 3.9 the magnitude and phase responses for both structures are plotted and compared. As can be observed, despite some minor discrepancies the magnitudes of the

transmission coefficients for both structures agree well. The phase curves show similar trends too. Besides, a 180° phase difference can be observed. This phase shift is attributed to the external coupling structure which is realized by two coupled-transmission-line (CTL) sections. Such a well-designed CTL structure can perform as an impedance inverter in the vicinity of the band of interest. Two additional inverters introduce the 180° phase difference we need.

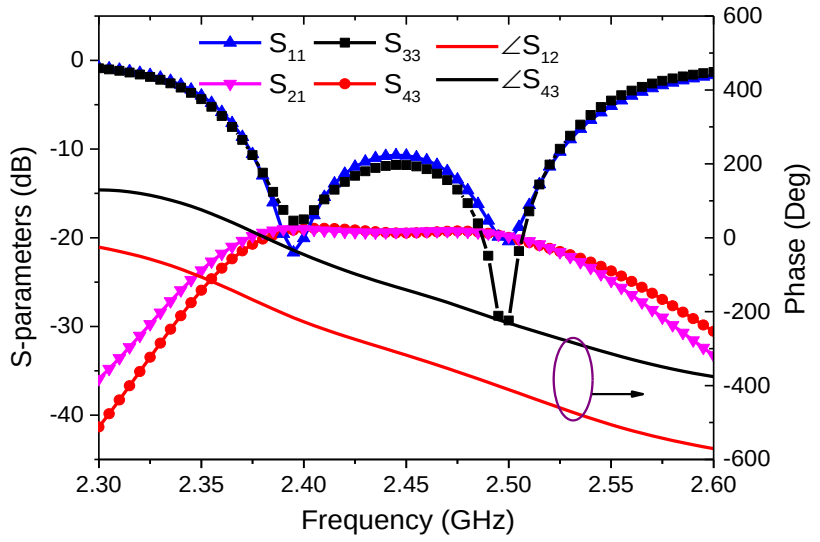

(a)

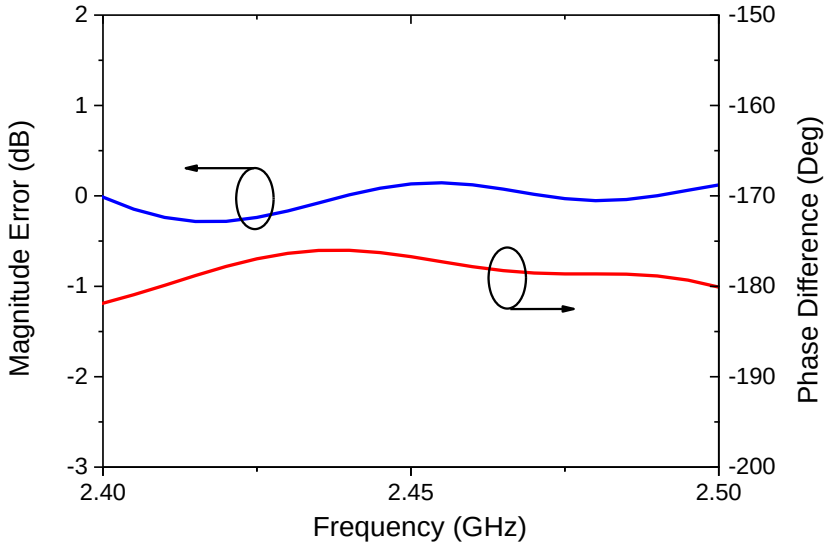

(b)

Fig. 3.9. Simulated results. (a) S-parameters. (b) Magnitude error and phase difference [39]. (S_{21} denotes the mutual coupling whereas S_{34} represents the decoupling path transmission coefficient. Magnitude error = S_{21}–S_{43}; Phase difference = $\angle S_{21}$–$\angle S_{43}$.)

Fig. 3.9(b) shows the magnitude error and phase difference between these two paths. As can be observed, in the band of interest, the magnitude error can be controlled in a very small range which is smaller than 0.27 dB. The phase difference between the two paths is in the range of 176° to 180°. By this method, the initial dimensions for the DN can be decided. In the subsequent step, we will connect the DN to the coupled filtering antennas for final adjustments.

3.1.3.3 Step 3: Parallel Connection

With all these efforts, it can be guaranteed that all the conditions are met now. In the last step, the realized decoupling network is connected with the dual-antenna module in parallel. After some fine-tuning, the final dimensions of the decoupled dual-antenna system can be decided. Fig. 3.10 shows the structure of the decoupled antennas. The dimensions are provided in Table 3-1. For the power injected into port 1, part of the power will be split into the decoupling path through the coupled transmission line power dividing structure. The 50 Ω transmission lines (TLs) are bent for the ease of soldering of the connectors and to avoid unexpected mutual coupling.

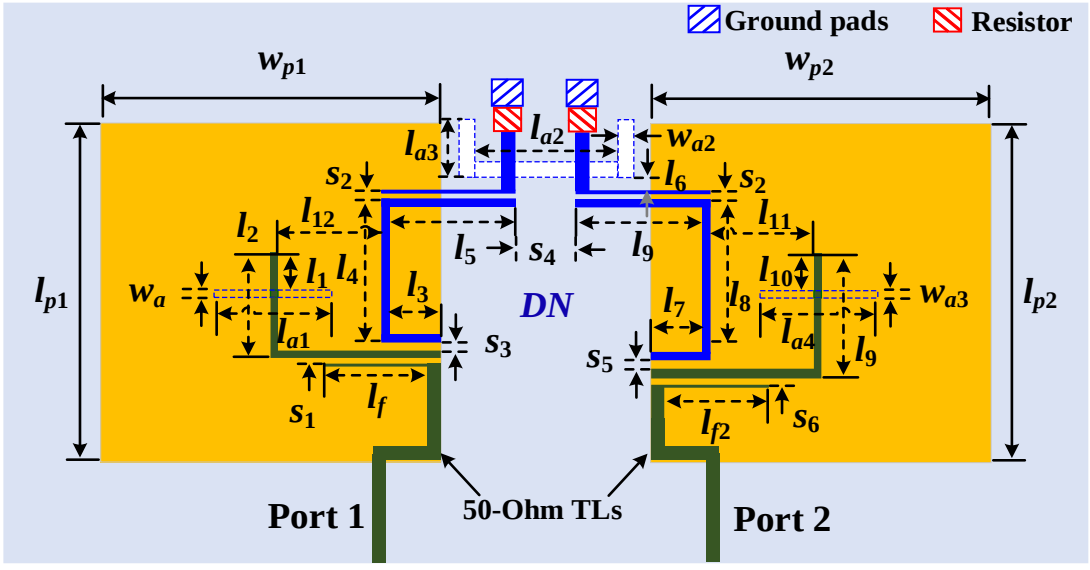

Fig. 3.10. Decoupled dual-filtenna structure for the in-band and adjacent-band application.

Table 3-1. Dimensions of the in-band and adjacent-band decoupled filtering antennas.

Dimensions		l_1	l_2	l_3	l_4	l_5	l_6	l_7	l_8
Values (mm)	In-band	3.94	14.35	9.4	11.49	17.09	2.07	11.39	11.49
	Adjacent-band							9.35	13
Dimensions		l_9	l_{10}	l_{11}	l_{12}	l_{a1}	l_{a2}	l_{a3}	w_a
Values (mm)	In-band	14.35	3.94	11.39	11.39	16.9	11.8	4.15	1
	Adjacent-band	17.04	4.34	11.44	11.39			4	
Dimensions		w_{a2}	w_{a3}	l_f	l_{f2}	S_1	S_2	S_3	S_4
Values (mm)	In-band	0.8	0.8	13.98	13.98	0.35	0.44	0.51	0.72
	Adjacent-band		1		14.5				
Dimensions		S_5	S_6	l_{p1}	w_{p1}	l_{p2}	w_{p2}		
Values (mm)	In-band	0.51	0.35	45.67	45.5	45.67	45.5		
	Adjacent-band	0.51	0.35			48.13	45.5		

3.1.4 Adjacent-Band Operation

Another key advantage of this DN is its ability to decouple two antennas operating over adjacent bands from different communication standards. This special characteristic is very important for modern highly integrated communication systems. For instance, B40 (2300–2400 MHz) is one of the bands close to the 2.4 GHz WiFi frequency. In real products antennas working for both standards are usually placed in a limited space. By using this DN, the mutual coupling between two antennas can be suppressed dramatically. For demonstration, a dual-antenna system is further developed based on the structure in Fig. 3.10. The dimensions are provided in Table 3-1. This design is built by simply changing the dimensions of the right half of the structure in Fig. 3.10. The electrical lengths of the filtering antenna in the right half part of the structure are increased for lower band operation, which covers the B40 band. Then, the DN on the right-hand side is changed accordingly. It should be noted here, that to make sure the filter function for both antenna and low mutual coupling between them simultaneously, the DN must be tuned synchronously.

3.1.5 Experimental Demonstration and Discussion

3.1.5.1 Impedance Behaviours

Two prototypes were fabricated and measured for demonstration. Fig. 3.11 shows the photograph of the fabricated in-band decoupled antennas. Fig. 3.12 presents the simulated and measured S-parameters for both in-band and adjacent-band scenarios. As can be observed from Fig. 3.12(a), despite some slight frequency shift, the antennas cover the 2.4 GHz WiFi band with a measured bandwidth of 2.36 GHz – 2.515 GHz (6.4%). The DN can improve the decoupling level up to 33.6 dB in simulation, which is about 34 dB in the measurement. Compared with the result given in Fig. 3.6, an improvement of 18.9 dB is achieved.

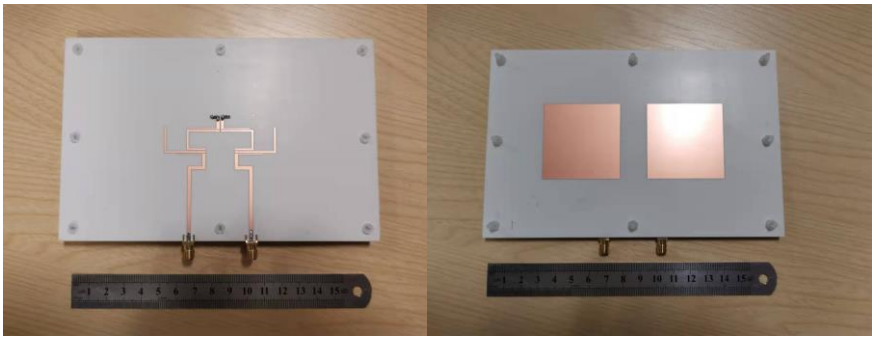

Fig. 3.11. Fabricated dual-antenna prototype for in-band operation [39].

In addition, for the adjacent-band case, a mutual coupling suppression of 30 dB can be guaranteed with this novel DN as shown in Fig. 3.12(b). The measured mutual coupling is lower than -33 dB in the band of interest, which is slightly better than the simulated result. This can be attributed to the fabrication and measurement error. Compared with the original coupled module, the dual-antenna system with DN shows an improvement of 18 dB on the isolation level. The results shown in Fig. 3.12(b) also indicate that a simple filtering antenna structure can hardly handle the mutual coupling problem between two extremely close bands. As the selectivity of a filter function is highly related to the order of the filter circuit, a higher-order filter function will show a higher roll-off ratio on its out-of-band skirts. Thus, a complicated cascaded resonator feeding network is needed to suppress the mutual coupling between two close or even

adjacent frequency bands. However, the experimental results given in this work indicate that instead of using a high-order filtering network to improve the isolation between two adjacent bands, the proposed DN offers another way to handle this problem with a smaller size, lower cost, and simpler structure.

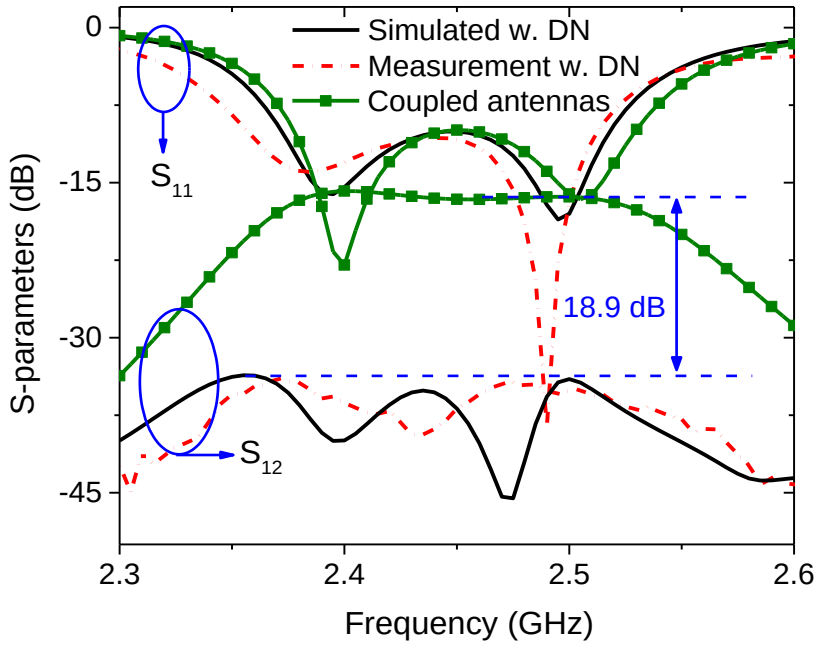

(a)

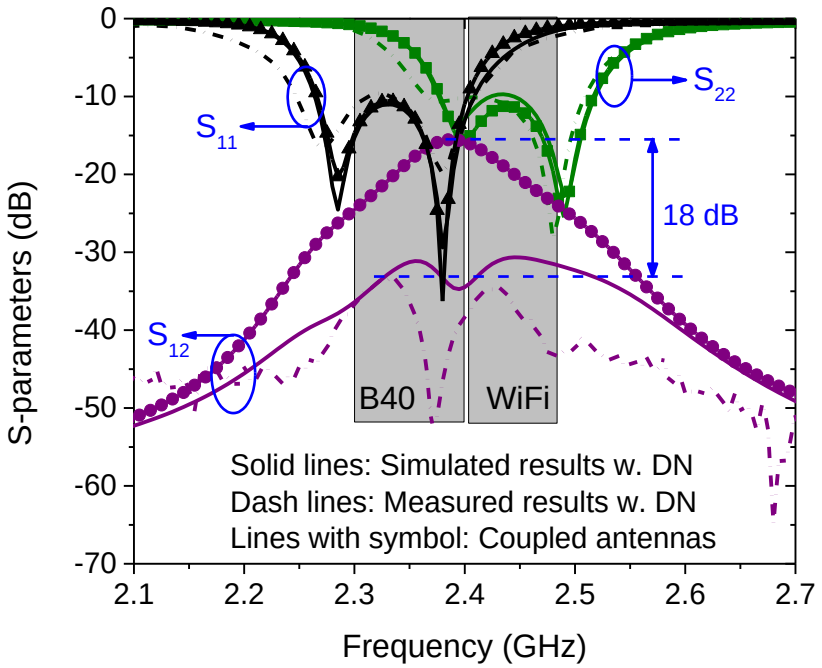

(b)

Fig. 3.12. Decoupling performance of the antennas. (a) Decoupling of two identical antennas. (b) Decoupling of two antennas operating over adjacent bands [39].

Additionally, it is worth noting that the transmission nulls shown in the isolation curves result from the cancellation of signals from two paths. This means the magnitude and phase error conditions align perfectly at these frequency points. In addition to the highly suppressed mutual coupling, another significant advantage of this DN is that it has little effect on the original S-parameters of the filtering antennas, as can be observed from Fig. 3.12. This is crucial for filtering antennas.

3.1.5.2 Radiation Performance

It is noteworthy that some resistors are utilized in both designs to maintain the impedance conditions for the filter functions. These resistors will inevitably introduce some loss to the circuits, which in terms results in some deteriorations in the radiation efficiency of the corresponding filtering antennas. Fig. 3.13 plots the measured and simulated total efficiencies of the filtering antenna for in-band operation. The total efficiency η_{total} is defined as [9]

$$\eta_{total} = (1 - S_{11}^2 - S_{21}^2)\eta_{radiation} \tag{3.5}$$

Here $\eta_{radiation}$ is the radiation efficiency of the antenna. Good filtering performance can be observed regarding the out-of-band selectivity. A high roll-off rate on the skirt of the curve is possible if a higher-order filter function is used. Also, as can be observed the measured total efficiency is about -1.94 dB in the band of interest. Through this investigation, the deterioration of the total efficiency is about 1.15 dB compared with the coupled dual-antenna structure in Fig. 3.5.

This drop in efficiency is mainly attributed to two factors. Part of the loss is attributed to the loss introduced by the transmission between two decoupling paths. Another reason is that two resistors will absorb some energy and hence deteriorate the efficiency. Fig. 3.14 provides the simulated total efficiencies for the in-band application with different edge-to-edge distances. As can be seen, with the antennas getting closer, the drop in the total efficiency is also increasing. This can be understood by the fact that to suppress higher mutual coupling, more energy needs to be assigned to the decoupling path, which also means more energy will be lost on the decoupling path. However, this

method still provides an effective method for suppressing the mutual coupling between two filtering antennas when isolation is of higher priority. Further work on eliminating the loss in such coupled-resonators DN will be carried out in the future. In this work, the distance between the two patches is about 0.13 λ_0. However, this distance could further be reduced to 0.02 λ_0 (2 mm) and still produce an improvement in isolation level of about 15.5 dB as shown in Fig. 3.15, which shows the decoupling performance with different antenna separations.

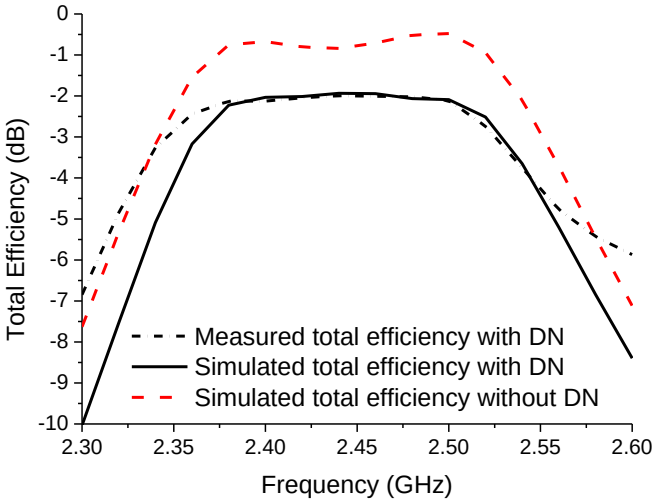

Fig. 3.13. The simulated and measured total efficiency of the dual-antenna system for in-band operation [39].

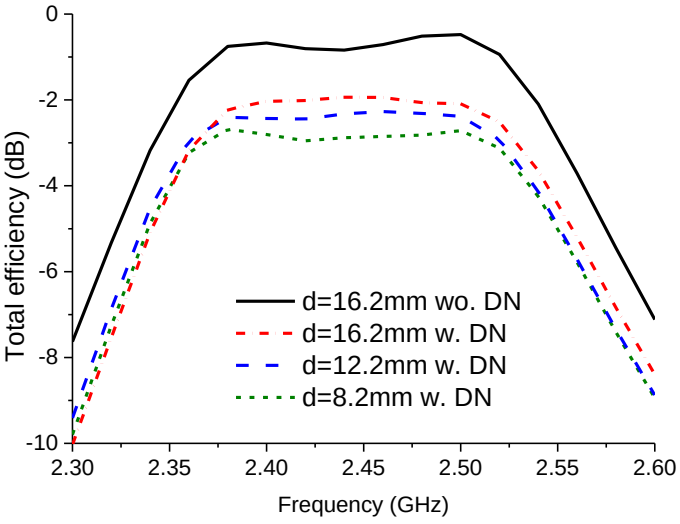

Fig. 3.14. Simulated total efficiencies with different edge-to-edge distances [39].

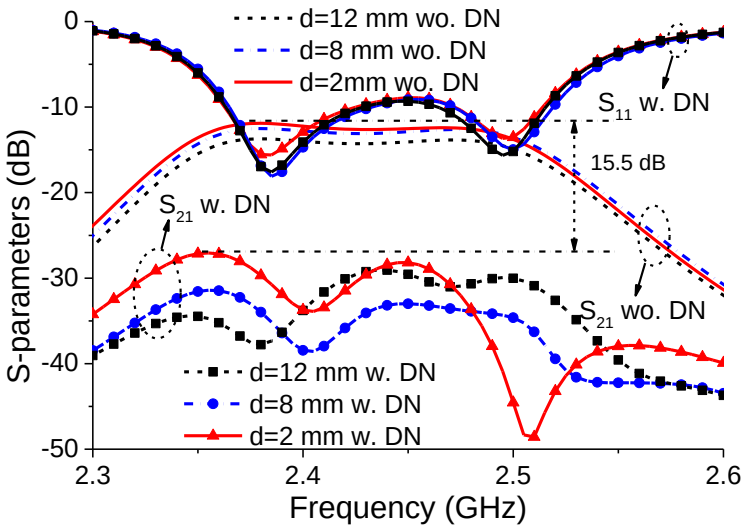

Fig. 3.15. Simulated decoupling performance with different antenna separations [39].

Fig. 3.16 displays both simulated and measured radiation patterns of the antennas for in-band applications (structure in Fig. 3.10). Because of the symmetry of the structure, only the radiation patterns for one antenna are provided here. During the measurement, one antenna is excited while the other one is 50 Ω terminated. The simulated and measured results agree well. The radiation pattern in its *H*-plane is slightly tilted from the broadside direction. This can be attributed to the reactive loading effect between two patches, which can also be observed in some other works.

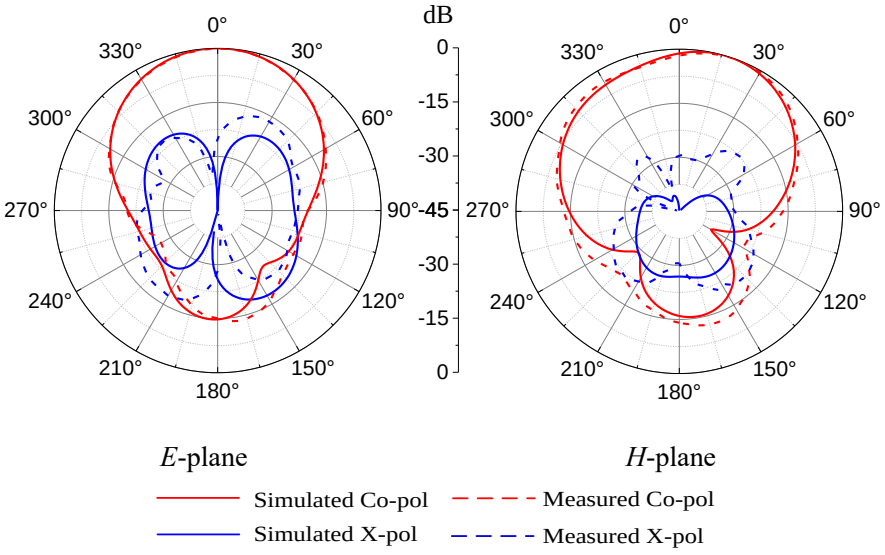

Fig. 3.16. Simulated and measured radiation patterns of the dual-antenna system for in-band operation [39].

3.1.6 Comparison and Discussion

Table 3-2. Comparison with previous works

Reference	Methods	Edge-to-edge Spacing (λ_0)	In-band/ adjacent-band	Isolation (dB)	Filtering Response
[10]	Network	N.G.	In-band	29.1	NO
[11]	Network	0.1	In-band	23.9	Yes
[12]	Network	0.2	In-band	32	NO
[13]	Network	2.58	Adjacent-band	30	N.A.
[14]	Stacked Decoupling Surface	0.2	In-band	25	No
[15]	Near-field resonator	0.016	In-band	20	No
[16]	Band-reject resonator	0.016	Adjacent-band	25	No
[17]	Filtering circuit	0.25	Adjacent-band	30	Yes
This work	Filtering circuit	0.13	In-band	34	Yes
			Out-of-band	33	

Notes: N.G.: Not given, N.A.: Not applicable.

Table 3-2 shows the comparison of the performance between other presented works and this work. As can be observed, considering the edge-to-edge spacing, this work achieves a very competitive decoupling performance. Although the decoupled antennas presented in [11] and [17] also with filtering ability, they can only work for either in-band or adjacent-band scenarios. This work is the only one which can serve both in-band and adjacent-band operations. Also, this work presents a possible solution for the decoupling between two filtering antennas. As the network is built based on the coupled resonators, the bandwidth of this decoupling network can be adjusted according to the bandwidths of the antennas to be decoupled. Using the general method introduced in this work, many other decoupling problems between two resonant filtering antennas can be solved, but not limited to some specific antenna forms only.

Besides, compared with the decoupling network presented in [10], the proposed method can achieve a more compact design. In this work, the phase behaviour is controlled by the coupled resonator, while in [10] a long transmission line and a phase shifter are needed for the adjustment of the phase response. Besides, two directional couplers are used in [10] for the power arrangement of the decoupling path which will also increase the cost and time of the design. However, by using a coupled resonator decoupling network, this design provides a more general, simple and cost-effective solution for the decoupling between two filtering antennas.

3.2 Dual-Polarized/Duplex Filtering Antennas

3.2.1 Dual-Polarized Filtering Antennas

The structure of the dual-polarized filtering antenna is depicted in Fig. 3.17. The whole structure is composed of two substrates separated by a 2 mm air gap. The inclusion of an additional substrate reduces the quality factor of the antenna resonator, leading to a broader bandwidth. The feeding circuit, composed of cascaded resonators and feedlines, is situated on the bottom side of the first substrate. The shorting vias in the design have a diameter of 0.4 mm. The common ground plane is located on the upper surface of the bottom substrate and contains three apertures that facilitate coupling between the feeding structure and the radiating patch. The patch is fabricated on the upper surface of the top substrate. For this design, Rogers 4003 substrates with a dielectric constant of 3.55, a loss tangent of 0.0027, and a thickness of 0.813 mm are utilized. The detailed dimensions for the structure are given as follows: l_1 = 18.45 mm, l_2 = 18.55 mm, l_3 = 13 mm, l_4 = 12.05 mm, l_5 = 7.9 mm, l_6 = 6.25 mm, l_7= 13.25 mm, l_8 = 4 mm, l_9 = 9.25 mm, l_{10} = 4.7 mm, l_p = 46.9 mm, w_p = 47.3 mm, l_{s1} = 20.2 mm, l_{s2}= 12.6 mm, w_{s1} = 1.2 mm, w_{s2} = 2 mm, s_1 = 0.2 mm, s_2 = 0.72 mm, s_3 = 0.25 mm, s_4 = 1.55 mm.

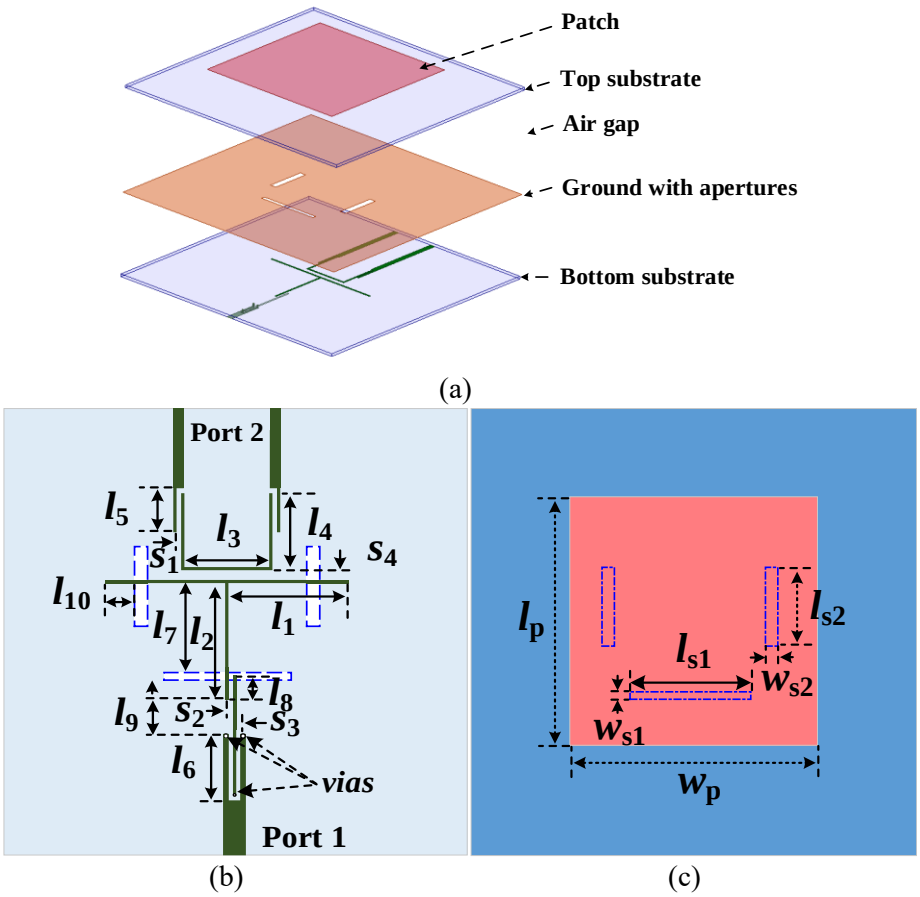

Fig. 3.17. Configurations of the dual-polarized filtering antenna. (a) Exploded view. (b) Bottom view. (c) Top view.

3.2.1.1 Hybrid Feeding Structure

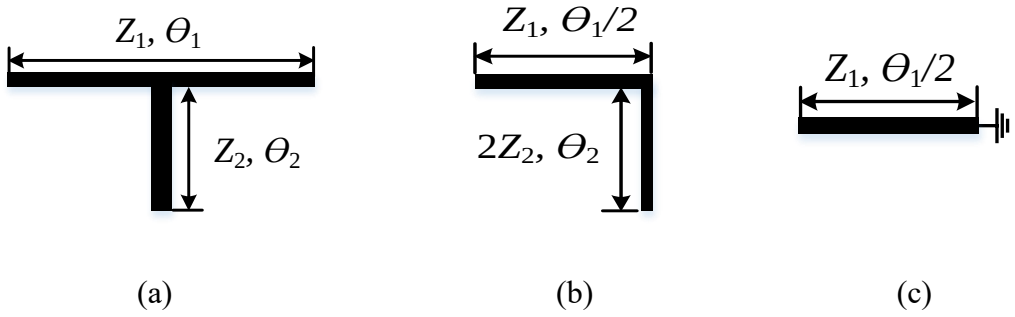

Fig. 3.18. Equivalent circuit for the stub-loaded resonator. (a) stub-loaded resonator. (b) even mode. (c) odd mode.

To comprehend the mechanism of the proposed dual-polarized antenna, it is imperative to investigate the feeding network. The stub-loaded resonator, as illustrated in Fig. 3.18, is commonly employed in bandpass filter designs due to its dual-mode

characteristic and uncomplicated structure [18-20]. This resonator is composed of a half-wavelength main resonator and an open-ended stub positioned at its centre. For this symmetrical configuration, even-odd-mode analysis can be utilized, which supports two modes: an even mode with a magnetic wall at its symmetric plane and an odd mode with an electrical wall at its symmetric plane, as shown in Fig. 3.18. The main resonator with a characteristic impedance of Z_1 and an electrical length of θ_1 governs the resonances of both modes, while the stub length (θ_2) only affects the resonance frequency of the even mode. Consequently, the resonance frequencies of these two modes can be adjusted independently by altering the dimensions of the dominant structure of each mode. In this study, it has been discovered that two highly isolated channels can be attained if each mode can be excited by an individual port.

Fig. 3.19 displays the current distributions of both modes at their resonance frequencies. For the even mode, the current on the main resonator is out of phase on its two arms, which is similar to a T-junction. Its symmetrical interface is open-circuited [19]. The current flows from the two arms of the main resonator to the open end of the stub. For the odd mode, the current on the main resonator is in phase, behaving like a conventional half-wavelength resonator with its central point virtually shorted to the ground, and ideally, no current shows on the stub. Therefore, if a balanced excitation is used to excite the stub-loaded resonator from its two arms, only the odd mode will be excited. In contrast, if an unbalanced excitation is used, only the even mode will be excited.

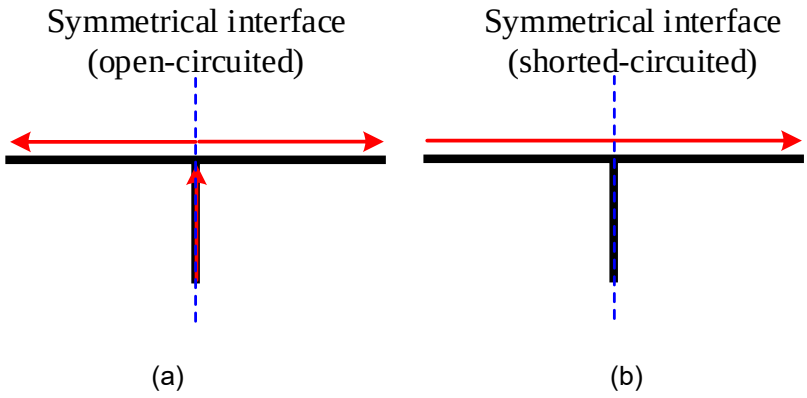

Fig. 3.19. Current vector distributions for even and odd modes. (a) even mode. (b) odd mode.

Based on these analyses, the feeding network shown in Fig. 3.20(a) is considered, and two virtual ports are added to investigate the behaviour of the energy coupled to the patch. It consists of a differentially-fed balun and a T-junction power divider. The differential port (port 2) excites the even mode of the half-wavelength resonator. Due to the standing wave characteristic, this open-ended half-wavelength resonator can operate as a wideband balun. Therefore, port 2 only excites the odd mode of the common resonator. Thus, ports 3 and 4 give out-of-phase signals. The even mode of the common resonator is excited from the stub of the dual-mode resonator by another resonator, and only the even mode of the shared resonator is activated. The stub-loaded resonator behaves as a 3-dB power divider and divides power from port 1 to ports 3 and 4 equally. In summary, for the odd mode-driven channel, the structure functions as a balun, while for the even mode-driven channel, it operates as a 3-dB power divider. Such a four-port network is a well-known 3 dB 180° hybrid.

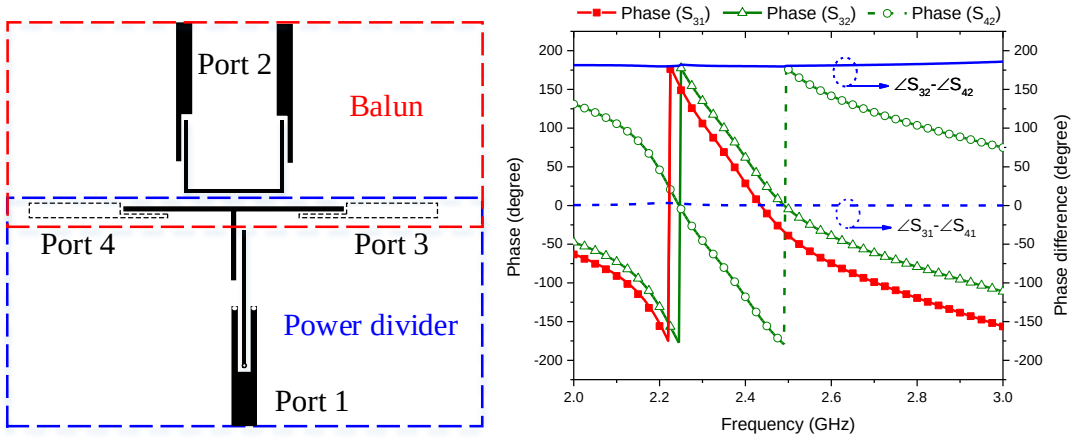

(a) (b)

Fig. 3.20. Hybrid feeding network. (a) structure. (b) response.

When a signal is injected into port 1, two equal amplitude in-phase outputs can be obtained at port 3 and port 4. A signal injected into port 2 will be divided equally into port 3 and port 4 but will be 180° out of phase. Then these two out-of-phase signals will cancel out with each other at the point where the stub is loaded, such that ideally port 1 and port 2 are perfectly isolated according to the reciprocity. Fig. 3.20(b) plots the phase responses of the test structure in Fig. 3.20(a). As a symmetric structure is used, only the

phase of S_{31} is shown here. The in-phase and out-of-phase relationship maintains over a very wide frequency range, which means this decoupling mechanism is frequency-independent over this frequency range. Thus, it is easy to understand that the isolation between two ports is highly related to the symmetry of the feeding structure and purity of the differential excitation.

3.2.1.2 Working Mechanism

By using such a hybrid-like structure as the feeding network of a patch antenna, a filtering dual-polarized antenna is realized. The feeding network is coupled to the radiating patch through three apertures on the ground. To get an insight into the working mechanism of the dual polarization, the current distributions are given in Fig. 3.21 for even and odd modes operations, respectively.

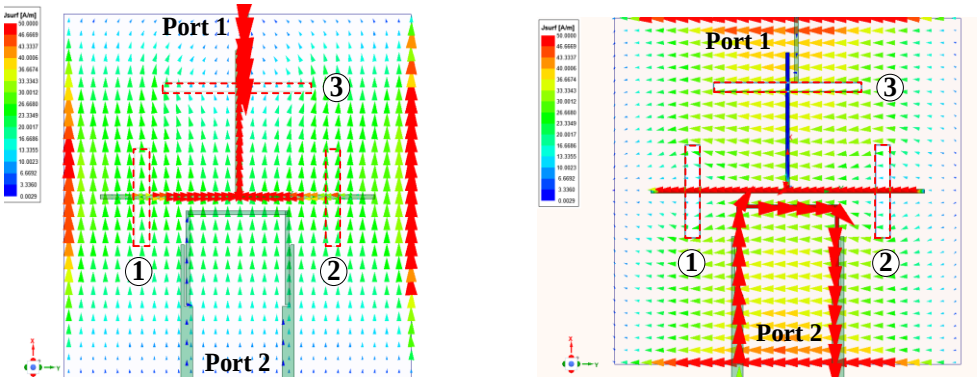

(a) (b)

Fig. 3.21. Current distributions for different channels. (a) Even mode driven channel. (b) Odd mode driven channel [30].

When port 1 is activated, the even mode of the stub-loaded resonator will be excited as shown in Fig. 3.21(a). The feeding structure acts as a 3 dB power divider, so the current on the two arms of the stub-loaded resonator is in phase as indicated. Consequently, for the case shown in Fig. 3.21(a), the effect of the equivalent magnetic current related to apertures 1 and 2 will cancel with each other when they are coupled to the same patch. As a result, the horizontal polarization will not be excited and only the vertical polarization will be excited by aperture 3 for the first channel.

For the odd-mode-driven channel, the corresponding field distributions are shown in Fig. 3.21(b). For this case, the current mainly concentrates on the central half-wavelength resonator, while almost no current can be found on the stub. Thus, aperture 3 cannot be excited. Besides, the current on the main resonator is in phase for its two arms, which makes the equivalent magnetic current in the aperture 1 and 2 in phase. As a result, only the horizontal polarization of the patch will be excited for this channel. By this means two highly isolated channels with orthogonal polarizations can be achieved using this hybrid feeding network.

3.2.1.3 Experimental Demonstration

A prototype with a centre frequency of 2.4 GHz is designed, fabricated and measured to demonstrate the idea. All the simulations are carried out in the HFSS. In this design, both channels are designed with 3rd order Chebyshev responses. The synthesis procedure follows the common methods in the open literature [2, 21, 22]. For brevity, it is not presented here.

The simulated and measured S-parameters and gains are shown in Fig. 3.22. During the gain measurement, a balun is used for a differential input to port 2. The antenna gain is characterized as the realized gain in the +z direction when the corresponding port is activated while the other one is 50 Ω terminated. The measured -10 dB impedance bandwidth for both channels is 2.31 GHz - 2.49 GHz (7.1%). The maximum measured realized gains for both channels are 8.14 dBi and 8.27 dBi, respectively. As can be observed from Fig. 3.23 the isolation between two channels is measured to be higher than 39 dB over the operating band. A gap of about 3 dB between the measured and simulated isolation can be observed here. The discrepancy in the isolation is attributed to measurement tolerance and fabrication error. It should be noted here that if an unbalanced excitation scheme is used for port 2, the isolation will decrease to 30 dB in the simulation according to this study.

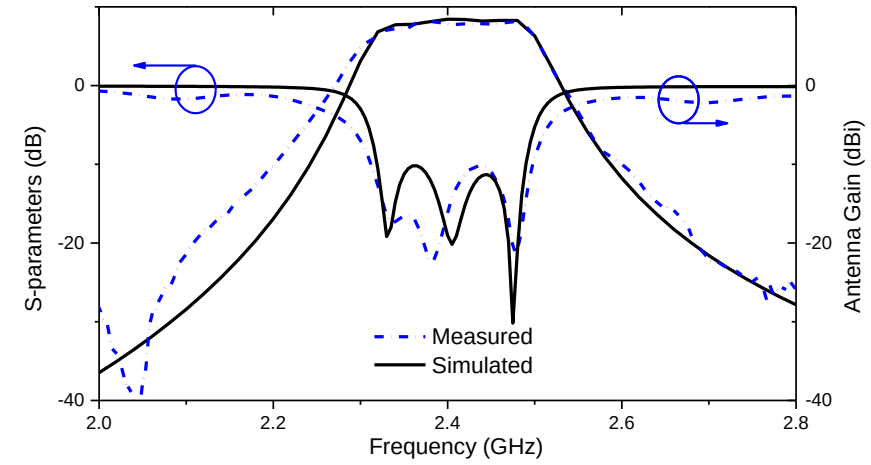

(a)

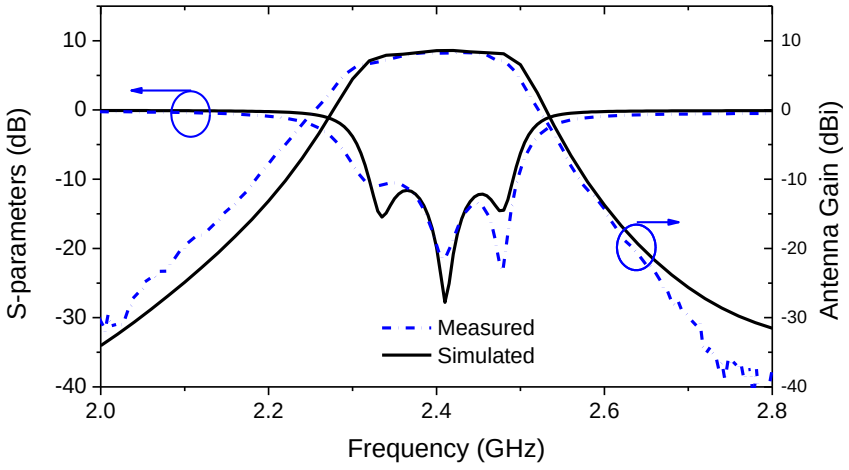

(b)

Fig. 3.22. Simulated and measured S-parameters and gains of the dual-polarized antenna. (a) Even-mode driven. (b) Odd-mode driven [30].

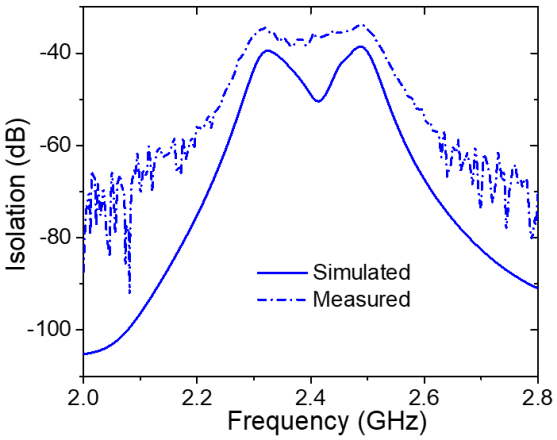

Fig. 3.23. Simulated and measured isolations [30].

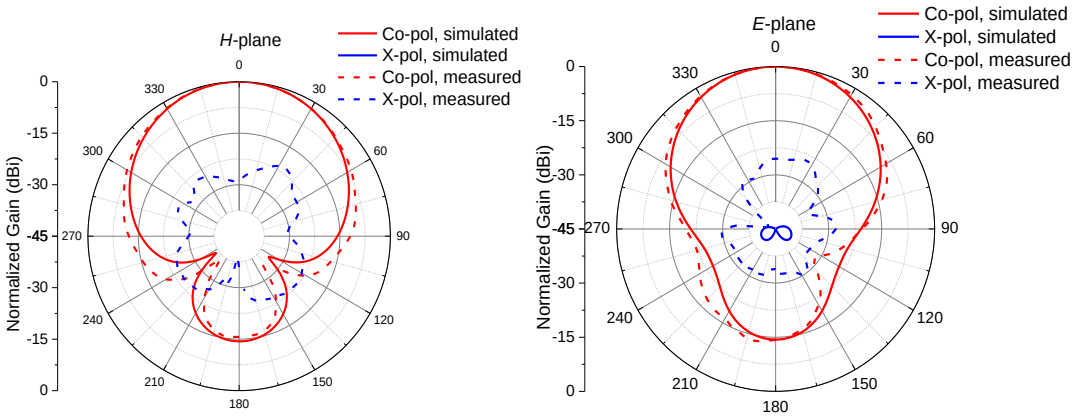

Fig. 3.24. Radiation patterns of the fabricated dual-polarized antenna when the differential port is excited [30].

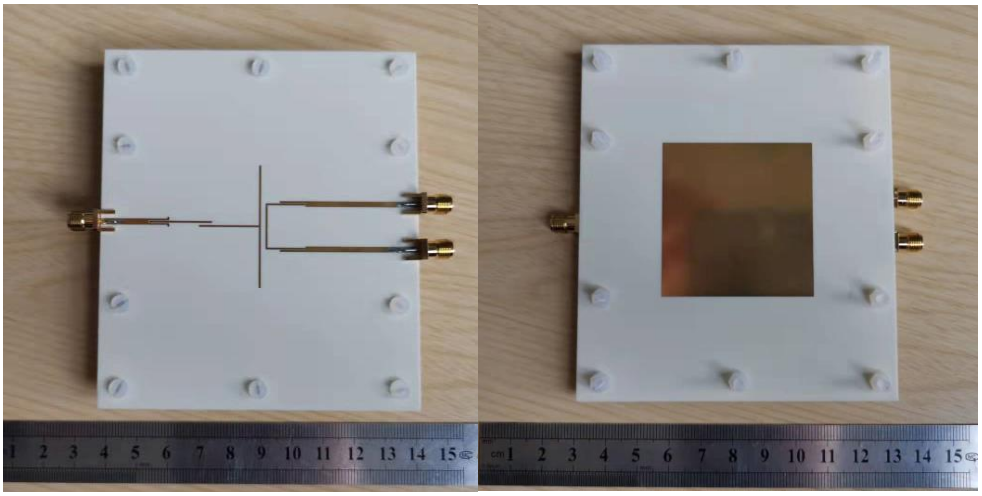

Fig. 3.25. Fabricated dual-polarized antenna.

Fig. 3.24 shows the measured and simulated radiation patterns of the fabricated antenna. For conciseness, only the radiation patterns for odd-mode driven channels are shown here. The measured results agree well with the simulations, showing high cross-polarization suppression up to 25 dB. Fig. 3.25 shows a photograph of the fabricated antenna.

3.2.2 Duplex Filtering Antenna

As mentioned earlier, the isolation mechanism of the proposed feeding network is realized by the interaction between a wideband balun and a power divider. According to Fig. 3.20(b), the resonator-based balun shows out-of-phase outputs over a very wide bandwidth. Besides, the power divider used can be regarded as a T-junction, which

exhibits in-phase output characteristics due to its symmetry and always provides in-phase signals at its two output ports over a wideband frequency range too. That is, even if the operating frequencies of both channels are different, these conditions remain satisfied, ensuring effective isolation. To verify this, a duplex antenna operating at two different bands is designed for the LTE B40 band (2300 to 2400 MHz) and 2.4 GHz WiFi band (2401 to 2495 MHz).

3.2.2.1 Antenna Structure

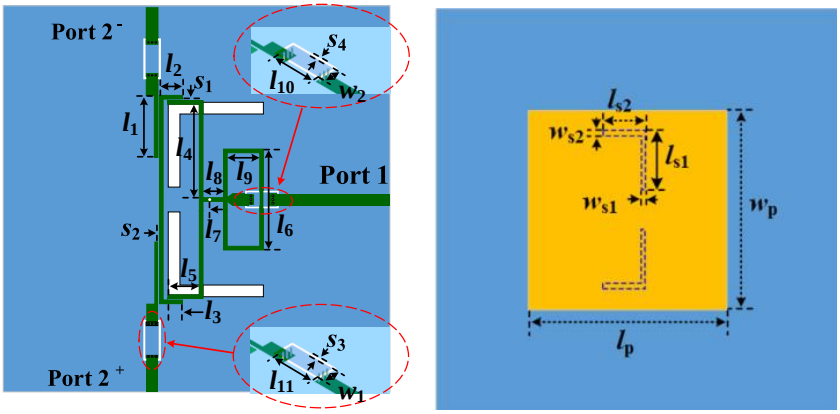

(a) (b)

Fig. 3.26. Configurations of the duplex filtering antenna. (a) Bottom view. (b) Top view.

Fig. 3.26 illustrates the structure of the proposed duplex filtering antenna. The antenna's stack-up is the same as that of the dual-polarized one. Several modifications were made to reduce the overall size of the structure. First, the original three apertures on the ground plane are merged into two L-shaped apertures. Fig. 3.27 illustrates the field distributions in the apertures for both channels. These modified apertures and their arrangement guarantee low cross-polarization and low mutual coupling for both channels.

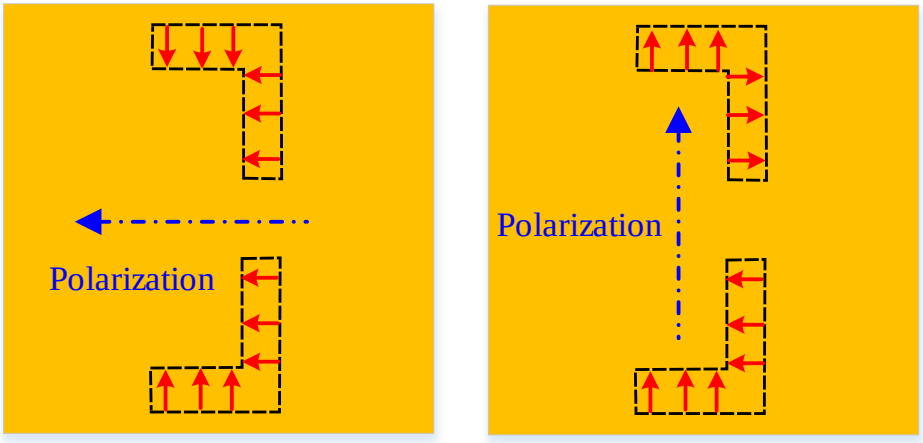

(a) (b)

Fig. 3.27. Electrical field distributions in the apertures. (a) Port 1 activated. (b) Port 2 activated.

In addition, the open-end stub is changed into a shorted one. As we mentioned before, the centre of the main resonator is virtually shorted for odd mode. Thus, putting a short pin at this point will not influence the resonating characteristic of the odd mode. Then another quarter-wavelength resonator is coupled to the shorted stub through the short circuit via by magnetic coupling [23]. After this, to reduce the area occupied by the resonator but not destroy the symmetry of the structure, a loop structure replaces the single open-ended quarter-wavelength resonator. In this way, this loop stub structure will not affect the behaviour of the odd mode of the resonator. Furthermore, due to the open-circuited boundary condition in the symmetric plane, these modifications do not impact the behaviour of the even mode.

3.2.2.2 Multi-Path Coupling Scheme

The coupling topology of the proposed duplex antenna is modified to introduce multiple gain zeros for higher selectivity. A novel source-patch coupling structure is introduced for the first time to achieve gain zeros. As is widely known the maximum achievable transmission zeros for an N_{th} order Chebyshev filter is N-2 without considering source/load coupling [24]. For a filtering antenna, it is not applicable to introduce source-load coupling as the output port is a radiative aperture that is coupled

to the free space. Thus, to introduce one more gain zero, the multi-path source-resonator coupling is utilized in such a third-order filtering circuit.

Take the even-mode-driven channels for example. The tapped excitation will introduce an inherent transmission zero at the frequency when the open-ended stub length equals a quarter wavelength. In this structure, this gain zero will appear at the higher stopband. Then to improve the selectivity at the lower stopband, the feedline is cross-coupled to the radiation patch, which works as the last stage of the corresponding filtering circuit.

This coupling topology is seldom used in filter designs, because in planar filters, it is often impractical to couple a resonator to both input and output ports simultaneously [25-27]. However, the multi-layer structure used here, which can be found in many antenna designs, makes it possible to realize such a coupling structure. A similar coupling topology is also used for the odd-mode-driven channel.

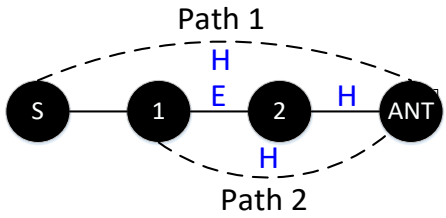

Fig. 3.28. Coupling typology for the higher band channel.

To get an insight into the physical realization of such a coupling topology, the mechanism of the higher band channel is explained as an example. The corresponding coupling topology for the higher channel is shown in Fig. 3.28 according to the theory in [24], where *S* represents the source and circles with numbers represent cascaded resonators. The solid lines mean direct coupling while dash lines mean cross-coupling. *E* represents the electrical coupling and *H* means the magnetic coupling. As can be seen, there are two cross-coupling paths in this topology. Path 1 represents the coupling between the source and patch and path 2 represents the coupling between the first resonator and patch. Path 2 introduces a well-known cascaded trisection (CT) structure here and realizes a lower band gain zero for the channel [24]. The primary challenge

for this topology is controlling the coupling mechanisms, as depicted in Fig. 3.28. This includes managing coupling from source to resonators and between resonators, such that the phase relationships between every path can be fulfilled.

In this design, the feeding network and upper radiator are coupled through the apertures on the ground. This coupling structure is widely used for patch antennas. The operating mechanism for such a coupling method has been theoretically analyzed by some researchers [28, 29]. For a strong coupling between the microstrip line and the patch, a long, thin rectangular slot has been proven to be optimal. By locating the aperture at the centre of the patch, the magnetic dipole coupling effect can be maximized while the electrical dipole coupling is small. For this design, all the coupling between the resonators and the patch will be magnetic. Then to realize the electrical coupling between the first two resonators they are coupled to each other face to face by their open ends, where the electric fields are strongest. The electrical coupling for source-resonator coupling is realized by a crossover structure built on the 50 Ω feedline as shown in the inset of Fig. 3.26(a). Cross-coupling is much weaker compared with the main-path coupling, so such a narrow aperture is a very good option. For such a small ground aperture etched away from the centre of the patch, the magnetic dipole effect is minimized and then electric coupling between source and patch can be obtained.

3.2.2.3 Experimental Demonstration and Discussion

For validation, the duplex filtering antenna is fabricated, and its detailed dimensions are provided in Table 3-3. The measured and simulated frequency responses are shown in Fig. 3.29. The simulated bandwidths for both channels are 2.21-2.4 GHz (channel 1) and 2.41-2.62 GHz (channel 2). The corresponding measured results are 2.18-2.40 GHz (channel 1) and 2.37-2.62 GHz (channel 2). The measured bandwidths are slightly wider than those obtained through simulation. The measured isolation between both channels is higher than 38 dB over the operating bands; the simulated value is 48 dB. The discrepancy between measured and simulated results might arise from fabrication and measurement errors. Such a low-magnitude response

is very sensitive to the environment and fabrication tolerance.

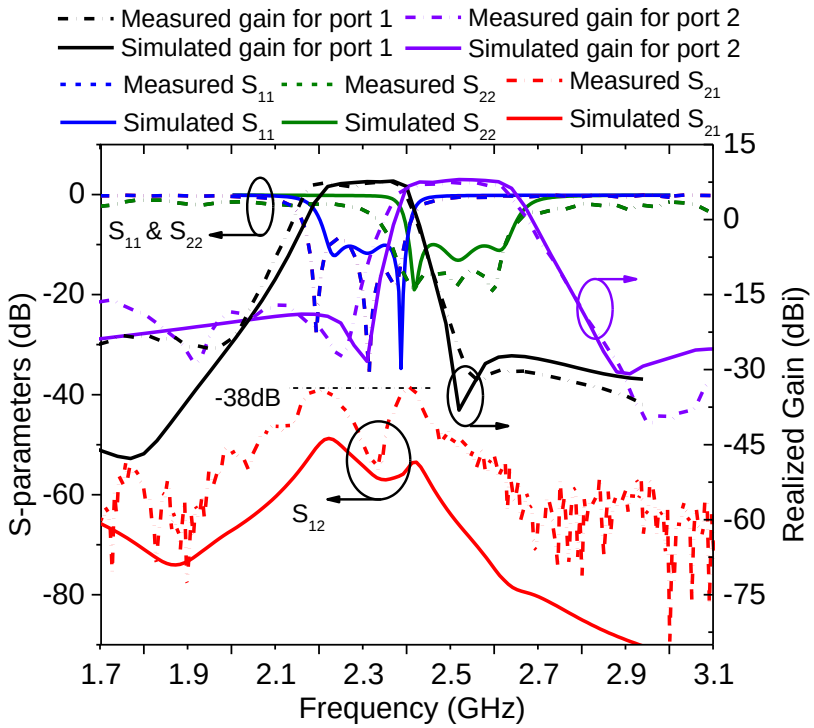

Fig. 3.29. Simulated (solid lines) and measured (dashed lines) performance for the duplex filtering antenna [30].

Table 3-3. Dimensions of the duplex antenna (unit: mm)

Parameter	l_1	l_2	l_3	l_4	l_5	l_6	l_7
Value	8.9	3.21	1.885	13.05	4.425	13.8	0.85
Parameter	l_8	l_9	l_{10}	l_{11}	l_p	w_p	l_{s1}
Value	3	4.25	4	5	48	44.6	10.9
Parameter	l_{s2}	w_{s1}	w_{s2}	s_1	s_2	s_3	s_4
Value	12.5	1.9	1.6	0.2	0.2	0.7	0.3

The isolation mechanism of this design is highly related to the balanced and unbalanced excitations. In real applications, the differential excitations are usually realized by baluns. It is impractical to achieve perfect anti-phase outputs over a wide frequency band. Thus, for such an even-odd-mode-based design, the isolation is also limited by this factor in experimental implementations. For a commercial lumped balun, the phase error is commonly in the level of 5° to 20°.

To verify the practical application prospect of this technique, the imperfect differential excitation should be considered. A parametric study is carried out on the phase error of the differential excitation of the duplex filtering antenna, to investigate its effect on the isolation performance. The 50 Ω TL extensions (l_{ex1} and l_{ex2} in Fig. 3.26) for the sub-ports of port 2 are set to be unequal in the study to simulate the phase error of the excitation. The length unbalance (LU) is the difference between these two extensions, namely $LU = l_{ex1} - l_{ex2}$. The reference frequency for the phase is 2.5 GHz. In the substrate used, a 2 mm 50 Ω TL will introduce about 10° phase error.

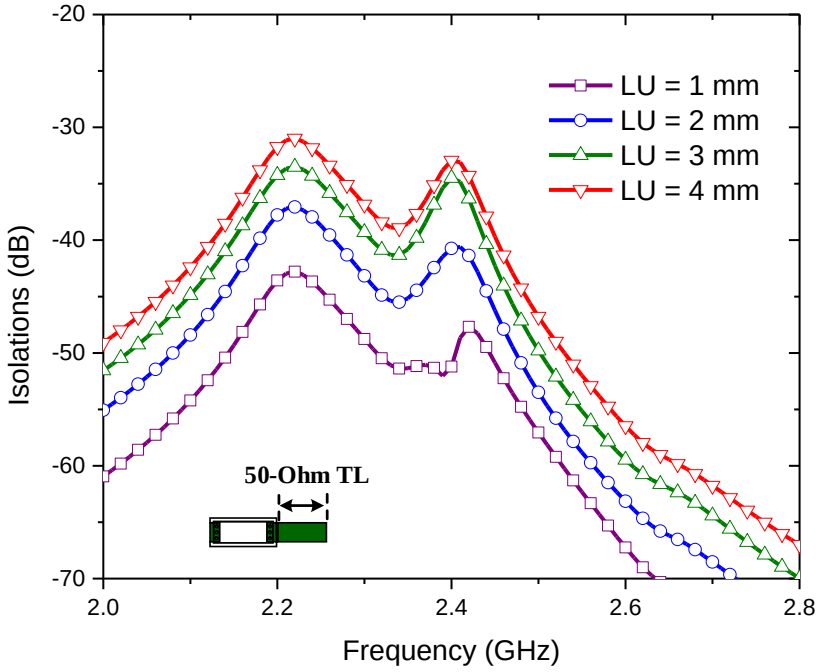

Fig. 3.30. Parametric study on the phase error of the differential excitation.

Simulated isolations with different LU are plotted in Fig. 3.30, which presents a parametric study on the phase error of differential excitation. As can be observed, an isolation of 31 dB between two channels can be maintained with a phase error of about 20°. Compared with other odd-even-mode designs the isolation of this work shows higher robustness to the excitation phase error. This is because the out-of-phase excitation of the even-odd mode of this structure is realized by the resonator-based

balun. This balun shows a more stable response over the frequency bands as its balun output characteristic is only related to the field distributions at its two open ends.

Fig. 3.31 shows the radiation patterns of the duplex antenna. Some of the simulated cross-polarizations are not visible in this figure due to their small magnitude. Both channels show high polarization purity. In the main beam direction, the measured co-polarizations for both the *E* and *H* planes are at least 25 dB higher than the cross-polarizations. In contrast, the simulated results show a difference of approximately 35 dB. A photograph of the fabricated antenna is shown in Fig. 3.32. As can be seen, the feeding network only occupies a small area of 0.62 $\lambda_g \times 0.34\ \lambda_g$, where λ_g is the guided wavelength at the centre frequency of the lower passband. Compared to other methods, the feeding network used in this design can be confined to the area beneath the radiation patch, which minimizes the surface area required on the system's printed circuit board.

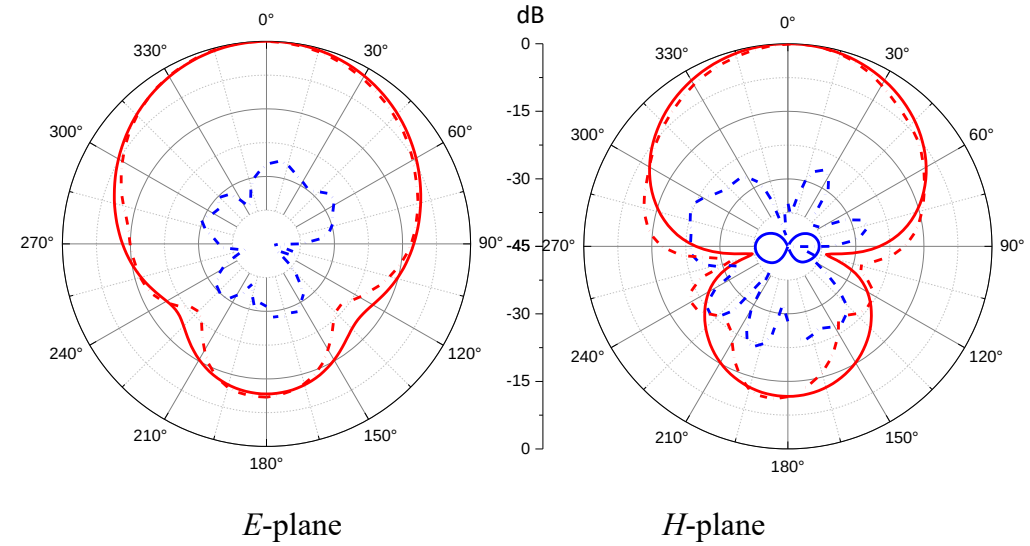

Fig. 3.31. Radiation patterns of the fabricated duplex filtering antenna. (a) Port 1 activated. (b) Port 2 activated [30].

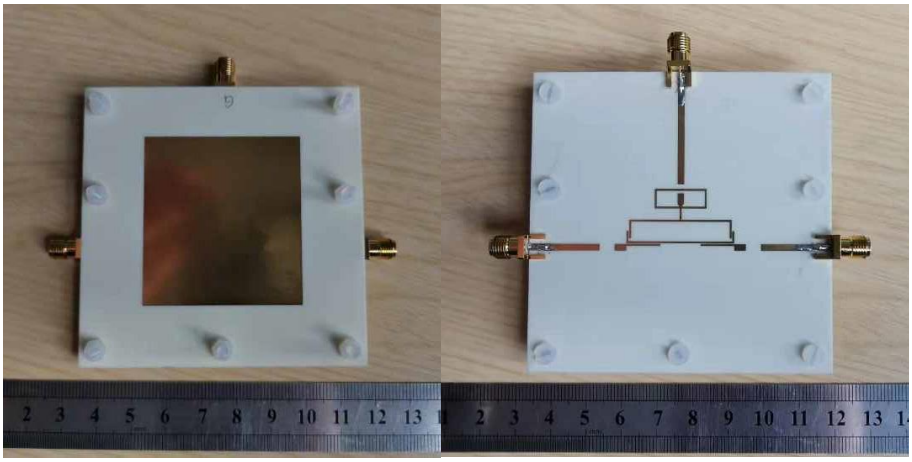

Fig. 3.32. Fabricated duplex antenna [30].

Table 3-4. Comparison of the performance between different works in the literature and this work [30].

Ref.	Dual-polarized /Duplex	Frequency ratio	Isolation (dB)	FBW	Profile (λ_0)
[31]	Dual-polarized	N.A.	20	4.8%	0.04
[32]	Dual-polarized	N.A.	20, 24	3.8%, 6%	0.063
[33]	Dual-polarized	N.A.	25	27.6%	0.11
[34]	Dual-polarized	N.A.	37	12.3, 7.6	0.13
[35]	Duplex	1.1	32	5%, 4.2%	0.05
[36]	Duplex	2.16	20	4.5%, 5.5%	0.014
[37]	Duplex	1.26	45	10.6%, 6.9%	0.08
[38]	Duplex	1.16	23	3.2%, 3.9%	0.03
This work	Duplex	1.08	34/38	7.8%, 8.8%	0.028

Note: λ_0 is the free space wavelength at the center frequency.

Table 3-4 compares the performance between other presented designs and this work. As can be observed, this work realizes high isolation for both in-band and out-of-band operations. Besides, it is the only work that can decouple two continuous filtering channels with no guard band between them. Most methods for decoupling two

antennas either suffer from a high-frequency ratio or can only serve for dual-polarized operation. The characteristic of frequency-independent isolation makes this method a better option for the design of two decoupled filtering antennas. It can relieve the requirement on the filters behind the antennas and offer two well-isolated channels operating over a very small frequency ratio. Also, as the filtering circuit is involved, the potential of the impedance bandwidth of the antenna is released. All the antennas provide sufficient bandwidth to support most modern wireless communication standards with a very low profile of only 0.028 λ_0.

3.3 Summary

This chapter introduces two novel techniques for decoupling two filtering antennas. The first technique uses an additional decoupling technique to introduce an additional path between two coupled filtering antennas. This decoupling network is co-synthesized with the coupled filtering antennas. Thus, it has a minor effect on the filtering performance of the original antennas. The second technique is based on a novel feeding network. The network can split the even and odd modes of a dual-mode resonator, to achieve two isolated channels. As a result, this technique is much more compact as it requires no additional decoupling structures. Both techniques are experimentally verified, showing good decoupling performance for filtering antennas operating over the same and adjacent bands. Since the filtering antenna's ability to suppress close-band mutual coupling is limited, the proposed techniques are very useful for this specific scenario.

References

[1] F.-C. Chen *et al.*, "Design of filtering microstrip antenna array with reduced sidelobe level," *IEEE Transactions on Antennas and Propagation,* vol. 65, no. 2, pp. 903-908, 2017.

[2] F.-C. Chen, J.-F. Chen, Q.-X. Chu, and M. J. Lancaster, "X-band waveguide filtering antenna array with nonuniform feed structure," *IEEE Transactions on Microwave Theory and Techniques,* vol. 65, no. 12, pp. 4843-4850, 2017.

[3] X. Guo, L. Zhu, and W. Wu, "Design of complex weighted feeding network based on generalized coupled-resonator filter theory," *IEEE Transactions on Microwave Theory and Techniques,* vol. 67, no. 11, pp. 4376-4385, 2019.

[4] K. Yoshida, T. Takahashi, and H. Kanaya, "Superconducting slot antenna with broadband impedance matching circuit," *IEEE Transactions on Applied Superconductivity,* vol. 11, no. 1, pp. 103-106, May 2001.

[5] R. E. Lovato, T. Li, and X. Gong, "Tunable filter/antenna integration with bandwidth control," *IEEE Transactions on Microwave Theory and Techniques,* vol. 67, no. 10, pp. 4196-4205, 2019.

[6] M. Meng, I. C. Hunter, and J. D. Rhodes, "The design of parallel connected filter networks with nonuniform *Q* resonators," *IEEE Transactions on Microwave Theory and Techniques,* vol. 61, no. 1, pp. 372-381, 2013.

[7] D. R. Jacjowski, "Passive enhancement of resonator *Q* in microwave notch filters," *IEEE MIT-S Int. Microw. Symp. Dig.*, pp. 13 15-13 18, 2004.

[8] V. Miraftab, and Y. Ming, "Advanced coupling matrix and admittance function synthesis techniques for dissipative microwave filters," *IEEE Transactions on Microwave Theory and Techniques,* vol. 57, no. 10, pp. 2429-2438, 2009.

[9] Shuai Zhang, Salman Naeem Khan, and S. He, "Reducing mutual coupling for an extremely closely-packed tunable dual-element PIFA array through a resonant slot antenna formed in-between," *IEEE Transactions on Antennas and Propagation,* vol. 58, no. 8, pp. 2771-2776, Aug. 2010.

[10] H. Makimura *et al.*, "Novel decoupling concept for strongly coupled frequency-dependent antenna arrays," *IEEE Transactions on Antennas and Propagation,* vol. 65, no. 10, pp. 5147-5154, 2017.

[11] Y.-M. Zhang, Q.-C. Ye, G. F. Pedersen, and S. Zhang, "A simple decoupling network with filtering response for patch antenna arrays," *IEEE Transactions on Antennas and Propagation,* vol. 69, no. 11, pp. 7427-7439, 2021.

[12] Y.-M. Zhang, S. Zhang, J.-L. Li, and G. F. Pedersen, "A transmission-line-based decoupling method for MIMO antenna arrays," *IEEE Transactions on Antennas and Propagation,* vol. 67, no. 5, pp. 3117-3131, 2019.

[13] L. Zhao, K.-W. Qian, and K.-L. Wu, "A cascaded coupled resonator decoupling network for mitigating interference between two radios in adjacent frequency bands," *IEEE Transactions on Microwave Theory and Techniques,* vol. 62, no. 11, pp. 2680-2688, 2014.

[14] K.-L. Wu, C. Wei, X. Mei, and Z.-Y. Zhang, "Array-antenna decoupling surface," *IEEE Transactions on Antennas and Propagation,* vol. 65, no. 12, pp. 6728-6738, 2017.

[15] M. Li, B. G. Zhong, and S. W. Cheung, “Isolation enhancement for MIMO patch antennas using near-field resonators as coupling-mode transducers,” *IEEE Transactions on Antennas and Propagation,* vol. 67, no. 2, pp. 755-764, 2019.

[16] J. Guo *et al.*, “Isolation improvement of two tightly coupled antennas operating in adjacent frequency bands using filtering structures,” *IEEE Open Journal of Antennas and Propagation,* vol. 1, pp. 207-214, 2020.

[17] Y. Zhang, X. Y. Zhang, L.-H. Ye, and Y.-M. Pan, “Dual-band base station array using filtering antenna elements for mutual coupling suppression,” *IEEE Transactions on Antennas and Propagation,* vol. 64, no. 8, pp. 3423-3430, 2016.

[18] J.-X. Xu, and X. Y. Zhang, “Compact high-isolation LTCC diplexer using common stub-loaded resonator with controllable frequencies and bandwidths,” *IEEE Transactions on Microwave Theory and Techniques,* vol. 65, no. 11, pp. 4636-4644, 2017.

[19] L. Gao, X. Y. Zhang, B.-J. Hu, and Q. Xue, “Novel multi-stub loaded resonators and their applications to various bandpass filters,” *IEEE Transactions on Microwave Theory and Techniques,* vol. 62, no. 5, pp. 1162-1172, 2014.

[20] Z.-C. Guo, L. Zhu, and S.-W. Wong, “A quantitative approach for direct synthesis of bandpass filters composed of transversal resonators,” *IEEE Transactions on Circuits and Systems II: Express Briefs,* vol. 66, no. 4, pp. 577-581, 2019.

[21] M. Ohira, and Z. Ma, “An efficient design method of microstrip filtering antenna suitable for circuit synthesis theory of microwave bandpass filters,” *2015 International Symposium on Antennas and Propagation (ISAP)*, Hobart, TAS, Australia, 2015, pp. 1-4.

[22] R. H. Mahmud, and M. J. Lancaster, “High-gain and wide-bandwidth filtering planar antenna array-based solely on resonators,” *IEEE Transactions on Antennas and Propagation,* vol. 65, no. 5, pp. 2367-2375, 2017.

[23] C. Qing-Xin, C. Fu-Chang, T. Zhi-Hong, and W. Huan, “A novel crossed resonator and its applications to bandpass filters,” *IEEE Transactions on Microwave Theory and Techniques,* vol. 57, no. 7, pp. 1753-1759, 2009.

[24] J. S. Hong, and M. J. Lancaster, *Microstrip filters for rf/microwave applications*, New York, NY, USA: Wiley, 2001.

[25] S. Amari, and M. Bekheit, “Physical interpretation and implications of similarity transformations in coupled resonator filter design,” *IEEE Transactions on Microwave Theory and Techniques,* vol. 55, no. 6, pp. 1139-1153, 2007.

[26] Z.-C. Guo, L. Zhu, and S.-W. Wong, “Synthesis of transversal bandpass filters on stacked rectangular *H*-plane waveguide cavities,” *IEEE Transactions on Microwave Theory and Techniques,* vol. 67, no. 9, pp. 3651-3660, 2019.

[27] M. Bekheit, S. Amari, and W. Menzel, “Modeling and optimization of compact microwave bandpass filters,” *IEEE Transactions on Microwave Theory and Techniques,* vol. 56, no. 2, pp. 420-430, 2008.

[28] D. M. Pozar, "Microstrip antenna aperture-coupled to a microstripline", *Electron. Lett.*, vol. 21, no. 2, pp. 49-50, Jan. 1985.

[29] M. Kahrizi, T. K. Sarkar, and Z. A. Maricevic, “Analysis of a wide radiating slot in the ground plane of a microstrip line,” *IEEE Trans. Microw. Theory Tech.,* vol. 41, no. 1, pp. 29-37, Jan. 1993.

[30] J. Qian *et al.*, “Compact dual-polarized/duplex filtering antenna with high isolation,” *IEEE Open Journal of Antennas and Propagation,* vol. 4, pp. 677-685, 2023.

[31] W. Duan *et al.*, “Dual-polarized filtering antenna with high selectivity and low cross polarization,” *IEEE Transactions on Antennas and Propagation,* vol. 64, no. 10, pp. 4188-4196, 2016.

[32] C.-X. Mao *et al.*, “A shared-aperture dual-band dual-polarized filtering-antenna-array with improved frequency response,” *IEEE Transactions on Antennas and Propagation,* vol. 65, no. 4, pp. 1836-1844, April 2017.

[33] S. J. Yang *et al.*, “Low-profile dual-polarized filtering magneto-electric dipole antenna for 5G applications,” *IEEE Transactions on Antennas and Propagation,* vol. 67, no. 10, pp. 6235-6243, 2019.

[34] Y. Li, Z. Zhao, Z. Tang, and Y. Yin, “Differentially fed, dual-band dual-polarized filtering antenna with high selectivity for 5G sub-6 ghz base station applications,” *IEEE Transactions on Antennas and Propagation,* vol. 68, no. 4, pp. 3231-3236, 2020.

[35] C.-X. Mao *et al.*, “Compact highly integrated planar duplex antenna for wireless communications,” *IEEE Transactions on Microwave Theory and Techniques,* vol. 64, no. 7, pp. 2006-2013, 2016.

[36] Y.-J. Lee, J.-H. Tarng, and S.-J. Chung, “A filtering diplexing antenna for dual-band operation with similar radiation patterns and low cross-polarization levels,” *IEEE Antennas and Wireless Propagation Letters,* vol. 16, pp. 58 - 61, Apr. 2016.

[37] X.-J. Lin, Z.-M. Xie, P.-S. Zhang, and Y. Zhang, “A broadband filtering duplex patch antenna with high isolation,” *IEEE Antennas and Wireless Propagation Letters,* vol. 16, pp. 1937-1940, 2017.

[38] K.-Z. Hu *et al.*, “Compact, vertically integrated duplex filtenna with common feeding and radiating siw cavities,” *IEEE Transactions on Antennas and Propagation,* vol. 69, no. 1, pp. 502-507, 2021.

[39] J. Qian *et al.*, “A cascaded resonator decoupling network for two filtering antennas,” *IEEE Antennas and Wireless Propagation Letters,* vol. 22, no. 12, pp. 3187-3191, 2023.

Chapter 4
Band-stop Radiative Quadruplex Slot Antenna

In this chapter, a novel four-port slot antenna designed for both 5G NR and WiFi operations is introduced. This work is inspired by the dispersive bandstop filter theory. First, wideband NR antennas are achieved using a hybrid mode concept. Then, two NR slot antennas are co-designed as a radiative bandstop structure. By moving the resonance frequencies of the hybrid modes close to the band-reject points of this bandstop filter, a wideband decoupled dual-antenna structure is achieved. To enhance functionality, two additional ports are incorporated into the dummy slot area between these two NR ports, resulting in a quadruplex antenna. In this final configuration, two of the antennas are optimized for 5G NR applications, covering the 5G N77, N78, and N79 bands (3.3-5.0 GHz), while the remaining two antennas serve the WiFi band (5.15-5.8 GHz). Compared to other presented works, the simulation and experimental results demonstrate that this work not only, for the first time, achieves simultaneously wideband in-band and small frequency ratio (1.05) out-of-band duplex in one single module, but also has the advantages of high isolation, compact size, and low cost.

In this chapter, all the prototypes were fabricated by HXP Circuits and assembled by the author. The S-parameters were measured by the author in the Antenna Lab at the University of Kent. The radiation performance of all the prototypes was measured using the anechoic chamber at the University of Kent, with the assistance of Technician Mr. Antonio Mendoza.

4.1 Bandstop Radiative Structure

Fig. 4.1 illustrates the basic concept of the proposed idea. In this work, two slot antennas are connected to form a bandstop filtering structure. As we know, the energy injected into the input port of a bandstop filter will be reflected back in its stopband, which results in an all-reflective response for S_{11}. To omit this reflected energy, the classic method is to absorb it with a resistor [1, 2].

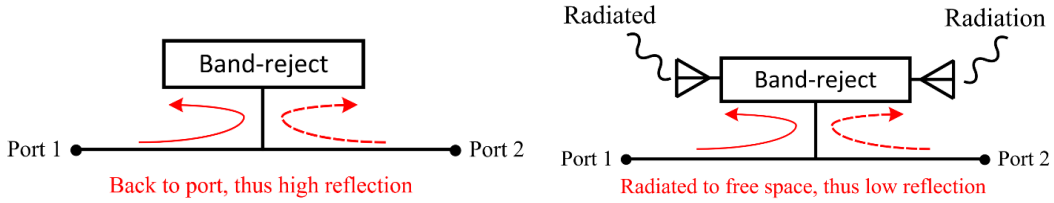

Fig. 4.1. Conceptual illustration of the proposed self-decoupled antennas. (a) Conventional bandstop network. (b) Proposed decoupled slot antennas using the radiative bandstop concept.

Inspired by this, we developed a bandstop structure in which the reflected energy is radiated to the free space as shown in Fig. 4.1(b). The basic mechanism of this structure is similar to the conventional dispersive bandstop filters. The only difference between them is that the resistors in conventional bandstop filters are replaced with the radiation resistance of the antenna structure. The detailed realization of the proposed dispersive bandstop structure will be introduced in the following sections.

4.2 Offset-Fed Slot Antennas

Fig. 4.2 displays the proposed hybrid slot radiator structure, which consists of a rectangular slot etched on a copper ground and a microstrip feedline. The substrate used here is Rogers 4003 with a dielectric constant of 3.55, a loss tangent of 0.0027, and a thickness of 0.813 mm. The slot is fed off-centre by the microstrip line for easier impedance matching. The response of the structure is plotted in Fig. 4.3. In contrast to the traditional probe-fed structure that connects the outer and inner conductors of a coaxial cable to the slot's edges, this feeding structure produces an extra hybrid-mode

resonance near the fundamental mode of the slot. This resonance is caused by the interaction between the microstrip line and the slotline. The frequency of this interaction is mainly determined by the feedline's position and the feeding stub's length.

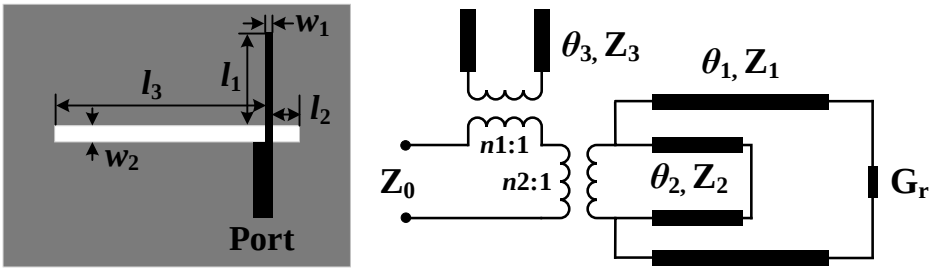

(a) (b)

Fig. 4.2. (a) Physical structure and (b) equivalent transmission line model of the hybrid slot radiator. Dimensions in mm: l_1=6, l_2=3.85, l_3=25.9, w_1=0.25, w_2=3.

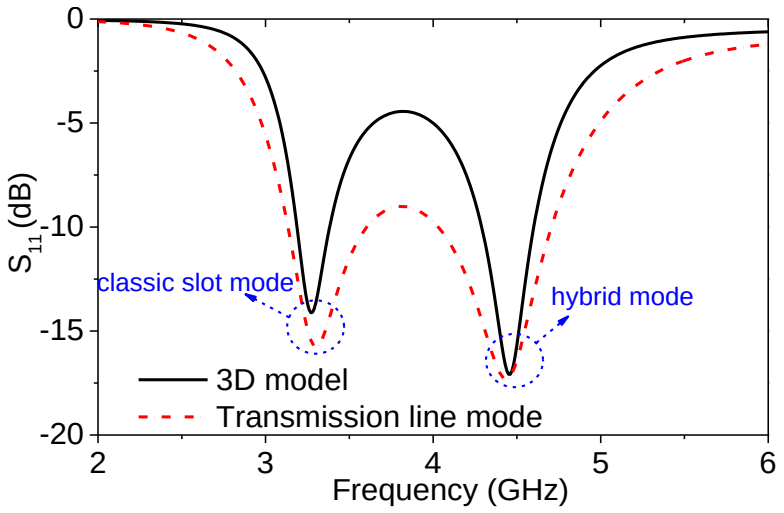

Fig. 4.3. S-parameters for the slot antenna and the transmission line model.

The current distributions at two resonances are shown in Fig. 4.4. The first resonance, which occurs at 3.3 GHz, is associated with the fundamental mode of the slot, where the total slot length is about half a wavelength. At this resonance, the current density peaks at the short ends of the slot and decreases to a minimum at its centre, as demonstrated in Fig. 4.4(a).

Fig. 4.4(b) depicts that the hybrid mode has a similar current distribution as the fundamental slot mode, but it utilizes the microstrip stub as the current boundary. This stub restricts the current from spreading to one end of the slot, resulting in a strong

current on the stub. This behaviour indicates that the second mode in Fig. 4.3 is a hybrid mode dominated by the dimensions of the microstrip line to slotline transition. This unique hybrid mode can provide inherent high isolation when two such slot antennas are placed in close proximity, which will be discussed in detail in the following sections.

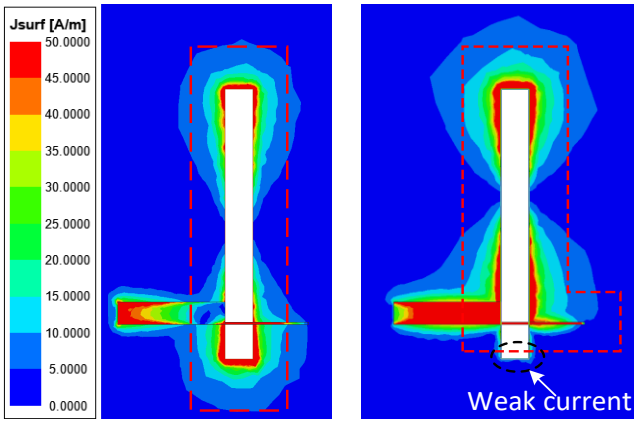

Fig. 4.4. Current distributions at different modes. (a) fundamental slot mode. (b) hybrid mode.

4.3 2-Element MIMO for 5G NR Applications

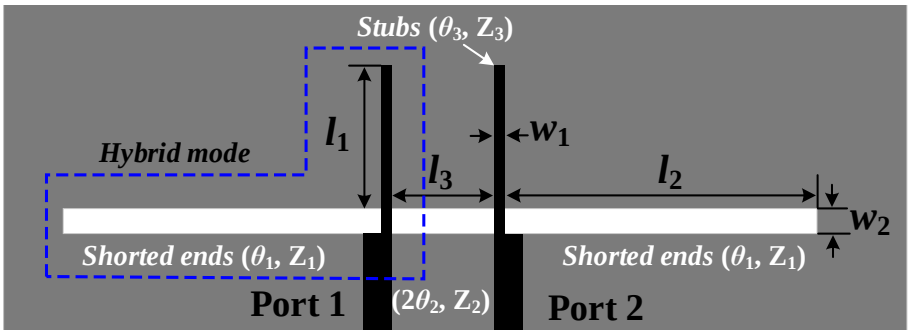

Fig. 4.5. Structure of the dual-antenna module.

Fig. 4.5 shows the structure in which two identical slot antennas are connected together sharing the same ground plane. It is found through this study that such architecture ensures two inherently isolated channels when the slot is operating over the hybrid mode. There are two factors that result in this phenomenon.

Firstly, the slotline structure of the two antennas acts as a dispersive band-stop filter, leading to a bandstop effect for the hybrid modes. An equivalent circuit model of the dual-antenna module is shown in Fig. 4.6(a). This model can be simplified into a

transmission path with two stubs, as shown in Fig. 4.6(b). Fig. 4.6(c) shows a transmission line model of a 3rd-order band-stop filter.

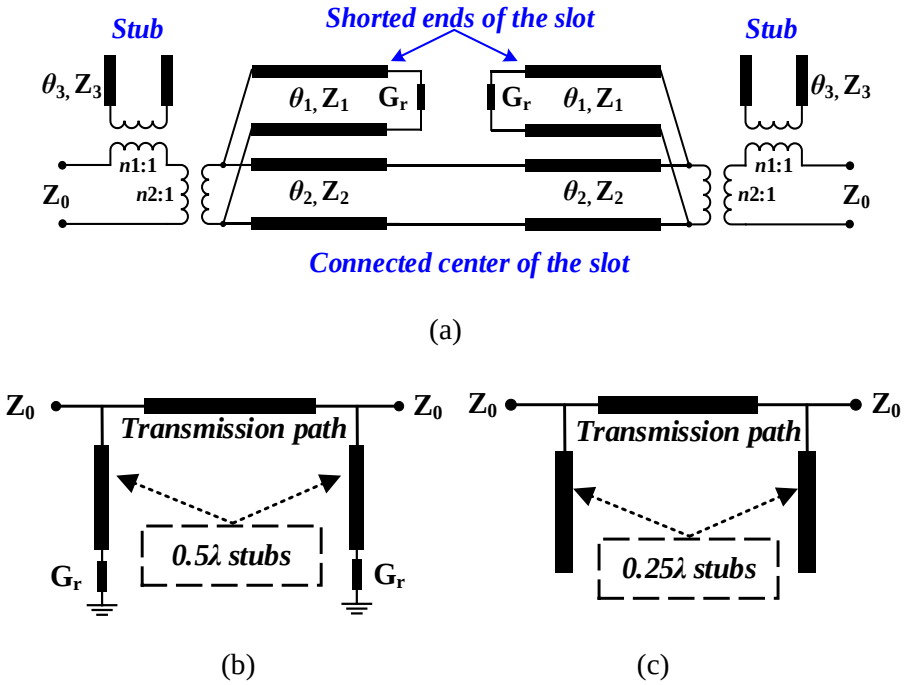

Fig. 4.6. (a) Transmission line model for the dual-antenna module. (b) Simplified conceptual model of the antenna module which shows a radiative bandstop response. (c) transmission line mode for a 3rd order bandstop filter.

When the length of the stub in Fig. 4.6(c) is a quarter wavelength at the centre frequency of the stopband, the virtual-short point blocks the transmission between two ports. Comparing the structure in Fig. 4.6(b) to Fig. 4.6(c), we can notice that the dual-antenna module is a lossy bandstop filter at the frequency where the length of θ_1 is about half-wavelength, which is near the resonance of the hybrid mode. With the transformation of a quarter-wavelength, the short ends of the slot will be inverted to open ends just like the structure of the bandstop filter in Fig. 4.6(c). Different from a conventional BSF in which the energy in the stopband will be reflected back to the input port, the energy reflected by the band-reject structures in this dual-port antenna module is radiated to the free space by the slot, as illustrated in Fig. 4.1. Thus, this structure can be regarded as a dispersive BSF. The energy which is supposed to be reflected back is

absorbed by the radiation resistance as shown in Fig. 4.6(a). As a result, the proposed hybrid mode will show a bandstop-radiative response near its resonance frequency.

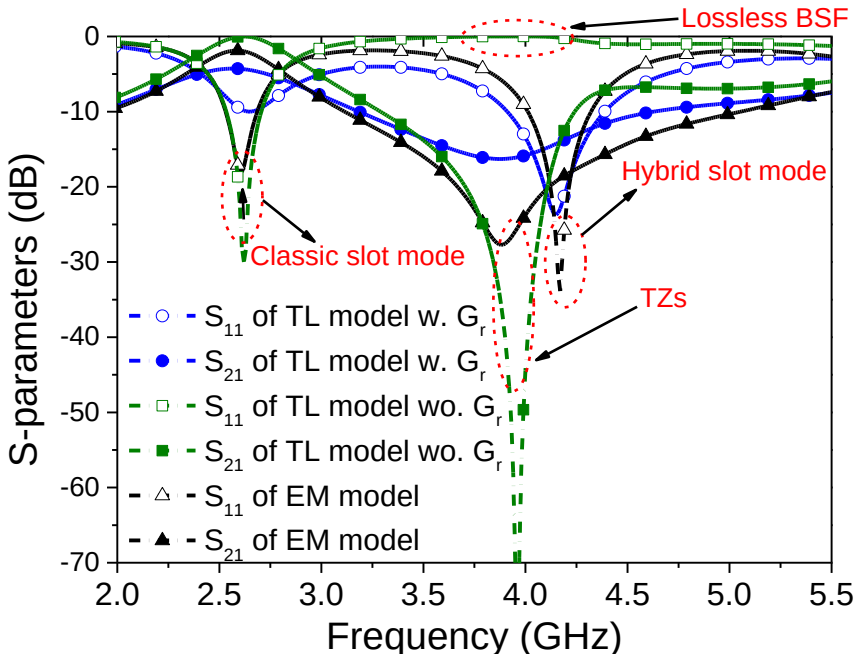

Fig. 4.7. Frequency responses of EM and transmission line models.

The responses for both transmission line and EM models are plotted and compared in Fig. 4.7 with the following initial circuit parameters: $Z_0 = 50\ \Omega$, $Z_1 = Z_2 = 187\ \Omega$, $Z_3 = 123\ \Omega$, $G_r = 0.023$ S, $\theta_1 = 150°$, $\theta_2 = 30°$, $\theta_3 = 63°$. The electric properties of the element in the model are set at 3.3GHz. Two resonances arise for each model. The first resonance is the classical slot mode. For this slot mode, the structure behaves like a bandpass filter with very high mutual coupling. However, for the hybrid mode which arises at about 4.2 GHz, the connected slots do not make these modes coupled together. At this frequency, the whole structure acts as a dispersive BSF. For a non-radiative BSF with G_r set zero, the energy will be reflected back to the input port in the stopband, resulting in an all-reflective S_{11}, as shown in Fig. 4.7. For the proposed radiative slot structure, the energy in the stopband is radiated and thus low reflection coefficient is achieved. A TZ slightly lower than the centre frequency of the antenna's operating band arises for both EM and transmission line models. The location of the null is dominated by the length of θ_1, which is related to the feed positions in the EM model. Thus, to

ensure the band-reject point is close to the operating band of the antenna, the slot should be off-centre fed.

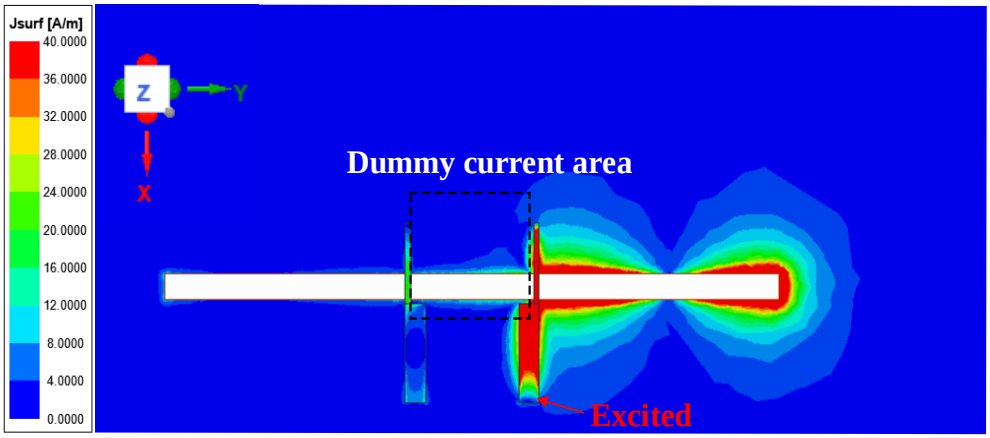

Fig. 4.8. Current distribution at the hybrid mode resonance.

Despite the radiative-bandstop characteristic introduced above, another factor that greatly affects the isolation between two antenna ports is the special current distribution for the hybrid modes. The current for these hybrid slot modes is concentrated only in the region limited by the microstrip-line-slotline transition. As shown in Fig. 4.8, when port 1 is excited, only the right-hand side slot area is activated. Only a very weak current can be observed in the central slot area, as depicted by the dashed box. This phenomenon reveals that the left-hand side port will not be strongly coupled with the activated port.

Parametric studies on different feeding positions and feedline lengths were carried out as illustrated in Fig. 4.9. The feed position, which governs the length of θ_1 in Fig. 4.6(a), affects both the operating band of the hybrid mode and the location of the TZ, as illustrated in Fig. 4.9(a).

The length of the feedline stub (l_1 in Fig. 4.5, θ_3 in Fig. 4.6(a)) can be utilized to shift the resonance frequency of the hybrid mode closer to the TZ, resulting in higher isolation, as shown in Fig. 4.9(b). When the stub length is increased, the resonance frequency of the hybrid mode shifts to a lower frequency while the position of the TZ remains unchanged. This is because the dimension of the stub only affects the length of

θ_3 in Fig. 4.6(a). However, it is important to note that the stub length not only affects the location of the hybrid mode but also has an impact on impedance matching. Consequently, a trade-off between impedance matching and mutual coupling level may arise when dealing with multiple hybrid modes.

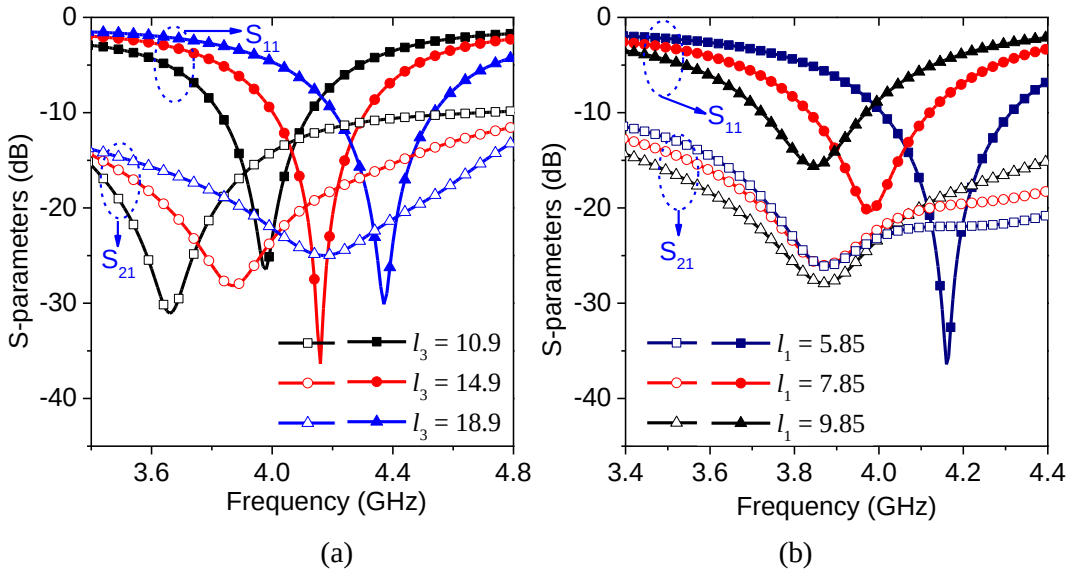

Fig. 4.9. Parametric studies with different feeding dimensions. (a) Feeding position. (b) Feedline lengths.

4.4 Wideband Slot MIMO Antenna for 5G NR Applications

The module discussed above achieves two inherently decoupled slot antennas. However, the bandwidth of each antenna is too narrow. In this section, a wideband design is developed based on the aforementioned narrow-band module.

The structure of the wideband MIMO array is shown in Fig. 4.10. Compared to the structure in Fig. 4.5, two loading resonators and four slot stubs are added to this wideband module. Fig. 4.11 shows the evolution of the proposed wideband slot antennas. First, two additional quarter wavelength resonators are loaded to the slot as illustrated in Fig. 4.11(a). Such a resonator-loading slot structure can also realize a hybrid resonant mode which has been analyzed in [3]. The concept from [3] is adopted here to introduce a lower band resonance together with a transmission zero. When the total length of the resonator is about a quarter wavelength, the bandstop effect will stop the signal from transmitting between the two ports. As a result, this resonator-slotline hybrid mode (RSHM) also features a null at the transmission coefficient between the

two ports. Additionally, this RSHM exhibits a current distribution similar to that of the microstrip-slotline hybrid mode (MSHM). Consequently, the passbands dominated by this RSHM are also inherently decoupled. Then, to further improve the bandwidth, multiple stubs are added to the slot as shown in Fig. 4.11(b) and Fig. 4.11(c). These stubs can introduce two additional hybrid resonances for each antenna [4]. By this method, the bandwidth of each antenna is significantly increased.

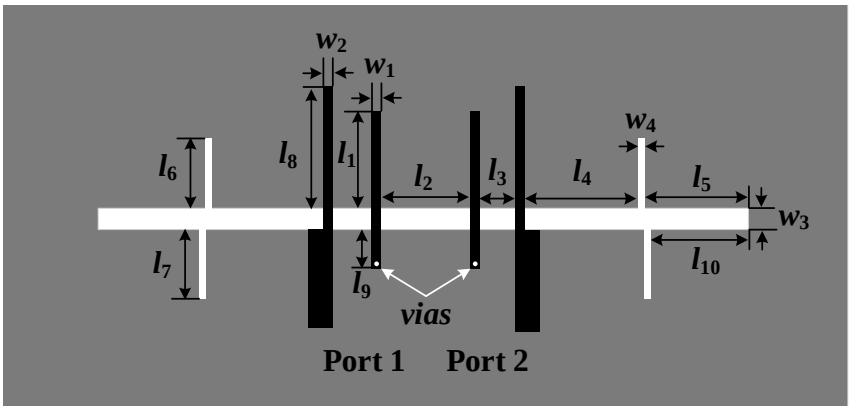

Fig. 4.10. Geometry of the wideband 2-element MIMO slot antenna. Dimensions in mm: $l_1 = 5.55$, $l_2 = 9$, $l_3 = 2.5$, $l_4 = 14.78$, $l_5 = 13.38$, $l_6 = 9.9$, $l_7 = 13.3$, $l_8 = 6.4$, $l_9 = 5.05$, $l_{10} = 13.58$, $w_1 = 1$, $w_2 = 0.6$, $w_3 = 3.2$, $w_4 = 1.25$.

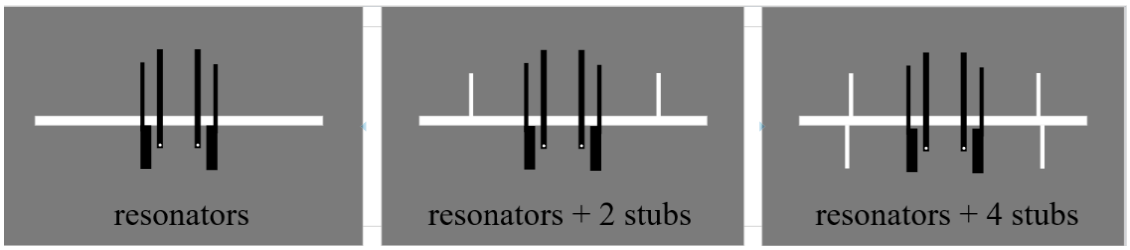

(a) (b) (c)

Fig. 4.11. Evolution of the wideband slot antennas. (a) reference design 1, (b) reference design 2, (c) reference design 3.

Fig. 4.12 presents the S-parameters of different structures. The initial design which is presented in Fig. 4.5 only has one resonance. With additional loading resonators, an additional lower-band resonance is achieved. Then, two slot stubs provide two additional higher-band resonances. Finally, a wideband response is achieved, covering the 5G N77, N78, and N79 bands. It should be noted that the impedance bandwidth is calculated when $S_{11} < -6$ dB, which is widely used for terminal antenna designs.

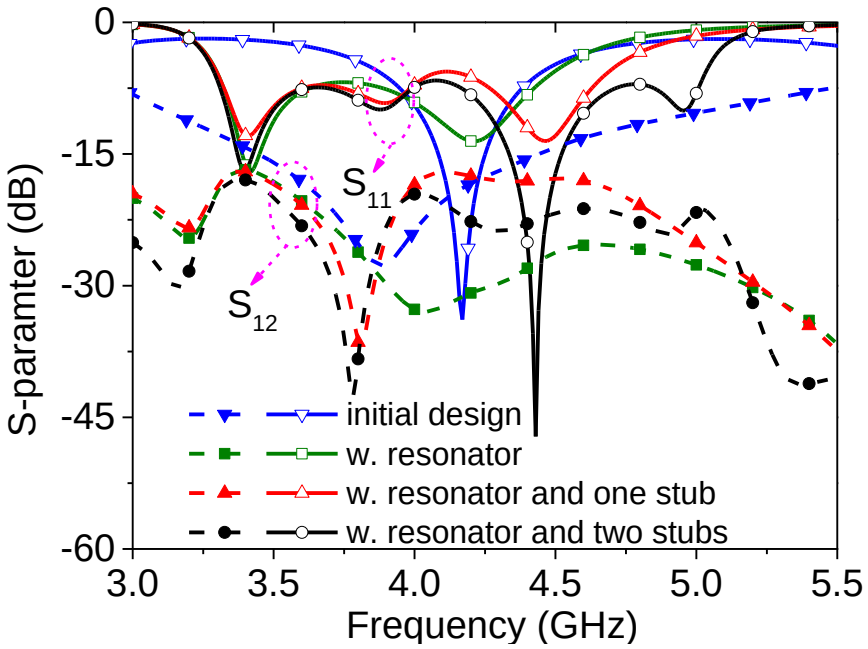

Fig. 4.12. S-parameters of different antenna structures.

With all these efforts, a dual-antenna module with both antennas showing four-resonance wide operating bands is obtained. More importantly, all these resonances are realized accompanied by a nearby band-reject point. Finally, a wideband slot MIMO array with isolation up to 18.5 dB in the band of interest is achieved. The antennas are designed for MIMO operation of sub-6G standards, which cover N77, N78, and N79 bands (3.3GHz-5.0GHz).

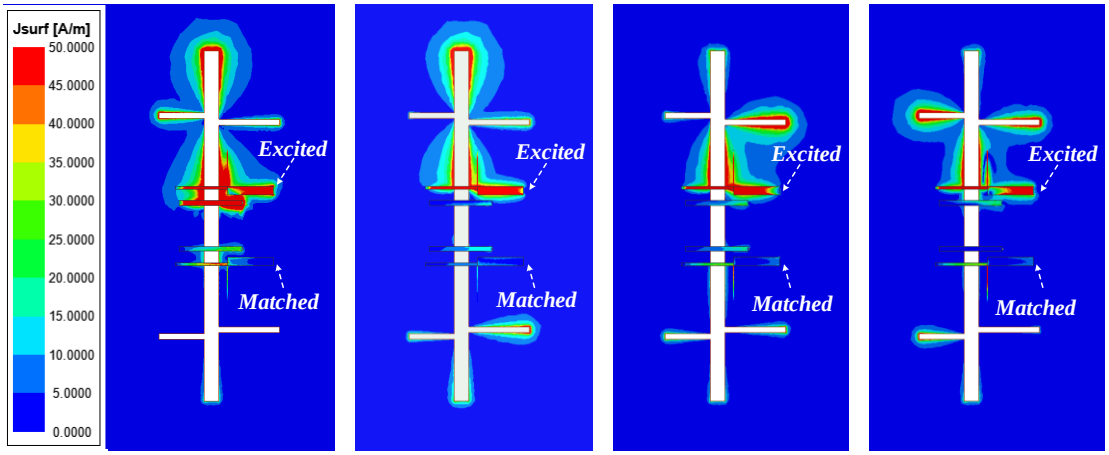

(a) (b) (c) (d)

Fig. 4.13. Current distributions at different frequencies when one antenna is excited. (a) 3.4 GHz. (b) 3.9 GHz. (c) 4.45 GHz. (d) 4.98 GHz.

Fig. 4.13 shows the current distributions at different frequencies. In the simulation, only one port is excited with the other port 50 Ω matched. The first resonance arises at 3.4 GHz. For this resonance, the strong current density can be seen at both the slot and loading resonator. The current flow terminates at the loading position of the resonator, which indicates that this mode is a hybrid mode of the slot and resonator. As the frequency gets higher, the current shifts to the area limited by the microstrip feedline. From 3.9 GHz to 5 GHz, different slot sections are activated. More specifically, the resonance at 3.9 GHz is dominated by the main slot. The behaviors of the other two resonances which arise at 4.45 GHz and 4.98 GHz respectively, are controlled by the slot stubs. For all these resonances, the current distributions only concentrate at the upper half part of the antenna structure whereas the current density at the other port is very weak.

4.5 Quadruplex Slot Antenna

Based on the structure obtained in the last section, two more ports are added to achieve a quadruplex operation. As aforementioned, the current for all the hybrid modes does not flow to the centre of the slot in its operating band, which means the NR ports will not detect the ports placed in this area from 3.3 GHz to 5 GHz. The geometry of the quadruplex antenna is shown in Fig. 4.14. Two more ports are placed between the NR antennas' ports. These two ports excite two more antennas to cover the 5-GHz WiFi band (5.15-5.8 GHz).

There are four antennas in this module, namely ANT1, ANT2, ANT3, and ANT4, correspond to the antennas excited by port 1, port 2, port 3, and port 4, respectively. To cover the whole 5 GHz WiFi band, filtering antenna architecture is adopted for the WiFi antennas (ANT3 and ANT4) to extend their impedance bandwidths. The detailed dimensions of the WiFi antennas are provided in Fig. 4.15(a) and Fig. 4.15(b).

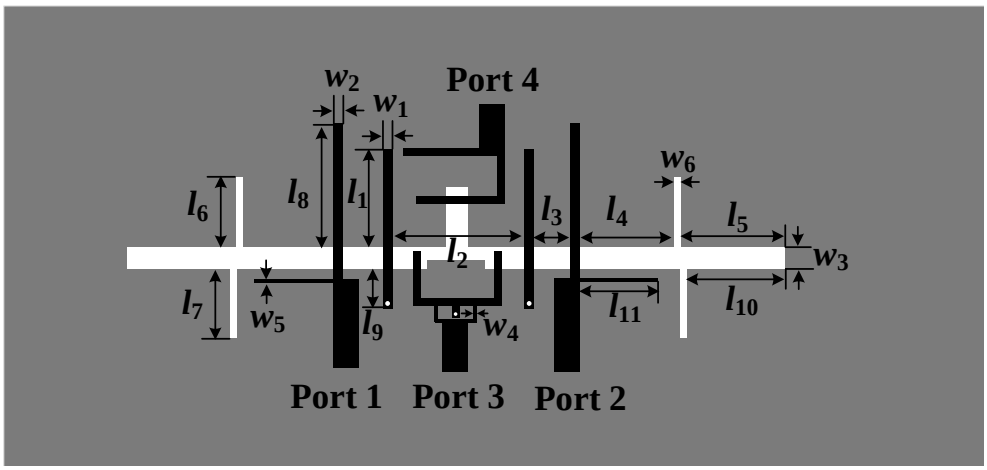

Fig. 4.14. Geometry of the quadruplex antenna. Dimensions in mm: $l_1 = 6.1$, $l_2 = 14.8$, $l_3 = 2.5$, $l_4 = 14.98$, $l_5 = 13.28$, $l_6 = 9.8$, $l_7 = 13.3$, $l_8 = 5.95$, $l_9 = 4.8$, $l_{10} = 14.78$, $l_{11} = 8.3$, $w_1 = 1$, $w_2 = 0.5$, $w_3 = 3$, $w_4 = 0.2$, $w_5 = 0.15$, $w_6 = 1.25$.

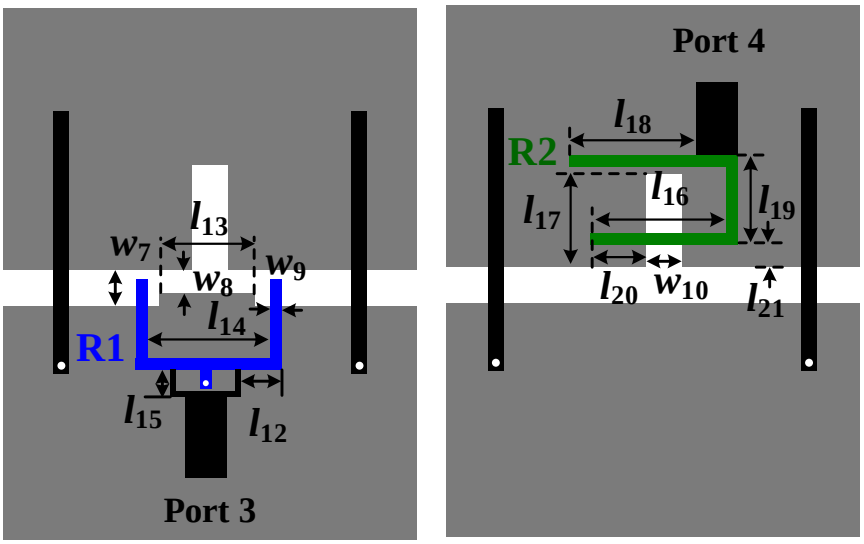

(a) (b)

Fig. 4.15. Structures of the WiFi antennas. (a) antenna 3. (b) antenna 4. Dimensions in mm: $l_{12} = 3.5$, $l_{13} = 10$, $l_{14} = 7.8$, $l_{15} = 2.6$, $l_{16} = 5.7$, $l_{17} = 10.35$, $l_{18} = 9.7$, $l_{19} = 2$, $l_{20} = 2.8$, $l_{21} = 8.95$, $w_7 = 3.3$, $w_8 = 1.65$, $w_9 = 0.8$, $w_{10} = 3$.

Fig. 4.16 presents the coupling topologies for both WiFi antennas. For the first WiFi antenna excited by port 3, to excite the even mode of the slot solely, a symmetric feeding structure is adopted. The port is tapped to a center-shorted resonator. The symmetric feeding scheme will then activate the even mode resonance of the slot radiator to form a second-order filtering response. For the second WiFi antenna related to port 4, an asymmetric feeding scheme is used as shown in Fig. 4.16(b). Port 4 is

tapped to a half-wavelength resonator. Then the resonance will excite the odd mode resonance of the slot through the microstrip-line-to-slot transition. The design process of such a simpler filtering antenna structure is available in [5, 6], so it is not provided here for the conciseness of the thesis.

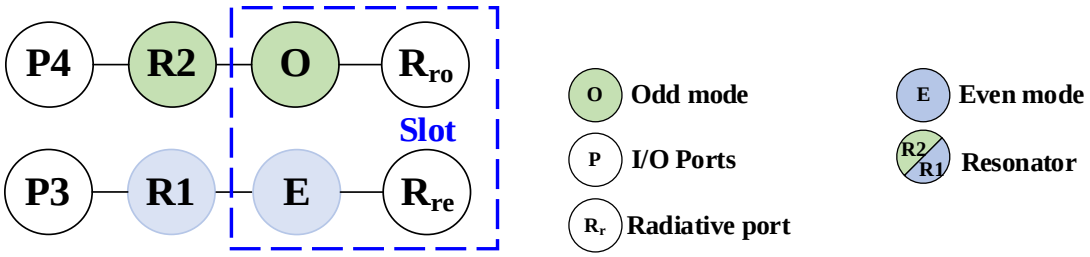

Fig. 4.16. Coupling topologies for the WiFi antennas.

4.6 Experimental Verification and Discussions

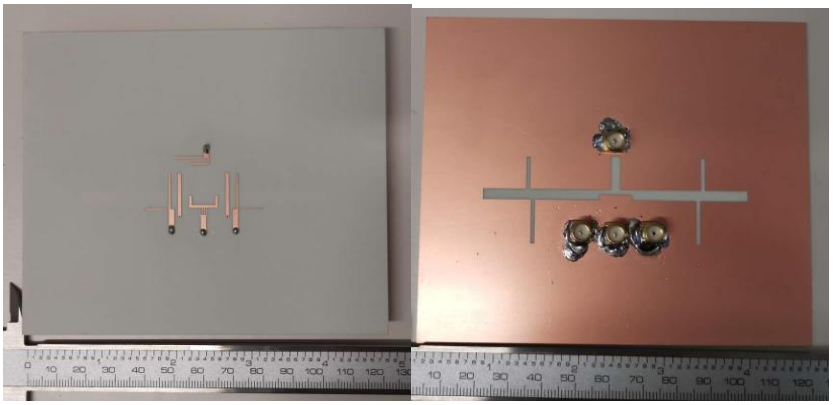

Fig. 4.17. Photograph of the fabricated prototype.

To verify the concept, a prototype of the proposed quadruplex antenna is fabricated and tested. Fig. 4.17 shows the photograph of the fabricated prototype. The final simulated and measured responses for the optimized quadruplex slot antenna are presented in Fig. 4.18, with the dimensions presented in Fig. 4.14 and Fig. 4.15. There are totally four ports in this module. These antennas can be divided into two 2-element MIMO arrays. One of which is designed for NR bands, whereas the other one serves for WiFi applications. Then the decoupling problems regarding this structure can be categorized into two parts: IBD and OBD.

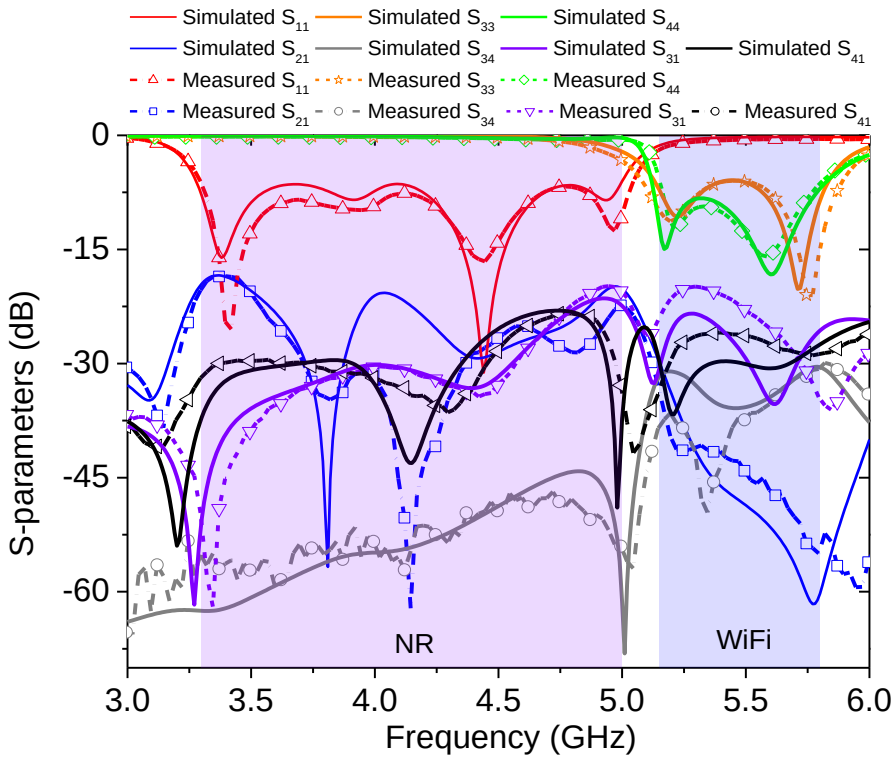

Fig. 4.18. Simulated and measured performance for the quadruplex antenna [7].

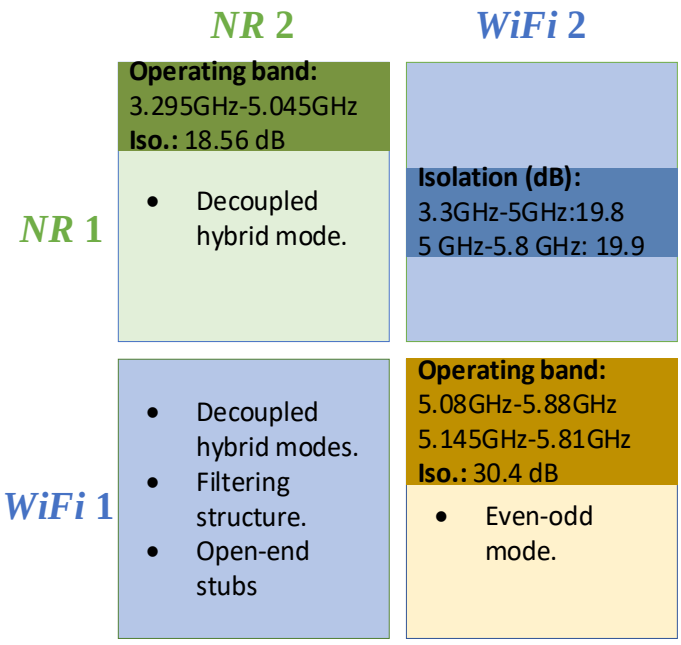

Fig. 4.19. Performance summary and decoupling techniques used in the proposed module.

The measured results show that the mutual coupling between all the ports is better than 18.5 dB. The measured performance of the fabricated antennas is summarized in Fig. 4.19 in brief. To keep all the ports isolated, the decoupling techniques used in this work have also been concluded in Fig. 4.19. Reading the matrix, the decoupling strategies for this work are concluded as follows:

1. The IBD for NR antennas is realized by the inherently decoupled hybrid modes. These hybrid modes arise with twin TZs in its operating band which improve the in-band isolation.
2. The IBD for WiFi antennas is achieved using two orthometric modes: even and odd modes. A deliberately designed feeding scheme ensures the sole excitation of each mode. Thus, two isolated channels can be achieved.
3. The OBD from 3-5 GHz is realized by two techniques: weak-current area resulting from hybrid modes and filtering antenna architectures. The first technique prevents the current excited by NR ports from flowing to the WiFi ports. The second technique then further improves the isolation by suppressing out-of-band signal at the WiFi ends.
4. The OBD from 5-5.8 GHz is realized by two open-end stubs at the feedlines of the NR ports. The TZs introduced by these stubs suppress the signal transmission between NR antennas and WiFi antennas, thus highly improving the isolation.

Detailed explanations of these decoupling techniques will be introduced and discussed in the next sections with corresponding experimental results.

4.6.1 In-Band Performance of the NR Antennas

Fig. 4.20(a) shows the simulated and measured reflection coefficients and IBD performance for NR antennas. The operating band with S_{11} < -6 dB is from 3.295 GHz to 5.045 GHz, which covers the frequency bands of N77, N78, and N79. The measured isolation between two NR antennas is higher than 18.5 dB from 3.3 GHz to 5 GHz. The NR antennas are decoupled by the hybrid mode theory introduced in the previous sections. Four hybrid modes are excited for each NR antenna as shown in Fig. 4.20(a). The first RSHM is dominated by the loading resonator. This mode comes with a band-reject frequency point at 3.145 GHz, which helps improve the isolation of the low-frequency band.

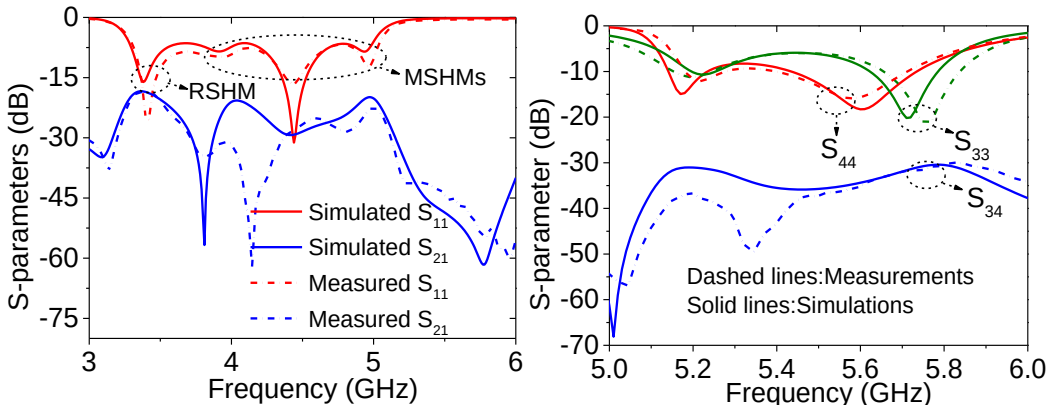

(a) (b)

Fig. 4.20. Simulated and measured reflection coefficients and IBD performance for (a) NR antennas and (b) WiFi antennas.

The other three resonances in the operating band are related to the MSHMs. These modes all have their corresponding twin TZs near their resonance frequencies, although some of these TZs may not have very deep nulls on the curves because of their low quality factors. These TZs greatly improve the isolation during operating band. With the aid of all these TZs, the isolation between two NR antennas is higher than 18.56 dB.

4.6.2 In-Band Performance of WiFi Antennas

The performance of the WiFi antennas is measured and plotted in Fig. 4.20(b). The measured -6 dB bandwidth for ANT3 and ANT4 are 5.08–5.88 GHz and 5.145-5.81 GHz, respectively. Within the operating band of ANT3 and ANT4, the measured isolation is higher than 30.4 dB. The measured bandwidth of ANT4 is slightly narrower than the simulation. The small discrepancy between the simulated and measured results can be attributed to the measurement and fabrication errors.

The IBD between two WiFi antennas is achieved using the even-odd mode theory [8]. Port 3 excites the even mode of the long slot. The central slot stub is inactivated for ANT3. Port 4 excites the odd mode of the slot structure through the central slot stub as shown in Fig. 4.15(b). For this mode, the electric wall should be applied to its symmetric plane. The even and odd modes are orthogonal with each other. Using this

architecture, the IBD problem for Wi-Fi antennas is resolved without using an additional decoupling structure.

4.6.3 OBD between WiFi and NR antennas

As this 4-port antenna module supports two standards with an extremely narrow guard band, the OBD problem should be carefully addressed to ensure the optimized performance for both RF channels. The measurement shows that the isolations between the WiFi antennas and NR antennas are higher than 19.8 dB for the whole band of interest as shown in Fig. 4.21. To achieve the low mutual coupling in such a wide frequency range, multiple different OBD techniques are used in this work.

Consider the NR frequency range first (3.3 GHz-5 GHz). The first factor that improves the adjacent-band decoupling is the MSHM structure. As has been studied in the previous sections, the NR antennas are composed of MSHMs. These hybrid modes do not show ground current distributions in the region between two NR ports. As a result, when two WiFi ports are placed in this area, the WiFi ports will be invisible to the NR ports. This effect greatly improves the isolation between these two channels in the frequency range of 3.3 GHz to 5 GHz.

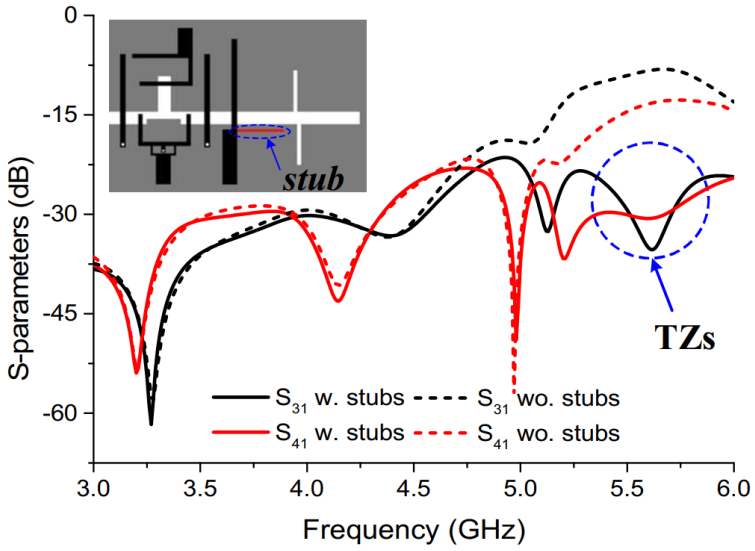

Fig. 4.21. Simulated OBD performance with (w.) and without (wo.) stubs [7].

The second technique that improves adjacent-band isolation is the filtering antenna architecture used for WiFi antennas. It is well-known that a filtering antenna design can increase the antenna bandwidth and filter out unwanted out-of-band signals. In this work, both WiFi antennas use filtering antenna designs. The filtering structures of the WiFi antennas decrease the interference between NR and WiFi antennas in the frequency range of NR bands. Especially for ANT4, an asymmetric tapped external coupling scheme is utilized as shown in Fig. 4.15(b). For such an excitation structure, a TZ can be obtained when the length of the open-end stubs l_{18} is about a quarter wavelength. In this work, this TZ is allocated at 4.98 GHz to suppress the mutual coupling between NR antennas and ANT4. With these two techniques, the lower frequency range (3.3–5 GHz) isolation is guaranteed.

The out-of-band decoupling in the frequency range from 5 GHz to 5.8 GHz is much easier as its bandwidth is much narrower. The OBD in this frequency range is mainly realized by two open-end stubs on the feedlines of the NR ports. Such an open-end stub will produce a transmission zero at the frequency where its total length (l_{11} in Fig. 14) is $\lambda_g/4$, where λ_g is the guided wavelength in the substrate. Fig. 4.21 compares the responses of the structures with and without the loading stubs. As can be seen, the stubs introduce a TZ at both the curves of S_{31} and S_{41}. When the stubs are removed from the structure, the isolation between the NR and WiFi antennas is only 8 dB at about 5.65 GHz. With a stub loaded at both input ports of the NR antennas, the isolation can be easily increased to 24 dB in the simulation.

4.6.4 Field Distributions

To validate the effect of the aforementioned techniques, the surface current distributions are studied and discussed in this section. As ANT1 and ANT2 are with the same structure, only three cases are studied here, these are ANT1 excited solely, ANT3 excited solely, and ANT4 excited solely. These cases are investigated in two frequency ranges.

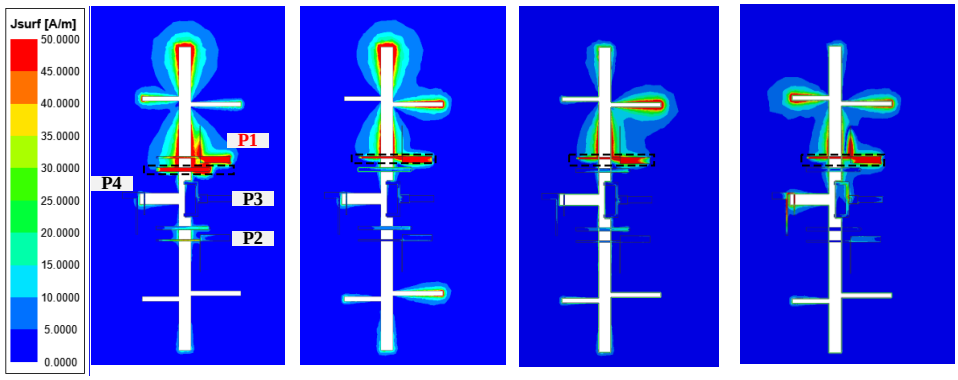

(a) (b) (c) (d)

Fig. 4.22. Current distributions at different frequencies when ANT1 is excited. (a) 3.4 GHz. (b) 3.9 GHz. (c) 4.4 GHz. (d) 4.9 GHz.

First, the current behaviour is studied in the frequency range of 3.3 GHz-5 GHz. Fig. 4.22 shows the field distributions when port 1 is excited. Current distributions at four different frequency points, where the reflection coefficient of port 1 reaches its deep null, are plotted. First, these current distributions reveal that when antenna 1 is activated, the current density at the other three ports is very weak for all four frequency points, which means that the signal injected into port 1 can hardly be coupled to other ports.

For all the frequency points the current always concentrates at the upper part of the module as shown in Fig. 4.22. This characteristic greatly improved the isolation performance at the low-frequency range. At the low-frequency band, the current is blocked by the loading resonator as shown in Fig. 4.22(a). For the frequency dominated by the MSHMs, the current boundary is the feedline stub as shown in Fig. 4.22(b), (c), and (d). When the frequency goes up to 4.9 GHz, which is very close to the lower edge of the WiFi band, the isolation is partly achieved by the filter circuit of the WiFi antennas. Especially for port 4, strong current distributions can be observed on the resonator as can be observed in Fig. 4.22(d). It should be noted that this strong current is a result of the band-reject response of the tapped external coupling structure of port 4.

For the higher decoupling band from 5-5.8 GHz, the current distributions are provided in Fig. 4.23. Fig. 4.23(a) and Fig. 4.23(b) show the current distributions when port 3 is excited. Port 3 activates the even mode of the slot. Owning to the decoupling

techniques used, all the other three ports show weak current density. Fig. 4.23(c) and Fig. 4.23(d) show the current distribution when port 4 is solely excited. Port 4 activates the odd mode of the slot, which shows strong current density at the centre stub of the slot. The orthogonality between the odd and even modes ensures good isolation between port 3 and port 4. The decoupling techniques adopted prevent the signal from port 4 transmitting to port 1 and port 2. Consequently, all the other three ports show weak current density.

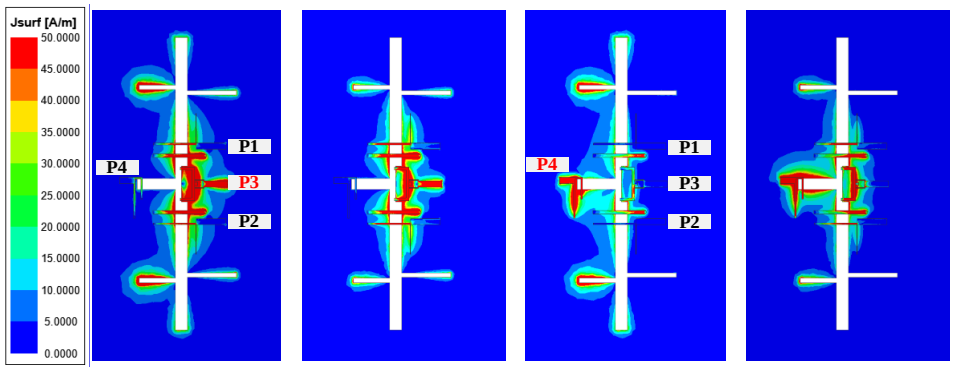

(a) (b) (c) (d)

Fig. 4.23. Current distributions at different frequencies. (a) 5.2 GHz w. ANT3 excited. (b) 5.8 GHz w. ANT3 excited. (c) 5.2 GHz w. ANT4 excited. (d) 5.8 GHz w. ANT4 excited.

The current analysis provides strong validation for the effectiveness of the technique described in this chapter. The results also reveal that the proposed 4-port antenna module achieves four isolated radiating channels supporting both 5G NR and WiFi applications with a very compact form factor.

4.6.5 Radiation Performance

The results are presented in Fig. 4.24. As ANT1 and ANT2 are identical, only three antennas are measured. It should be noted that in this process, the other three ports are all 50 Ω terminated when one antenna is tested. The measured total efficiency for the NR antennas is higher than 56%. For the NR MIMO, the envelope correlation coefficient (ECC) value calculated from radiation patterns is lower than 0.07. For the WiFi antennas, the total efficiencies for the ANT3 and ANT4 are better than 69% and 53%, respectively. The ECC for the WiFi MIMO array is lower than 0.02. The

measured efficiencies are generally lower than the corresponding simulations, which can be attributed to the fabrication and measurement errors and unwanted leakage from the cable during the radiation performance measurement, which is very common for slot antenna measurement with finite ground plane. This effect can be reduced by increasing the ground plane size or using ferrite RF chocks [17].

The normalized radiation patterns 2-D cuts at *xoz* and *yoz* planes are measured with results provided in Fig. 4.25. Good omnidirectional radiation patterns can be observed for all the antennas, which is desirable for terminal applications. The small ripples in the radiation patterns are mostly due to the scattering effect of the cable and connectors used in the measurement process. This phenomenon is commonly observed in many other MIMO slot antennas.

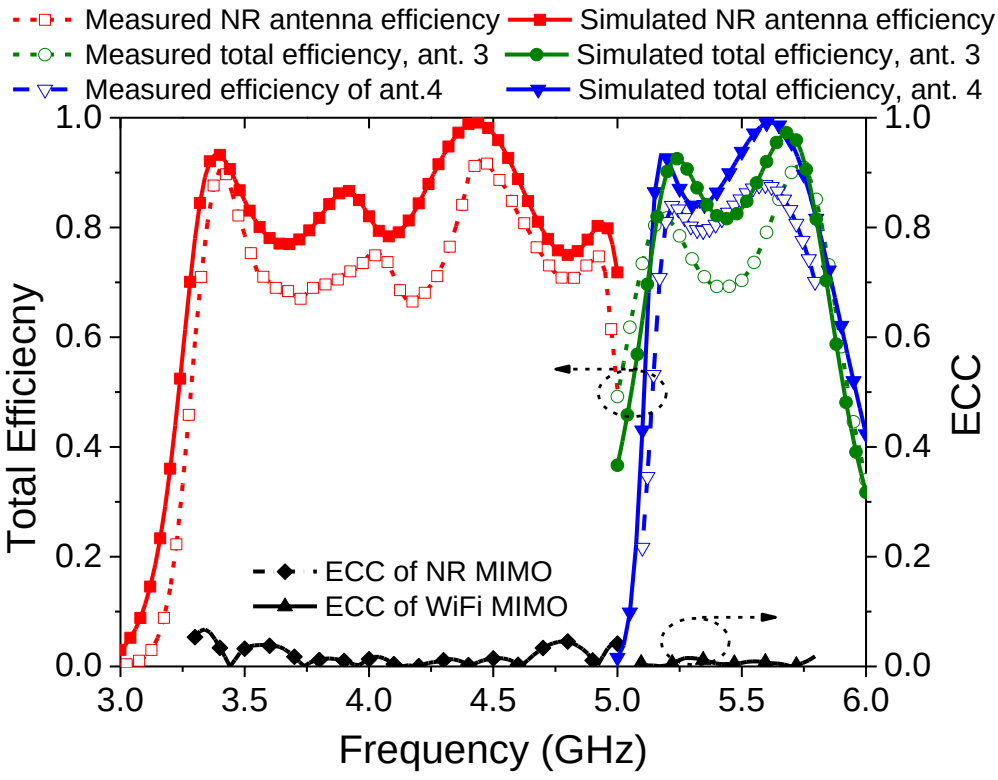

Fig. 4.24. The simulated and measured radiation performance of the quadruplex antenna.

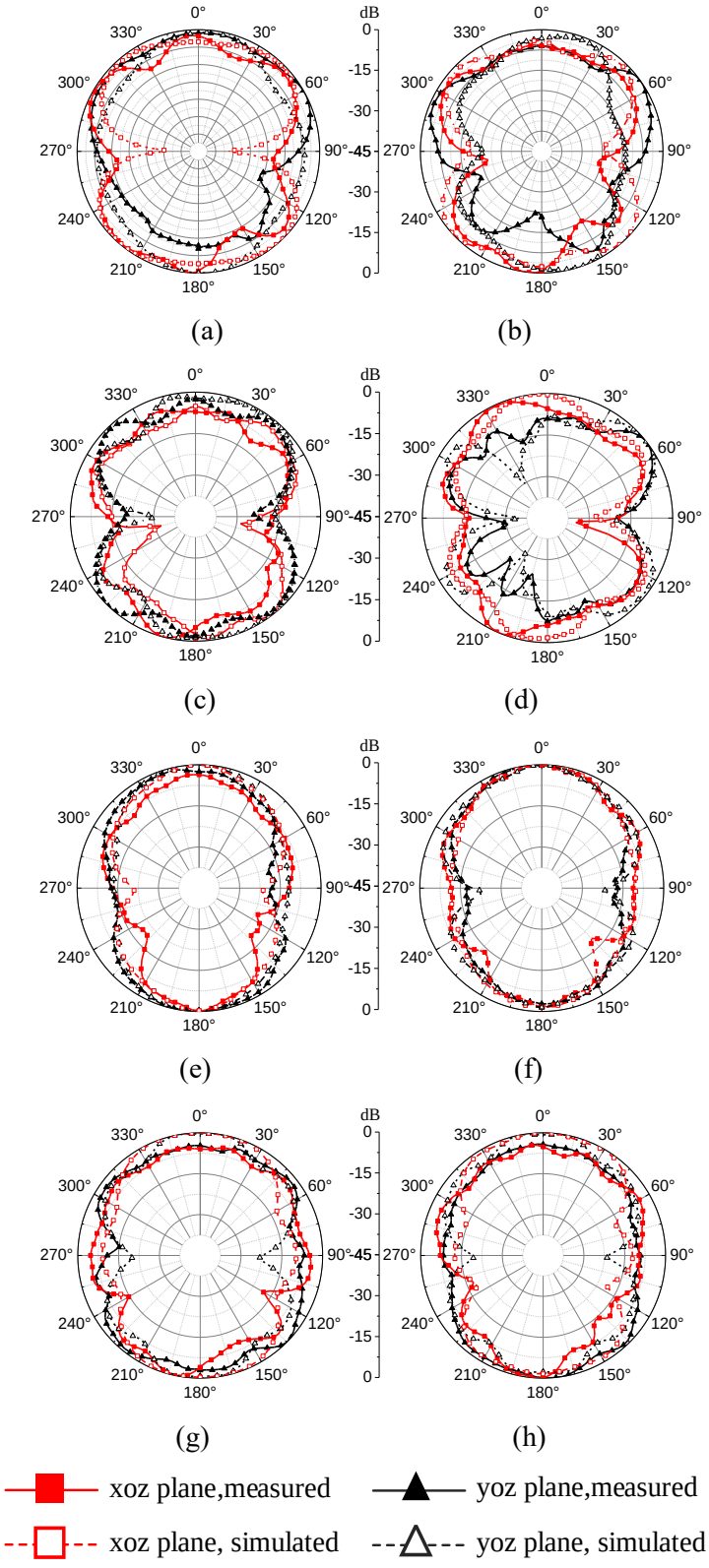

Fig. 4.25. Measured radiation patterns of the antenna in Fig. 4.17. (a) 3.4 GHz w. ANT1 excited. (b) 3.9 GHz w. ANT1 excited. (c) 4.4 GHz w. ANT1 excited. (d) 4.9 GHz w. ANT1 excited. (e) 5.2 GHz w. ANT3 excited. (f) 5.8 GHz w. ANT3 excited. (g) 5.2GHz w. ANT4 excited. (h) 5.8 GHz w. ANT4 excited.

4.6.6 Environmental Sensitivity

It is widely acknowledged that the slot structure is very sensitive to the environment. To investigate the robustness of the proposed structure in different environmental conditions, some measurements are carried out in this section.

From the results presented in Fig. 4.26, it can be seen that in a handheld scenario, the proposed bandstop radiative structure works well, maintaining a minimum isolation of 20 dB across the entire NR bands. However, due to the dielectric loading effect of the human tissue, a slight frequency shift is observed. This shift becomes more significant when the hands approach closer to the antenna. In an extreme scenario where human fingers make contact with the dielectric substrate at the backside of the slot region, the in-band responses of the antennas are strongly distorted.

According to these results, it is found that this module is not well-suited for portable devices. Instead, it is very useful for applications such as routers and customer premise equipment products, which are typically mounted on a platform.

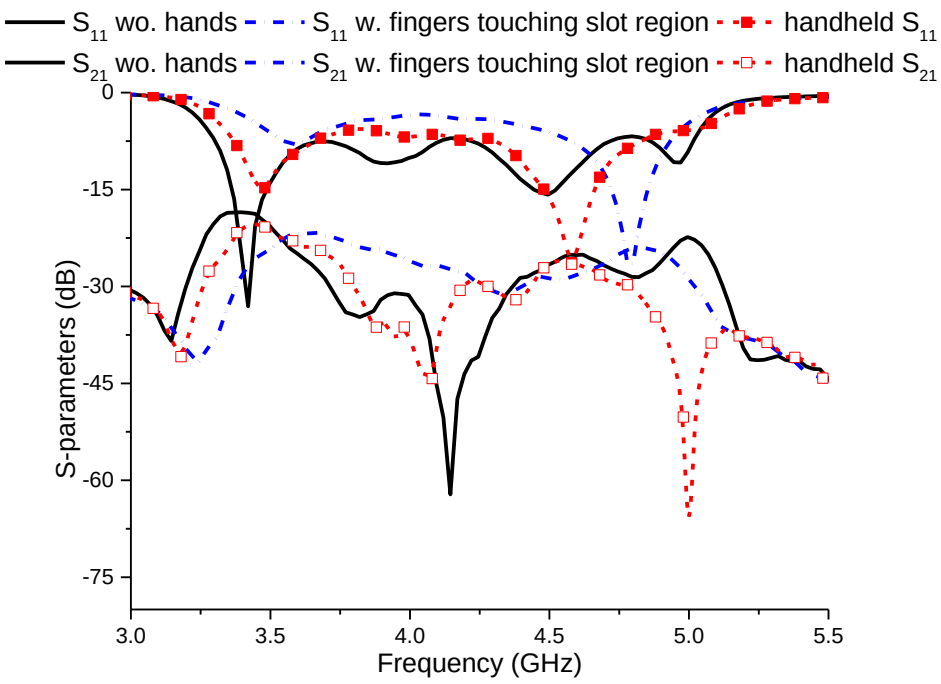

(a)

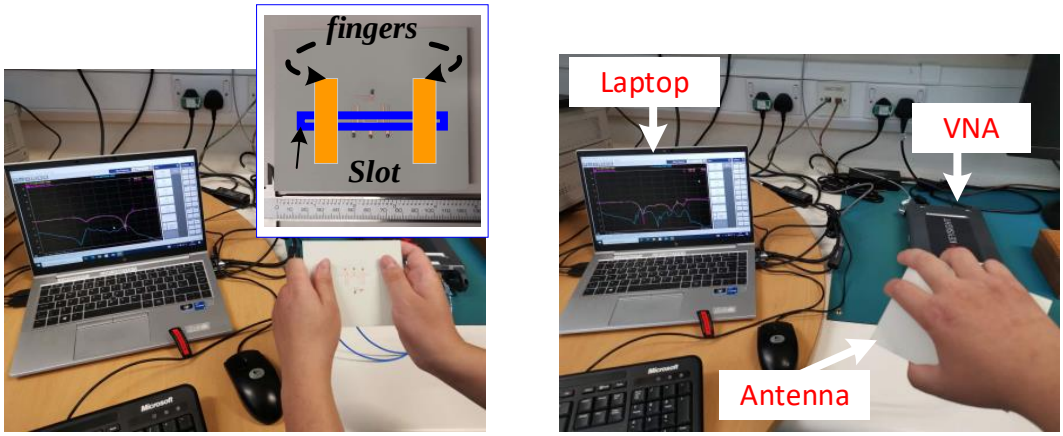

(b)

Fig. 4.26. (a) Measured antenna performance in different environments. (b) Photographs for the test environment.

4.7 Comparison and Discussion

The performance of the proposed quadruplex antenna is compared with state-of-the-art multiplex antenna designs in the literature and summarized in Table 4-1. Notably, this proposed design addresses both in-band and out-of-band decoupling problems for the first time. Additionally, it achieves out-of-band operation with a frequency ratio of

only 1.03, which is the smallest to the best of the authors' knowledge when compared to other presented multiplex-antennas. Although some designs also achieve multiplex operation at different frequency bands, they are only verified with relatively larger frequency ratios and narrow bandwidths. Regarding bandwidth, the proposed structure demonstrates a much wider frequency bandwidth than other planar designs. The general isolation level of 18.5 dB is also adequate for most terminal applications. In summary, the proposed design achieves highly competitive performance regarding bandwidth, isolation, and size.

Table 4-1. Performance comparison between this work and other presented works

Ref.	FR	IBD/ OBD	NoP	BW	Iso. (dB)	Size (S×H)
[9]	1	IBD	3	7%, 8%, 4.5%	24, 30, 30	$0.32\lambda_g^2 \times 0.077\lambda_g$
[10]	1	IBD	4	41%	13	$0.77\lambda_g^2 \times 0.14\lambda g$
[11]	1	IBD	3	5.7%	11	$0.14\lambda_g^2 \times 0.056\lambda_g$
[12]	1.97,1.5	OBD	3	19%, 17.8%, 9.5%	28.9, 19.1, 19.3	$0.19\lambda_g^2 \times 0.016\lambda_g$
[13]	2.24	OBD	2	4%, 12%	26	$0.16\lambda_g^2 \times 0.015\lambda_g$
[14]	1.05	OBD	2	<10%	22	$0.1\lambda_g^2 \times 0.012\lambda$
[15]	1.18,1.1, 1.07	OBD	4	5%, 3%, 2.8%, 4.4%	28, 29, 31.7	$1.36\lambda_g^2 \times 0.034\lambda_g$
[16]	1	IBD	2	6%	23	$0.2\lambda_g^2 \times 0.09\lambda_g$
This work	1.03	Both	4	41.8%, 12%	18.5, 19.8, 30	$0.93\lambda_g^2 \times 0.016\lambda_g$

Notes: FR: Frequency ratio; NoP: Number of ports; BW: Bandwidth; Iso.: Isolation; S×H: Surface area × height; λ_g: Guided wavelength in the substrate.

4.8 Summary

In this chapter, a quadruplex slot antenna has been introduced. The module is composed of two MIMO arrays. Two antennas operating over 3.3-5 GHz are designed for 5G NR MIMO application. The other two antennas target the 5-GHz WiFi application. A new multiplex antenna design method is introduced. The proposed module has achieved four isolated channels in a very compact form factor. Multiple decoupling techniques have been utilized in this work, including hybrid mode theory, even-odd mode theory, filtering antenna architecture, and band-rejective open-end stubs. For the first time, an antenna module addressing both wideband in-band duplex and small frequency ratio out-of-band duplex has been achieved. With this module, two wireless standards have been covered in a very compact structure, showing promising application prospects for modern communication systems.

.

4.9 References

[1] D. R. Jacjowski, "Passive enhancement of resonator *Q* in microwave notch filters," *IEEE MIT-S Int. Microw. Symp. Dig.*, pp. 13 15-13 18, 2004.

[2] M. Meng, I. C. Hunter, and J. D. Rhodes, "The design of parallel connected filter networks with nonuniform *Q* resonators," *IEEE Transactions on Microwave Theory and Techniques,* vol. 61, no. 1, pp. 372-381, 2013.

[3] J.-F. Qian, F.-C. Chen, K.-R. Xiang, and Q.-X. Chu, "Resonator-loaded multi-band microstrip slot antennas with bidirectional radiation patterns," *IEEE Transactions on Antennas and Propagation,* vol. 67, no. 10, pp. 6661-6666, 2019.

[4] H. Wang *et al.*, "Modal analysis and excitation of wideband slot antennas," *IET Microwaves, Antennas & Propagation,* vol. 11, no. 13, pp. 1887-1891, 2017.

[5] Z. H. Jiang, and D. H. Werner, "A compact, wideband circularly polarized co-designed filtering antenna and its application for wearable devices with low sar," *IEEE Transactions on Antennas and Propagation,* vol. 63, no. 9, pp. 3808-3818, 2015.

[6] J.-F. Qian *et al.*, "A wide stopband filtering patch antenna and its application in MIMO system," *IEEE Transactions on Antennas and Propagation,* vol. 67, no. 1, pp. 654-658, 2019.

[7] J. Qian *et al.*, "Quadruplex slot antenna for dual-standard operation with small frequency ratio," *IEEE Transactions on Antennas and Propagation,* vol. 72, no. 3, pp. 2909-2914, 2024.

[8] L. Sun, Y. Li, and Z. Zhang, "Decoupling between extremely closely spaced patch antennas by mode cancellation method," *IEEE Transactions on Antennas and Propagation,* vol. 69, no. 6, pp. 3074-3083, 2021.

[9] X. Gao *et al.*, "Low-profile planar tripolarization antenna for WLAN communications," *IEEE Antennas and Wireless Propagation Letters,* vol. 9, pp. 83-86, 2010.

[10] K.-L. Wong, J.-Z. Chen, and W.-Y. Li, "Four-port wideband annular-ring patch antenna generating four decoupled waves for 5G multi-input–multi-output access points," *IEEE Transactions on Antennas and Propagation,* vol. 69, no. 5, pp. 2946-2951, 2021.

[11] B. Yang *et al.*, "Tri-port antenna with shared radiator and self-decoupling characteristic for 5G smartphone application," *IEEE Transactions on Antennas and Propagation,* vol. 70, no. 6, pp. 4836-4841, 2022.

[12] P. Cheong, K.-F. Chang, W.-W. Choi, and K.-W. Tam, "A highly integrated antenna-triplexer with simultaneous three-port isolations based on multi-mode excitation," *IEEE Transactions on Antennas and Propagation,* vol. 63, no. 1, pp. 363-368, 2015.

[13] Y.-C. Lu, and Y.-C. Lin, "A mode-based design method for dual-band and self-diplexing antennas using double T-stubs loaded aperture," *IEEE Transactions on Antennas and Propagation,* vol. 60, no. 12, pp. 5596-5603, 2012.

[14] A. Boukarkar, X. Q. Lin, Y. Jiang, and Y. Q. Yu, "A tunable dual-fed self-diplexing patch antenna," *IEEE Transactions on Antennas and Propagation,* vol. 65, no. 6, pp. 2874-2879, 2017.

[15] K. Kumar, S. Priya, S. Dwari, and M. K. Mandal, "Self-quadruplexing circularly polarized siw cavity-backed slot antennas," *IEEE Transactions on Antennas and Propagation,* vol. 68, no. 8, pp. 6419-6423, 2020.

[16] A. Zhang, K. Wei, Y. Hu, and Q. Guan, “High-isolated coupling-grounded patch antenna pair with shared radiator for the application of 5G mobile terminals,” *IEEE Transactions on Antennas and Propagation,* vol. 70, no. 9, pp. 7896-7904, 2022.

[17] N. Bondarenko, P. Shao, A. Orlando, M. Y. Koledintseva, D. G. Beetner and P. Berger, "Prediction of common-mode current reduction using ferrites in systems with cable harnesses," 2012 IEEE International Symposium on Electromagnetic Compatibility, Pittsburgh, PA, USA, 2012, pp. 80-84.

Chapter 5
Low-Cost Decoupling Techniques for Patch Antennas

This chapter investigates the application of the electric and magnetic coupling theory and the coupled transmission line theory on antenna designs. First, it is found that two closely placed patch antennas can be easily decoupled by controlling the electric and magnetic coupling mechanisms between them. The control of these two distinctive mutual coupling mechanisms is realized by simply etching the edges of the radiator. Using this technique, the mutual coupling between two patch antennas can be reduced to -20 dB without using any extra decoupling process.

In section 5.2, the classical coupled transmission line theory is studied and used to guide the decoupling of two patch antennas. Through simulations and measurements, it is proved that two closely packed patch antennas can be self-decoupled by making them operate over TM_{20} mode, instead of classical fundamental TM_{10} mode. The mechanism of this technique is analyzed from both field and circuitry perspectives. The proposed method is verified with three different application scenarios, including a 2-element MIMO array, a 2-antenna system with adjacent operating bands, and a 4-element MIMO array.

In this chapter, all the prototypes were fabricated by HXP Circuits and assembled by the author. The S-parameters were measured by the author in the Antenna Lab at the University of Kent. The radiation performance of all the prototypes was measured using the anechoic chamber at the University of Kent, with the assistance of Technician Mr. Antonio Mendoza.

5.1 Low-Cost Decoupling Technique Using Electric and Magnetic Coupling Cancellation

This section presents a novel low-cost method for decoupling two closely-placed patch antennas. The idea is inspired by the electric and magnetic coupling theory which is widely used in filter designs. This new electric and magnetic coupling cancellation (EMCC) decoupling concept is simple yet highly effective, requiring no additional decoupling structures or complicated manufacturing processes. According to the proposed concept, the mutual coupling between two patches can be suppressed by controlling the weight of the electric (*E*) and magnetic (*H*) coupling between them. When the *E*-coupling and *H*-coupling are comparable, a deep null will arise on the mutual coupling curve, resulting in high isolation in the band of interest. To validate the approach, two prototypes for both 2-element and 4-element MIMO arrays, are designed, fabricated, and measured. The experimental results agree well with the simulations, highlighting the advantages of this method, including low cost, high isolation, and simple antenna structures.

5.1.1 Electric and Magnetic Coupling in Filter Designs

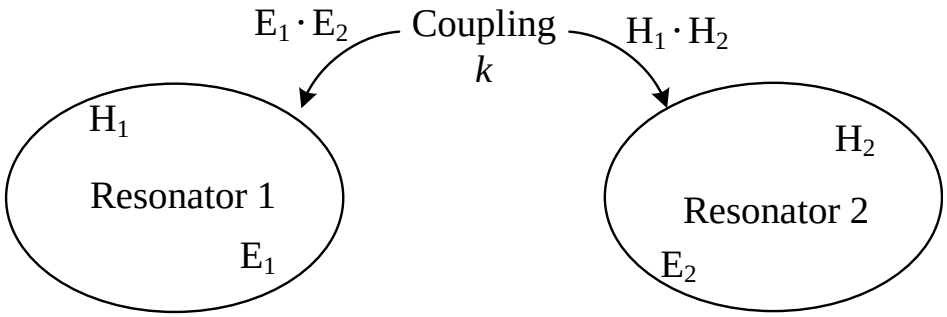

Fig. 5.1. General coupled resonators.

In filter theory, the coupling coefficient *k* between two coupled resonators can be defined based on a ratio of coupled energy to stored energy as (5.1) [1]: where all fields

are determined at resonance, and the volume integrals are over entire effective regions with permittivity of ε and permeability of μ.

$$k = \frac{\iiint \varepsilon E_1 \cdot E_2 dv}{\sqrt{\iiint \varepsilon |E_1|^2 dv \times \iiint \varepsilon |E_2|^2 dv}} + \frac{\iiint \mu H_1 \cdot H_2 dv}{\sqrt{\iiint \mu |\boldsymbol{H}_1|^2 dv \times \iiint \mu |\boldsymbol{H}_2|^2 dv}} \quad (5.1)$$

The first term on the right-hand side represents the electric coupling while the second term is the magnetic coupling. These two coupling mechanisms dominate the coupling strength between two resonators in conventional filter designs. This theory is widely used in many presented works in the literature for achieving bandpass filters with different filtering functions.

Through this study, it is found that the mutual coupling between two resonating antennas, such as patch antennas, can also be regarded as an interaction of electric and magnetic fields. When it comes to antennas, the only difference is that the resonator in the coupled circuit is always lossy, which means the unloaded quality factor of the resonator is very low.

In the electric and magnetic coupling theory, their mathematical forms always have different signs, which means a mixed electric and magnetic coupling may weaken each other and result in a lower coupling coefficient [2]. Inspired by this concept, the electric and magnetic coupling mechanism is studied in this chapter. It is found that the mutual coupling between two patch antennas can be easily suppressed by balancing the coupling components dominated by the *E*-field and *H*-field.

5.1.2 Two-Element MIMO Array

5.1.2.1 Antenna Structure

Fig. 5.2(a) depicts the physical structure of the proposed decoupled antennas, illustrating two patches placed in extremely close proximity. The distance between the two patches is set to 0.1 mm. The antennas are fed by a metal probe with a radius of 0.35 mm. The substrate employed in this design is Roger 4003, with a dielectric

constant of 3.55, a loss tangent of 0.0029, and a thickness of 0.3 mm. Notably, Fig. 5.2(a) shows only two modified patch antennas without any additional decoupling elements. The only modification applied to the antennas involves cuts made at their corners. The specific design rules to decide the patch dimensions will be elaborated upon in sections 5.1.2.3 and 5.1.2.4.

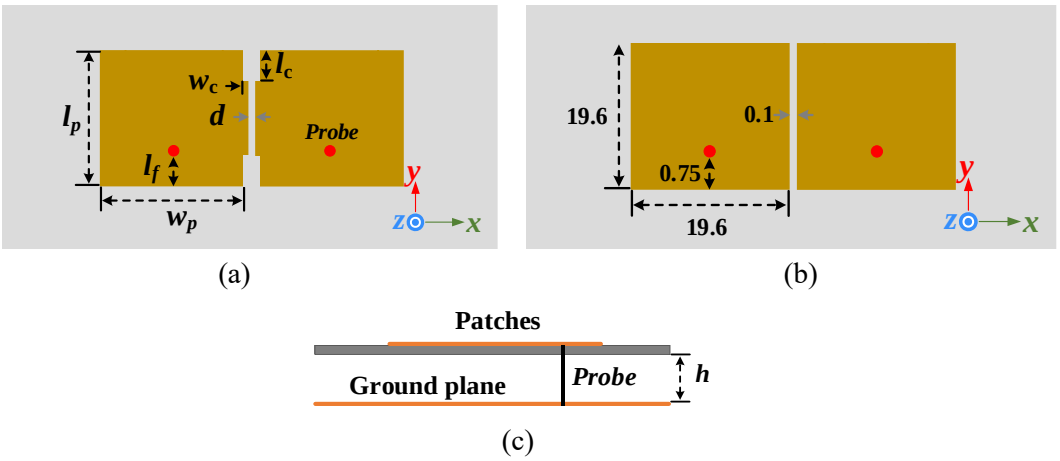

Fig. 5.2 Structure of the proposed decoupled patch antennas. (a) Decoupled patch antennas. (b) Reference design of coupled antennas with dimensions in mm. (c) Side view. Dimensions in mm: l_f = 1.45, l_p = 21, l_c = 5, w_c = 0.2, w_p = 22, d = 0.1, h = 3.

5.1.2.2 Antenna Performance

According to classical antenna theory, the mutual coupling between patch antennas is closely associated with the separation distance between them [3, 4]. As the antennas are placed in closer proximity, the mutual coupling becomes stronger. In cases where the patches are positioned in an extremely small vicinity to each other, the mutual impedance has a significant impact on the impedance response of the coupled antennas.

First, a reference design without any decoupling process is simulated. The dimensions of the reference design are outlined in Fig. 5.2(b). In this reference design, two patches are strongly coupled, as illustrated by the response plotted in Fig. 5.3. The antennas operate at a centre frequency of 5.9 GHz over their fundamental TM10 modes. A potential application for these antennas is V2X communication (5855–5925 MHz). The total lengths of the patches in the y-direction are approximately half-wavelength at 5.9 GHz. The edge-to-edge distance between the patches is 0.1 mm, which corresponds

to $\lambda_0/555.6$ at the antenna's centre frequency. Here λ_0 is the free-space wavelength at 5.9 GHz.

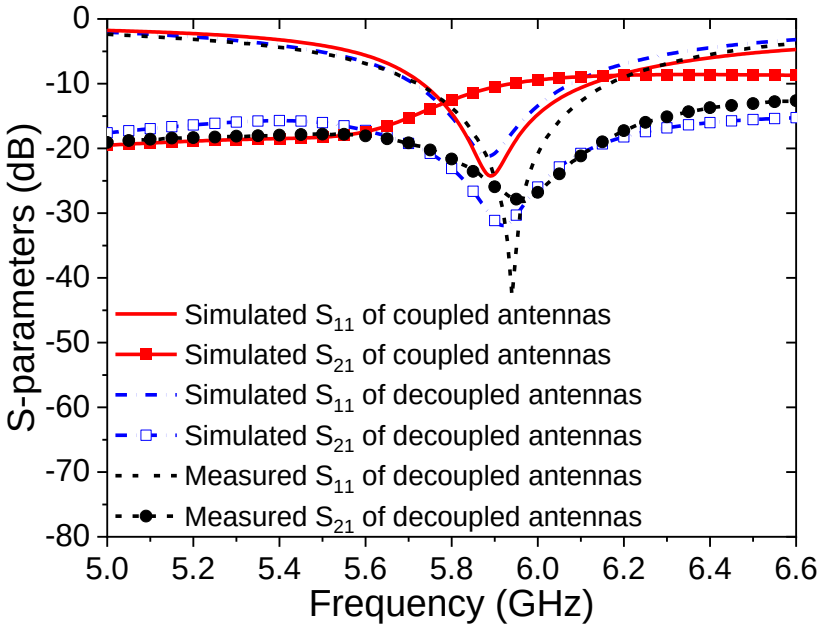

Fig. 5.3. Simulated and measured responses for the reference design and proposed decoupled antennas.

Without any modifications to the rectangular patches, the two antennas exhibit strong coupling, resulting in a low isolation of only 6.8 dB within their operating band when arranged at a distance of 0.1 mm. This strong coupling implies that a significant amount of energy will be consumed by one antenna when the other antenna is transmitting.

For the verification of the effect of the proposed novel decoupling concept, a prototype of the decoupled patch antennas is fabricated and measured with its photograph shown in Fig. 5.4. The ground plane size of the fabricated prototype is 110 mm × 130 mm. The simulated and measured S-parameters for the proposed decoupled antennas are presented in Fig. 5.3. The measured -10 dB bandwidth is 5.72 GHz to 6.16 GHz, while the simulated bandwidth ranges from 5.71 GHz to 6.08 GHz. The center frequency of the operating band exhibits a slight shift towards the higher frequency range due to fabrication errors.

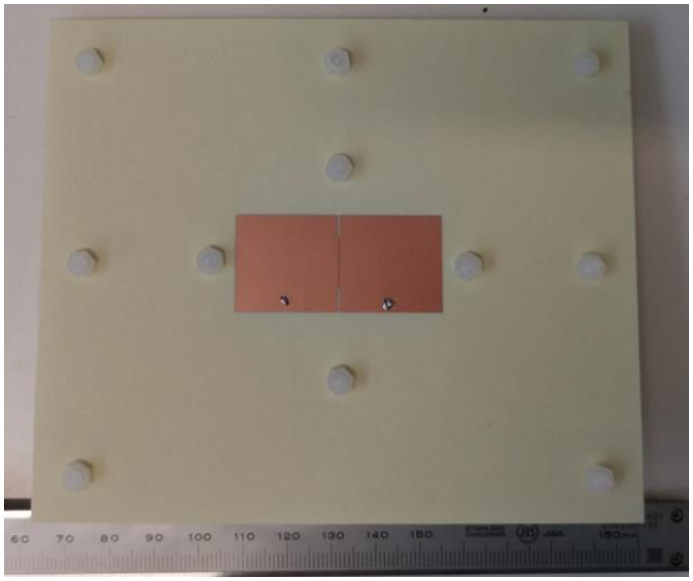

Fig. 5.4. Prototype of the proposed MIMO array.

Using the proposed decoupling technique, the measured mutual coupling between the two antennas was reduced to 18.7 dB. The only change to the proposed MIMO compared to the reference design is introducing some simple cuts at the patches' corners. With such a small change, a deep null is observed in the transmission curve of the decoupled antennas in Fig. 5.3, leading to a substantial improvement in isolation of up to 19.8 dB at the center frequency, compared to the coupled reference design.

Through this study, it is found that when the separation between the patches is extremely small, the electric field dominates the mutual coupling. To mitigate the *E*-coupling, the four corners of the patch are cut, effectively moving the electric field beneath the patches away from each other. By doing so, the *E*-coupling can be reduced while the weight of the *H*-coupling can be increased consequently. Within a certain tuning range, the *E*- and *H*-couplings become comparable in the antennas' operating band. In this specific scenario, the two coupling mechanisms cancel each other out, resulting in a low level of mutual coupling. The detailed mechanism and design principles are given in sections 5.1.2.3 and 5.1.2.4.

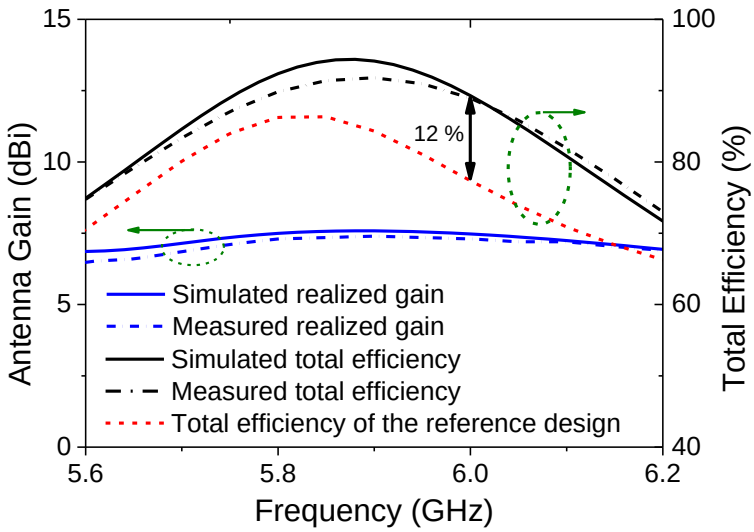

Fig. 5.5. Simulated and measured gain and efficiency of the antennas.

Fig. 5.5 illustrates the simulated and measured gain and efficiency of the antennas. During the measurement process, one antenna is measured while the other one remains terminated with a 50 Ω load. As the entire structure is symmetric, only one antenna measurement is required. The measured realized gain is 7.42 dBi, which is 7.57 dBi for the simulation. The measured total efficiency exceeds 77% within the whole operating band, with S_{11} less than -10 dB. The peak total efficiency reaches 91%.

Fig. 5.6 shows the simulated and measured radiation patterns of the fabricated decoupled antennas, whose structure is shown in Fig. 5.4. Due to the structural symmetry, only one antenna is measured, while the other inactive antenna is terminated with a 50 Ω wideband load. Broadside radiation is observed in both planes. The simulated and measured radiation patterns agree well. For both planes, the measured cross-polarization is lower than -16.7 dB and -15 dB, respectively. Because of the integrity of the ground plane, the antennas show good directional radiation for both planes with very weak backside radiation.

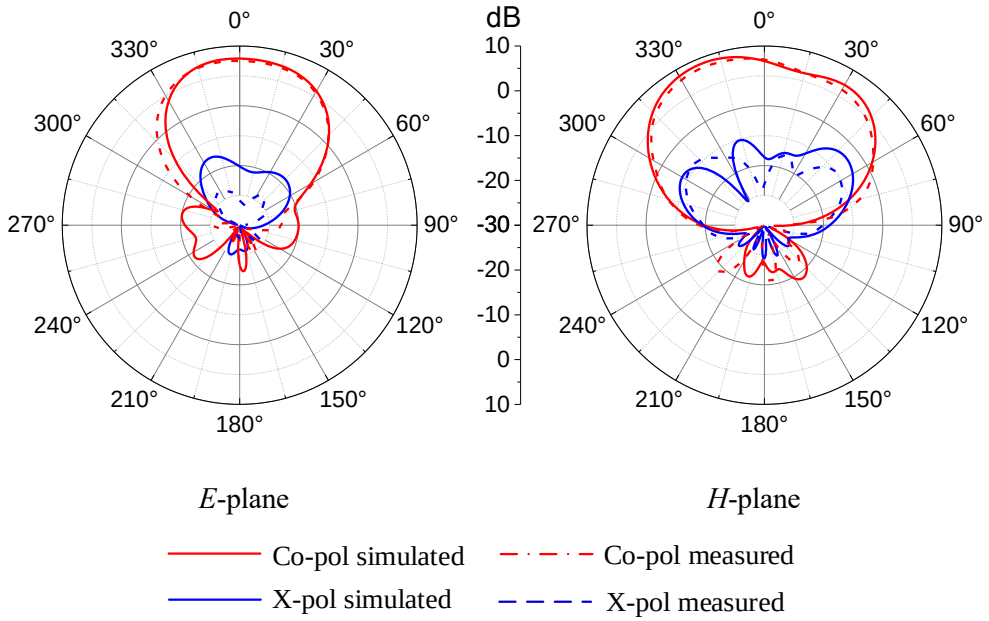

Fig. 5.6. Simulated and measured radiation patterns of the antenna in Fig. 5.4 (5.9 GHz).

5.1.2.3 Decoupling Mechanism

To gain insight into the physical behavior of this structure, it is important to study the electric field distribution for the TM_{10} mode. Fig. 5.7(a) illustrates the electric field distribution beneath the patch for its non-radiating edges. As known, the TM_{10} mode exhibits a half-wavelength standing wave field distribution at its two non-radiating edges. The electric field reaches its peak at the open ends of the patch (regions A and A'), while it drops to a minimum at the center (region B). Conversely, a strong magnetic field distribution occurs at the virtually shorted center of the patch (region B), while it weakens at the open ends (regions A and A').

When two patches are positioned in close proximity, they will be strongly coupled through the electric (*E*) and magnetic (*H*) near fields, as depicted in Fig. 5.7(b). By altering the structures of the coupled edges, the *E*- and *H*-couplings can be controlled. When they are comparable, the overall mutual coupling will be decreased by their cancellation. This EMCC behavior can be explained by the fact that electric and magnetic couplings always possess opposite signs when they coexist within the same network as shown in Fig. 5.7(c). This characteristic is commonly utilized in filter

designs to control the positions of TZs. In this work, the theory is borrowed to minimize the coupling between two patches. In filter designs, TZs are typically positioned at out-of-band frequencies to improve selectivity. However, for effective decoupling performance in antennas, the TZs must be located within the antennas' operating bands. To accomplish this, the electric and magnetic couplings should have the same magnitude. Consequently, the cuts on the patches need to be carefully designed to ensure the EMCC occurs in the frequency band of interest.

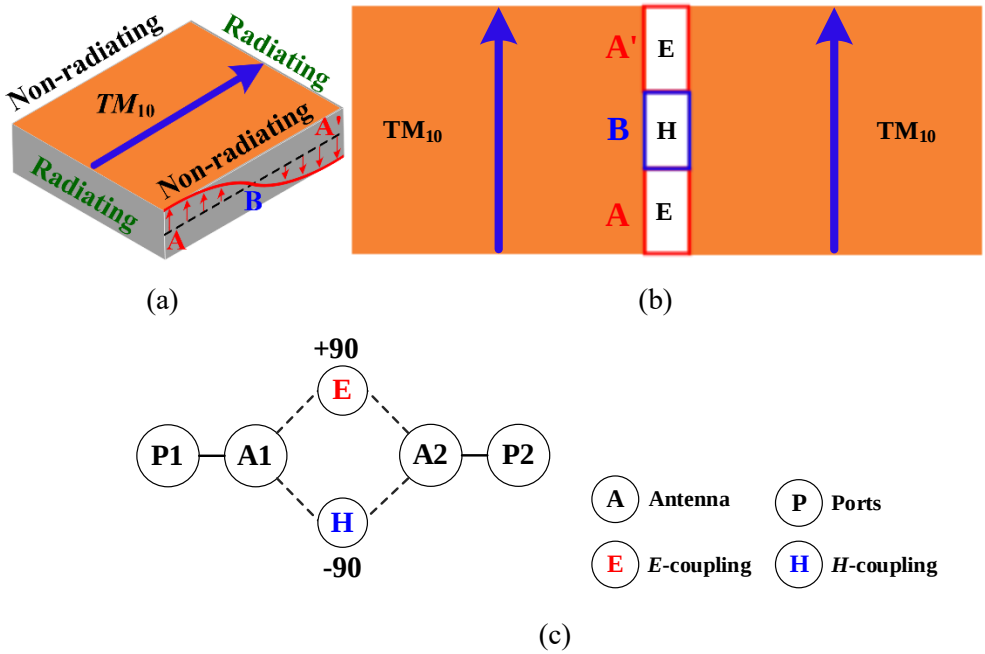

Fig. 5.7. (a) Electric field distribution under the patch for its fundamental TM_{10} mode, (b) coupling between two patch antennas through *E*- and *H*-fields. (c) coupling topology for the coupled patch antennas.

5.1.2.4 Parametric Studies

To provide a better understanding of the design philosophy behind the proposed decoupling technique, several key parameters are investigated in this section using HFSS. It is important to note that when studying one parameter, the remaining parameters are kept at the values specified in Fig. 5.2.

First, the most important parameter that affects the decoupling performance is the depth of the cut on the patch. The frequency responses for the dual-patch module with different cut depths are simulated and provided in Fig. 5.8. When there is no cut on the

patch, namely $w_c = 0$, the two patches are electrically coupled, resulting in a high transmission level between the antenna ports. According to the theory mentioned in [5], electric-coupled patches exhibit a TZ below the operating band.

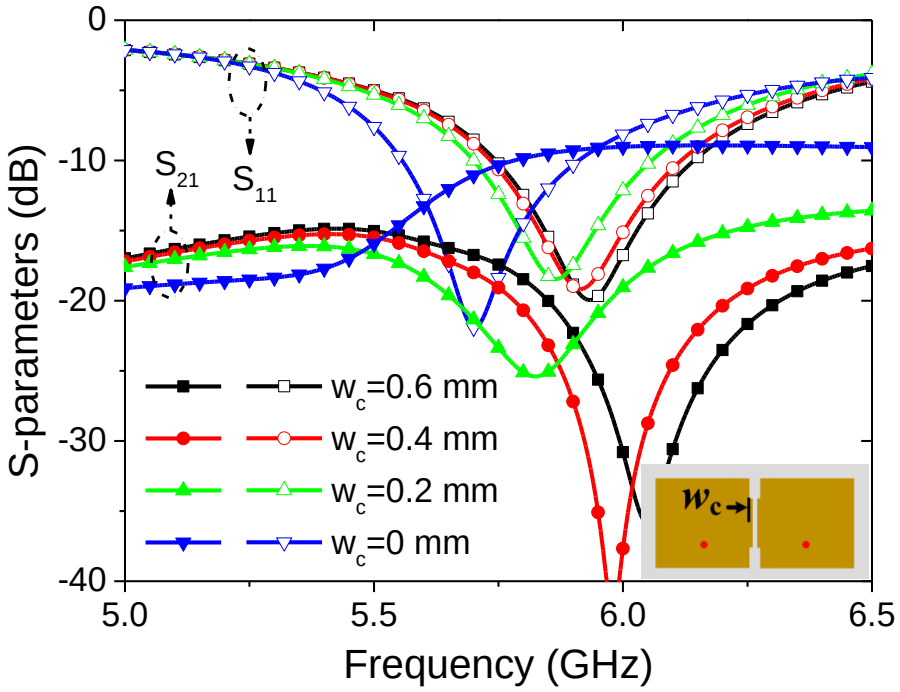

Fig. 5.8. Responses for the antennas with different cut depths.

As the edges of the patch are modified and the cut depth increases, the electric coupling decreases while the magnetic coupling becomes dominant. This leads to a gradual frequency shift of the TZ to higher frequencies. By carefully designing the cut depth, the transmission zero can be positioned near the resonances of the antennas, resulting in a deep null in the transmission coefficient and achieving high isolation.

Another factor affecting the coupling behaviour between two patches is the length of the cut on the patch (l_c). A parametric sweep is done on the cut length (l_c) with the simulated results provided in Fig. 5.9. The curves indicate that when the cut is very short ($l_c = 3$ mm), the transmission zero is located at a lower frequency band compared to the antenna's resonance frequency. As the cut length increases ($l_c = 5$ and 7 mm), the transmission zero shifts to higher frequencies. However, when the cut length exceeds

an even larger value (l_c = 9 mm), the transmission zero moves back to the lower frequency band.

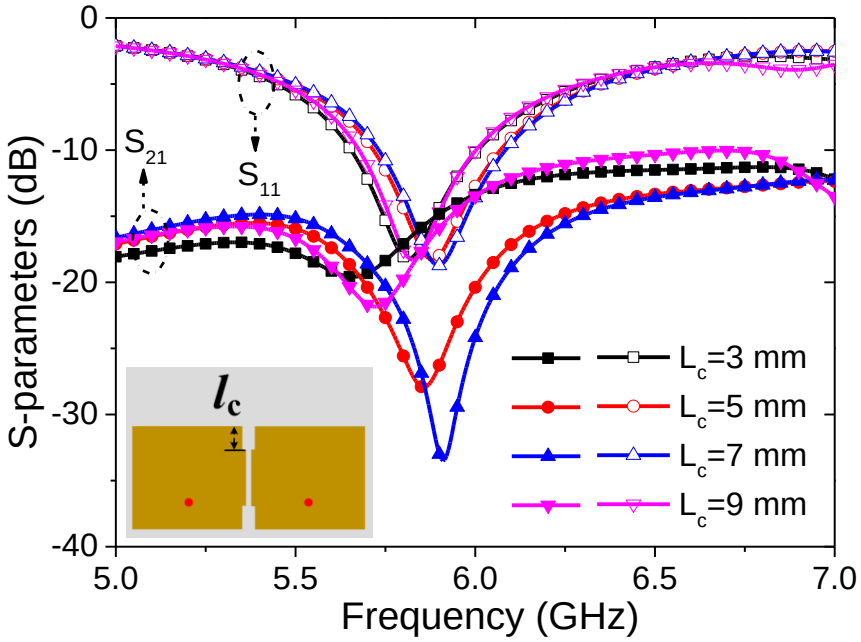

Fig. 5.9. Responses for the antennas with different cut lengths.

This phenomenon can be explained by studying the field distributions illustrated in Fig. 5.7. The electric field in regions A and A' is very high, so even a small variation in the cut length has a significant effect on the coupling strength related to the electric field. As the cut length increases, the electric field strength decreases, causing the transmission zero to shift to higher frequencies. However, when the cut reaches region B, further increasing the cut length weakens the *H*-coupling more than the *E*-coupling. Consequently, with a very long cut (l_c = 9 mm), the magnetic coupling may become smaller than the electric coupling again, leading to the dominance of the electric coupling mechanism. This results in the TZ moving back to the lower frequency band in terms of S-parameters. From this parametric study, an important design rule can be derived: the cut should be designed with an appropriate length. An excessively long cut can deteriorate the decoupling performance, so it is crucial to optimize the cut length to

achieve the desired coupling characteristics. According to the author's experience, a cut length smaller than one-third of the patch length is recommended.

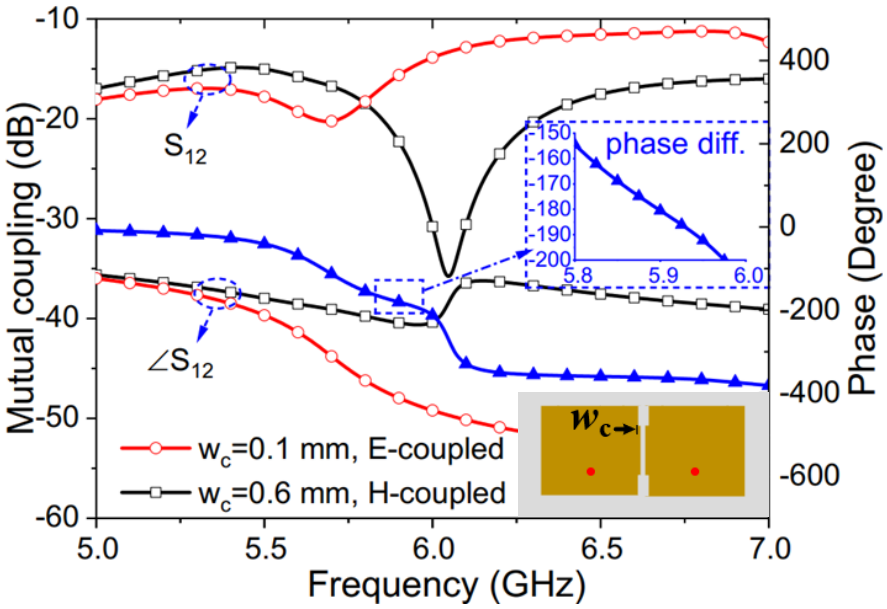

Fig. 5.10. Phase responses of the mutual couplings for *E*-coupled and *H*-coupled patches.

In addition to the previous studies, another important parametric study for the phase response of the mutual coupling is carried out to further reinforce the validity of the proposed decoupling concept. The results are presented in Fig. 5.10. Two cases are studied here. In the first case, where the electric coupling dominates, a shallow cut (red line with d_c = 0.1 mm) is implemented. Conversely, in the second case, the patches are magnetically coupled with a deeper cut (black line with d_c = 0.6 mm).

When the patches are electrically coupled, the TZ is at the lower frequency band. When the patches are magnetically coupled, the TZ is at the higher frequency band. The phase responses of the two cases exhibit distinct trends at the resonance frequency of the patch. Notably, the difference between the phases (phase diff.) is calculated and plotted. As can be seen, the phase difference between both cases approaches approximately 180° near the resonance frequency of the patch (5.9 GHz) where the perfect EMCC occurs. This phenomenon provides strong evidence that supports the proposed decoupling concept.

5.1.2.5 Field Distributions

To gain a deeper understanding of the proposed decoupling concept, the field distributions at the non-radiating edges, where the coupling occurs, are investigated. Specifically, the electric and magnetic field distributions are analyzed. Fig. 5.11 depicts the field magnitudes along a line between two patches for two different cases: one with unmodified patches (strongly coupled) and the other with decoupled patches.

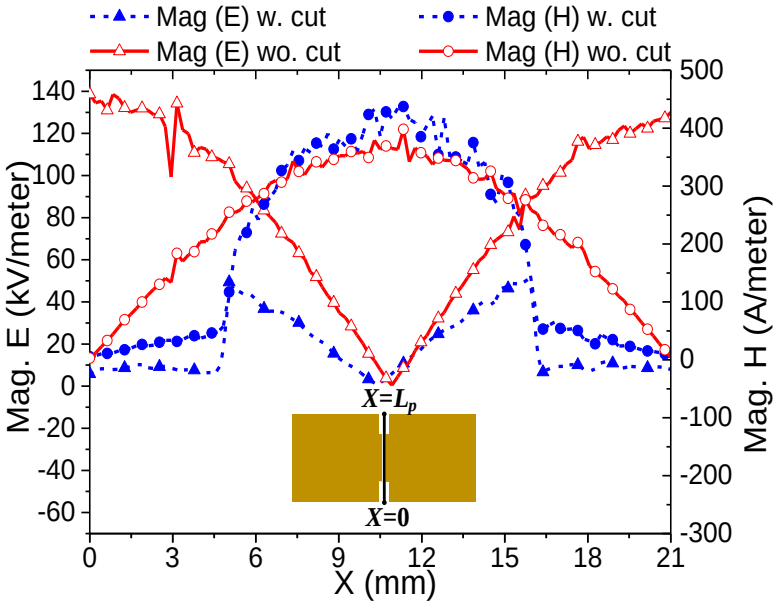

Fig. 5.11. Simulated *E* and *H* field distributions along the coupled edge.

In the case of strongly coupled patches without any modification, strong electric field density can be observed at the regions where X=0-4.5 mm and X=16.5-21 mm, which corresponds to the two open ends of the patches. When the patches' corners are cut, the field density at the open ends is significantly reduced. This reduction is more significant for the electric field because the *H*-field is inherently weak at the open ends. Since the fringing electric field at the non-radiating edges is weak, the magnitude of the electric field at these edges is significantly reduced when the mutual coupling is decreased, as shown in Fig. 5.11.

The field distributions depicted in Fig. 5.11 provide insight into the underlying physical reality of the proposed decoupling concept. The cuts at the ends of the non-

radiating edges have a stronger effect on the electric coupling, allowing for separate control of the electric and magnetic coupling.

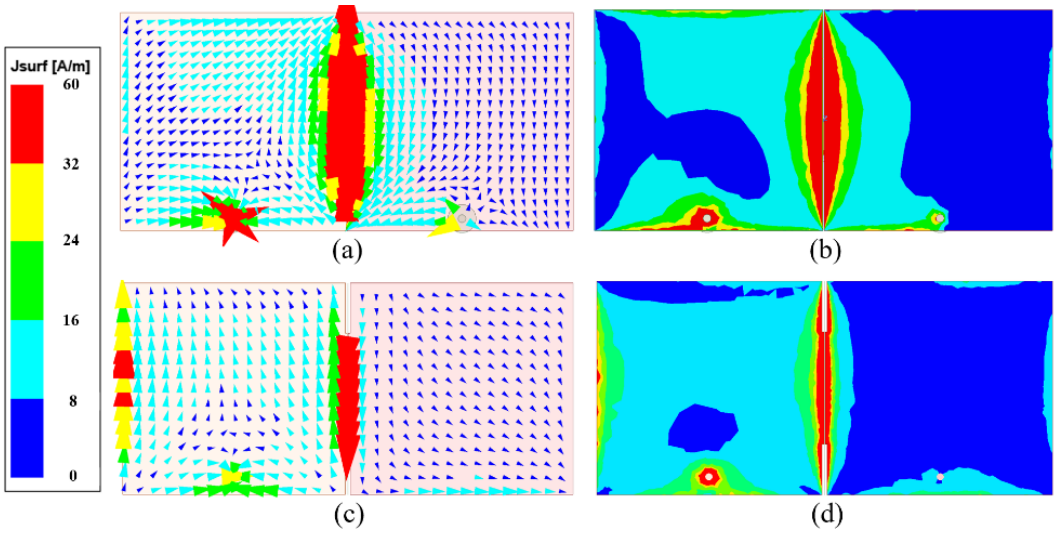

Fig. 5.12. Current distributions on the patches when the left-hand side patch is excited. (a) Vector plot for the coupled patches. (b) Magnitude plot for the coupled patches. (c) Vector plot for the decoupled patches. (d) Magnitude plot for the decoupled patches.

Current distributions on the patches are plotted in Fig. 5.12 with the left-hand side port excited. Strong current distributions can be observed on both patches when they are coupled as shown in Fig. 5.12(a) and Fig. 5.12(b). The current distributions indicate that the port excites both patches simultaneously because of the strong mutual coupling. After decoupling, only the non-radiating edges of the patches, where the coupling cancellation happens, show strong current distribution. This is not strange as this method does not block the coupling between two non-radiating edges. On the contrary, this phenomenon indicates that coupling cancellation happens here. Besides, the current in the other region of the coupled patch is weak, which means that the mutual coupling between the two antenna ports is small. The current distribution also indicates that only the left-hand side patch is activated when the corresponding port is excited. In addition, the symmetry of the TM_{01} mode on the excited patch is improved.

5.1.3 Supplementary Case Study

To further demonstrate the effectiveness of the proposed decoupling concept, an additional case study is presented in this section. This case explores the decoupling performance of the proposed technique for two closely positioned patches utilizing only a thin dielectric substrate. A 1.5-mm thick Roger 4003 substrate is used here. The configuration of the decoupled antennas is illustrated in Fig. 5.13(a).

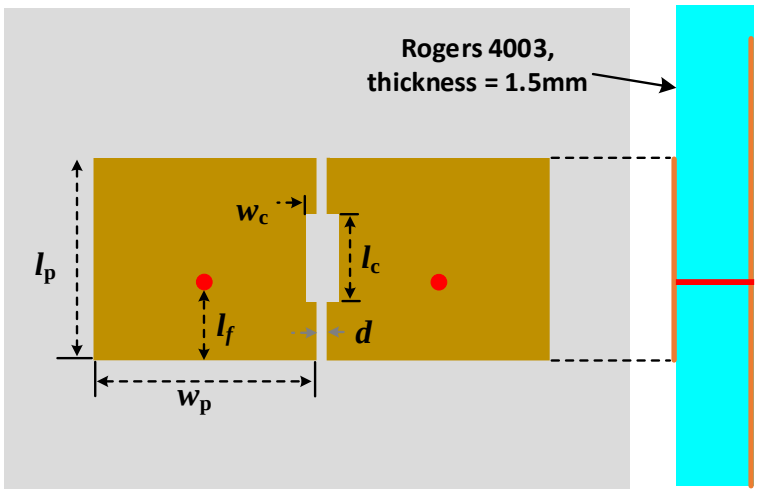

(a)

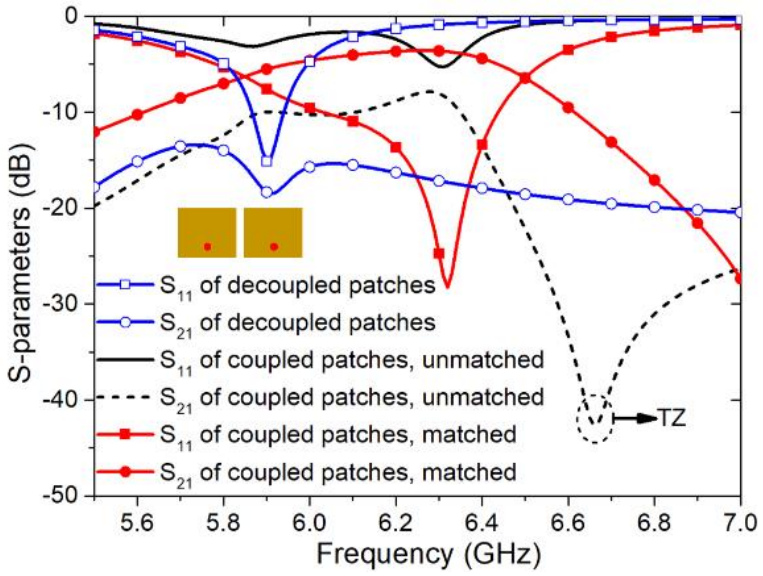

(b)

Fig. 5.13. Decoupled patch antennas without air substrate. (a) Structure of the decoupled patches. Dimensions in mm: l_f= 4.75, l_p= 12, l_c= 4.5, w_c = 0.72, w_p = 13, d = 0.1. (b) Simulated responses.

In this scenario, the mutual coupling between the two patches is predominantly governed by magnetic coupling. Original transmission zero is observed at the upper frequency range of the antennas' operating bands. Based on the theory introduced in previous sections, the weight of electric coupling should be increased to balance the magnetic coupling. To achieve this, grooves are incorporated by cutting the central region of the non-radiating edges of the patches. This modification is particularly effective due to the presence of a strong magnetic field in this region. Consequently, this alteration serves to reduce the magnetic coupling and facilitate electric and magnetic coupling cancellation.

The S-parameters of the decoupled patches are plotted in Fig. 5.13(b). The observed results indicate a notable enhancement in isolation between two patches, reaching 16.6 dB within the operational band where S_{11} < -10 dB. In the absence of any modifications to the patches, the considerable mutual coupling diminishes the impedance matching for both antennas, as illustrated in Fig. 5.13(b). It is important to note that although both ports can be optimized to achieve matching, the resulting structure would operate similarly to a bandpass filter with a very high mutual coupling up to -3.6 dB. In this scenario, the stronger the mutual coupling, the wider the bandwidth. The energy injected into one port will mainly be transferred to another port, instead of radiating to free space.

5.1.4 Four-element MIMO Array

The proposed EMCC decoupling concept can also be easily extended to the design of larger-scale MIMO arrays. For demonstration, a four-element MIMO array is designed with the same stack-up as the previous 2-element one. The structure of the four-element MIMO array is depicted in Fig. 5.14, where the four patches are positioned along their *H*-plane. Following the design concept introduced in section 7.3, the corners of the patches are all modified. Due to the asymmetric environment for the first antenna (ANT1) and fourth antenna (ANT4), these two antennas are designed with slightly different dimensions from the other two antennas at the outer sides (ANT2 and ANT3).

The dimensions of the structure are provided in Fig. 5.14. The antenna is fabricated and measured. Fig. 5.15 presents a photograph of the fabricated antenna.

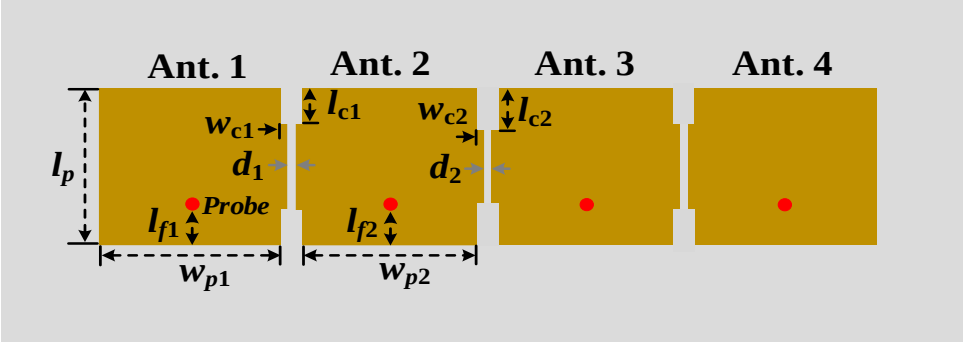

Fig. 5.14. Structure of the 4-element MIMO array. Dimensions in mm: l_{f1} = 1.05, l_{p1} = 20.4, l_{c1} = 4.65, l_{f2} = 0.6, l_{p2} = 20.4, l_{c2} = 5.65, w_{c1} = w_{c2} =0.12, w_{p1} = 23.9, w_{p2} = 26.1, d_1 = 0.85, d_2 = 1.45.

Fig. 5.15. Prototype of the proposed 4-element MIMO array.

The simulated and measured S-parameters of the four-element MIMO array are presented in Fig. 5.16. The measured -10 dB bandwidths for ANT1 and ANT2 are 5.78–6.1 GHz and 5.79-6.14 GHz, respectively, while the simulated results indicate bandwidths of 5.72–6.08 GHz and 5.74-6.09 GHz, respectively. Within their -10 dB bandwidths, the minimum isolation between these antennas is 19.3 dB. Specifically, the measured isolations between adjacent patches are 19.3 dB (S_{12}) and 20.1 dB (S_{23}), which correspond to simulated values of 19.1 dB and 19.5 dB, respectively. The isolations between non-adjacent patches are 25 dB (S_{13}) and 29 dB (S_{14}), with corresponding simulated values of 26 dB and 32 dB, respectively. In terms of the reflection coefficients, the simulation and measurement exhibit good agreement, despite minor differences in resonance frequencies that can be attributed to fabrication

errors. The isolation curves for adjacent elements (S_{12} and S_{23}) agree well. Some slight variations in the isolation curves for non-adjacent elements (S_{13} and S_{14}) can be attributed to the sensitivity of low-magnitude transmission coefficients to the surrounding environment in the measurement.

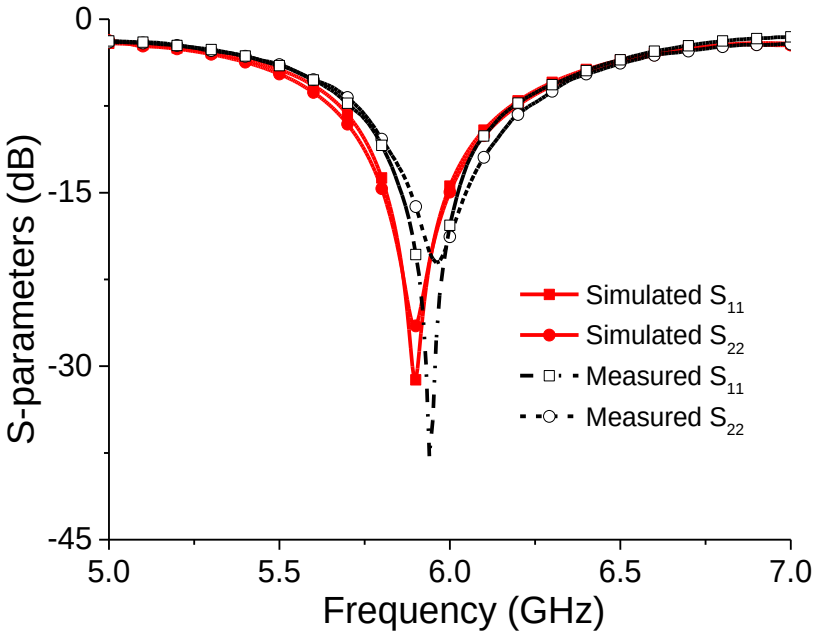

(a)

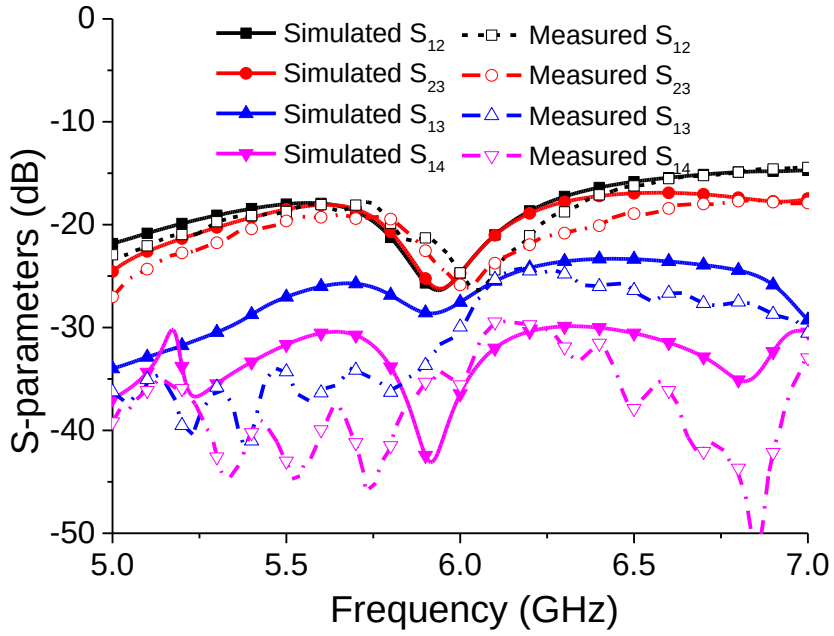

(b)

Fig. 5.16. Simulated and measured S-parameters for the 4-element MIMO array. (a) reflection coefficients. (b) isolations.

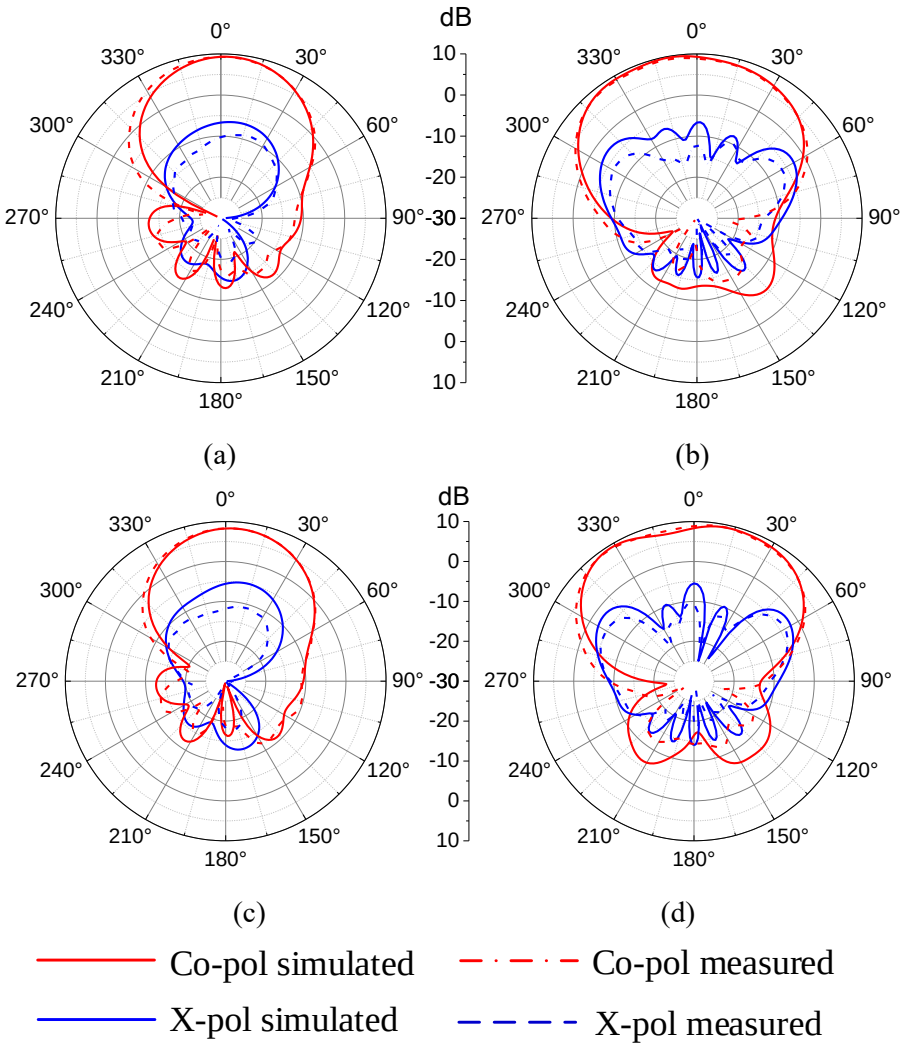

Fig. 5.17. Radiation patterns for the 4-element MIMO array in Fig. 5.15. (a) *E*-plane with ANT1 excited. (b) *H*-plane with ANT1 excited. (c) *E*-plane with ANT2 excited. (d) *H*-plane with ANT2 excited.

Simulated and measured radiation patterns of the fabricated 4-element MIMO are presented in Fig. 5.17. Two cases are measured here. Generally, broadside radiation patterns can be observed for both cases. Because no modification is introduced to the ground plane, the antennas show very low backside radiation. Besides, as only small changes are made to the geometry of the patches, good TM_{10} mode radiation is preserved for all the antennas. Thus, all these antennas show low cross-polarizations. More specifically, when ANT1 is activated whereas the other antennas are terminated with 50 Ω loads, the measured cross-polarization levels are 18.8 dB and 19 dB lower than the co-polarization for the *E*- and *H*-planes, respectively. For the ANT2, the cross-

polarization levels are lower than 19.4 dB and 19.6 dB in the broadside direction for the *E*- and *H*-planes, respectively.

5.1.5 Comparison and Discussion

Table 5-1. Comparison of the performance

Ref.	Decoupling Scheme & center frequency	Extra space	IAD (dB)	Isolation impro. (dB)	NoE	Edge-to-edge distance (λ_0)	BW (%)	Profile (λ_0)
[6]	Resonant slot on the ground @ 5.8 GHz	Yes	30	N.G.	2	0.031	1.7	N.G.
[7]	Slot on the ground @ 2.45 GHz	Yes	20	13.7	2	0.009	4.1	0.05
[8]	Stacked near-field resonators @ 2.45 GHz	Yes (Extra layer)	20/20	10	2/8	0.016/ 0.028	1.4/ 0.4	0.053
[9]	Co-planar resonator @ 3.16 GHz	Yes	18	11	2	0.02	1.43	0.02
[10]	Mixed modes @5.8 GHz	No	20	N.G.	2	0.12	2.9	0.039
[11]	Weak filed @3.5 GHz	No	30	6	2	0.18	N.G.	0.037
[12]	Higher-order mode operation @ 5.25 GHz	Yes	20.2/ 21.5	12	2 / 4	0.007 / 0.02	4/3.6	0.063
[13]	Structural parameter @ 5 GHz	No	24.6	7.4	2	0.033	6.6	0.054
[14]	Inductors @ 2.45 GHz	Yes (Dummy patches)	15.4/ 12.2	10.4/7.2	2/4	0.016	5.5/ 3.5	0.049
This work	Modified patches @ 5.9 GHz	NO	18.7	11.9	2	0.0018	7.4	0.065
			19.3	12.5	4	0.026	6	

N.G.: not given; IAD: Isolation after decoupling; NoE: Number of Elements; BW: Bandwidth

In Table 5-1, the performance of the proposed EMCC decoupling method is compared to other state-of-art decoupling techniques. First, the proposed decoupling technique shows the simplest structure without using any additional decoupling structure, additional layer, or increased antenna area. Some of these presented designs also suffer from the time-consuming design process. In contrast, the proposed EMCC method has an extremely simple design flow. From the parametric studies carried out, designers only need to pay attention to two key parameters during the decoupling process. Secondly, the proposed 2-element MIMO design achieves the smallest antenna separation, which is only 0.002 free-space wavelength. For the isolation level, the proposed technique ensures a general mutual coupling of up to 18.7 dB within the band of interest, with a minimum isolation improvement of 11.9 dB. Although the isolation performance in [6] is higher than this value, the decoupling method in [6] requires a long slot on the ground plane. Besides, the decoupling ability of this resonating slot is very sensitive to the ground size. These limitations make it unsuitable for applications where system ground plane integrity is important.

Furthermore, when compared to other self-decoupled patch antennas presented in previous works [10-12], the proposed technique exhibits the smallest edge-to-edge distance along with enhanced design flexibility. In contrast, the methods outlined in references [10-12] need specific patch-to-patch distances and predetermined structures. Similarly, the approach presented in reference [13] is constrained by limitations associated with the dielectric constant of the substrates and the inherent isolation levels. The proposed EMCC concept is also verified as effective for both 2-element and 4-element MIMO arrays. Regarding the specific design examples presented in this chapter, the proposed method shows the widest decoupling bandwidth compared to other presented works. Some decoupling techniques require resonating structures to accomplish reduced mutual coupling in the band of interest. Nevertheless, a resonant structure always shows frequency-relevant impedance characteristics, which means that these decoupling structures may only work well in a limited frequency range. This explains why some decoupled antennas show very narrow impedance bandwidths.

In summary, considering the size, fabrication complexity, decoupling ability, and antenna separation, the proposed technique provides a very attractive decoupling solution for small-separation multi-antenna systems.

5.2 Decoupled Patch Antennas Using Higher Order Modes

5.2.1 Transmission Line Model of Coupled Transmission Lines

Electromagnetic coupled microstrip TLs have been widely used in filter and coupler designs. The coupling behaviour of between two simple parallel coupled TLs has been intensively studied by many researchers [15, 16]. Depending on the coupling scheme, there are multiple different arrangements for this coupled TL structure, showing different filtering responses.

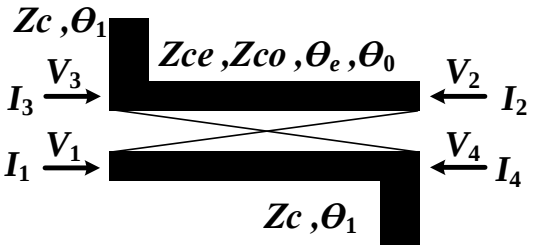

Fig. 5.18. General coupled microstrip TL.

Fig. 5.18 shows the equivalent circuit of terminal-loaded coupled transmission lines. It is composed of a parallel coupled transmission line section loaded with two open-end stubs, which are characterized by their even-mode and odd-mode impedance (Z_{ce}, Z_{co}) and corresponding electric lengths (θ_e, θ_o). This structure can be studied through the four-port network equation. For a conventional four-port network, the impedance equation of the coupled-line section can be written as

$$V_1 = Z_{11c}I_1 + Z_{12c}I_2 + Z_{13c}I_3 + Z_{14c}I_4 \tag{5.2}$$

$$V_2 = Z_{21c}I_1 + Z_{22c}I_2 + Z_{23c}I_3 + Z_{24c}I_4 \tag{5.3}$$

$$V_3 = Z_{31c}I_1 + Z_{32c}I_2 + Z_{33c}I_3 + Z_{34c}I_4 \tag{5.4}$$

$$V_4 = Z_{41c}I_1 + Z_{42c}I_2 + Z_{43c}I_3 + Z_{44c}I_4 \tag{5.5}$$

where $Z_{11c} = Z_{22c} = Z_{33c} = Z_{44c}$, $Z_{12c} = Z_{21c} = Z_{34c} = Z_{43c}$, $Z_{13c} = Z_{31c} = Z_{24c} = Z_{42c}$, and $Z_{14c} = Z_{41c} = Z_{23c} = Z_{32c}$. The four-port impedance parameters are given as

$$
\begin{aligned}
Z_{11c} &= -\frac{j}{2}(Z_{ce}\cot\theta_e + Z_{co}\cot\theta_o) \\
Z_{12c} &= -\frac{j}{2}(Z_{ce}\csc\theta_e - Z_{co}\csc\theta_o) \\
Z_{13c} &= -\frac{j}{2}(Z_{ce}\cot\theta_e - Z_{co}\cot\theta_o) \\
Z_{14c} &= -\frac{j}{2}(Z_{ce}\csc\theta_e + Z_{co}\csc\theta_o)
\end{aligned}
\tag{5.6}
$$

To make the analysis simple, a homogeneous medium is assumed. Thus, the even and odd mode phase velocities in the coupled line are the same ($\theta_e = \theta_o = \theta$).

In Fig. 5.18, port 3 and port 4 are terminated by two open-ended stubs whose impedance can be calculated from their length (θ_1) and characteristic impedance (Z_c) as

$$Z_L = -jZ_c\cot(\theta_1) \tag{5.7}$$

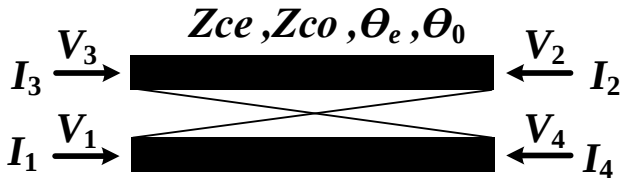

Fig. 5.19. Simplified coupled microstrip transmission line.

Consider a special frequency point where the length of the stub is a half wavelength. Thus, the loading impedance of these stubs will be infinity, and $I_3 = I_4 = 0$. Then, the structure in Fig. 5.18 will be degenerated to the model in Fig. 5.19. The transmission characteristics of this structure can be studied through its image impedance, which can be written as

$$Z_{i1} = \frac{\sqrt{(Z_{0e}-Z_{0o})^2 - (Z_{0e}+Z_{0o})^2\cos^2\theta}}{2\sin\theta} \tag{5.8}$$

This image impedance shows a bandpass filter response. When the coupled line length is a quarter wavelength, the structure shows a bandpass filter response. When the coupled TL length is half-wavelength, the structure shows a transmission zero [17].

Consequently, when both the stubs and coupled transmission lines have half wavelengths, the whole structure will show a transmission zero and no signal can be transmitted from one port to another.

5.2.2 Physical Model

A microstrip model of the proposed circuit is constructed for demonstration as shown in Fig. 5.20. The substrate used has a dielectric constant of 2.55, a loss tangent of 0.0027, and a thickness of 0.8. The structure is composed of two resonators. Part of the resonators are coupled together, forming a coupled transmission line (CTL) structure. The whole structure is gap-excited by a microstrip feedline.

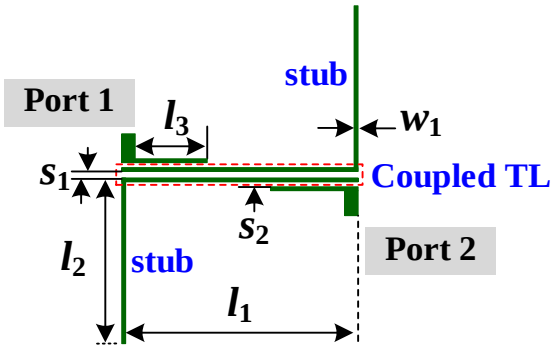

Fig. 5.20. Structure of a coupled TL with two open-end stubs. Dimensions in mm: $l_1 = 26$, $l_2 = 19.8$, $l_3 = 11$, $w_1 = 1$, $S_1 = 0.3$, $S_2 = 0.3$,

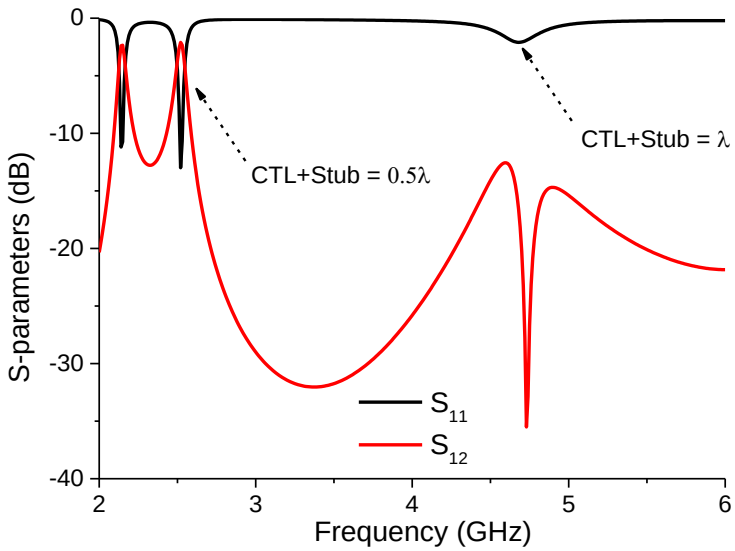

Fig. 5.21. Wideband response of the proposed test structure.

The response is shown in Fig. 5.21. When the total length of the resonator (CTL+stub) is about half-wavelength, two resonators are strongly coupled. The mutual coupling between two resonators shifts their natural resonances away from each other. In the filter theory, the further their distance the larger the coupling strength. In contrast, for the second resonance mode, where the total length of the resonator is one wavelength, the whole structure shows low mutual coupling. A TZ is observed near the resonance. This TZ prevents the energy from transmitting from one port to another. The energy is reflected back to the port, resulting in high reflection coefficients. In this scenario, the length of the CTL section is about half-wavelength whereas the lengths of the stubs are also about half wavelength, which agrees with the case that has investigated in 5.2.1.

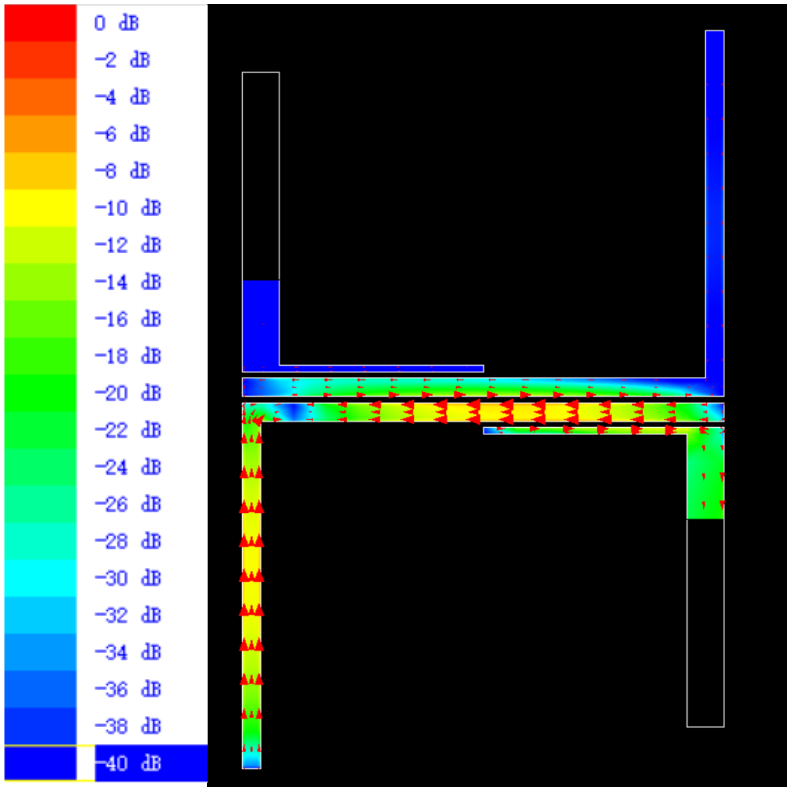

Fig. 5.22. Current distribution at the frequency of the TZ (4.73 GHz).

From this analysis, it is found that for a coupled transmission line structure terminated with two half-wavelength stubs, a transmission zero will arise at the same frequency as the first higher order mode, where the total length of the resonator is about one wavelength. This concept will be further extended to the decoupled antenna design in this chapter.

The current distribution at the TZ is plotted in Fig. 5.22. As can be seen, in the real microstrip structure, the length of the CTL and stubs are not precisely half-wavelength, due to the inhomogeneous medium for a microstrip structure. This unbalance will be more significant for an antenna structure with higher profile.

5.2.3 Decoupling for In-Band Operation

Many decoupling techniques can be found in the literature [8, 14, 18-21]. Through this study, almost all of them are concentrating on the decoupling between two fundamental TM_{10} modes because at this mode the patches' dimensions are of about

half-wavelength at their operating frequency. In this work, it is found that by making patch antennas operating over their higher order TM_{20} modes, the decoupling between them can be easily achieved by simply introducing an offset between them.

5.2.3.1 Basic Physical Structure

Inspired by the CTL theory, two patch antenna are coupled together to form a CTL-like structure. However, due to the radiation characteristic of patch resonators, the behaviour of such terminal-loaded coupled patch resonators is slightly different from the low-loss case in Fig. 5.20. Firstly, the medium of the patch resonator is inhomogeneous and an analytical solution for the impedance characteristics of such a lossy resonator is difficult. Secondly, the radiative loss of the patch resonator is much higher, thus the energy blocked by the TZ at the first higher order mode in Fig. 5.21 will be radiated, instead of reflected back to the ports. In addition, the patch radiator must be modified to ensure broadside radiation. Due to these differences, the behaviour of this radiative CTL structure is slightly different from the predicted responses of a lossless transmission line. However, in the next sections, we will see that this concept indeed can provide some guidance for antenna decoupling designs. The simulation and measurement will also prove that this CTL concept can also be applied to antenna decoupling designs.

Fig. 5.23 shows the structure of the dual-antenna system for demonstration in this chapter. It consists of two substrates which are all Rogers 4003 with a dielectric constant of 3.55, a loss tangent of 0.0027, and thickness of 0.813 mm. Between the substrates, a 2 mm air gap is introduced to improve the bandwidths and efficiencies of the antennas. Note that the technique described here provides a similar decoupling level when no air gap is present, and the antenna is lower in profile (e.g: total height of 0.813 mm). The radiators are placed on the top substrate's upper surface, and the common ground plane is located on the lower surface of the bottom substrate. Slotted stub-loaded patches are used as radiators. A classical probe-feeding structure is used for the excitations of these antennas. All the probes used in this work have a diameter of 0.7 mm.

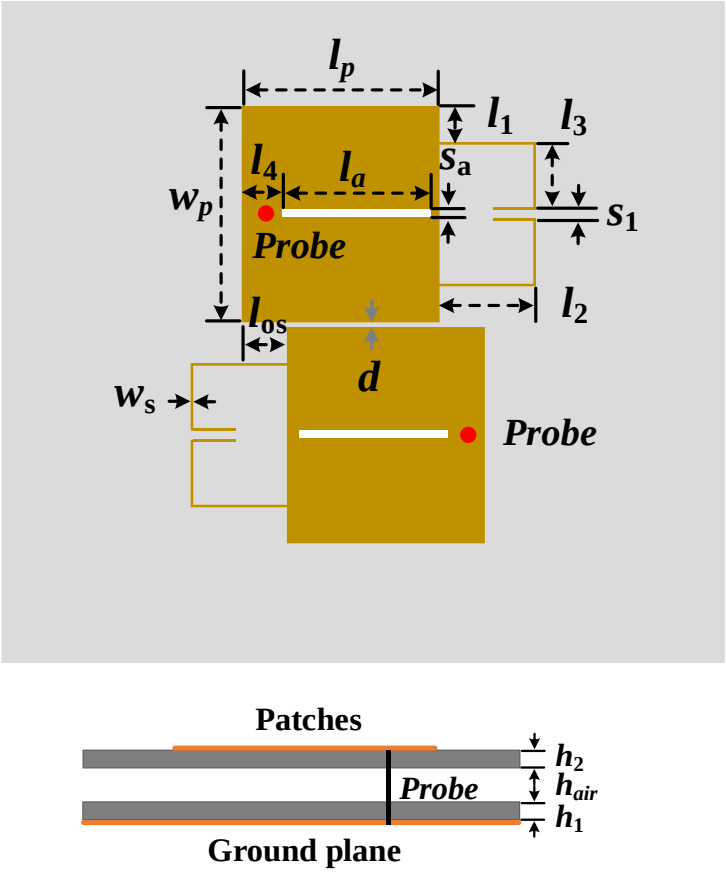

Fig. 5.23. Dimensions of the dual-antenna system (Unit: mm): l_1 = 3.8, l_2 = 6.65, l_3 = 7.7, l_4 = 3.375, l_{os} = 5.2, l_p = 22.15, w_s = 0.3, w_p = 23.2, S_a = 1, l_a = 18, d= 0.4, h_1 = 0.813, h_2 = 0.813, h_{air} = 2.

In contrast to previous works in the literature which study classical rectangular patches, stub-loaded patches are used here as the antenna elements. It is well-known that the fundamental TM_{10} mode of a rectangular patch shows half-wavelength standing wave distribution along its non-radiating edges as shown in Fig. 5.24(a). The in-phase fringe fields at their two radiating edges ensure a good broadside radiation characteristic. When two such antennas are placed very close to each other, the mutual coupling between these two antennas will be very strong, resulting in deteriorated radiation and impedance performances.

The original TM_{20} mode of a patch antenna has a radiation null in its broadside direction due to out-of-phase current distributions at its two radiating edges as shown in Fig. 5.24(b). In this work, to circumvent this problem, two open-ended stubs are loaded onto one of the radiating edges. This results in the reconfiguration of the field distribution beneath the patch, leading to in-phase current distributions at the open ends

and a shift in the frequency band of the TM_{20} mode as illustrated in Fig. 5.24(c). Besides, because the stubs are too narrow to radiate effectively, the TM_{20} mode demonstrates improved broadside radiation characteristic which is similar to the TM_{10} mode. This phenomenon can be observed in some other presented works [22], [23].

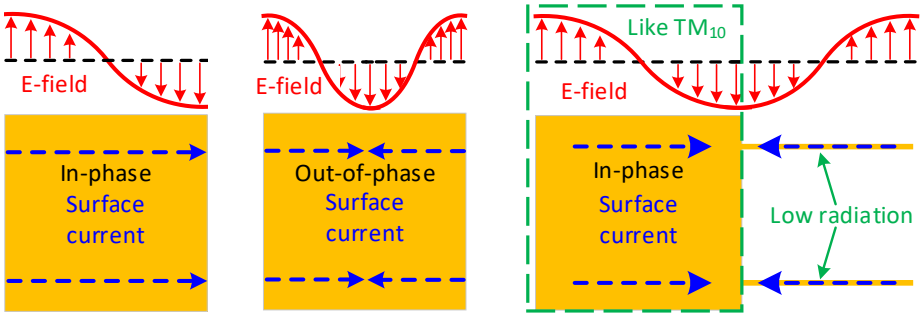

Fig. 5.24. E-field and surface current distributions. (a) TM_{10} mode and (b) TM_{20} mode of a conventional patch antenna. (c) TM_{20} mode of a stub-loaded patch antenna.

By increasing the length of the stub, the resonant frequency of the TM_{20} mode can be moved to the same frequency band as the original TM_{10} mode. Compared with other presented works in which shorter stubs are used, here the stub is longer such that the TM_{10} mode is suppressed by the band-reject response introduced by the open-ended stubs. If two such antennas are placed very close to each other, very high isolation can be achieved by simply introducing an offset along its non-radiating edges. This is described in the following sections.

5.2.3.2 Decoupling Mechanism (From the Field's Perspective)

To get an insight into the working mechanism of the proposed method, field distributions of the patch resonator are investigated. The field distributions on the patches are shown in Fig. 5.25. As can be seen, when two TM_{20} mode-based patch antennas are placed closely, the field distributions along the non-radiating edges, which is also the area where coupling occurs, can be divided into four regions. In regions *a* and *d*, the current vectors on both antennas are in phase, whereas in regions *b* and *c*, the currents are out of phase. By deliberately designing the offset along the polarization direction to control the weight of each region, the mutual coupling related to region *a*

will cancel the counterparts dominated by region *b*. A similar result can be found for regions *c* and *d*.

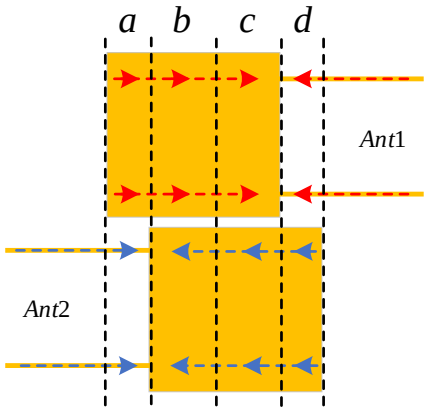

Fig. 5.25. Conceptual diagram for the current distributions for the dual-antenna system.

This decoupling process is similar to that in an even- and odd-mode cancellation process. Fig. 5.26 shows an even/odd-mode radiator pair. According to the theory presented in [14], such a radiator-pair show low mutual coupling due to the cancellation between the even- and odd-mode fields. Comparing the structure in Fig. 5.26 to that in Fig. 5.25, one can find that the radiating portions in regions *a* and *b* form an even- and odd-mode radiator pair. The weights of the in-phase and out-of-phase regions are controlled by the offset distance between two patches. Then mutual coupling can be suppressed dramatically by optimising the offset between these two antennas.

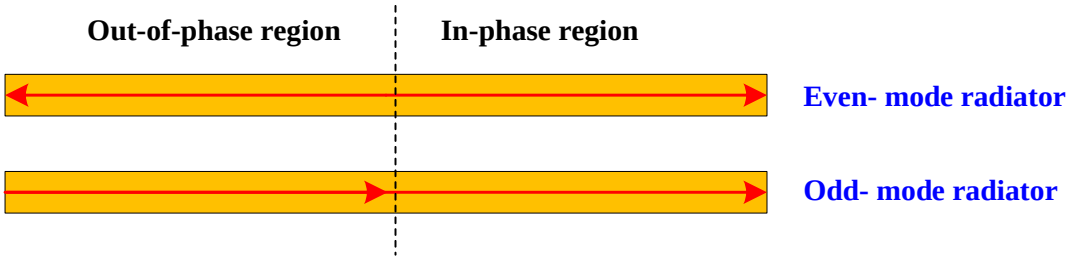

Fig. 5.26. Even- and odd-modes cancellation process.

A properly design offset will result in a similar response as the structure in Fig. 5.20. However, due to the radiative characteristics of the patch resonators, the energy reflected by the TZ is radiated. Thus, low reflection coefficients at both antennas can be obtained. To further understand the working mechanism of this method, some key parameters are

studied. To ensure a fair comparison, the other dimensions are all kept as the values given in Fig. 5.23 when one parameter is studied. The simulations are all carried out using HFSS.

The responses with different offsets (l_{os}) are plotted in Fig. 5.27(a). As the offset between two antennas increases, the null of mutual coupling shifts to the lower band. Regarding the frequency band of interest, the offset strongly affects the in-band mutual coupling level, which corresponds with the theoretical analysis. A slight frequency shift can also be observed when the offset changes because of the variation of the loading effect between two antennas. It can be observed that the null on the S_{21} can be controlled by adjusting the offset distance (l_{os}) between two patches. A properly designed offset can move the transmission null to the frequency band where the patch is resonant so that two antennas can be decoupled.

Once the location of the null is shifted to the desired location, good suppression can be achieved by optimising the weight of different regions as indicated in Fig. 5.25. As the contribution of regions *b* and *c* to the total mutual coupling is mainly decided by the distance between two antennas, another critical parameter which dominates the mutual coupling suppression is the location of the stub (l_1). The coupling strength related to the regions *a* and *d* in Fig. 5.25 is highly related to the distance between the stub of one antenna to the non-radiating edge of the other antenna. By adjusting the locations of the stubs, the mutual coupling dominated by regions *a* and *d* will neutralize the counterpart related to regions *b* and *c.* Fig. 5.27(b) shows the effect of the stub location on the mutual coupling. By varying the location of the stub, the depth of the null on S_{21} can be improved, so that higher isolation can be obtained. Together with Fig. 5.27(a), the mutual coupling between two patches can be decreased by adjusting the offset between patches (l_{os}) and the locations of the stubs (l_1). These two parameters are the key factors which have the strongest effect on the decoupling performance.

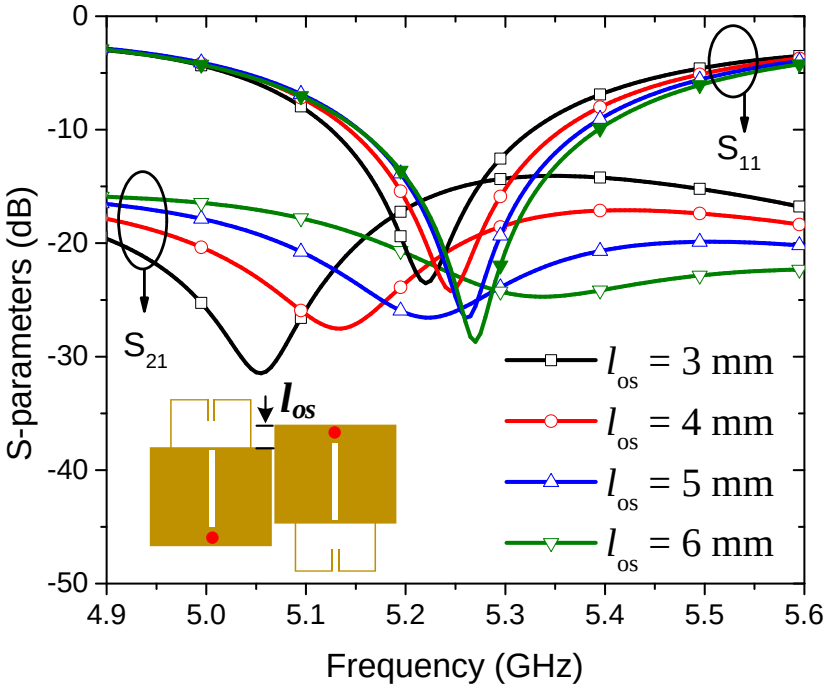
0
-10
-20
-30
-40
-50
S-parameters (dB)
4.9
5.0
5.1
5.2
5.3
5.4
5.5
5.6
Frequency (GHz)
S11
S21
los
los = 3 mm
los = 4 mm
los = 5 mm
los = 6 mm

(a)

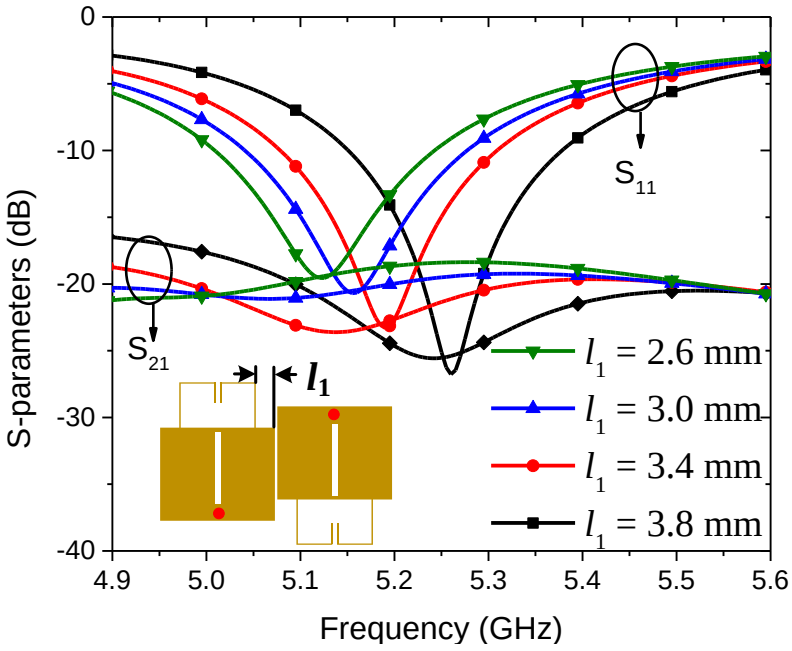
0
-10
-20
-30
-40
S-parameters (dB)
4.9
5.0
5.1
5.2
5.3
5.4
5.5
5.6
Frequency (GHz)
S11
S21
l1
l1 = 2.6 mm
l1 = 3.0 mm
l1 = 3.4 mm
l1 = 3.8 mm

(b)

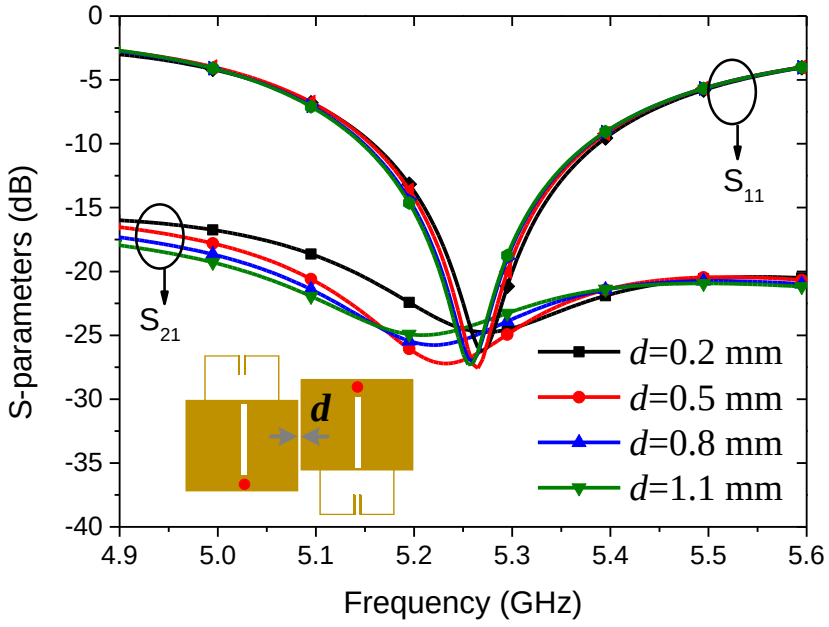

(c)

Fig. 5.27. Simulated S-parameters with different (a) Offsets (l_{os}), (b) Stub locations (l_1), and (c) Antenna distances (d).

One interesting fact that needs to be emphasized is that this decoupling method can handle the mutual coupling problem of extremely closely placed antennas. As shown in Fig. 5.27(c), the edge-to-edge distance between two antennas (d) is studied. According to the previous discussion, the mutual coupling is mainly decided by the alignment of the field, which is controlled by the offset between patches and cancellation of coupling, the final decoupling performance is not very sensitive to the distance between patches. Stable -20 dB mutual coupling can still be guaranteed when two antennas are placed very close to each other as shown in Fig. 5.27(c). When the patch separation is swept from 0.2 mm to 1.1 mm, the low mutual coupling is always maintained. The distance between two antennas can be even decreased, but a 0.5 mm distance is chosen for demonstration in this work after a compromise between performance and fabrication tolerance.

5.2.3.3 Case Studies

In this research, the stubs have been designed in a bent configuration to achieve a more compact size. However, straight stubs can lead to a further enhancement in the isolation performance. To demonstrate this, a design incorporating straight stubs has been developed and its parameters are provided in Fig. 5.28. The straight stubs provide an improvement of approximately 5 dB in the isolation performance in the relevant frequency range compared to the bent stub design. This is attributed to the fact that the electric field distribution of the straight stub design more closely aligns with the ideal scenario, as depicted in Fig. 5.24(c). Conversely, when the stubs are bent, the field distribution in the vicinity of the stubs becomes more complex, which can result in inevitable coupling between the open ends of the stubs and the adjacent patch. Therefore, there is a trade-off between the achieved isolation performance and the occupied circuit area.

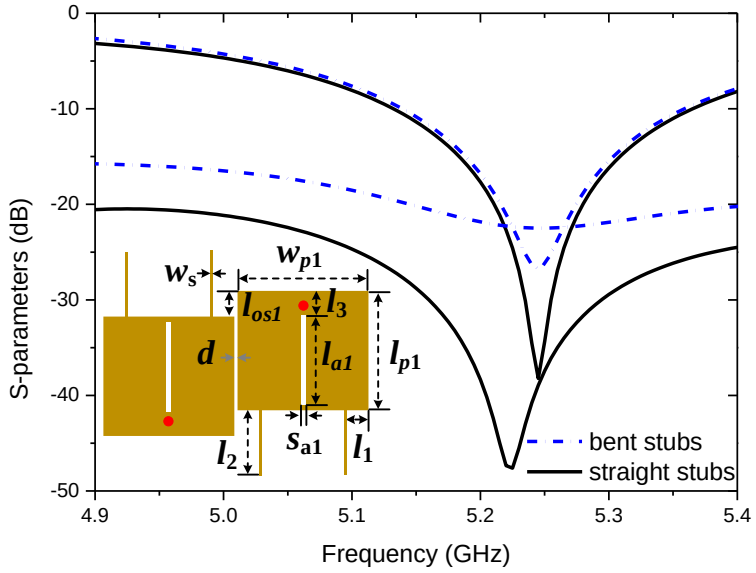

Fig. 5.28. Comparison of the S-parameters of the designs with bent (Fig. 5.23) and straight stubs. Dimensions of the antennas with straight stubs in mm: $l_1 = 4$, $l_2 = 16.15$, $l_3 = 3.375$, $l_{os1} = 5$, $l_{p1} = 22.2$, $w_s = 0.3$, $w_{p1} = 23.2$, $S_{a1} = 1$, $l_{a1} = 18$, $d = 0.4$, $h_1 = 0.813$, $h_2 = 0.813$, $h_{air} = 2$.

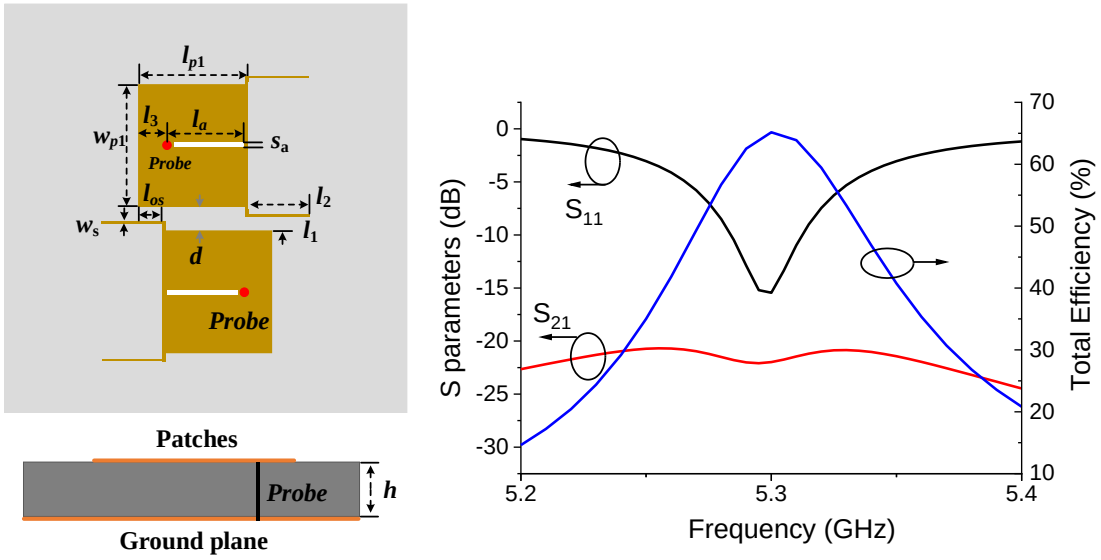

(a) (b)

Fig. 5.29. Dimensions of the low-profile dual-antenna system (Unit: mm): $l_1 = 0.35$, $l_2 = 20.33$, $l_3 = 5.79$, $l_{os} = 4.5$, $l_p = 13.58$, $w_s = 0.5$, $w_p = 10$, $S_a = 0.5$, $l_a = 6$, $d = 1.5$, $h = 0.813$.

This structure is also suitable for a low-profile design. Fig. 5.29(a) shows the structure where the air gap has been removed and the height has been reduced to 0.813 mm (low-profile). The structure is simulated in HFSS. The stubs have been optimized accordingly. When a thin substrate is used, we found that the stubs should be designed to be closer to the other patch to increase the coupling strength dominated by regions *a* and *d*, as illustrated in Fig. 5.25. The performance of the antenna is given in Fig. 5.29(b). The simulated impedance bandwidth is 5.28-5.31 GHz. The isolation between two antennas is higher than 20.9 dB in the simulation. The maximum total efficiency of the antenna is 65%.

5.2.3.4 Cross-Polarization Suppression

In this section, the effect of the slots on the patches will be introduced. The simulated surface current distributions on the patches at the resonant frequency are shown in Fig. 5.30(a) when there are no slots etched on the patches. In the simulation, only the left-hand side antenna is excited. The current distributions indicate that the TM_{20} mode of the patch is excited by the probe. The out-of-phase current portion is shifted to the loading stubs. The narrow stubs contribute little to the radiation and

current distribution on the dominating patch, similar to that of a classical TM_{10} mode. Besides, it can be observed that the current on the stub is stronger than the current on the main radiating patch. This asymmetric current distribution characteristic indicates that the stubs have a more substantial effect on the mutual coupling. As a result, regions *a* and *d* should be smaller than regions *b* and *c* to compensate for this effect.

The properly designed offset between two closely placed antennas makes them well-isolated. Only an extremely weak current can be found on the antenna on the right-hand side. However, when the excitation phase angle of the driven antenna is 90°, it is found that the current vectors on the right-hand side patch show components in the *y* direction. This current will increase the cross-polarization as shown in Fig. 5.30(a). The emergence of the *y* component of the current on the other antenna is a result of the excitation of its TM_{01}. As illustrated in Fig. 5.31, because of the offset between the two patches, the in-phase electrical field in region *B* will couple to the second patch and activate its TM_{01} mode. Thus, the activated TM_{01} mode of the second patch will radiate with polarization in the *y*-direction. To mitigate this effect, a long narrow slot is cut at the centre of the patch along with the direction of the polarization of the TM_{20} mode.

Fig. 5.30(b) shows the current distributions on the patches with slots. The incorporation of a long slot leads to a shift in the resonant frequency of the TM_{01} mode to a lower frequency band. Compared with the current distribution in Fig. 5.30(a), it can be observed that the slots have little effect on the original current behaviour of the driven patch as the slot is etched in the same direction as the current of the TM_{20} mode. However, it can be observed that the current vectors in the *y*-direction on the coupled patch are effectively suppressed.

The comparison of S-parameters for the cases with and without loading slots is presented in Fig. 5.30(c). A reference design featuring conventional rectangular patches operating over the first fundamental modes has also been evaluated. The inter-patch distance and offset have been kept constant across all cases. The proposed technique demonstrates a significant improvement in isolation performance, with a 12 dB increase

relative to the reference design utilizing classic patch antennas. Moreover, the loading slots exhibit a minimal impact on the S-parameters of the antenna module, which is consistent with the previous current studies. It is noteworthy to mention that the reference design, which operates over the TM_{10} modes, exhibits a wider impedance bandwidth. This can be attributed to the higher-order modes' higher quality factors compared to the first fundamental mode. Further investigation on the bandwidth improvement of a TM_{20} mode patch antenna will be carried out in future studies.

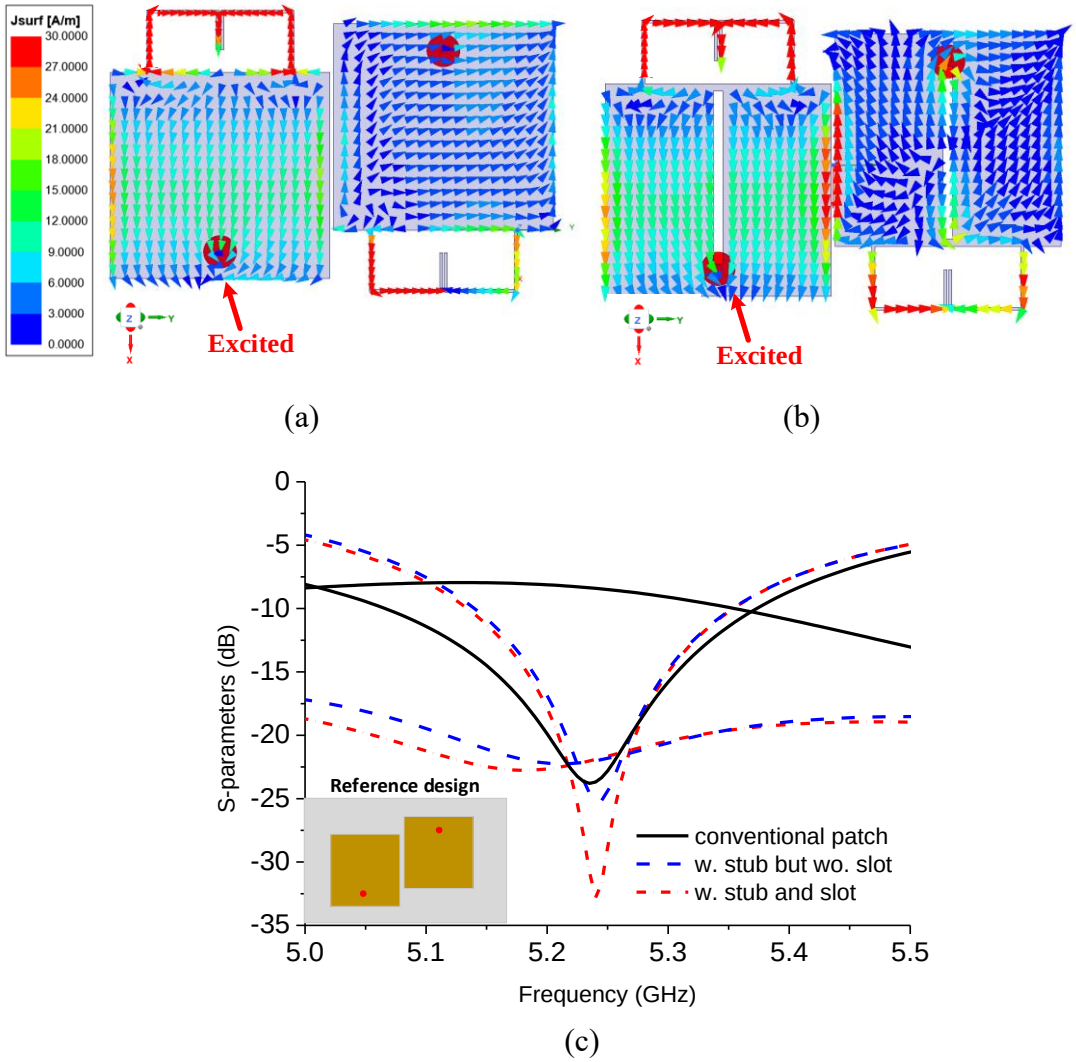

Fig. 5.30. (a) Surface current distributions on the patches without slots. (b) Surface current distributions on the patches with slots. (c) Simulated S-parameters for three different cases.

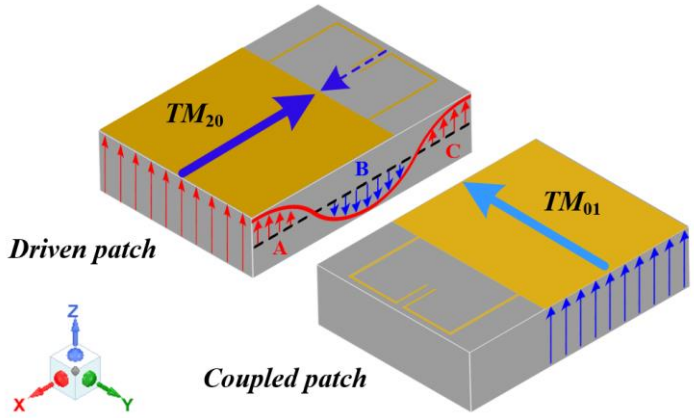

Fig. 5.31. Illustration for the field distributions of different modes.

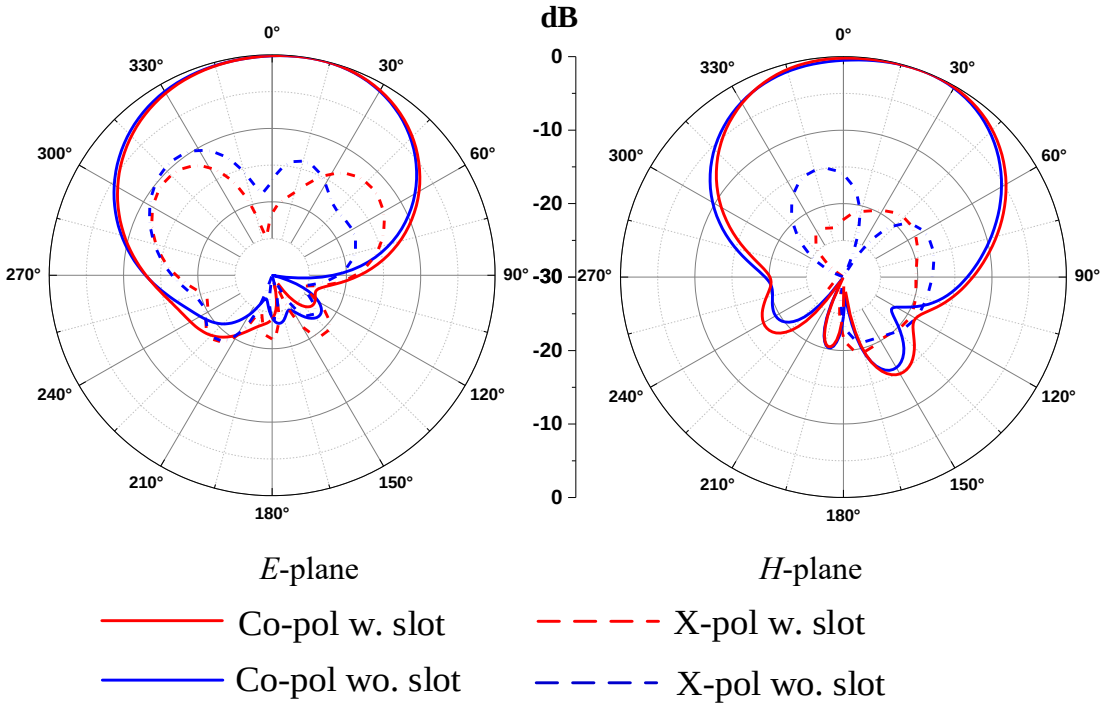

Fig. 5.32. Comparison of radiation patterns for antennas with/without loading slots.

With these loading slots, the radiation from TM_{01} mode can be decreased. Hence the cross-polarization which results from TM_{01} mode can be decreased too. Fig. 5.32 compares the radiation patterns for the antennas with and without slots. Benefiting from the loading slots, the cross-polarization levels in the broadside direction are decreased by about 5 dB for the *H*-plane, which is about 6 dB for the *E*-plane.

5.2.3.5 Measurement of 2-element MIMO

To verify the concept, a prototype is fabricated and measured. The S-parameters are plotted in Fig. 5.33(a). A photograph of the fabricated antenna is also inset in Fig. 5.33(a). Very good in-band performance regarding impedance matching and bandwidths is observed. More specifically, the measured -10 dB impedance bandwidth is 5.14-5.35 GHz. Isolation between two antennas is higher than 20 dB across the operating band.

With the mismatch loss considered, the measured radiation performance is plotted in Fig. 5.33(b). The measured total efficiency is higher than 84% in the band of interest. The measured realized gain at the broadside direction is 6.98 dBi at 5.25 GHz, which is 7.24 dBi for the simulation. The reasonable discrepancy between simulated and measured results can be attributed to fabrication tolerance and measurement errors.

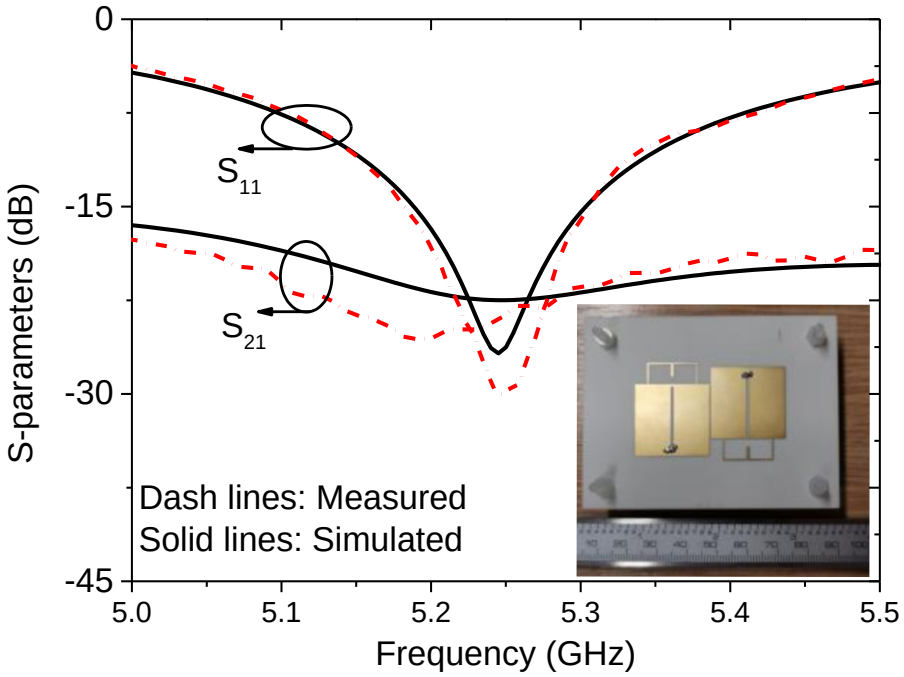

(a)

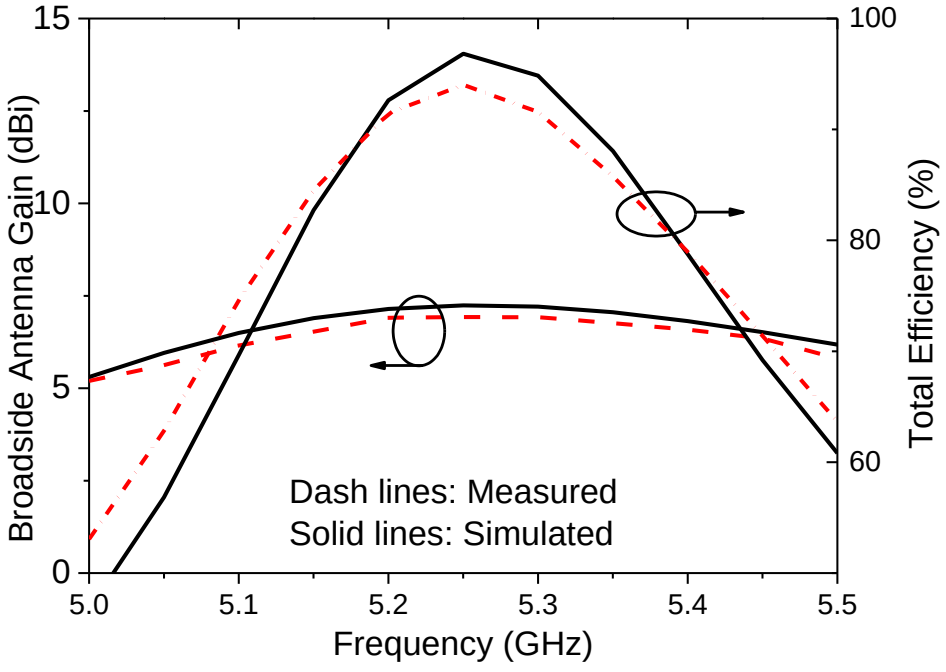

(b)

Fig. 5.33. Simulated and measured (a) S-parameters and (b) radiation performance for the dual-antenna system [12]

5.2.3.6 Four-Element MIMO Array

In this section, two potential application prospects for the proposed decoupling method will be introduced with two design examples. Firstly, based on the results in the previous section, this dual-antenna system can be easily scaled to a multi-antenna MIMO system. In Fig. 5.34, a four-element MIMO antenna is illustrated for the demonstration of the potential of this method in MIMO applications. As can be observed, four antenna elements are placed extremely close to each other. The structure is rotationally symmetric, which means the geometry of ANT1 is the same as ANT4 and the geometry of ANT2 is the same the ANT3. Compared with ANT1, ANT2 is coupled with ANT1 and ANT3 simultaneously. Thus, there are some minor discrepancies in their sizes.

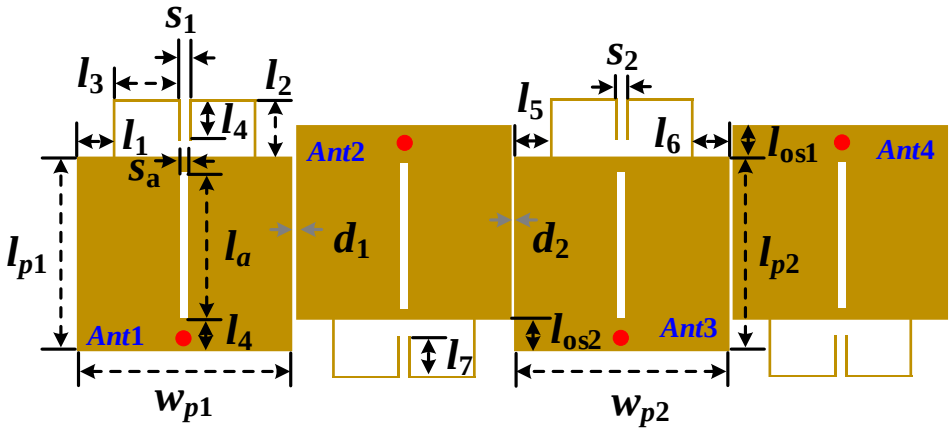

Fig. 5.34. Dimensions of the 4×4 MIMO array (Unit: mm): l_1 = 4.85, l_2 = 5.85, l_3 = 5.3, l_4 =4.05, l_5 = 2.45, l_6 = 3.45, l_7 = 3.55, l_{os1} = 6, l_{os2} = 5.75, l_{p1} = 22.1, l_{p2} = 22.85, w_s = 0.3, w_{p1} = 22.4, w_{p2} = 21.8, S_a = 0.7, S_1 = 4.3, S_2 = 5.3, l_a = 16, d_1= 1.4, d_2= 0.5.

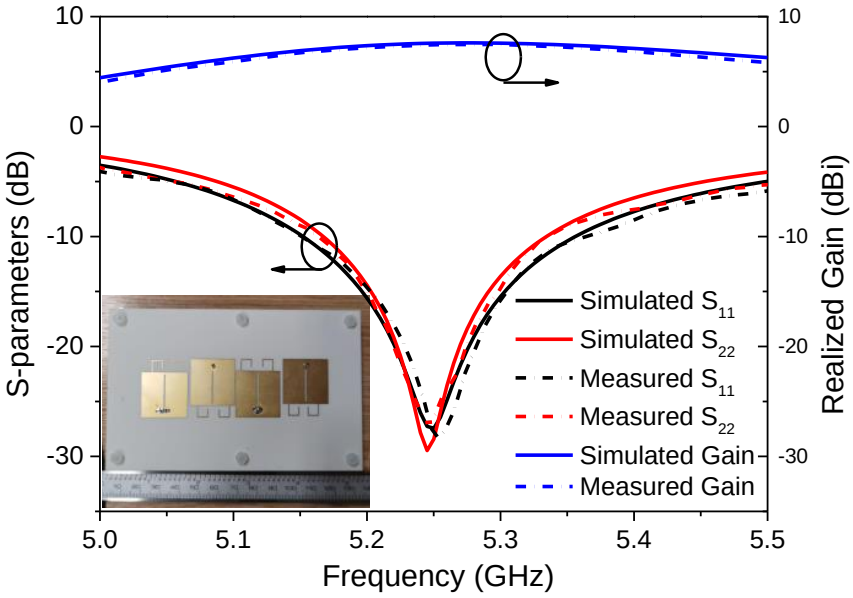

(a)

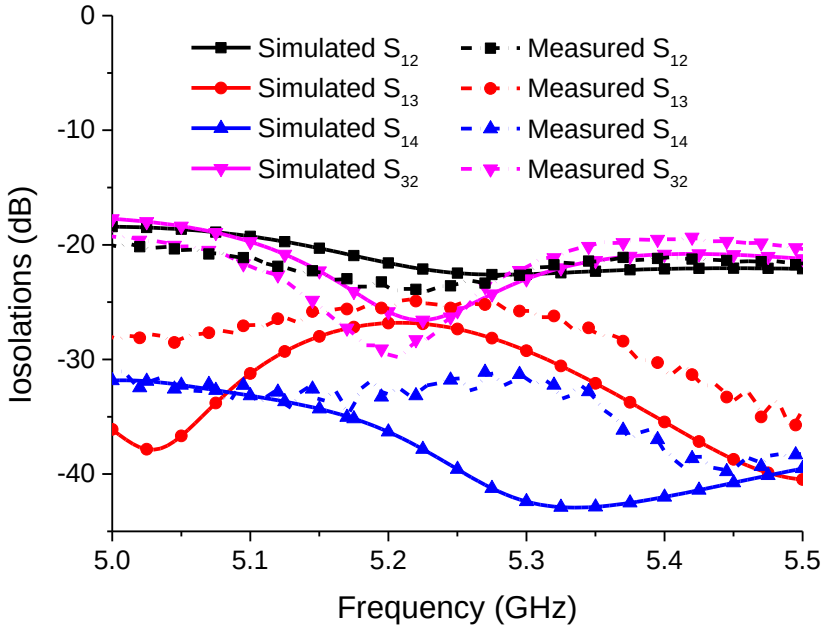

(b)

Fig. 5.35. Simulated and measured performance for the MIMO array [12]. (a) Reflection coefficients and broadside gain. (b) Isolations.

The simulated and measured S-parameters of the fabricated MIMO array are given in Fig. 5.35, together with an inserted photograph of the antennas. The measured decoupled bandwidth, with S_{11} and S_{22} < -10 dB and S_{12} < -20 dB, is 5.15-5.34 GHz. The measured realized gain at the broadside direction is 7.45 dBi at 5.25 GHz, which is 7.58 dBi for the simulation.

The radiation patterns for the MIMO array at 5.25 GHz in the *E*- and *H*-planes are plotted in Fig. 5.36. Benefiting from the loading slots, the measured ratio between the co-polarization to cross-polarization is higher than 25 dB in the broadside direction. The measured 3 dB beamwidth for *E*- and *H*-planes are 84° and 87°, respectively.

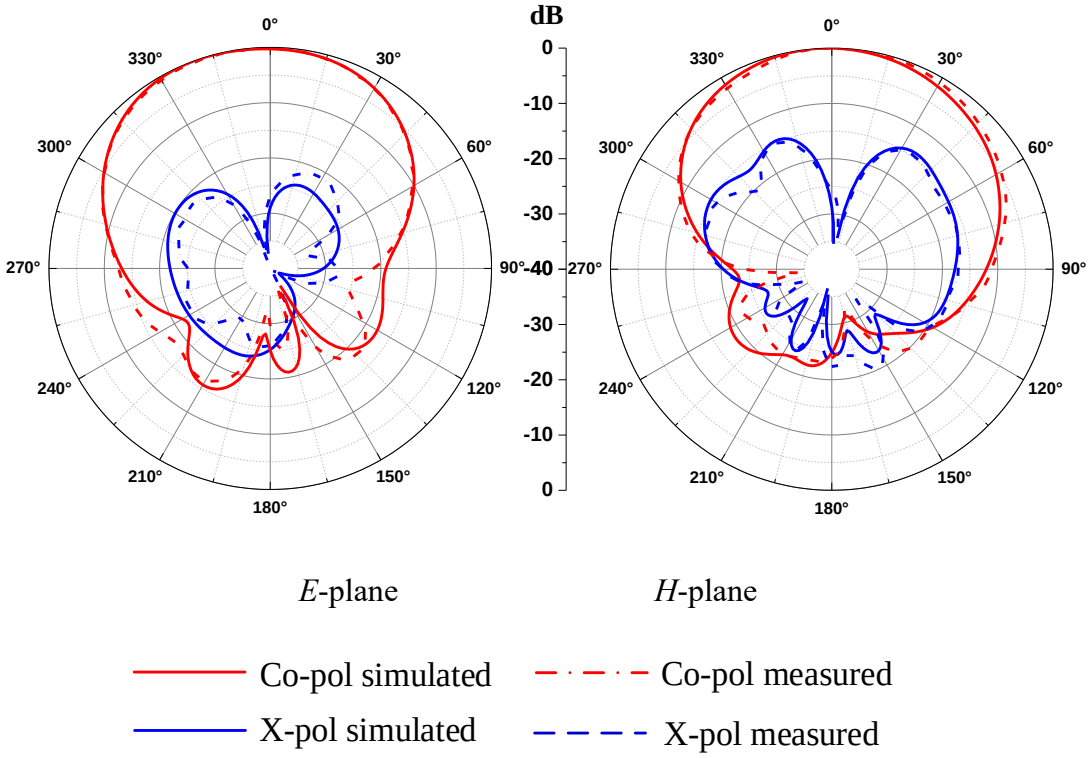

Fig. 5.36. Simulated and measured radiation patterns of the 4-element MIMO array [12].

5.2.4 Adjacent-Band Decoupling

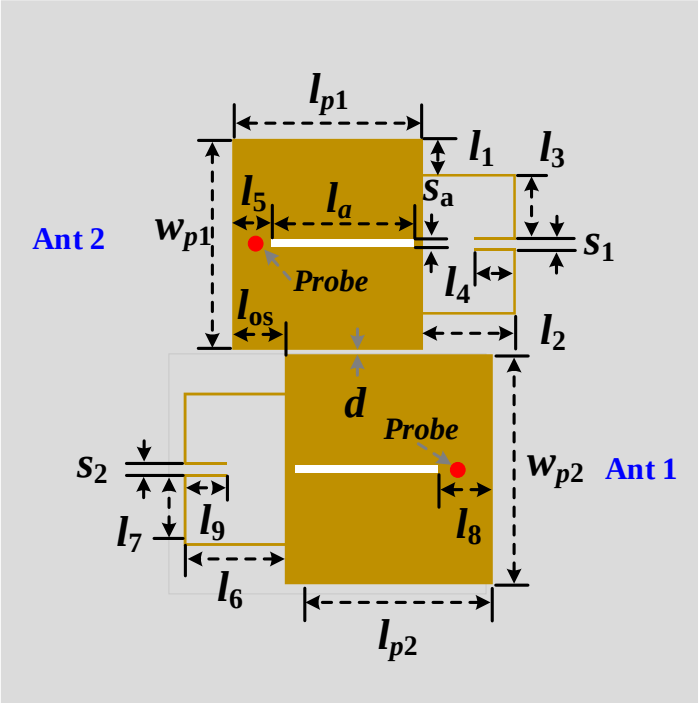

Fig. 5.37. Structure of the dual-antenna module with different operating bands. Dimensions in mm: $l_1 = 3.8$, $l_2 = 6.675$, $l_3 = 7.4$, $l_4 = 3.725$, $l_5 = 3.2$, $l_6 = 6.675$, $l_7 = 7.4$, $l_8 = 4$, $l_9 = 4.425$, $l_{os} = 5.4$, $l_{p1} = 21.8$, $l_{p2} = 23.4$, $w_s = 0.3$, $w_p = 24.1$, $w_p = 26.1$, $S_a = 1$, $l_a = 18$, $d = 0.7$.

Another promising prospect of this method is that it can be applied for decoupling two antennas operating for two adjacent bands. In modern customer premises equipment, multiple standards should be simultaneously satisfied for WiFi and mobile communication. With all these antennas placed in a limited space, to make sure that the transmitted signal from one channel will not be received by the receiving channel of the other channel, the isolation between these antennas should be high enough, especially for two antennas operating over adjacent bands with very small guard band. As analysed earlier, the decoupling mechanism of this method is achieved by designing coupling portions between antennas. One of its advantages is that it is still effective when both antennas operate at different frequency bands.

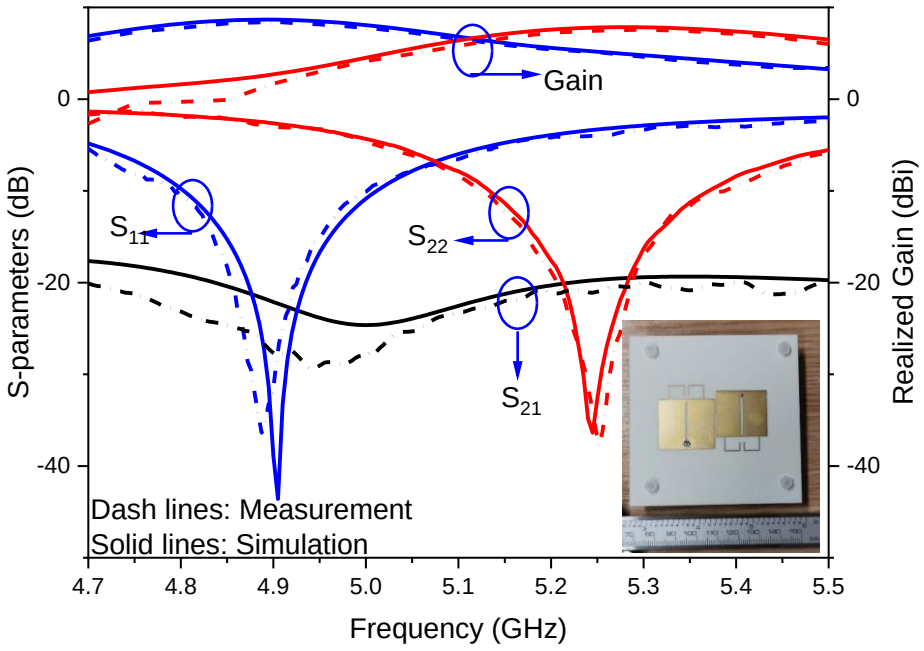

Fig. 5.38. Simulated and measured S-parameters and gain for the adjacent band operation design [12].

For demonstration, another design is developed based on the method presented in this work. The geometry of this dual-antenna system is shown in Fig. 5.37. ANT1 operates for the lower band, while ANT2 works for the higher band. Following the design guides introduced in section 5.2.3, the two antennas can be decoupled using the same method. The distance between two antennas is 0.7 mm in this case. The antennas were fabricated and measured with measured results plotted in Fig. 5.38.

The measured -10 dB bandwidths for both antennas are 4.79-5.0 GHz and 5.13-5.37 GHz, respectively. The measured isolation in the band of interest is higher than 20 dB. The measured broadside gains for both antennas are 8.42 dBi and 7.84 dBi, respectively. It should be noted here when two antennas are with different dimensions, the maximum gain will not arise at the $+z$ direction because of the asymmetric module structure. This scenario studies the case for two antennas operating for 5G band N79 (4400-5000 MHz) and 5 GHz WiFi band (5150-5925 MHz). Although the antennas in this case only cover part of these frequency bands, this design is still a good example that demonstrates the adjacent-band decoupling ability of the proposed method.

5.3 Summary

This chapter presents two novel decoupling solutions for patch antennas positioned in extreme proximity. The EMCC technique eliminates the need for additional decoupling structures or layers by introducing very simple modifications to the patch structure itself. The effectiveness of the concept is demonstrated through the design and analysis of both 2-element and 4-element MIMO arrays. Comparative evaluations against existing state-of-the-art decoupling techniques highlight several advantages of the proposed method, including its simplicity in structure, cost-effectiveness, and suitability for applications requiring minimal antenna separation.

The higher-order modes patch antennas are used to achieve self-decoupled antenna arrays. With an extremely small antenna distance, patch antennas have been decoupled to – 20 dB with no extra decoupling process. In addition to 2-element and 4-element MIMO arrays, this technique is also verified with two patch antennas operating over different bands.

In summary, the proposed decoupling solutions offer promising low-cost approaches to address the mutual coupling challenges for closely placed patch antennas.

5.4 References

[1] J. Hong, "Coupling of asynchronously tuned coupled microwave resonators," *Proc. Inst. Elect. Eng.,* vol. 147, no. 5, pp. 354-358, Oct. 2000.

[2] J. B. Thomas, "Cross-coupling in coaxial cavity filters-A tutorial overview," *IEEE Transactions on Microwave Theory and Techniques,* vol. 51, no. 4, pp. 1368-1376, 2003.

[3] H. King, "Mutual impedance of unequal length antennas in echelon," *IRE Transactions on Antennas and Propagation,* vol. 5, no. 3, pp. 306-313, July 1957.

[4] N. Alexopoulos, and I. Rana, "Mutual impedance computation between printed dipoles," *IEEE Transactions on Antennas and Propagation,* vol. 29, no. 1, pp. 106-111, Jan. 1981.

[5] J.-F. Qian *et al.*, "A novel electric and magnetic gap-coupled broadband patch antenna with improved selectivity and its application in MIMO system," *IEEE Transactions on Antennas and Propagation,* vol. 66, no. 10, pp. 5625-5629, 2018.

[6] J. OuYang, F. Yang, and Z. M. Wang, "Reducing mutual coupling of closely spaced microstrip MIMO antennas for wlan application," *IEEE Antennas and Wireless Propagation Letters,* vol. 10, pp. 310-313, 2011.

[7] S. Zhang *et al.*, “Mutual coupling reduction of two pifas with a t-shape slot impedance transformer for MIMO mobile terminals,” *IEEE Transactions on Antennas and Propagation,* vol. 60, no. 3, pp. 1521-1531, 2012.

[8] M. Li, B. G. Zhong, and S. W. Cheung, “Isolation enhancement for MIMO patch antennas using near-field resonators as coupling-mode transducers,” *IEEE Transactions on Antennas and Propagation,* vol. 67, no. 2, pp. 755-764, 2019.

[9] T. Pei, L. Zhu, J. Wang, and W. Wu, “A low-profile decoupling structure for mutual coupling suppression in MIMO patch antenna,” *IEEE Transactions on Antennas and Propagation,* vol. 69, no. 10, pp. 6145-6153, 2021.

[10] Q. X. Lai, Y. M. Pan, S. Y. Zheng, and W. J. Yang, “Mutual coupling reduction in MIMO microstrip patch array using tm10 and tm02 modes,” *IEEE Transactions on Antennas and Propagation,* vol. 69, no. 11, pp. 7562-7571, 2021.

[11] H. Lin *et al.*, “Weak-field-based self-decoupling patch antennas,” *IEEE Transactions on Antennas and Propagation,* vol. 68, no. 6, pp. 4208-4217, 2020.

[12] J.-F. Qian *et al.*, “Mutual coupling suppression between two closely placed patch antennas using higher order modes,” *IEEE Transactions on Antennas and Propagation*, pp. 1-1, 2023.

[13] L.-L. Yang *et al.*, “Dielectric patch antenna self-decoupling by proper structural parameters,” *IEEE Antennas and Wireless Propagation Letters,* vol. 21, no. 7, pp. 1447-1451, 2022.

[14] L. Sun, Y. Li, and Z. Zhang, “Decoupling between extremely closely spaced patch antennas by mode cancellation method,” *IEEE Transactions on Antennas and Propagation,* vol. 69, no. 6, pp. 3074-3083, 2021.

[15] E. M. T. Jones, “Coupled-strip-transmission-line filters and directional couplers,” *IRE Transactions on Microwave Theory and Techniques*, vol. 4, no. 2, pp. 75-81, April 1956.

[16] S. Yamamoto, T. Azakami, and K. Itakura, “Coupled strip transmission line with three center conductors,” *IEEE Transactions on Microwave Theory and Techniques,* vol. 14, no. 10, pp. 446-461, October 1966.

[17] D. M. Pozar, *Microwave engineering*: John Wiley & Sons, 2012.

[18] J.-G. Yook, and L. P. B. Katehi, “Micromachined microstrip patch antenna with controlled mutual coupling and surface waves,” *IEEE Transactions on Antennas and Propagation,* vol. 49, no. 9, Sept. 2001.

[19] Y.-F. Cheng, X. Ding, W. Shao, and B.-Z. Wang, “Reduction of mutual coupling between patch antennas using a polarization-conversion isolator,” *IEEE Antennas and Wireless Propagation Letters,* vol. 16, pp. 1257-1260, 2017.

[20] Y. Xin Mi, L. Xue Guan, Z. Xiao Yang, and C. Tie Jun, “Reduction of mutual coupling between closely packed patch antennas using waveguided metamaterials,” *IEEE Antennas and Wireless Propagation Letters,* vol. 11, pp. 389-391, 2012.

[21] A. Habashi, J. Nourinia, and C. Ghobadi, “Mutual coupling reduction between very closely spaced patch antennas using low-profile folded split-ring resonators (fsrrs),” *IEEE Antennas and Wireless Propagation Letters,* vol. 10, pp. 862-865, 2011.

[22] J.-D. Zhang, L. Zhu, N.-W. Liu, and W. Wu, “Dual-band and dual-circularly polarized single-layer microstrip array based on multiresonant modes,” *IEEE Transactions on Antennas and Propagation*, vol. 65, no. 3, pp. 1428-1433, 2017.

[23] Q. Tan and F. -C. Chen, "Triband circularly polarized antenna using a single patch," *IEEE Antennas and Wireless Propagation Letters*, vol. 19, no. 12, pp. 2013-2017, Dec. 2020.

Chapter 6
Conclusion and Future Work

6.1 Conclusion

This thesis has looked into the application of filter theory for designing multi-port antenna modules. Several high-performance decoupled antenna designs have been presented. It has been found that some filter design concept can also be applied to multi-antenna module designs, such as filtering network, bandstop filtering theory, coupled transmission theory, and electric and magnetic coupling theory.

By designing antennas with filtering ability, the out-of-band decoupling has been significantly reduced. Using the idea of dispersive band-stop filter, multiple slot antennas have been co-designed as a radiative bandstop structure. This concept has opened up a new direction for multi-port antenna design. Besides, it has been found that mutual coupling between two patches can be simply suppressed by controlling the electric and magnetic coupling. Finally, inspired by coupled-resonator theory, patch antennas operating over higher order modes have been decoupled with an extreme simple design process.

As the co-existence of multiple antennas becomes increasing challenging, the general theory and methodologies proposed in this thesis will find numerous applications in future antenna designs.

6.2 Future Work

Based the researchers conducted in this work, there are still more to explore. Possible extensions include:

- Co-design of multi-port filtering feeding network, in which more than two antennas are sharing one common feeding network without affecting each other.

- Extend the radiative bandstop concept to more antenna types, such as dipoles and PIFAs.
- Applying electric and magnetic coupling cancellation technique to other antenna types, such as slot antenna, PIFAs, dielectric resonator antenna, and SIW antennas.
- A lossless decoupling network which can be co-synthesized with the pre-given antenna structure.
- A long-term goal of my future research will be establishing a general theory and methodology for the design of filtering antenna and their extended systems.